



**Multiscale modeling of atomic transport phenomena
in ferritic steels**

LUCA MESSINA

Doctoral Thesis in Physics
Stockholm, Sweden 2015

TRITA-FYS 2015-80
ISSN 0280-316X
ISRN KTH/FYS/--15/80--SE
ISBN 978-91-7595-764-7

KTH Reaktorfysik
AlbaNova Universitetscentrum
Roslagstullsbacken 21
SE-106 91 Stockholm
SWEDEN

Akademisk avhandling som med tillstånd av Kungl Tekniska högskolan framlägges till offentlig granskning för avläggande av teknologie doktorsexamen i fysik fredagen den 11 december 2015 klockan 13:00 i FD5, AlbaNova Universitetscentrum, Roslagstullsbacken 21.

© Luca Messina, December 2015

Tryck: Universitetsservice US AB

Abstract

Defect-driven transport of impurities plays a key role in the microstructure evolution of alloys, and has a great impact on the mechanical properties at the macroscopic scale. This phenomenon is greatly enhanced in irradiated materials because of the large amount of radiation-induced crystal defects (vacancies and interstitials). For instance, the formation of nanosized solute clusters in neutron-irradiated reactor pressure vessel (RPV) ferritic steels has been shown to hinder dislocation motion and induce hardening and embrittlement. In Swedish RPV steels, this mechanical-property degradation is enhanced by the high content of manganese and nickel impurities. It has been suggested that the formation of Mn-Ni-rich clusters (which contain also Cu, Si, and P) might be the outcome of a dynamic process, where crystal defects act both as nucleation sites and solute carriers. Solute transport by point defects is therefore a crucial mechanism to understand the origin and the dynamics of the clustering process.

The first part of this work aims at modeling solute transport by point defects in dilute iron alloys, to identify the intrinsic diffusion mechanisms for a wide range of impurities. Transport and diffusion coefficients are obtained by combining accurate *ab initio* calculations of defect transition rates with an exact mean-field model. The results show that solute drag by single vacancies is a common phenomenon occurring at RPV temperature (≈ 300 °C) for all impurities found in the solute clusters, and that transport of phosphorus and manganese atoms is dominated by interstitial-type defects. These transport tendencies confirm that point defects can indeed carry impurities towards nucleated solute clusters. Moreover, the obtained flux-coupling tendencies can also explain the observed radiation-induced solute enrichment on grain boundaries and dislocations.

In the second part of this work, the acquired knowledge about solute-transport mechanisms is transferred to kinetic Monte Carlo (KMC) models, with the aim of simulating the RPV microstructure evolution. Firstly, the needed parameters in terms of solute-defect cluster stability and mobility are calculated by means of dedicated KMC simulations. Secondly, an innovative approach to the prediction of transition rates in complex multicomponent alloys is introduced. This approach relies on a neural network based on *ab initio*-computed migration barriers. Finally, the evolution of the Swedish RPV steels is simulated in a "gray-alloy" fashion, where impurities are introduced indirectly as a modification of the defect-cluster mobilities. The latter simulations are compared to the experimental characterization of the Swedish RPV surveillance samples, and confirm the possibility that solute clusters might form on small interstitial clusters.

In conclusion, this work identifies from a solid theoretical perspective the atomic-transport phenomena underlying the formation of embrittling nanofeatures in RPV steels. In addition, it prepares the ground for the development of predictive KMC tools that can simulate the microstructure evolution of a wide variety of irradiated alloys. This is of great interest not only for reactor pressure vessels, but also for many other materials in extreme environments.

Sammanfattning

Transport av orenheter genom kristalldefekter (vakanser och interstitiella atomer) har en stor inverkan på mikrostrukturen och de mekaniska egenskaperna i bestrålade legeringar, där defekterna produceras i stora mängder. Bildandet av nanokluster som innehåller lösningsatomer i neutronbestrålade ferritiska kärnreaktorstanker har visat sig hindra dislokationsrörligheten och leda till härdning och försprödning. Denna förlust av mekanisk hållfasthet försämras i svenska tankstål även på grund av de höga mangan- och nickelkoncentrationerna. Uppkomsten av Mn-Ni-kluster, som innehåller koppar, kisel och fosfor, har föreslagits vara förorsakad av en dynamisk process, där kristalldefekter funkar både som kärnbildningsplats och bärare av lösningsatomer. Ursprunget av och dynamiken för klusterbildningen måste därför utredas genom att fokusera på förhållandet mellan kristalldefekter och transport av lösningsatomer.

Syftet med den första delen i detta arbete är att modellera transport av lösningsatomer i låglegerat järn, för att identifiera de diffusionsmekanismerna för många olika typer av orenheter. Transport- och diffusionskoefficienter erhålls genom att kombinera *ab initio*-beräkningar av migrationsbarriärer med en exakt fältteoretisk modell. Resultaten visar att vakanser kan transportera lösningsatomerna vid relevanta temperaturer (≈ 300 °C), speciellt för de orenheterna som hittats i nanoklustren. Dessutom transporteras fosfor- och manganatomer helst av interstitiella defekter. Dessa transportmekanismer bekräftar defekternas förmåga att föra lösningsatomer mot existerande kluster. Detta kan också förklara den strålningsinducerade anrikningen av lösningsatomer vid korngränser och dislokationer som observerats experimentellt.

I den andra delen av arbetet överförs dessa kunskaper om transportmekanismer till kinetiska Monte Carlo (KMC) modeller, för att simulera utvecklingen av reaktortankens mikrostruktur. För det första behöver man beräkna parametrar angående stabiliteten och rörligheten av defektklustren som innehåller lösningsatomer. Dessa parametrar erhålls med hjälp av dedikerade KMC simuleringar. Därefter introduceras en innovativ metod för att förutsäga okända migrationsbarriärer i komplexa multikomponentlegeringar, som utnyttjar ett neuralt nätverk baserat på *ab initio*-beräkningar. Slutligen simuleras utvecklingen av det svenska tankstålet genom att modifiera rörligheten av defektklusterna, med avsikten att indirekt imitera inverkan av lösningsatomerna. Dessa simuleringar jämförs med mikrostrukturkarakteriseringen av övervakningsproverna och bekräftar antagandet att kluster med lösningsatomer bildas på små kluster av interstitiella atomer.

Som slutsats har detta arbete identifierat de atomära transportfenomen som driver bildandet av försprödande nanokluster i bestrålade kärnreaktorstanker, genom en pålitlig teoretisk modellering. Dessutom är detta första steget mot ett generellt KMC-prognosverktyg som kan simulera mikrostrukturen för många olika bestrålade legeringar. Detta är av stort intresse för kärnreaktorstanken liksom för många andra material under extrema villkor.

Sommario

SIMULAZIONI MULTISCALE DI FENOMENI DI TRASPORTO ATOMICO IN ACCIAI FERRITICI

Le proprietà meccaniche degli acciai dipendono dalla composizione chimica del materiale. Le impurità (soluti) inizialmente presenti possono diffondere nel reticolo cristallino grazie all'interazione con difetti puntuali (vacanze e interstiziali), che sono prodotti in grandi quantità quando gli acciai sono sottoposti a irraggiamento neutronico. Questo può portare alla perdita di integrità strutturale del componente. Per esempio, nei reattori nucleari le proprietà meccaniche del vessel sono peggiorate dalla formazione di cluster di soluti su scala nanometrica, che ostacolano la deformazione plastica del materiale ostruendo il movimento delle dislocazioni, e provocano l'indurimento e l'infragilimento del vessel, mettendone in pericolo l'integrità strutturale. In particolare, l'effetto nei vessel svedesi è accentuato dall'elevato contenuto di manganese e nickel, che comporta la formazione di cluster contenenti principalmente questi elementi, ma con tracce aggiuntive di rame, silicio e fosforo. Questo fenomeno potrebbe essere il risultato di un processo dinamico, per cui gli interstiziali, rallentati dalla presenza di atomi di manganese, diventano centri di nucleazione per il cluster, attirando altri difetti che possono trasportare con essi altre impurità. Il trasporto di impurità rappresenta perciò la chiave per comprendere le origini e il processo di formazione di questi agglomerati.

La prima parte di questo studio è dedicata al trasporto di soluti da parte di difetti puntuali in leghe ferritiche binarie, con l'intento di identificare i meccanismi di diffusione propri di una vasta gamma di impurità chimiche nel ferro. I coefficienti di diffusione e di trasporto sono ottenuti grazie all'utilizzo di accurati calcoli *ab initio* in un modello *mean-field* esatto. I risultati mostrano che alla temperatura del vessel (≈ 300 °C) le singole vacanze possono trasportare in maniera efficiente tutti i soluti che partecipano alla formazione dei cluster. Inoltre, il trasporto di atomi di fosforo e manganese avviene principalmente per mezzo di difetti interstiziali. Questi trend confermano la capacità dei difetti di trasportare impurità verso i centri di nucleazione. In aggiunta, grazie a questi risultati è possibile spiegare l'accumulo di soluti presso bordi di grano e dislocazioni, fenomeno osservato sperimentalmente durante l'irraggiamento.

Nella seconda parte, la conoscenza acquisita sui meccanismi di trasporto viene trasferita in un modello cinetico Monte Carlo, con l'obiettivo di simulare l'evoluzione microstrutturale degli acciai da vessel. In primo luogo vengono calcolati i parametri necessari per queste simulazioni, che comprendono la stabilità e la mobilità di cluster di vacanze e soluti. Successivamente, si propone un approccio innovativo per calcolare le frequenze di salto dei difetti in leghe ad elevata complessità chimica. Questo approccio prevede l'utilizzo di una rete neurale basata su precisi calcoli *ab initio*. Infine, l'evoluzione degli acciai svedesi viene simulata con una modalità *gray-alloy*, secondo cui l'effetto di impurità chimiche è introdotto indirettamente modificando la mobilità

dei cluster di difetti. Il confronto di queste ultime simulazioni con l'analisi sperimentale dei campioni estratti dai vessel svedesi permette di stabilire che i cluster di soluti si formano effettivamente a partire da agglomerati di interstiziali molto piccoli, invisibili al microscopio elettronico.

In conclusione, questo lavoro permette di determinare da un punto di vista teorico i fenomeni di trasporto atomico alla base della formazione di cluster nanometrici di soluti che provocano l'infragilimento del vessel nei reattori nucleari. Inoltre, vengono poste le basi per sviluppare un modello Monte Carlo completo che possa simulare l'evoluzione microstrutturale di una vasta gamma di leghe irraggiate. Questo permetterà di prevedere il comportamento e migliorare la progettazione di svariati materiali sottoposti a condizioni operative estreme.

Acknowledgments

During these years spent on modeling, I felt like I missed some experimental work. For this reason, I decided to arrange a homemade social experiment on... myself. My statement is that PhD acknowledgments are greatly biased by the euphoria (and the relief) of finishing up the work, since they are often written at last, just before sending the manuscript to the printing office. In this way, they are not really representative of the multiscale and multicolored feelings characterizing a five-year project. In order to prove this, I wrote the acknowledgments before the beginning of the thesis-writing process, some four months before the defense. I leave them to your free interpretation.

“It was a rainy Christmas Eve of almost five years ago when a younger, lighthearted and somewhat reckless version of myself decided to become a PhD student, only semiconscious of the consequences it would have had upon my psyche and my life path. Now I reached the other end of this warm hole, and I can look back with some satisfaction and no regrets. ”Caution: this project may be hazardous to your health”: if my first contract had come in a box, this would have been surely the warning message on top. After all, it is surely not so healthy to keep working on the same topic for 1655 days, many of which spent working with nobody else than myself. Besides my unquestionable tendency to make everything overdramatic, I am grateful for the accomplishments achieved during this long journey, which has been exciting and inspiring at times, monotonous and frustrating in other moments. Many people helped me pulling through these years, but the risk of sounding inane and banal in these lines is rather high. Because of my incurable aversion to anything that is mainstream and conformist, I will not mention anybody here. Everybody who has been close and helpful has already been thanked in person.”

Experiments and interpretations aside, it is really my pleasure to acknowledge the institutions that have hosted me and created such a stimulating working environment: the Reactor Physics department at KTH, the SRMP group at CEA Saclay, the material group of SCK-CEN, the R&D group of EDF, and the community of the recently renamed n-Fame workshop. The guidance of my supervisors Pär

Olsson, Nils Sandberg and Pål Efsing, as well as that of Maylise Nastar, Christophe Domain, Lorenzo Malerba and Nicolas Castin, have been fundamental and inspirational. A deserved acknowledgment goes also to the supercomputer facilities where my calculations were performed, not only for the corehours provided but also for the night shifts spent by keen technicians to fix the crashes caused by my sometimes erroneous scripts: the Swedish National Infrastructure for Computing (SNIC), the Swiss National Supercomputing Centre (CSCS), the Computational Simulation Centre of the International Fusion Energy Research Centre (IFERC-CSC), as well as the computational power provided by EDF. Finally, since none of this would have been possible without the most fundamental source of energy, I acknowledge the decisive financial support provided by Vattenfall AB, Göran Gustafsson Stiftelse, and the European Commission in the frameworks of the MATISSE and SOTERIA projects.

List of publications

Included publications

- I **Luca Messina**, Maylise Nastar, Thomas Garnier, Christophe Domain, and Pär Olsson, *Exact ab initio transport coefficients in bcc Fe-X (X=Cr, Cu, Mn, Ni, P, Si) dilute alloys*, Physical Review B **90**, 104203 (2014).
- II **Luca Messina**, Maylise Nastar, Nils Sandberg, and Pär Olsson, *Systematic electronic-structure investigation of substitutional impurity diffusion and flux coupling in bcc iron*, submitted to Physical Review B.
- III **Luca Messina**, Maylise Nastar, and Pär Olsson, *Ab initio-based investigation of solute-dumbbell transport and radiation induced segregation in Fe-X (X=Cr, Cu, Mn, Ni, P, Si) dilute alloys*, submitted to Physical Review B.
- IV **Luca Messina**, Lorenzo Malerba, and Pär Olsson, *Stability and mobility of small vacancy-solute complexes in Fe-MnNi and dilute Fe-X alloys: A kinetic Monte Carlo study*, Nuclear Instruments and Methods in Physics Research B **352**, 61-66 (2015).
- V **Luca Messina**, Nicolas Castin, Christophe Domain, and Pär Olsson, *Introducing ab initio-based neural networks for transition-rate prediction in kinetic Monte Carlo simulations*, submitted to The Journal of Chemical Physics.

Author's contributions

The author has performed the calculations and given interpretations and conclusions to the results for Papers I, II, III, and IV. In Paper V, the author has not performed the neural network training, but has conducted all the kinetic Monte Carlo simulations, and provided interpretations to the results. In addition, the author has developed a computational tool for the transport coefficient calculations in Paper III.

Publications not included

- VI **Luca Messina**, Zhongwen Chang, and Pär Olsson, *Ab initio modelling of vacancy-solute dragging in dilute irradiated iron-based alloys*, Nuclear Instruments and Methods in Physics Research B **303**, 28-32 (2013).
- VII **Luca Messina**, Pär Olsson, Maylise Nastar, and Waclaw Gudowski, *Multi-scale modeling of radiation-induced embrittlement in reactor pressure vessel steels*, Proceedings of ICAPP 2015, May 3-6, 2015 (Nice, France), 15572.
- VIII Nils Sandberg, Zhongwen Chang, **Luca Messina**, Pär Olsson, and Pavel Korzhavyi, *Modeling of the magnetic free energy of self-diffusion in bcc Fe*, Physical Review B **92**, 184102 (2015).

List of acronyms

AKMC	Atomistic kinetic Monte Carlo
ANN	Artificial neural network
APT	Atom-probe tomography
bcc	Body-centered cubic
BOL	Beginning of life
BWR	Boiling-water reactor
CPG	Chemical-potential gradient
CRP	Copper-rich precipitate
DBTT	Ductile-to-brittle transition temperature
DFT	Density-functional theory
dpa	Displacements per atom
EFPY	Equivalent full-power year
fcc	Face-centered cubic
FISE	Final-to-initial-state energy
KMC	Kinetic Monte Carlo
LAE	Local atomic environment
LBP	Late-blooming phases
LDA	Local-density approximation
MD	Molecular dynamics
MEP	Minimum-energy path
MFRT	Mean-field rate theory
MNP	Manganese-nickel precipitate
NEB	Nudged elastic band
nn	Nearest neighbor
NPP	Nuclear power plant
OKMC	Object kinetic Monte Carlo
PAS	Positron-annihilation spectroscopy
PAW	Projector-augmented wave
PBE	Perdew-Burke-Ernzerhof
PD	Point defect
PDC	Partial diffusion coefficient
PWR	Pressurized-water reactor

RIS	Radiation-induced segregation
RPV	Reactor pressure vessel
SANS	Small-angle neutron scattering
SCMF	Self-consistent mean field
TEM	Transmission-electron microscopy
US-NRC	United States Nuclear Regulatory Commission

Contents

Acknowledgments	vii
List of publications	ix
List of acronyms	xi
Contents	xiii
List of Figures	xv
List of Tables	xvii
1 Introduction	1
1.1 Radiation damage in RPV steels	2
1.2 Radiation damage in Ringhals reactors	3
1.3 Embrittlement at the atomic scale	7
1.4 Formation of "late-blooming phases"	9
1.5 Solute transport	10
1.6 Thesis objectives	11
2 Methodology	13
2.1 Qualitative description of flux coupling	13
2.2 Diffusion coefficients	18
2.3 Phenomenological transport coefficients	20
2.4 Radiation-induced segregation model	22
2.5 Self-consistent mean-field theory	24
2.6 Effect of external strain fields	31
2.7 Electronic-structure calculations	34
2.8 Kinetic Monte Carlo methods	39
3 Results I: Solute-transport mechanisms	49
3.1 Vacancy-assisted transport	49
3.2 Interstitial-assisted transport	54

3.3	Radiation-induced segregation tendencies	56
3.4	Effect of strain on interstitial transport	58
4	Results II: Kinetic Monte Carlo simulations	63
4.1	Vacancy drag in AKMC simulations	63
4.2	Stability and mobility of vacancy-solute clusters	65
4.3	ANN-KMC simulations of thermal aging in FeCu alloys	67
4.4	Microstructure evolution of Ringhals steels	70
5	Conclusions	75
	Bibliography	79

List of Figures

1.1	Schematic view of PWR vessel, and position of surveillance capsules . . .	4
1.2	Measured DBTT shifts in Ringhals surveillance samples	6
1.3	APT characterization of Ringhals surveillance samples	7
2.1	Vacancy and dumbbell jump mechanisms	14
2.2	Multifrequency framework for vacancy-assisted solute diffusion	16
2.3	Examples of solute-defect flux-coupling mechanisms.	17
2.4	Qualitative description of RIS tendencies in different flux-coupling regimes	18
2.5	Schematic representation of solute and defect concentration gradients near a sink	24
2.6	Symmetric pair kinetic interactions in the SCMF method	26
2.7	Summary of kinetic interactions in an extended SCMF model for inter- stitial diffusion	29
2.8	Explanation of one-point kinetic equations for the SCMF interstitial method	30
2.9	Elementary strain types	33
2.10	Representation of band forces in the NEB method	37
2.11	Schematic description of migration-barrier models in KMC simulations .	41
2.12	Structure of a one-layer artificial neural network	44
2.13	Extraction of cluster stability and mobility parameters from KMC sim- ulations	46
3.1	Vacancy-drag tendencies for selected impurities in Fe	50
3.2	Convergence of Cr and Ni vacancy-drag tendencies with respect to the interaction range	51
3.3	Transition-metal impurity group trends of several flux-coupling and dif- fusion properties	53
3.4	Solute transport via dumbbell mechanism for selected impurities in Fe .	55
3.5	Vacancy and interstitial RIS tendencies for selected impurities in Fe . .	57
3.6	Strain effects on mixed-dumbbell stability and solute transport via dumbbell mechanism	59
3.7	Variation of interstitial-solute flux coupling in dislocation strain fields .	59

4.1	Comparison of vacancy drag between SCMF and AKMC	64
4.2	Stability and mobility of vacancy-solute pairs	65
4.3	Stability and mobility of vacancy-solute clusters	66
4.4	Vacancy-cluster properties as functions of solute concentration	68
4.5	Properties of Cu clusters by ANN-based AKMC simulations	70
4.6	ANN-based thermal-aging evolution of a Fe-1.34%Cu alloy	71
4.7	OKMC simulation of Ringhals RPV steels	72
4.8	OKMC parametric study of Ringhals RPV steels	74

List of Tables

1.1	Properties of last extracted surveillance capsules	5
3.1	Summary of diffusion and flux-coupling properties for several impurities in Fe	60
4.1	Experimental characterization of Ringhals welds for OKMC simulations	73

"We are all born naked.. and the rest is drag"
Rupaul Andre Charles

Chapter 1

Introduction

Many of today's challenges from an environmental, social, and economical perspective are related to climate changes and extreme disparities among countries in terms of health, wealth, and distribution of resources. Immediate counteracting actions are not only desirable but most likely necessary in order to preserve the environment and improve living standards worldwide. In this context, a wise planning in terms of energy supply and resource exploitation is required. In particular, the mix of energy sources for electricity production must be gradually readjusted, with a substantial phase-out from fossil fuels, in order to meet a drastic reduction of carbon-dioxide (CO₂) emissions and guarantee the sustainability of the inevitable increase of energy demand in the emerging developing countries, as well as in those that will hopefully develop in the future. Alongside renewable energies, nuclear power is a candidate in the future energy mix, thanks to its high reliability, low production price and considerably lower CO₂ emissions with respect to fossil fuels [1]. However, it has to face diversified public opinion, or severe opposition in some cases, as well as the issue of long-lived nuclear waste disposal. In this sense, it is important to promote the research on Generation-IV reactors¹ and fusion reactors, which can potentially solve the issue of long-lived nuclear waste and improve the public acceptance of nuclear-powered electricity production [2, 3].

The path towards commercially-ready Generation-IV reactors is still long [3], and that towards fusion reactors even longer [2]. Moreover, given the polarization in the public opinion, the possibility of replacing old-generation power plants with new ones is in many countries object of strong political debate, independently of the actual economical and environmental advantages and disadvantages [4, 5]. While waiting for political decisions about this matter, it becomes therefore extremely important to monitor and sustain the health of currently-operating nuclear power plants (NPP), as their prolonged operation can provide stable and low-cost elec-

¹Generation IV refers to a group of innovative nuclear-reactor concepts that are currently under research and development and are aimed at improving safety and fuel utilization, as well as eliminating long-lived nuclear waste by fuel recycling. For more information, see the Gen-IV platform website (<https://www.gen-4.org>).

tricity supply. It is needless to say that this must not occur at the expense of safety. In regard to this debate, the situation in Sweden is not dissimilar to other countries. The currently-operating 10 reactors, 3 pressurized-water reactors (PWR) and 7 boiling-water reactors (BWR), are now passing 30 years of operation, and lifetime extensions are granted on a periodic bases after careful safety assessments [6]. However, the possibility of building new reactors has so far been the object of vacillating political decisions. Monitoring the safety conditions of current NPP's is therefore a primary concern in order to secure the electricity supply.

The integrity of the reactor structural components during operation is challenged by extreme conditions in terms of temperature, mechanical loads and neutron irradiation, and the conditions vary considerably depending on the position and the task the component is to fulfill. But whereas most of the internal components can be replaced as soon as they cannot guarantee a safe operation, the same cannot be stated for the most massive component of all, the reactor pressure vessel (RPV). The RPV plays a determinant role in preserving the reactor integrity. The even remote risk of RPV failure would lead not only to environmental hazards, but also to unaffordable replacement costs. Radiation-damage phenomena in RPV steels are therefore extremely important to investigate, in order to fully understand and predict the evolution of the RPV microstructure, and consequently of its macroscopic mechanical properties. Such issues are of interest not only for the current NPP generations, but also for the development of Generation-IV reactors. Different types of steels are in fact used in many other internal and structural components in present and future reactor concepts, including fusion reactors, and are all prone to radiation damage to different extents [7, 8]. Research about radiation damage is hence becoming nowadays more and more crucial for the development of new reactors and for the future of nuclear power itself.

1.1 Radiation damage in RPV steels

Radiation damage in NPP components is mainly caused by neutrons hitting the structures inside and around the reactor core. The interaction with the material crystal structure produces a large amount of crystal defects, triggering a chain of events that lead to a severe degradation of the mechanical properties [9]. In current NPP's, austenitic stainless steels are normally employed for internal components [10], whereas ferritic steels² are used for RPV's [11]. The reason lies in their mechanical properties and the different response to radiation. Internals must withstand higher irradiation fluxes and damage doses³ at usually higher temperatures. Austenitic steels are then chosen because of their excellent high-temperature mechanical properties, creep strength and corrosion resistance [10]. Nevertheless,

²Ferrite and austenite are two stable phases in the iron-carbon phase diagram. Ferrite is the stable phase at room temperature, whereas austenite is stabilized at room temperature by the addition of nickel.

³The damage dose corresponds to the integral of the damage flux over time.

they are subjected to severe void swelling [12]. On the other hand, RPV's must withstand an apparently less harsh environment in terms of flux, dose, and temperature, but for much longer times. Ferritic steels are then the best choice thanks to their better resistance to thermal stresses [11]. However, in spite of the less severe environment, radiation-induced degradation still occurs.

RPV steels usually operate at 290-300 °C and are subjected to a low but continuous neutron flux. The high-energy neutrons (> 1 MeV) create defects in the crystal structure, and since the RPV is not replaceable, the damage is accumulated throughout the reactor lifetime. The steel contains varying combinations of impurities that depend on the design and the manufacturing process. From the radiation-damage standpoint, the most critical area of the vessel is the beltline region around the core (see Fig. 1.1a), and the most severe effects are observed in welds, because they usually contain the highest amount of impurities [13]. The link between crystal defects and impurities is the key point to understand such effects.

Since the construction of Generation-II reactors, surveillance programs have been established in order to monitor the change of mechanical properties with time and accumulated dose. Therefore, several capsules mimicking the composition of the base and weld metals are placed inside the vessel, and are progressively removed in order to test their mechanical properties. They are usually located next to the wall but at a closer distance to the core (Fig. 1.1b). In such a way, the capsules receive a higher neutron flux, and they anticipate the evolution of the actual RPV steel [13]. For instance, capsules removed after about 20 years of operation in Swedish PWRs have actually absorbed the equivalent dose of 60 years [15]. If the effect of different neutron-flux levels (the flux effect) is known, it is possible to infer the RPV end-of-life properties by analyzing the extracted capsules.

Regardless of the specific composition, neutron irradiation has been observed to yield the same effect on any RPV steel: it decreases the fracture toughness of the material by increasing the yield strength (hardening) and the ductile-to-brittle transition temperature (DBTT) (embrittlement) [11]. This has been found for many types of RPV steels worldwide [15, 16, 17, 18]. The effect is more prominent in PWR's with respect to BWR's, because in the former the RPV wall is closer to the core and is hence subjected to a higher neutron flux. The DBTT shift represents the most severe issue: if the DBTT temperature rises excessively close to the operation temperature, the operation becomes unsafe, since the material might become brittle during shutdown, and the reactor must be decommissioned.

1.2 Radiation damage in Ringhals reactors

Ringhals is a nuclear site in the south-west of Sweden, hosting the three Swedish PWR units and one BWR. Unit R1 and R2 are older (1976 and 1975, respectively), whereas unit R3 and R4 were opened in 1981 and 1983 [19]. For the latter units, a surveillance program was enforced, and the capsules were progressively removed and analyzed. The last (and final) ones were removed in 2007, at a dose level

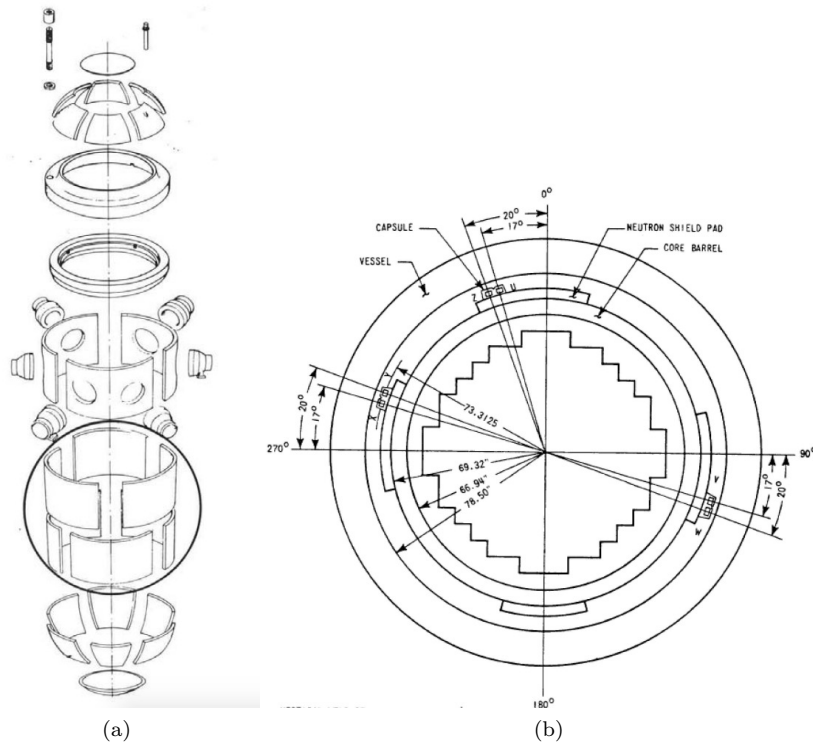


Figure 1.1: (a) Schematic view of a PWR vessel before welding [13]. The area in the circle marks the beltline region around the core, which is subjected to the highest neutron flux. (b) Reactor section showing the position of the surveillance capsules (U, V, W, X, Y, Z) in Ringhals PWR's [14].⁴

corresponding to over 60 years of operation [14], and are now being tested and characterized. The composition and operation conditions of the last extracted weld-metal specimens are shown in Table 1.1.

Fracture-toughness and Charpy tests have shown a yield-strength increase and a severe DBTT shift, far above the prediction of the US-NRC Regulatory Guide 1.99 [21] (Fig. 1.2). The DBTT shifts are the highest ever recorded in commercial power plants [20]. In addition, the mechanical degradation has seemingly not reached a saturation level, as opposed to the regulatory prediction. The higher shifts observed for unit R3 have not been yet explained, but have been associated to different heat treatments before the reactor start [14], or to the slightly higher copper content in R3 [20]. By means of accelerated irradiation experiments [22], no flux effect was

⁴Fig. 1.1a reprinted, with permission, from ASTM STP 1547 Effects of Radiation on Nuclear Materials: 25th Volume, copyright ASTM International, 100 Barr Harbor Drive, West Conshohocken, PA 19428. Fig. 1.1b reprinted with explicit permission by the IAEA.

Table 1.1: Initial and operation conditions, composition [14], and post-irradiation microstructure characterization [20] of the last surveillance capsules (U) extracted from Ringhals units R3 and R4 in 2007.

Reactor (Specimen)	R3 (E6)	R4 (N11)
Temperature	284 °C	284 °C
Flux	$1.47 \cdot 10^{15}$ n/m ² s	$1.49 \cdot 10^{15}$ n/m ² s
Fluence	$6.39 \cdot 10^{23}$ n/m ²	$6.03 \cdot 10^{23}$ n/m ²
EFPY ^[a]	13.8 years	12.8 years
DBTT at BOL ^[b]	-75 °C	-75 °C
DBTT shift	192 °C	162 °C
Average cluster radius	1.1 ± 0.29 nm	1.2 ± 0.39 nm
Cluster number density	$3.3 \cdot 10^{23}$ m ⁻³	$4.3 \cdot 10^{23}$ m ⁻³
Chemical composition (at.%)		
Cu	0.07	0.04
Ni	1.50	1.58
Mn	1.48	1.37
Si	0.42	0.28
P	0.016	0.027
Cr	0.07	0.04
C	0.24	0.31
Mo	0.31	0.29
other	0.082	0.067

^[a] Equivalent full-power years.

^[b] Beginning of life.

found on the change of mechanical properties: this confirms that the properties of the extracted capsules are very likely to correspond to those of the actual RPV steels. The chemical composition of the alloy is similar to that of other RPV steels worldwide, with the exception of a simultaneous high concentration of manganese and nickel in the weld metal, along with a low copper concentration [15]. Manganese and nickel are therefore strongly suspected to play a major role. Only a careful investigation of the microstructure phenomena triggered by neutron irradiation can therefore shed a light on the causes of such a behavior.

After the mechanical testing, the samples have been characterized by atom-probe tomography (APT) [23, 20, 24], small-angle neutron scattering (SANS) [23], and transmission-electron microscopy (TEM) [25, 26], in order to analyze the post-irradiation microstructure. All the APT and SANS analyses consistently revealed the presence of a high density of solute-rich clusters, as for instance the ones shown in Fig. 1.3a, which can be directly linked to the change of mechanical properties. The measured mean cluster size depends on the analysis technique, but is always between 2 and 5 nm in diameter. The composition analysis shows that such nanostructures are still iron-rich (60 at.%), and contain nickel (20 at.%), manganese (15 at.%), silicon (5 at.%), and traces of copper that are surprisingly large compared to the initial low copper content in the matrix. Rather than solute clusters, it is there-

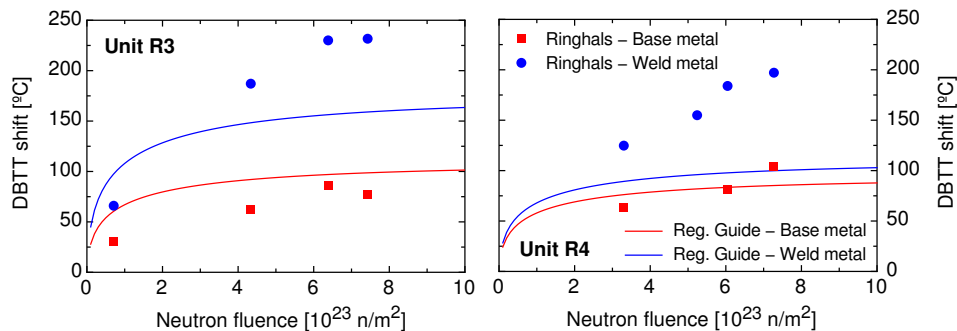


Figure 1.2: Measured ductile-to-brittle transition temperature (DBTT) shifts [14] of the surveillance samples extracted from Ringhals units R3 and R4, as functions of accumulated dose, and comparison with predictions of the US-NRC Regulatory Guide 1.99 [21].

fore more correct to define such features as *solute-rich complexes*. Such complexes are observed both in the bulk metal and along dislocation lines [23]. Moreover, a heavy segregation of phosphorus [20] (Fig. 1.3b) as well as a less pronounced manganese segregation were observed [23]. On the other hand, TEM analysis showed the formation of some oxide particles [25, 26], some manganese-rich iron-based particles, and smaller molybdenum-rich particles on grain boundaries [25], although the smallest size was approximately 15 nm. No evidence for dislocation loops was found [26].

Post-irradiation annealing was performed on the same type of samples [27, 24] in order to test the mechanical property recovery. Thermal annealing (usually at 400–500 °C) is often operated on RPV's to restore the initial mechanical properties, as it allows for the dissolution of the embrittling nanofeatures formed during irradiation [15]. Other countermeasures, such as the placement of neutron-shielding pads, or the use of dummy fuel elements, are possible but have more invasive consequences on reactor operation [15]. The annealed Ringhals samples showed a marked property recovery at 500 °C. Only at this point, and not at lower temperature, it was possible to observe the partial dissolution of the Mn-Ni-Si-rich clusters, mainly by migration of manganese atoms [24]. This observation led to the conclusion that manganese migration might occur thanks to a correlation with point defects (whose diffusion is strongly enhanced at this annealing temperature with respect to the operation temperature); it was also speculated that this would be the underlying driving mechanism for the formation of these clusters in first place. Such results suggest that impurity-transport phenomena at the atomistic level might be the main actors in play.

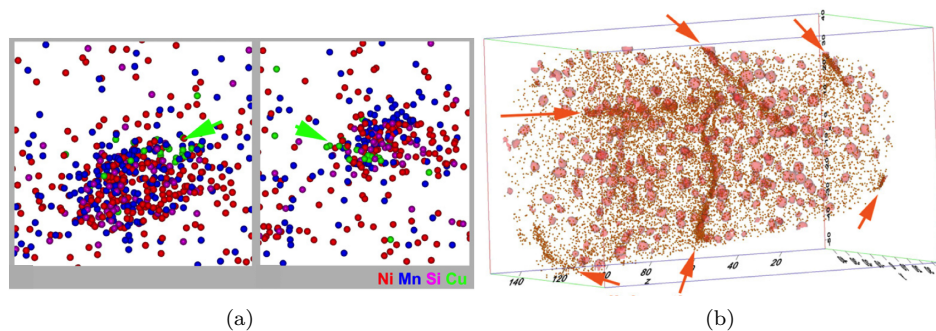


Figure 1.3: Atom-probe tomography characterization of Ringhals surveillance samples[20]. (a) Examples of 1-nm thick atom-map slices through a solute-rich cluster in Ringhals unit R3. (b) Evidence of phosphorus segregation on dislocation lines in Ringhals unit R4.⁵

1.3 Embrittlement at the atomic scale

Dislocation motion is the link between the observed post-irradiation microstructure and the degradation of mechanical properties. The material ductility is related to the capability of dislocations to move across the crystal in presence of external loads. It is well known that solute clusters can act as hindrances for dislocation motion [28, 29, 30]. The yield-strength increase (hence the hardening) is due to the energy increment needed by the dislocation to pass the solute cluster. Moreover, in normal conditions the material is brittle below a threshold temperature (the DBTT), at which dislocation motion is severely impeded. Then, under irradiation a DBTT shift occurs because the presence of solute clusters is capable of obstructing dislocation motion at higher temperatures [31, 13]. Solute segregation on dislocations has a similar effect, as it makes the dislocation motion more difficult [32]. Another radiation-damage phenomenon (*intergranular embrittlement*) is related to the segregation of solute atoms on grain boundaries: solute accumulation leads to a decrease of the cohesive energy between grains, and favors intergranular fracture [13].

In order to understand such phenomena, it is necessary to analyze them from the atomic-scale perspective. The RPV ferritic steels are dilute iron alloys with a body-centered cubic (bcc) structure. They contain several impurities, among which the most important ones from the radiation-response standpoint are copper, nickel, manganese, silicon, and phosphorus (see for instance the composition of Ringhals steels in Table 1.1). During operation, high-energy neutrons sporadically hit the

⁵Reprinted, with permission, from Journal of Nuclear Materials, vol. 37, M. K. Miller, K. A. Powers, R. K. Nanstad, and P. Efsing, *Atom probe tomography characterizations of high nickel, low copper surveillance RPV welds irradiated to high fluences*, pp. 107-115, © 2013 Elsevier B.V.

RPV and produce the *primary damage*: a lattice atom is displaced from its site and form a *Frenkel pair* (one vacant site and one interstitial atom). The displaced atom causes in turn a cascade of displacements by colliding with several neighboring atoms. After the process, many Frenkel pairs immediately recombine, but some of them survive. Depending on the incoming neutron energy, some small defect clusters (voids and loops) might also form. This is traditionally referred to as *matrix damage* [31]. In RPV's, since the neutron flux is low, such cascades are not very frequent in a given local neighborhood of the crystal. For this reason, thermal diffusion of defects occurs undisturbed, leading to defect recombination, migration to sinks (grain boundaries or dislocations) or coalescence of the small clusters into bigger ones. Along their path, defects may also encounter impurity atoms. In certain conditions, the solutes can be transported by the defects towards preferential areas of the crystal, where solute-rich atmospheres or precipitates can form. In addition, it has been demonstrated that some solute atoms are also capable of slowing or even trapping specific defect types, as is the case for chromium or manganese on small interstitial loops [33, 34]. This can strongly affect the microstructure evolution, as it alters the rate of recombination or migration to sinks. Moreover, an immobilized defect cluster can act as a nucleation site for solute clusters, as it attracts other defects that are possibly coupled with solute atoms [35, 34]. This speculated complex kinetic mechanism might be at the origin of the experimental observations in the Ringhals RPV steels, as well as in many other RPV steels [36, 37, 38].

However, the observation of solute precipitation is definitely not a novelty of the recent years. Such phenomena have been known for a long time. As a matter of fact, RPV embrittlement was expected since the early phases of nuclear-power production. For instance, the regulatory prediction of Fig. 1.2 depends on the concentrations of copper and nickel impurities, because RPV embrittlement has been traditionally associated to the formation of copper-rich clusters, sometimes enhanced by the presence of nickel [13]. Copper precipitation is expected and dictated by the phase diagram, since such steels are manufactured in order to contain copper quantities far above the (very low) solubility limit. There exists hence a thermodynamic driving force for copper clusters to form, or in other words the formation of copper clusters decreases the free energy of the alloy. For a long time, only copper-rich clusters were visible, both in irradiated and non-irradiated conditions. Under irradiation, the precipitation process is faster because of the increased defect concentration. This phenomenon is therefore *radiation enhanced*, i.e. it is accelerated by irradiation but would also occur without it. At high damage doses, copper precipitation is expected to reach a saturation level, because the matrix is progressively depleted in copper and the bulk copper concentration approaches the solubility limit. This is the reason why the embrittlement prediction of Fig. 1.2 reaches a plateau.

1.4 Formation of "late-blooming phases"

In order to limit the expected DBTT shifts, the maximum allowed copper content in RPV steels was set to 0.1 at.% or lower in many countries [13]. However, when higher damage doses in operating RPV's were reached, the surveillance programs showed a surprising deviation from prediction. Solute clusters were observed even in low-copper or copper-free alloys, and contained other impurities such as manganese, nickel, and silicon. This is the case, for instance, of the nanoclusters observed in Ringhals low-copper samples. With respect to copper precipitation, this phenomenon was much less understood, because the manganese and nickel concentrations were much below the solubility limit of the respective iron binary alloys. Hence there would be no apparent thermodynamic driving force for these clusters to form.

The formation of these nanofeatures led to the necessity of redefining the predictive curves used to design RPV alloys and monitor the evolution of the existing ones. This required a deeper physical understanding of the whole precipitation process, and much effort has been devoted since then to this scope. These new type of features were initially named *late blooming phases* (LBP) [39], and this name has been in use for many years, even in the public announcement of this thesis project. These clusters were defined as "late blooming" because they were observed only above a certain dose threshold, and were "phases" because they appeared thermodynamically stable. Their effective thermodynamic stability was anyway not certain, because the phase diagram of this multicomponent alloy was (and still is) largely unknown.

The LBP name has been strongly criticized in recent years and has been now almost abandoned. The most common definition nowadays is *manganese-nickel precipitates* (MNP). Many studies [40, 41, 42] have shown that "the so-called *late blooming phases* might as well be neither *late*, nor *phases*" [40]. Their formation is observed from the very beginning of irradiation, and their effective thermodynamic stability is uncertain, since such clusters are not observed in thermally-aged alloys. The "late-blooming" effect is late only in copper-rich alloys, since the growth rate of traditional copper-rich precipitates is much faster thanks to the strong driving force acting on copper. The overall effect on macroscopic properties is therefore initially overshadowed, and becomes visible only after copper precipitation has reached saturation. It has been shown that in copper-rich alloys two types of precipitates can be distinguished: copper-rich (CRP) and manganese-nickel precipitates [37, 40]. The former are characterized by a copper core and can be decorated by other impurities, whereas the latter are enriched in manganese and nickel, and decorated by other solutes (such as silicon and phosphorus). The different compositions suggest the formation mechanisms to be different.

The thermodynamic stability of MNP's has been object of several studies, aiming at calculating the phase diagram of the Fe-MnNiCu multicomponent alloy [40, 43, 38]. It was shown that some stable complexes might exist in the phase diagram [38], although the variety of compositions and structures of the observed

precipitates is unlikely to be a feature of an ordered phase. On the other hand, recent calculations suggest that the MNP's might be stabilized in presence of point defects, and specifically self-interstitial clusters [41, 44]. Furthermore, the authors of [41] claim the existence of a small window in the phase diagram which would allow for solute precipitation, but the driving force is so weak that it would never occur without the aid of irradiation. In case this phases are not thermodynamically stable (at least not without the presence of defects), they would be *radiation induced*, rather than *radiation enhanced*, since defect-induced solute transport would be required.

1.5 Solute transport

The MNP's might form as well as the result of a purely kinetic process, exclusively involving the coupling between defect motion and solute atoms. One of the suggested formation mechanisms is the following [37, 40, 45]. Some impurities such as manganese might reduce the mobility of interstitial loops. The loop gathers progressively more and more manganese atoms, until it is completely immobilized. At this point, the sessile loop, decorated with some manganese atoms, will attract other single vacancies or interstitials. In case defects are capable of dragging solute atoms with them, they would come to the immobilized loop carrying solute atoms with them. In this way the former loop act as a nucleation site and gets decorated with more and more solutes: a solute cluster is born.

The solute clusters that are observed in many APT works would therefore contain an interstitial loop in their core. From an experimental point of view, this theory has not been confirmed yet because of the small size of such loops with respect to the current TEM resolution [HernandezMayoral:2010tm]. At any rate, recent experimental observations have actually observed the formation of ring-shaped solute-rich complexes, which would strongly support this hypothesis [46]. Moreover, the analysis of irradiated Fe-Mn binary alloys has shown that manganese increases the density of interstitial clusters, and this increase can be directly linked to the observed irradiation-induced hardening [35].

Modeling can provide an important contribution to the investigation and the possible confirmation of this atomic-scale mechanism that cannot be experimentally observed. However, the modeling of such phenomena requires the detailed knowledge of the solute-transport mechanisms, which are unknown or explained only from a qualitative standpoint. For instance, it has been argued from positron-annihilation spectroscopy (PAS) analysis that the formation of solute-vacancy clusters [47, 48] in irradiated iron alloys would prove the capability of vacancies to drag these impurities. In addition, the heterogenous precipitation of manganese-rich clusters next to defect sinks has been linked to the possibility of manganese drag by point defects [42], although no work has been so far able to determine precisely the mechanisms driving the diffusion of manganese solutes. As a further example of unknown solute-transport phenomena, the evolution of an Fe(C)-MnNi model alloy

was well reproduced by a kinetic Monte Carlo (KMC) study, only assuming the substantial immobilization of small vacancy clusters due to the presence of solute atoms [49], but such effect was postulated without evidence.

Given the lack of knowledge about solute-transport mechanisms in this type of alloys, which has been evidenced in previous works [42, 43], solute-transport phenomena have been chosen as the main subject of this thesis. In summary, two theories have been advanced to explain the formation of MNP's: the radiation-enhanced theory (existence of a thermodynamic driving force for precipitation, accelerated by radiation), and the radiation-induced theory (clusters are a consequence of kinetic coupling between solutes and defects). The latest investigations suggest something in between: there might be both a weak thermodynamic driving force and a strong kinetic coupling [43]. In either case, the solute-transport mechanisms need to be carefully investigated, in order to possibly confirm (or disprove) the suggested formation mechanisms and explain the observed segregation of solute atoms on dislocations and grain boundaries.

1.6 Thesis objectives

This thesis aims therefore at providing the missing link between the experimental observation and the atomic diffusion processes, by analyzing the details of impurity transport in ferritic alloys. The primary objective is to contribute to the understanding of clustering and segregation phenomena in current RPV steels, in the general effort of explaining the reasons for the observed accelerated degradation of mechanical properties, and of providing an ultimate tool that could model such phenomena on a multi-scale basis, from the atomistic level to the macroscopic properties [50, 51]. The study here presented is applicable to a much wider range of materials and applications, which involve not only ferritic steels that might be used in Generation-IV reactors [52] and fusion reactors [7, 8], but also metallurgical processes, where the knowledge of solute-transport mechanisms is crucial for driving the process to the desired microstructure [53, 54].

The thesis objectives are therefore summarized as follows.

1. Cover the gap in the knowledge of solute-defect kinetic coupling in RPV alloys, by investigating the properties of point defects as solute carriers, in order to demonstrate their capability of causing solute clustering and segregation, regardless of the possible existence of thermodynamic driving forces. This is achieved through the calculation of transport coefficients of dilute binary alloys, which reveal the intrinsic solute-defect flux-coupling tendencies and determine the diffusion mechanisms and correlations that are likely to guide the precipitation and segregation processes.
2. Apply the acquired solute-transport knowledge to the development of predictive KMC modeling tools of RPV microstructure evolution. This is achieved by investigating different approaches to the parameterization of such tools,

and by providing a database of solute-defect cluster properties that can be readily implemented in KMC simulations. In addition, such tools are applied to the specific case of the Ringhals RPV steel in order to support the surveillance campaign and aid the interpretation of the microstructure characterization. The development of reliable predictive tools, reproducing the correct solute-transport mechanisms, can greatly contribute to the understanding of the long-term RPV evolution beyond the current lifetime span.

The manuscript is organized as follows. Chapter 2 is dedicated to a qualitative description of the atomistic diffusion mechanisms and to a review of the modeling methods that have been employed in the papers attached at the end of the manuscript (from I to V). The results of the thesis are included in Chapters 3 and 4. The former presents the investigation of solute-transport mechanisms by vacancies (Papers I and II) and interstitials (Paper III). In the latter are presented the KMC calculations of solute-vacancy cluster properties (Paper IV), the application of an innovative KMC model based on the use of neural networks (Paper V), and the simulated microstructure evolution of Ringhals RPV steels. Finally, the achievements of this work are summarized in the last chapter, which also provides several suggestions for future work.

Chapter 2

Methodology

2.1 Qualitative description of flux coupling

The crystal lattice of a ferritic alloy is a body-centered cubic structure. Transport of substitutional impurities occurs mainly through point defects (PD), namely vacancies or self-interstitial atoms. Non-substitutional impurities, such as carbon or oxygen, can diffuse independently on an interstitial sublattice [55]. At any rate, all impurities included in this study¹ are substitutional, i.e. they replace one iron atom in the bcc lattice, and can diffuse only through exchange with vacancies or self-interstitials.

In thermal-equilibrium conditions, the PD concentration depends on the formation free energy [58]:

$$c_x^{\text{eq}} = \exp\left(-\frac{G_x^{\text{f}}}{k_{\text{B}}T}\right) \quad (2.1)$$

with $G_x^{\text{f}} = H_x^{\text{f}} - TS_x^{\text{f}}$ ($x = \text{V}, \text{I}$). H_x^{f} and S_x^{f} are respectively the formation enthalpy and entropy, k_{B} is the Boltzmann constant and T the absolute temperature. Since the formation energy of self-interstitials is much larger than that of vacancies [59], self-interstitials do not form in thermal conditions. Nevertheless, under neutron irradiation there is a constant and equal production of both PD types, much above the thermal-equilibrium concentrations. Atomic diffusion is then considerably enhanced by the supersaturation of mobile PD's, and the interstitial contribution to diffusion must be included in the picture.

The PD diffusion mechanisms are depicted in Fig. 2.1. The vacancy moves by exchange with one of the eight nearest neighbors (nn). Concerning self-interstitials, the most stable configuration in bcc iron is represented by the $\langle 110 \rangle$ dumbbell (Fig. 2.1b) [59]. The dumbbell migration mechanism is more complex than vacancies: either one of the two dumbbell atoms can migrate to a neighboring target site (two

¹Phosphorus can be in solution in iron both as a substitutional and a foreign-interstitial impurity [56, 57].

per atom, marked with 'X' in Fig. 2.1), and the final configuration can have the same orientation (translation mechanism) or be rotated by 60° (rotation-translation mechanism) [60]. For each rotation-translation there are two possible final configurations, e.g. a $\langle 110 \rangle$ dumbbell can rotate during the transition to a $\langle 011 \rangle$ or a $\langle 101 \rangle$ orientation. Therefore, a given dumbbell can perform a total of 12 distinct jumps. In addition, four 90° onsite rotations can also take place.

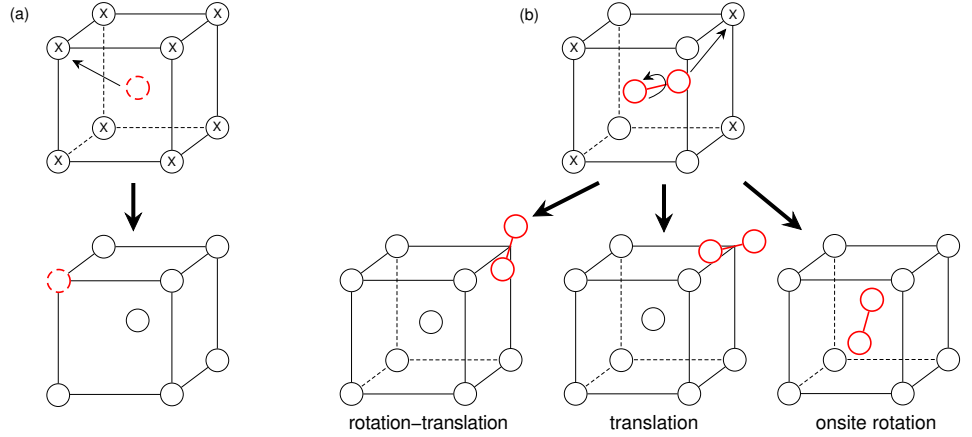


Figure 2.1: Possible transitions of (a) a vacancy and (b) a $\langle 110 \rangle$ -dumbbell in bcc iron. The allowed target sites are marked with 'X'.

Each of these transitions is normally modeled in the framework of transition-state theory as a thermally-activated jump with rate [58]:

$$\omega = \nu \exp\left(\frac{-G^m}{k_B T}\right) = \nu \exp\left(\frac{-H^m}{k_B T} + \frac{S^m}{k_B}\right). \quad (2.2)$$

H^m is the migration enthalpy (commonly referred to as migration energy or barrier), S^m the migration entropy, and ν the attempt frequency. S^m is often neglected as it is usually small compared to the enthalpy contribution [61]. The migration free energy is provided by random thermodynamic fluctuations of the lattice, whose frequency (related to ν) is driven by phonon vibrations. In kinetic studies, the correct description of migration rates is crucial, and represents therefore the focus of this work.

In a pure crystal, a defect has an equal probability to move to any of the target sites. However, this is no longer valid when substitutional impurities are present. Firstly, the exchange frequency between a vacancy and a neighboring impurity differs from that of the host atom. In addition, the interaction between impurities and PD's alters the jump frequencies of the iron atoms next to the vacancy. The same applies for self-interstitial defects next to a solute atom. It is this perturbation of the network of jump frequencies around the solute atom that determines diffusion

mechanisms, rates, and flux coupling. The extent of the solute-defect interactions and the number of chemical species determine the amount of jump frequencies that are perturbed and must therefore be considered separately. For instance, the most traditional multifrequency model [62] for vacancy diffusion in dilute² bcc alloys considers interactions up to the 2nn distance, and entails the distinction of nine types of transitions. The latter are the solute jump frequency and all vacancy jumps starting from or ending into a configuration where the solute-vacancy distance is shorter or equal to the 2nn one. In this work, original multifrequency frameworks for both vacancy and dumbbell-mediated diffusion have been developed, extending those of previous studies [63, 64], and are presented in details in Papers I and III. Fig. 2.2 shows the extended multifrequency model for vacancy migration. The solute-vacancy interaction range extends to the 5nn, as some impurities have a non-negligible interaction at such distance. This yields a network of 26 distinct frequency types that are perturbed by the solute, with the perturbation progressively fading out with distance.

The defect jump frequency depends therefore on the chemical composition of the *local atomic environment* (LAE), i.e. the ensemble of atoms included in the interaction area. In a non-dilute alloy, the number of possible LAE configurations grows quickly with the interaction range and the number of chemical species. Hence, even in a concentrated binary alloy, the number of configurations is too large for each jump frequency to be calculated separately. This issue is discussed in Section 2.8. At any rate, the study of impurity-transport mechanisms in dilute binary alloys represents the necessary starting point of solute-transport modeling, as it allows for the investigation of the intrinsic kinetic interactions between each solute species and each PD type.

The combination of defect jump rates around the solute atom determines the way the solute atom diffuses in the crystal. Normally, vacancy-assisted diffusion occurs through the inverse Kirkendall mechanism [58]: the atomic flux is opposed to the vacancy flux, because the vacancy moves by exchanging with either solute or host atoms. In this situation, the solvent and solute diffusion rates are different, as they depend on the jump frequencies and the solute-vacancy interactions. However, in given conditions the solute flux can reverse into the direction of the vacancy flux. This phenomenon is known as *vacancy drag* [65]. It occurs when the dissociation probability of a solute-vacancy pair is low, and the combination of jump frequencies in the vacancy LAE allows for the vacancy to "turn around" the solute and produce consecutive solute jumps in the same direction, as depicted in Fig. 2.3a.

Dumbbells can induce solute transport in a different way. In this case, the solute can move only in a mixed-dumbbell configuration, as depicted in Fig. 2.3b. The possibility of solute transport then depends on the mixed-dumbbell stability and mobility: the latter can diffuse through a sequence of rotation-translation jumps,

²In the dilute-alloy limit, the interaction of only one solute atom and one point defect is considered, as the probability of having two or more solutes or defects in the same local neighborhood is negligible.

The type of solute-defect flux coupling drives the evolution of the alloy. PD's usually flow towards sinks (e.g. dislocation lines, grain boundaries, free surfaces, and so on) [66]. Hence, the mechanisms described above can cause solute atoms to segregate on such sinks, and to change the alloy composition around them. This is exemplified in Fig. 2.4, for what concerns radiation-induced segregation (RIS). Vacancy drag leads to solute enrichment, because vacancies carry solute atoms along. In the opposite case, the diffusion rates of the two species determine the enrichment or depletion tendency: namely, depletion occurs if the solute diffusivity is larger. For what concerns interstitial transport, a flux of mixed dumbbells yields enrichment, whereas a lack of solute-dumbbell transport causes the solute to deplete because of the supplementary influx of iron atoms. The global RIS tendency is obtained by combining the vacancy and interstitial tendencies. A similar reasoning can explain heterogeneous solute-cluster growth. A solute-defect complex acts as a defect sink, and can therefore attract defects to the cluster. In case of vacancy drag or dumbbell transport, the solute atoms carried by the defects are deposited on the cluster, allowing for it to grow. Such coupling regimes depend mainly on temperature, chemical composition, and possible strain fields in the lattice.

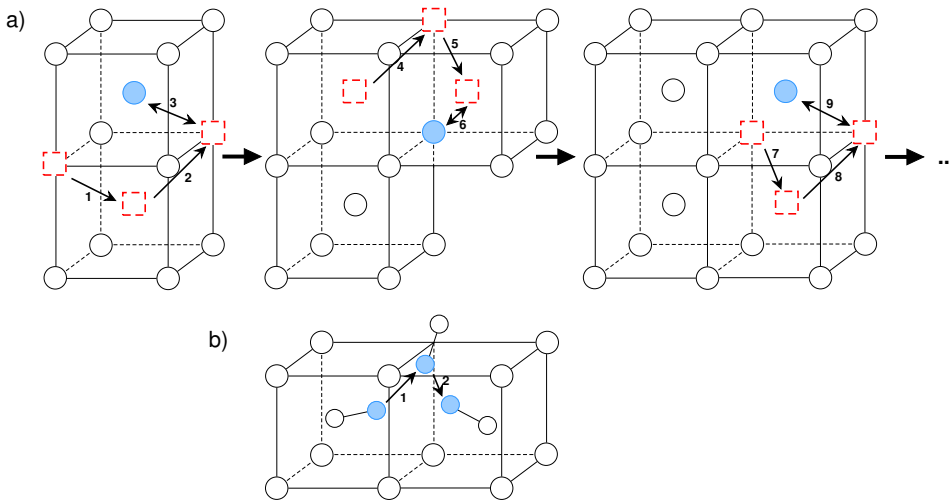


Figure 2.3: a) Example of correlated vacancy path producing solute drag. b) Example of mixed-dumbbell migration sequence that allows for solute transport without dumbbell dissociation.

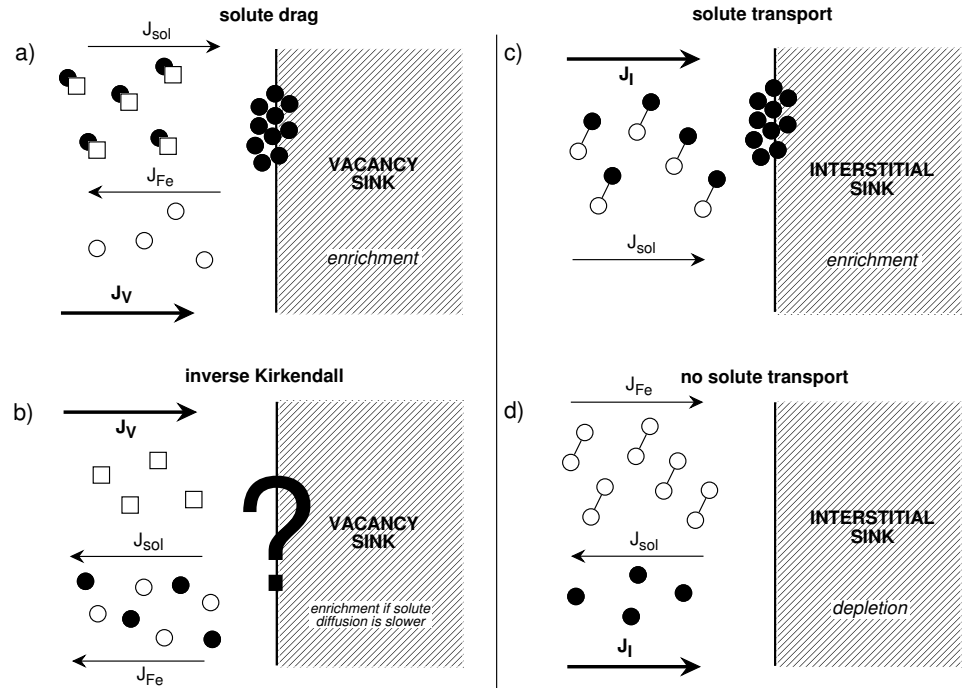


Figure 2.4: Qualitative description of RIS tendencies in different flux-coupling regimes. a) Solute drag by vacancies leads to solute enrichment at sinks. b) In the absence of vacancy drag, the species (iron or solute) with the lower diffusivity is enriched next to the sink. c) Solute transport via the mixed-dumbbell mechanism leads to solute enrichment. d) No solute transport occurs because the mixed dumbbell is not stable, which leads to solute depletion because of the additional influx of iron atoms.

2.2 Diffusion coefficients

Diffusion coefficients relate the flux of a given species to the concentration gradients, according to Fick's law [58]:

$$J_\alpha = -D_\alpha \nabla c_\alpha . \quad (2.3)$$

In a dilute alloy AB, the impurity diffusion coefficient can be measured by assuming that the reference frame of the solvent atoms is fixed, and is then referred to as *tracer diffusion coefficient* (D_B^*). By the same approach, the *tracer self-diffusion coefficient* (D_A^*) in a pure material can be obtained by measuring the diffusion of a self tracer, i.e. a radioactive isotope of the same chemical species. In more concentrated alloys, the assumption of a fixed reference frame is not valid, and the

Kirkendall effect (i.e. the relative motion of the diffusion zone with respect to the non-diffusion zone in the same material) cannot be neglected. In this case, the *intrinsic diffusion coefficients* D_A and D_B can be obtained from the measurement of the chemical interdiffusion coefficient and the Kirkendall velocity [58].

The self-diffusion coefficient for vacancy-mediated diffusion can be computed as [62]:

$$D_A^* = a_0^2 f_0 \omega_0 c_V^{\text{eq}} = a_0^2 f_0 \nu_0 \exp\left(-\frac{H_V^f + H_V^m}{k_B T}\right) \exp\left(\frac{S_V^f}{k_B}\right), \quad (2.4)$$

where a_0 is the lattice constant (2.87 Å for Fe [67]), c_V^{eq} the equilibrium vacancy concentration (as in Eq. 2.1), ω_0 and ν_0 the vacancy jump frequency and attempt frequency in pure iron, and f_0 a geometric correlation factor, equal to 0.727 in bcc crystals [62]. In experiments, the diffusion coefficient is usually provided through the prefactor $D_0 = a_0^2 f_0 \nu_0 \exp(S_V^f/k_B T)$ and the activation energy $Q = H_V^f + H_V^m$. In ferromagnetic materials such as iron, the activation energy decreases with increasing temperature because of the progressive loss of ferromagnetic character. This must be taken into account when comparing computed diffusion coefficients which experimental measurements, which are conducted at high temperatures. A model [68] accurately describing the change of Q with temperature due to the magnetic transition is described in Papers I and II.

The solute tracer diffusion coefficient is expressed by a similar formula [62]:

$$D_B^* = a_0^2 f_B \omega_2 c_V^{\text{eq}} p_{1\text{nn}} = a_0^2 f_B \nu_B \exp\left(\frac{S_V^f}{k_B}\right) \exp\left(-\frac{H_V^f + H_B^m + H_{BV}^{\text{b},1\text{nn}}}{k_B T}\right), \quad (2.5)$$

where ω_2 and ν_B are the solute jump frequency and attempt frequency, f_B the solute correlation factor, and $p_{1\text{nn}}$ the probability of having a solute-vacancy pair at 1nn distance, which depends on the 1nn binding energy $H_{BV}^{\text{b},1\text{nn}}$ (here, the binding energy is negative when attractive). The minor entropic contributions to the migration and binding free energies are here neglected. The solute diffusion coefficient is thus determined by three factors: the solute migration barrier, the 1nn binding energy, and the correlation factor. The influence of each factor is discussed in Paper II.

The correlation factor is a key-concept in this work. It represents the effect of consecutive non-random solute (or solvent) jumps that do not produce a net solute displacement, as is for instance the case when the solute exchanges with a vacancy several consecutive times. It can be derived from Einstein's definition of the diffusion coefficient [69]:

$$D_B = \frac{\langle (\sum_i \vec{r}_i)^2 \rangle}{6\tau}, \quad (2.6)$$

where \vec{r}_i are a series of displacements of B during time τ . The square of the sum

can be developed as:

$$\left\langle \left(\sum \vec{r}_i \right)^2 \right\rangle = \sum \langle \vec{r}_i^2 \rangle + 2 \sum_{i=1}^{n-1} \sum_{j=1}^{n-i} \langle \vec{r}_i \cdot \vec{r}_{i+j} \rangle . \quad (2.7)$$

The first term on the right-hand side is the uncorrelated part of the diffusion coefficient. The correlation factor is then given by:

$$f_B = 1 + \left(2 \sum_{i=1}^{n-1} \sum_{j=1}^{n-i} \langle \vec{r}_i \cdot \vec{r}_{i+j} \rangle / \sum \langle \vec{r}_i^2 \rangle \right) . \quad (2.8)$$

If the jumps in the sequence are completely uncorrelated, the sum of the cross products is null and the correlation factor is unitary. This is not the case for self diffusion, as after a jump of atom A a vacancy is immediately available to perform a backward jump (hence the factor f_0). For solute diffusion, a strong correlation between the vacancy and the solute causes consecutive solute jumps to be highly correlated. This effectively slows down the diffusion of the solute, as well as that of the vacancy. The same applies to solute diffusion via the dumbbell mechanism, although the correlation factors are different because of the different jump mechanisms. The factor can be calculated as a function of the atomic jump frequencies, by using one of the multifrequency models such as the one depicted in Fig. 2.2. Analytical equations have been developed for bcc and face-centered cubic (fcc) structures and different interaction ranges [62]. In Paper II, a new, more complete expression is provided, based on the self-consistent mean-field approach presented in Section 2.5.

2.3 Phenomenological transport coefficients

The correlation factor includes the effects of solute-vacancy interactions and flux coupling on solute diffusion. However, such effects are seen only as a solute slow-down and do not allow for the determination of the flux direction. Hence, Eqs. 2.4 and 2.5 are very useful in a vast range of applications and models, but they are not well suited for the description of flux-coupling phenomena.

Atomic fluxes arise in non-equilibrium conditions to counteract thermodynamic forces. These tendencies are in general controlled by the phenomenological coefficients (transport coefficients) of the Onsager matrix [66]. The thermodynamic forces are represented by the gradients of chemical potential of each species α : $\nabla \mu_\alpha / k_B T$. They represent the deviation of the system from equilibrium, which tends to be compensated by the atomic fluxes, assumed to be proportional to such forces:

$$J_\alpha = - \sum_{\beta} L_{\alpha\beta} \frac{\nabla \mu_\beta}{k_B T} . \quad (2.9)$$

The proportionality factors are the phenomenological coefficients $L_{\alpha\beta}$. They represent the kinetic response of a system subjected to thermodynamic forces, hence allowing for a clear separation between kinetic behavior and thermodynamic driving forces. In a binary alloy, the Onsager matrix has three independent coefficients: L_{AA} , L_{AB} , and L_{BB} , as the matrix is symmetric for any crystal structures [70]. The off-diagonal coefficient describes the flux of one chemical species induced by forces acting on the other species, allowing therefore for the determination of the flux-coupling tendency.

The coefficients depend on the temperature, on the nominal alloy composition, and on external stresses. They can also be distinguished depending on the diffusion mechanism. The total vacancy flux is given by the opposite sum of the fluxes of all species: $J_V = -\sum_{\alpha} J_{\alpha}^V$, whereas the interstitial flux is the sum with the same sign: $J_I = \sum_{\alpha} J_{\alpha}^I$. Moreover, the vacancy and interstitial contributions are assumed to be additive. The flux of a given species α can therefore be written as [66]:

$$J_{\alpha} = J_{\alpha}^V + J_{\alpha}^I = -\sum_{\beta} L_{\alpha\beta}^V \frac{\nabla\mu_{\beta} - \nabla\mu_V}{k_B T} - \sum_{\beta} L_{\alpha\beta}^I \frac{\nabla\mu_{\beta} + \nabla\mu_I}{k_B T}. \quad (2.10)$$

The driving forces can be obtained from concentration gradients and thermodynamic properties. For instance, the chemical potential gradient of a species α in a binary alloy can be written as [66]:

$$\frac{\nabla\mu_{\alpha}}{k_B T} = \Phi \frac{\nabla c_{\alpha}}{c_{\alpha}}, \quad (2.11)$$

where the thermodynamic factor Φ is proportional to the second derivative of the Gibbs free energy, and can therefore be easily calculated from thermodynamic databases. On the other hand, the Onsager matrix has to be obtained by theoretical models, because the three independent coefficients cannot be all inferred from diffusion experiments [66]. Moreover, since interstitials are missing in thermal conditions, interstitial-related diffusion coefficients are not usually available. In addition, experimental diffusion coefficients are available only at high temperatures, and extrapolation to low temperatures can be very inaccurate (as is explained in Papers I and II). For such reasons, one must rely on theoretical models to compute the Onsager coefficients. In this project, these coefficients are calculated by means of self-consistent mean-field (SCMF) theory, based on atomic jump frequencies ω that are obtained by *ab initio* calculations. Then, they are employed to investigate the following properties.

- a) The tracer solute diffusion coefficients $D_B^* = L_{BB}/nc_B$, where n is the atomic density.
- b) The vacancy-drag tendency, which can be inferred from the ratio L_{BV}/L_{BB} (also called the *wind factor*), where $L_{BV} = -(L_{AB} + L_{BB})$. This factor is positive when vacancy drag occurs, and negative otherwise.

- c) The correlation factor $f_B = L_{BB}/L_{BB}^0$, where L_{BB}^0 is the uncorrelated part of the L_{BB} coefficient (Eq. 2.18).
- d) The combined vacancy-interstitial RIS steady-state tendencies, according to the model described in the next section.

Alternatively, the transport coefficients can be calculated by means of KMC simulations (see Section 2.8), as they can be defined in a way similar to diffusion coefficients [71]:

$$L_{\alpha\beta} = \frac{\langle \Delta \vec{R}_\alpha \cdot \Delta \vec{R}_\beta \rangle}{6\Omega\tau}, \quad (2.12)$$

where $\Delta \vec{R}_\alpha = \sum_i \vec{r}_i^\alpha$ and $\Delta \vec{R}_\beta = \sum_i \vec{r}_i^\beta$ are the total displacements of all atoms of species α and β in time τ , within a given volume Ω . The transport coefficients yielded by the KMC and SCMF methods have been shown in previous works [63, 60, 64], as well as in Paper I, to match perfectly, which proves the reliability of both methods.

2.4 Radiation-induced segregation model

RIS refers to the coupling of irradiation-induced defects with the alloy chemical species, leading to localized composition changes near sinks [66]. The RIS tendency deriving from PD-driven diffusion can be inferred from the transport coefficients with the following model. The atomic fluxes can be written by means of Eq. 2.10 and the equations for J_V and J_I :

$$\begin{cases} J_A &= -\gamma [L_{AA}^V \nabla(\mu_A - \mu_V) + L_{AB}^V \nabla(\mu_B - \mu_V) + L_{AA}^I \nabla(\mu_A + \mu_I) + L_{AB}^I \nabla(\mu_B + \mu_I)] \\ J_B &= -\gamma [L_{BA}^V \nabla(\mu_A - \mu_V) + L_{BB}^V \nabla(\mu_B - \mu_V) + L_{BA}^I \nabla(\mu_A + \mu_I) + L_{BB}^I \nabla(\mu_B + \mu_I)] \\ J_V &= +\gamma [L_{AA}^V \nabla(\mu_A - \mu_V) + L_{AB}^V \nabla(\mu_B - \mu_V) + L_{BA}^V \nabla(\mu_A - \mu_V) + L_{BB}^V \nabla(\mu_B - \mu_V)] \\ J_I &= -\gamma [L_{AA}^I \nabla(\mu_A + \mu_I) + L_{AB}^I \nabla(\mu_B + \mu_I) + L_{BA}^I \nabla(\mu_A + \mu_I) + L_{BB}^I \nabla(\mu_B + \mu_I)] \end{cases}, \quad (2.13)$$

where $\gamma = 1/k_B T$. The chemical potential gradients can be obtained from Eq. 2.11, whereas the additional driving forces acting on PD's under irradiation can be written as [66]:

$$\frac{\nabla \mu_x}{k_B T} = \frac{\nabla c_x}{c_x} - \frac{\partial \ln c_x^{\text{eq}}}{\partial \ln c_B} \frac{\nabla c_B}{c_B}, \quad (2.14)$$

($x = V, I$). Expressions for the equilibrium defect concentration as a function of the solute concentration can be obtained, for instance, by means of a low-temperature expansion of the equilibrium distribution function [72].

The system of equations can be solved in steady-state conditions by setting the atomic fluxes to zero ($J_A = J_B = 0$) and the equality of the PD fluxes ($J_I = J_V$).

This is justified because an equal amount of vacancies and interstitials is created in the bulk under irradiation, and at steady-state an equal amount is absorbed at sinks (neglecting any absorption bias) [73].

Under such assumptions, the solution of the system is given by [66]:

$$\frac{\nabla c_B}{\nabla c_V} = \frac{c_A c_B d_{AV} d_{AI}}{c_A d_{AI} D_B + c_B d_{BI} D_A} \left(\frac{d_{BV}}{d_{AV}} - \frac{d_{BI}}{d_{AI}} \right). \quad (2.15)$$

The sign of the gradient ratio determines the solute enrichment tendency, as depicted in Fig. 2.5, because the vacancy concentration gradient near a sink is always negative. The same equation is obtained when solving for $\nabla c_B / \nabla c_I$. D_A and D_B are the interdiffusion coefficients, whose expressions in terms of transport coefficients can be found in [66]. The sign of the expression is determined by the ratio of partial diffusion coefficients (PDC) in parenthesis. They are defined as:

$$d_{AV} = \frac{L_{AA}^V + L_{AB}^V}{c_A c_V}, \quad d_{BV} = \frac{L_{AB}^V + L_{BB}^V}{c_B c_V}; \quad (2.16)$$

$$d_{AI} = \frac{L_{AA}^I + L_{AB}^I}{c_A c_I}, \quad d_{BI} = \frac{L_{AB}^I + L_{BB}^I}{c_B c_I}. \quad (2.17)$$

The RIS tendencies can be therefore discussed based exclusively on the PDC ratios, which are directly derived from the transport coefficients. The amplitude of the enrichment or depletion tendency has a more involved dependence on the irradiation conditions. But for the dilute limit, a simplified expression can be obtained. The elements of the Onsager matrix are proportional to the defect and the solute concentrations, with the exception of L_{AA} that has a solute-independent term. Therefore, it is convenient to write the coefficients as:

$$\begin{cases} L_{AA}^x &= c_x \left(l_{AA}^{x,0} + c_B l_{AA}^{x,1} \right) \\ L_{AB}^x &= c_x c_B l_{AB}^x \\ L_{BB}^x &= c_x c_B \left(l_{BB}^{x,0} + l_{BB}^{x,1} \right) = c_x c_B l_{BB}^x \end{cases}. \quad (2.18)$$

The quantities marked with '0' represent the uncorrelated terms of the matrix, hence corresponding to the values of the diagonal coefficients in absence of correlations. By applying the dilute limit (first order in c_B), the RIS equation 2.15 becomes:

$$\frac{\nabla c_B}{\nabla c_V} = \frac{l_{AA}^{V,0}}{l_{BB}^V + \frac{c_I}{c_V} l_{BB}^I} \left(\frac{d_{BV}}{d_{AV}^0} - \frac{d_{BI}}{d_{AI}^0} \right) \frac{c_B}{c_V}, \quad (2.19)$$

where the steady-state ratio c_I/c_V depends on the temperature and the sink density, but is in most cases equal to the ratio of diffusion coefficients of vacancies and interstitials (D_V/D_I) [74]. The results yielded by this model are shown in Paper III and are summarized in Chapter 3.

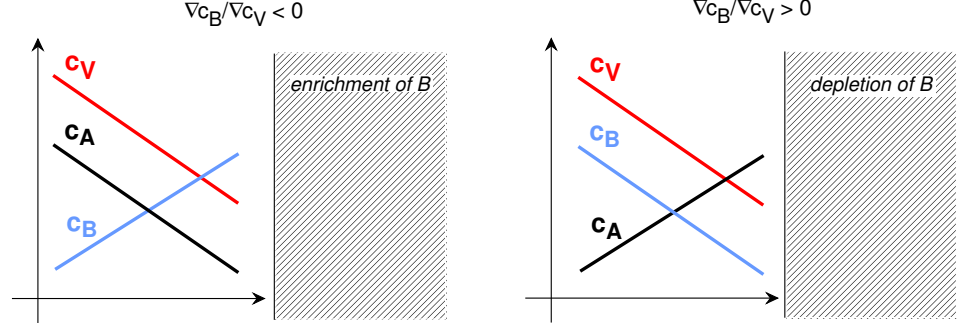


Figure 2.5: Schematic representation of vacancy (V), iron (A), and solute (B) concentration gradients in the vicinity of a sink, depending on the sign of the concentration gradient ratio $\nabla c_B/\nabla c_V$ (Eq. 2.15). Since the vacancy concentration gradient is always negative, a negative ratio yields solute enrichment (left panel), whereas depletion occurs if the ratio is positive (right panel).

2.5 Self-consistent mean-field theory

SCMF theory is an analytical atomic diffusion model that allows for the calculation of transport coefficients in a near-equilibrium alloy. This near-equilibrium condition is determined by the presence of thermodynamic driving forces (i.e. gradients of chemical potentials) that perturb the equilibrium distribution function³ of the alloy and produce atomic and defect fluxes.

The state of an alloy at a given time t can be described by the occupation numbers of all lattice sites: $\vec{n}(t) = \{n_i^\alpha\}$. The index α refers to the chemical species (e.g. A and B in a dilute alloy) and i to the lattice sites. Each occupation number n_i^α is 1 if site i is occupied by species α , or 0 otherwise. The evolution of the alloy in time is described by the Master equation [63]:

$$\frac{d\hat{P}(\vec{n}, t)}{dt} = \sum_{\vec{m}} \left[\hat{W}(\vec{m} \rightarrow \vec{n}) \hat{P}(\vec{m}, t) - \hat{W}(\vec{n} \rightarrow \vec{m}) \hat{P}(\vec{n}, t) \right], \quad (2.20)$$

where $\hat{P}(\vec{n}, t)$ is the distribution function of the alloy at time t (i.e., the probability for the alloy to be in state \vec{n} at time t), and $\hat{W}(\vec{m} \rightarrow \vec{n})$ represents the transition rate from state \vec{m} to state \vec{n} . The sum is performed over all possible configurational states \vec{m} . Transitions from one state to another are driven by defect migration.

At equilibrium, no atomic flux occurs because of the absence of thermodynamic forces, and the equilibrium distribution function is given by

³In kinetic theory, $P(\vec{r}, \vec{v}, t) \partial\vec{r} \partial\vec{v}$ defines the number of particles included in a small volume element $\partial\vec{r}$ and in a small velocity-space element $\partial\vec{v}$, at time t . The configuration space is in general continuous, but in a crystal lattice it is reduced to a discrete space of configurations \vec{n} , corresponding to the occupation of lattice sites by each chemical species.

$\hat{P}_0(\vec{n}) = \exp[-H(\vec{n})/k_B T]/Z$. The normalization constant Z is the partition function, given by $Z = \sum_{\vec{m}} \exp[-H(\vec{m})/k_B T]$, whereas $H(\vec{n})$ is the equilibrium Hamiltonian of state \vec{n} , which depends on the thermodynamic atomic interactions. The departure of the system from equilibrium is modeled in SCMF as a perturbation of the equilibrium distribution function [63]:

$$\hat{P}(\vec{n}, t) = \hat{P}_0(\vec{n}) \cdot \hat{P}_1(\vec{n}, t). \quad (2.21)$$

The perturbation function \hat{P}_1 is assumed to hold the same mathematical structure as \hat{P}_0 . It depends hence on the non-equilibrium Hamiltonian:

$$\hat{h}(t) = \frac{1}{2} \sum_{\alpha\beta, i \neq j} v_{ij}^{\alpha\beta}(t) n_i^\alpha n_j^\beta, \quad (2.22)$$

where the $v_{ij}^{\alpha\beta}$ are *effective interactions* that are null at equilibrium⁴. SCMF provides a self-consistent method to calculate these effective interactions, which in turn allow for the derivation of the transport coefficients based on atomic jump frequencies ω and equilibrium concentrations, as explained below.

In order to calculate the $v_{ij}^{\alpha\beta}$, the non-equilibrium distribution function is written in terms of two-point averages, for instance:

$$\langle n_i^\alpha n_j^\beta \rangle = \sum_{\alpha\beta, i \neq j} \hat{P}(\vec{n}, t) n_i^\alpha n_j^\beta. \quad (2.23)$$

The Master equation (Eq. 2.20) combined with Eq. 2.21 allows for the derivation of the time derivative of these two-point averages as a function of the effective interactions. Afterwards, the one-point averages $\langle n_i^\alpha \rangle$ yield a flux equation for each species, from which the transport coefficients can be obtained. The derivation is rather involved, and its full presentation is outside the scope of this manuscript. It is presented in details in [63] for vacancy-mediated diffusion, and in [60] for interstitial-mediated diffusion. Useful explanations can also be found in [75, 76]. In Papers I and II, the vacancy method [63] has been applied without modifications, by using a dedicated computer code [76]. Conversely, in Paper III the SCMF interstitial method presented in [60] (and for dilute alloys in [64]) has been extended in this work to include a larger set of effective interactions. For this reason, a few details are provided here about the SCMF interstitial method, along with the improvements to the method developed during this project.

⁴Here the effective Hamiltonian is expanded in terms of pair interactions only, although nothing prevents one from introducing as well multibody interactions [63].

SCMF interstitial method

In case of dumbbell-assisted diffusion, the effective Hamiltonian of Eq. 2.22 is written as [60]:

$$\hat{h}(t) = \sum_I v_i^I(t) n_i^I + \frac{1}{2} \sum_{\sigma, I, i \neq j} v_{ij}^{I, \sigma}(t) n_i^I n_j^\sigma. \quad (2.24)$$

In addition to the pair interactions between a dumbbell I and species σ , an internal dumbbell interaction v_i^I (between the dumbbell atoms) is introduced. In a binary dilute alloy, the possible dumbbells are AA and AB . The summations are performed over all dumbbells I included in the alloy, of any composition and orientation. This model is limited to $\langle 110 \rangle$ dumbbells, which can adopt six equivalent orientations. This section is focused on the specific case of a dilute binary alloy.

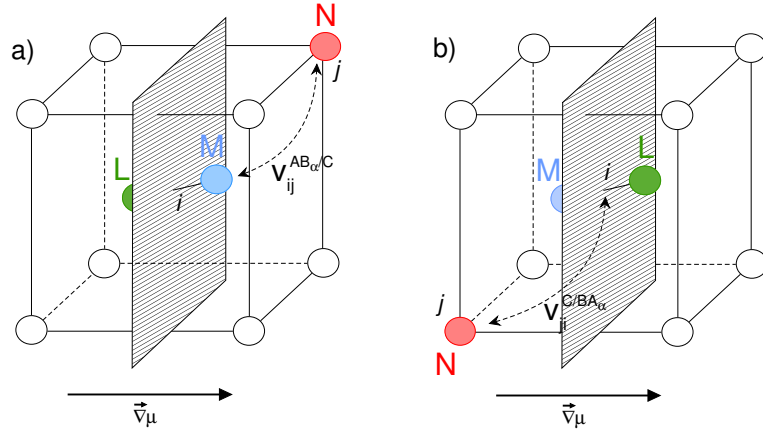


Figure 2.6: Example of symmetric pair interactions ($v_{ij}^{N, ML\alpha} = -v_{ji}^{LM\alpha, N}$) between a dumbbell LM with orientation α and a third atomic species N in 1nn position. The shaded planes mark the symmetry planes, perpendicular to the direction of the chemical potential gradient $\vec{\nabla}\mu$.

The amount of effective interactions to be distinguished is determined by the kinetic interaction range and by symmetries. The kinetic interaction range should be at least as large as the thermodynamic interaction range (discussed in Section 2.1). In [64], the range was limited to 1nn sites, and this work extends it to 1nn of 1nn sites. Different interactions must be defined for dumbbells AA and AB , as well as for pairs $AA-B$. Moreover, interactions of type $AA-B$ within the same nearest-neighbor distance must be distinguished according to symmetries defined by the crystal structure and the chemical potential gradient (CPG) direction. The effective interactions are defined as symmetric with respect to the plane perpendicular to

the CPG direction. Therefore, the following symmetry operations apply:

$$v_{ML\alpha} = -v_{LM\alpha} , \quad (2.25)$$

$$v_{ij}^{N,ML\alpha} = -v_{ji}^{LM\alpha,N} , \quad (2.26)$$

where α refers to one of the possible 6 orientations. Here, L and M are generic dumbbell atoms (they can be either A or B), and N is a third atom on site j . A pair of symmetric effective interactions corresponding to Eq. 2.26 is shown in Fig. 2.6. This implies that interactions involving equal chemical species are null. In a dilute binary alloy, then, only interactions of type v_{AB} and $v_{AA,B}$ are kept. Also, interactions that are fully perpendicular to the CPG (i.e. both the dumbbell orientation and the dumbbell-third atom bond) are also null. In addition, two interactions are not symmetric (and must therefore be distinguished) if one of the following three conditions is true:

1. the absolute value of the bond projection on the CPG direction is different;
2. the absolute value of the dumbbell orientation on the CPG direction is different;
3. the absolute value of the bond projection on the direction of the dumbbell orientation is different.

The combination of these rules yields the set of effective interactions shown in Fig. 2.7. Under the assumption that the CPG direction coincides with one of the main axes, there are two equivalent dumbbell orientations that are perpendicular to the CPG (index '0'), and four equivalent orientations that are not perpendicular (index '+'). The 3-atom interactions are then classified according to the nomenclature defined in Paper III. The interactions above the dashed line were introduced in [64], whereas the others have been added here. A computer code has been developed in this work in order to analyze these symmetries automatically for any kinetic interaction range, and to calculate transport coefficients of a wide range of alloys in an efficient way, solving the set of SCMF analytical equations.

Once the set of independent kinetic interactions has been defined, one kinetic equation for each interaction can be written, analogously to Eq. 2.23. A kinetic equation for the internal dumbbell interaction v_{AB} can also be written. The procedure to derive such equations is considerably involved; in order to describe the general idea behind this procedure, the simplest kinetic equation is reported in Eq. 2.29. The explanation that follows is not meant, therefore, to be exhaustive. The equation represents the one-point kinetic equation for a dumbbell of type AB in orientation α on a site i , which corresponds to the kinetic interaction $v_{AB\alpha}$. This equation describes the rate at which the average occupation number of this dumbbell in site i changes. Any change is caused by three types of events: I) migration of atom A towards its target sites s (second line of the equation), II) migration

of atom B towards its target sites s (third line), and III) onsite rotation of the dumbbell, leading to a dumbbell with a different orientation β (fourth line). The sums are performed over all possible target orientations β , and all possible species σ (A or B) that can be on the target site.

In simple terms, the change of the one-point average is determined by all kinetic interactions that are involved during all the transitions just described. The multiplicative factors are the average transition rates, corresponding to the jump frequencies discussed in Section 2.1, and are described in details in Papers I and III. The index '(0)' refers to thermodynamic equilibrium conditions, which allows the transition rates to be calculated by means of common atomistic simulations, as is shown in Paper I, II, and III. The factor $y_{si}^{\beta\alpha}$ (0 or 1) is introduced to ensure that forbidden transitions in terms of target sites or dumbbell rotations are excluded. The averages are calculated from the equilibrium concentrations of the transition starting configuration, which can be obtained from binding energies (a model is presented in the appendix of [64]). The equation has been derived under the detailed-balance assumption, which states that at equilibrium each transition rate is equal to the rate of the reverse jump, e.g.:

$$\langle n_s^{\sigma A\beta} n_i^B y_{si}^{\beta\alpha} \omega_{\sigma A/B}^{\beta\alpha} \rangle^{(0)} = \langle n_i^{AB\alpha} n_s^{\sigma} y_{is}^{\alpha\beta} \omega_{BA/\sigma}^{\alpha\beta} \rangle^{(0)}. \quad (2.27)$$

Fig. 2.8 depicts event II), where atom B moves to a target site s . In the equation appears always the difference between interactions involved in the dissociation jump (Fig. 2.8a), and during the association jump (Fig. 2.8b). The total contribution is given by internal dumbbell interactions and by the sum over all 3-atom interactions with atom species γ within sites k inside the kinetic interaction shell (in Fig. 2.8 limited, for simplicity, to the 1nn).

Analogous equations can be written for 3-point averages such as $d\langle n_i^{AB\alpha} n_j^A \rangle / dt$, describing all possible transitions leading to the dissociation (and the formation) of a pair consisting of a dumbbell AB on site i and another atom A on site j . In the framework of this thesis, these equations are derived analytically, in order to generalize the work of [64] to any extent of the kinetic interaction range. Furthermore, the developed computer code is aimed at computing all terms of the kinetic equations and at solving the SCMF model analytically.

All kinetic equations form a self-consistent system of equations that can be solved numerically with inexpensive calculations. Each point-average derivative in time is set to zero, which entails that the system is solved in steady-state conditions. The system can be written in matrix form as:

$$\hat{T}\vec{V} = \vec{b}_{\nabla\mu_\sigma}, \quad (2.28)$$

where \vec{V} is the vector of the kinetic interactions (the unknowns), \hat{T} is the matrix of the average transition rates, and $\vec{b}_{\nabla\mu_\sigma}$ ($\sigma = A, B$) is the vector of constant terms depending on the CPG of each species (the first line of Eq. 2.29). The inversion of \hat{T} allows for the computation of σ -species dependent kinetic interactions $\vec{V}_{\nabla\mu_\sigma}$. A more rigorous formulation of the matrix problem can be found in [75, 76].

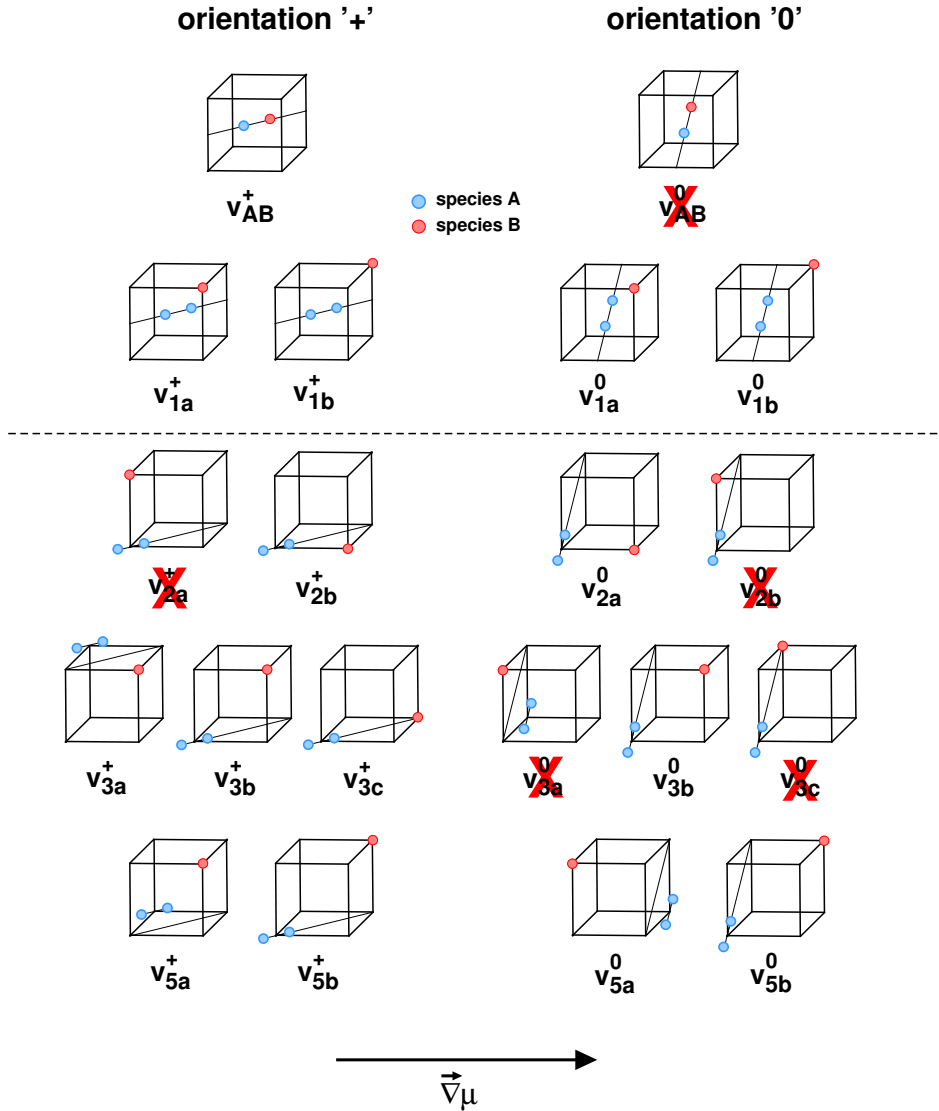


Figure 2.7: Summary of independent effective kinetic interactions inside the dumbbell (v_{AB}) and between a dumbbell AA and a solute atom B . The configurations are distinguished according to the dumbbell orientation ('+' if perpendicular to the chemical potential gradient $\vec{\nabla}\mu$, '+' otherwise). The nomenclature $v_{x\alpha}$ marks the nearest-neighbor distance (x) between the dumbbell and the solute, as well as the symmetry class (α) related to the distance between the solute and each dumbbell atom, according to the definitions of Fig. 1 in Paper III. The dashed line separates the interactions defined in the previous work [64] (above) from the ones introduced in this work (below).

$$\begin{aligned}
0 = (k_B T) \frac{d\langle n_i^{AB\alpha} \rangle}{dt} &= \sum_{s \neq i, \beta, \sigma} \langle n_s^{\sigma A \beta} n_i^B y_{si}^{\beta \alpha} \omega_{\sigma A/B}^{\beta \alpha} \rangle^{(0)} (\mu_s^A - \mu_i^A) + \sum_{s \neq i, \beta, \sigma} \langle n_s^{\sigma B \beta} n_i^A y_{si}^{\beta \alpha} \omega_{\sigma B/A}^{\beta \alpha} \rangle^{(0)} (\mu_s^B - \mu_i^B) + \\
&+ \sum_{s \neq i, \beta, \sigma} \left\{ \langle n_s^{\sigma A \beta} n_i^B y_{si}^{\beta \alpha} \omega_{\sigma A/B}^{\beta \alpha} \rangle^{(0)} v_{AB\alpha} - \langle n_s^{\sigma A \beta} n_i^B y_{si}^{\beta \alpha} \omega_{\sigma A/B}^{\beta \alpha} \rangle^{(0)} v_{\sigma A \beta} + \sum_{k \neq i, \gamma} \langle n_s^{\sigma A \beta} n_i^B n_k^\gamma y_{si}^{\beta \alpha} \omega_{\sigma A/B}^{\beta \alpha} \rangle^{(0)} v_{ik}^{AB\alpha, \gamma} - \sum_{k \neq s, \gamma} \langle n_s^{\sigma A \beta} n_i^B n_k^\gamma y_{si}^{\beta \alpha} \omega_{\sigma A/B}^{\beta \alpha} \rangle^{(0)} v_{sk}^{\sigma A \beta, \gamma} \right\} \\
&+ \sum_{s \neq i, \beta, \sigma} \left\{ \langle n_s^{\sigma B \beta} n_i^A y_{si}^{\beta \alpha} \omega_{\sigma B/A}^{\beta \alpha} \rangle^{(0)} v_{AB\alpha} - \langle n_s^{\sigma B \beta} n_i^A y_{si}^{\beta \alpha} \omega_{\sigma B/A}^{\beta \alpha} \rangle^{(0)} v_{\sigma B \beta} + \sum_{k \neq i, \gamma} \langle n_s^{\sigma B \beta} n_i^A n_k^\gamma y_{si}^{\beta \alpha} \omega_{\sigma B/A}^{\beta \alpha} \rangle^{(0)} v_{ik}^{AB\alpha, \gamma} - \sum_{k \neq s, \gamma} \langle n_s^{\sigma B \beta} n_i^A n_k^\gamma y_{si}^{\beta \alpha} \omega_{\sigma B/A}^{\beta \alpha} \rangle^{(0)} v_{sk}^{\sigma B \beta, \gamma} \right\} \\
&+ \sum_{\beta \neq \alpha} \left\{ \langle n_i^{AB\beta} y_{R}^{\beta \alpha} \omega_R^{AB} \rangle^{(0)} v_{AB\alpha} - \langle n_i^{AB\beta} y_{R}^{\beta \alpha} \omega_R^{AB} \rangle^{(0)} v_{AB\beta} + \sum_{k \neq i, \gamma} \langle n_i^{AB\beta} n_k^\gamma y_{R}^{\beta \alpha} \omega_R^{AB} \rangle^{(0)} v_{ik}^{AB\alpha, \gamma} - \sum_{k \neq i, \gamma} \langle n_i^{AB\beta} y_{R}^{\beta \alpha} \omega_R^{AB} \rangle^{(0)} v_{ik}^{AB\beta, \gamma} \right\}
\end{aligned} \tag{2.29}$$

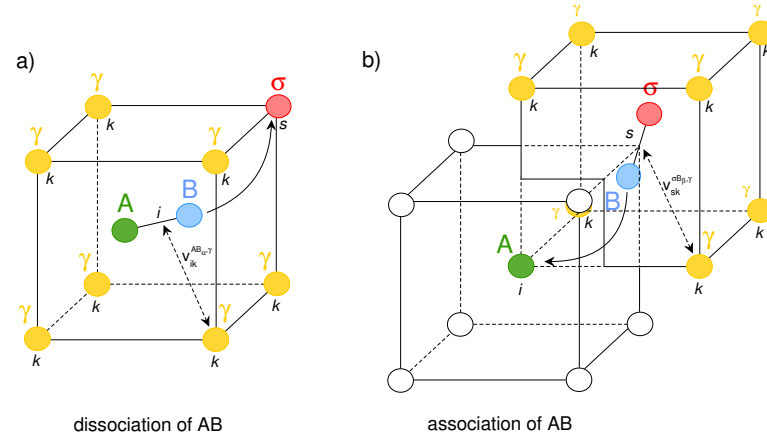


Figure 2.8: Representation of the third line of Eq. 2.29, featuring the dissociation (and association) of dumbbell AB through the migration of B towards a target site s , where a dumbbell σB is formed.

Finally, the transport coefficients can be obtained from the calculated kinetic interactions by writing the atomic flux equations. The equation of matter conservation yields [60]:

$$\frac{d\langle N_i^\sigma \rangle}{dt} = \frac{dc_i^\sigma}{dt} = - \sum_{s \neq i} J_{i \rightarrow s}^\sigma, \quad (2.30)$$

where N_i^σ is the *generalized occupation number*, counting the total amount of atoms of species σ in site i (it can be 0, 1, or 2 for the $\sigma\sigma$ dumbbell).

By the same procedure used to derive the kinetic equations, the flux of species σ is:

$$J_{i \rightarrow s}^\sigma = -l_\sigma^{(0)} \left(\frac{\mu_s^\sigma - \mu_i^\sigma}{k_B T} \right) - \vec{l}_\sigma^{(1)} \cdot \vec{V}_{\nabla \mu_A} \left(\frac{\mu_s^A - \mu_i^A}{k_B T} \right) - \vec{l}_\sigma^{(1)} \cdot \vec{V}_{\nabla \mu_B} \left(\frac{\mu_s^B - \mu_i^B}{k_B T} \right), \quad (2.31)$$

where $l_\sigma^{(0)}$ and $\vec{l}_\sigma^{(1)}$ depend on the average equilibrium transition rates. It is possible to recognize in Eq. 2.31 the flux equation used for the definition of transport coefficients (Eq. 2.9). By comparison, the transport coefficients are therefore obtained as:

$$\begin{cases} L_{AA} &= l_A^{(0)} + \vec{l}_A^{(1)} \cdot \vec{V}_{\nabla \mu_A} \\ L_{AB} &= \vec{l}_A^{(1)} \cdot \vec{V}_{\nabla \mu_B} \\ L_{BA} &= \vec{l}_B^{(1)} \cdot \vec{V}_{\nabla \mu_A} \\ L_{BB} &= l_B^{(0)} + \vec{l}_B^{(1)} \cdot \vec{V}_{\nabla \mu_B} \end{cases}. \quad (2.32)$$

2.6 Effect of external strain fields

In real alloys, the crystal is subjected to different types of stress fields, in particular next to large defects such as clusters, grain boundaries, and dislocations. The interaction of such fields with the elastic field induced by a point defect can modify the interactions with solute atoms, the diffusion rates, and flux-coupling tendencies [77]. This applies in particular for self-interstitial defects, as they introduce a greater distortion in the lattice with respect to vacancies.

In continuous linear elasticity theory, a point defect can be modeled as a distribution of forces with zero net resultant and torque [78]. At first order, the defect is fully characterized by its elastic dipole P_{ij} . The interaction energy with an external strain field can be written as [77]:

$$\Delta E^{\text{el}} = -P_{ij} \varepsilon_{ij}, \quad (2.33)$$

where the product on the right-hand side is to be interpreted as an Einstein product: $P_{ij} \varepsilon_{ij} = P_{11} \varepsilon_{11} + P_{22} \varepsilon_{22} + P_{33} \varepsilon_{33} + 2(P_{12} \varepsilon_{12} + P_{13} \varepsilon_{13} + P_{23} \varepsilon_{23})$. In experimental

conditions (null stress field), the elastic dipole can be obtained from the measured strain. Conversely, in atomistic simulations P_{ij} can be obtained by measuring the residual stress field, if the calculation is performed at constant volume (null strain field):

$$P_{ij} = -\frac{\Omega}{N_{\text{PD}}}\sigma_{ij}. \quad (2.34)$$

N_{PD} is the number of defects in a simulation cell with total volume Ω . The residual stress tensor σ_{ij} is measured here by DFT calculations.

In this way, it is possible to calculate the change of all energy properties of the defect as a function of any externally applied strain. The variation with strain of the dumbbell formation energy, the dumbbell-solute binding energy, and the migration energy are calculated as follows:

$$\Delta E^{\text{f}}(\varepsilon) = \Delta E_{\text{I}}(\varepsilon) - \frac{N+1}{N}\Delta E_{\text{Fe}}(\varepsilon); \quad (2.35)$$

$$\Delta E^{\text{b}}(\varepsilon) = \Delta E_{\text{I,sol}}(\varepsilon) + \Delta E_{\text{Fe}}(\varepsilon) - \Delta E_{\text{I}}(\varepsilon) - \Delta E_{\text{sol}}(\varepsilon); \quad (2.36)$$

$$\Delta E^{\text{m}}(\varepsilon) = \Delta E_{\text{sad}}(\varepsilon) - \Delta E_{\text{ini}}(\varepsilon). \quad (2.37)$$

The precedent formulas are derived from the definitions of formation, binding and migration energies that can be found in Papers I and II. In addition, the modification of RIS tendency due to the strain field can be obtained, in first approximation, by applying these energy perturbations to the interstitial partial diffusion coefficient ratio of Eq. 2.15:

$$\frac{d_{\text{BI}}}{d_{\text{AI}}} \approx \frac{w_1}{w_0} = \exp \left\{ -\frac{[Q_B^{\varepsilon=0} - Q_A^{\varepsilon=0}] + [\Delta Q_B(\varepsilon) - \Delta Q_A(\varepsilon)]}{k_{\text{B}}T} \right\}. \quad (2.38)$$

Q_A refers to the activation energy of a pure-iron dumbbell in a pure-iron environment, whereas Q_B is the activation energy of the mixed dumbbell. The strain-dependent variation of activation energies are obtained as:

$$\Delta Q_A(\varepsilon) = -k_{\text{B}}T \ln \left[\sum_{\alpha=1}^6 \frac{1}{6} \exp \left(-\frac{\Delta E_{\alpha}^{\text{f}}(\varepsilon) + \Delta E_{\alpha}^{\text{m},A}(\varepsilon)}{k_{\text{B}}T} \right) \right], \quad (2.39)$$

and

$$\Delta Q_B(\varepsilon) = -k_{\text{B}}T \ln \left[\sum_{\alpha=1}^6 \frac{1}{6} \exp \left(-\frac{\Delta E_{\alpha}^{\text{f}}(\varepsilon) + \Delta E_{\alpha}^{\text{b}}(\varepsilon) + \Delta E_{\alpha}^{\text{m},B}(\varepsilon)}{k_{\text{B}}T} \right) \right], \quad (2.40)$$

where the energy quantities are averaged on the six possible equivalent orientations of a $\langle 110 \rangle$ dumbbell. This average is needed because dumbbells in different orientations are affected differently by non-isotropic strains.

In Eq. 2.38, any correlation effect is neglected. This represents a very first application aimed at verifying the magnitude of this effect, and a possible RIS tendency reversal. As a matter of fact, the strain field induces a modification of the transport coefficients, and consequently of the flux-coupling tendencies. This perturbation can be as well obtained by means of the SCMF theory, by analyzing the strain-induced distortion of the bcc cell symmetry and the consequent increase of the number of independent effective interactions. Hence, a new set of kinetic equations needs to be derived, as was done for vacancy diffusion under stress in NiSi alloys [79]. This will be the object of future work.

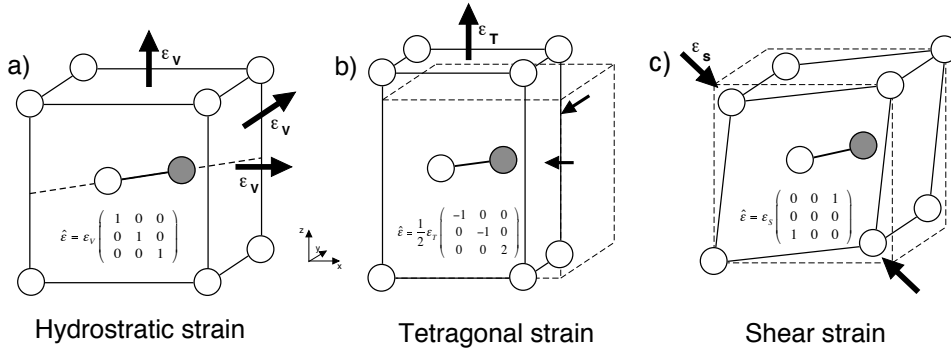


Figure 2.9: Elementary strain types used for the calculation of strain effects on RIS tendencies.

In Chapter 3, the results are shown as function of elementary strain types, which are summarized in Fig. 2.9. Any strain field can be decomposed in these three components [78, 79, 77]. Moreover, the model is applied to the strain field of a screw and an edge dislocation with Burger's vector $\vec{b} = \frac{1}{2}a_0\langle 111 \rangle$. For a screw dislocation, the isotropic strain field is given by [80]:

$$\begin{cases} \varepsilon_{13}(x, y) = -\frac{b}{4\pi} \cdot \frac{y}{x^2+y^2} \\ \varepsilon_{23}(x, y) = \frac{b}{4\pi} \cdot \frac{x}{x^2+y^2} \\ \varepsilon_{11} = \varepsilon_{22} = \varepsilon_{33} = \varepsilon_{12} = 0 \end{cases} \quad (2.41)$$

For an edge dislocation, the strain field is derived from the stress field σ_{ij} as $\varepsilon = C\sigma$, where C is the compliance matrix [81]. The isotropic expression of the stress field reads [80]:

$$\begin{cases} \sigma_{11}(x, y) = -\xi y \frac{3x^2+y^2}{(x^2+y^2)^2} \\ \sigma_{22}(x, y) = \xi y \frac{x^2-y^2}{(x^2+y^2)^2} \\ \sigma_{12}(x, y) = \xi x \frac{x^2-y^2}{(x^2+y^2)^2} \\ \sigma_{33} = \sigma_{13} = \sigma_{23} = 0 \end{cases} \quad (2.42)$$

where $\xi = bG/2\pi(1 - \nu)$. ν is the Poisson ratio (0.29 in iron), $G = E/2(1 + \nu)$ the shear modulus, and E the Young modulus (211 GPa in iron) [81].

2.7 Electronic-structure calculations

Defect properties, binding energies and jump frequencies are calculated in this work by means of *ab initio* electronic-structure calculations. The aim of such class of methods is to calculate the ground-state energy (i.e. the lowest energy at absolute zero temperature) in a system composed by a collection of ions and electrons, by solving the time-independent multibody Schrödinger equation. The problem is divided between electronic and ionic relaxation thanks to the Born-Oppenheimer approximation [82]: since the time scales of electronic and ionic motion are different, the electrons can be regarded as moving in a fixed ionic potential that depends only on the position of the nuclei. The ground-state energy of the system is therefore found by the combination of two iterative loops, one for the electrons and one for the ions. The energy corresponding to a given ionic configuration is calculated by means of Density Functional Theory (DFT) [83], and numerical algorithms are applied in order to find the ionic configuration that minimizes the energy of the system.

The purpose of DFT is to avoid the direct solution of the multi-electron Schrödinger equation by assuming that the energy of the system is a unique functional of the charge density ρ . In the Kohn-Sham scheme [84], a fictitious system of non-interacting electrons is introduced, which allows for the energy functional $E[\rho]$ to be written in the following way:

$$E[\rho] = T_s[\rho] + \int v_{\text{ext}}\rho(\vec{r})d\vec{r} + V_C[\rho] + E_{\text{xc}}[\rho]. \quad (2.43)$$

The terms on the right-hand side are respectively the kinetic energy of the non-interacting electrons, the external potential (caused by the interaction with the nuclei), the classical Coulomb interaction between electrons, and the exchange-correlation function. The latter term represents the error made by using the non-interacting kinetic energy, and by treating the electron-electron interactions classically [83].

The energy obtained by means of Eq. 2.43 represents the exact ground-state energy of the system [83], but the exchange-correlation function is unknown and requires the introduction of some approximations. The most common is the *local density approximation* (LDA) [83], according to which the exchange-correlation functional at a given point in space is given by that of a homogeneous electron gas, with density equal to the local density in that point. For a simple system such as an electron gas, the exchange-correlation function is known. However, the LDA is not accurate enough for calculations in e.g. transition metals, for which reason the *generalized-gradient approximation* was developed. It provides a correction to the LDA by postulating that the exchange-correlation function not only depends on the

local value of the density, but also on the local value of the density gradient [83]. This correction allows for a great improvement in the prediction of transition-metal properties. A number of functionals exist, the most common ones for metals being that of Perdew and Wang [85] and that of Perdew, Burke, and Ernzerhof (PBE) [86]. Spin-polarized systems can be treated by separating the electron density into the spin components: $\rho(\vec{r}) = \rho_{\text{up}}(\vec{r}) + \rho_{\text{down}}(\vec{r})$.

The iterative method to calculate the energy in the electronic loop is as follows: starting from an initial guess of the electron density ρ , the exchange-correlation functional is calculated. This allows for the solution of the Kohn-Sham equation [84]:

$$\left[-\frac{1}{2}\nabla^2 + v_{\text{ext}}(\vec{r}) + \int \frac{\rho(\vec{r}')}{|\vec{r} - \vec{r}'|} d\vec{r}' + \frac{\partial E_{\text{xc}}[\rho]}{\partial \rho} \right] \phi_i(\vec{r}) = \varepsilon_i \phi_i(\vec{r}). \quad (2.44)$$

The wave-function solution $\phi_i(\vec{r})$ is used to calculate a new value of the electron density as $\rho(\vec{r}) = \sum_i |\phi_i(\vec{r})|^2$, and the total energy of the system can be obtained with Eq. 2.43. If the energy difference with respect to the previous step is larger than the desired tolerance, a new value of $E_{\text{xc}}[\rho]$ is calculated and the scheme is repeated until convergence.

The implementation of such a scheme in computer codes requires the discretization of the wave functions and the external potential. In *pseudopotential methods*, this is done by expanding both of them in a finite basis set of plane waves. Moreover, in such methods two distinct descriptions of the valence (outer) and the core regions are applied, in order to avoid the many oscillations of the physical wavefunction that would require a large amount of elements in the basis set. In the valence region, normal plane waves are used, whereas inside the core the pseudo wave function and the pseudopotential are smoothed. The *cutoff energy* is the maximum energy of the basis set of plane waves. A more efficient scheme is provided by the projector-augmented wave (PAW) method [87]. In this case, the description of the core region is improved by expanding the wave function in terms of atomic orbitals, whereas in the valence region plane waves are still used.

Bloch's theorem allows for the wave function of electrons in a periodic potential to be written as [88]:

$$\phi_k(\vec{r} + \vec{T}) = e^{i\vec{k}\cdot\vec{T}} \phi_k(\vec{r}), \quad (2.45)$$

which in turn allows for all properties to be computed by solving the Kohn-Sham equation in the first Brillouin zone. Several of these properties are obtained by numerical integration in k -space, which requires the definition of a k -point mesh. In this work, a Monkhorst-Pack k -point mesh (i.e., with equally-spaced points) centered in the Γ point is always employed. Moreover, in order to avoid abrupt step-wise changes in the integrand, the Fermi distribution is smeared around the Fermi energy with a parameter σ , which allows for the use of a limited number of

mesh points. This smearing is equivalent to introducing some non-zero temperature electronic excitation.

Calculation of energy barriers

Much of the work in this thesis relies on the calculation of migration barriers between atomic configurations. These barriers can be computed with DFT calculations combined with the nudged elastic-band (NEB) method [89]. It is a method that allows for the minimum energy path (MEP) between two configurations to be found. The maximum along the MEP corresponds to the saddle-point energy, which gives the activation energy barrier.

Generally speaking, elastic-band methods rely on a chain of images between the end-point configurations, which are connected to each other by springs. These images are optimized simultaneously by changing step by step the atomic configuration of each of them. The algorithm aims at minimizing the total path energy, given by the sum of the DFT energy of each state and the elastic energy. The total force acting on each image i is given by [89]:

$$\vec{F}_i = \vec{F}_i^t + \vec{F}_i^s . \quad (2.46)$$

The first term is the true force $\vec{F}_i^t = -\nabla V(\vec{R}_i)$, and the second term is the spring force, namely:

$$\vec{F}_i^s = k_{i+1}(\vec{R}_{i+1} - \vec{R}_i) - k_i(\vec{R}_i - \vec{R}_{i-1}) , \quad (2.47)$$

where k_i are the spring constants and \vec{R}_i is the position of image i in the energy space.

This generic *plain elastic-band method* has two issues. In first place, the true force along the band "pushes" the images away from high-energy regions towards the shallow areas, reducing the image density in the saddle-point region, which is therefore poorly described. Secondly, the spring force perpendicular to the band might interfere with the MEP search, pushing the images upwards in the steepest region. The NEB method circumvents these issues by retaining only the true-force component perpendicular to the local tangent of the band, and the spring-force component along this tangent [89]:

$$\vec{F}_i^{\text{neb}} = \vec{F}_i^t \perp + \vec{F}_i^s \parallel . \quad (2.48)$$

In this way, spring forces allow the band to maintain a spread distribution of images, while the true force pushes the band towards the MEP. This is schematically depicted in Fig. 2.10a. Once the MEP has been found, however, there is no condition ensuring that one of the images is located exactly at the saddle point, and a spline interpolation between images is necessary. Alternatively, it is possible to apply the *climbing-image algorithm* [90]. In this algorithm, after a few regular NEB

steps the image with the highest energy is identified. At this point, the total force acting on this image is no longer defined as in Eq. 2.48, but is replaced with the total true force, where the component along the band has been reversed:

$$\vec{F}_{i_{\max}}^{\text{neb}} = \vec{F}_i^{\text{t}} - 2\vec{F}_{i_{\max}}^{\text{t}} \parallel \quad (2.49)$$

This can be better visualized with Fig. 2.10b. The reversed parallel component of the true force pushes the image upwards towards the saddle point, whereas the perpendicular component of the true force (with the correct sign) prevents the image to climb sideways. In this way, the true saddle-point can be found with great accuracy, whereas the other images with the regular NEB forces ensure that the algorithm keep the elastic band on the MEP.

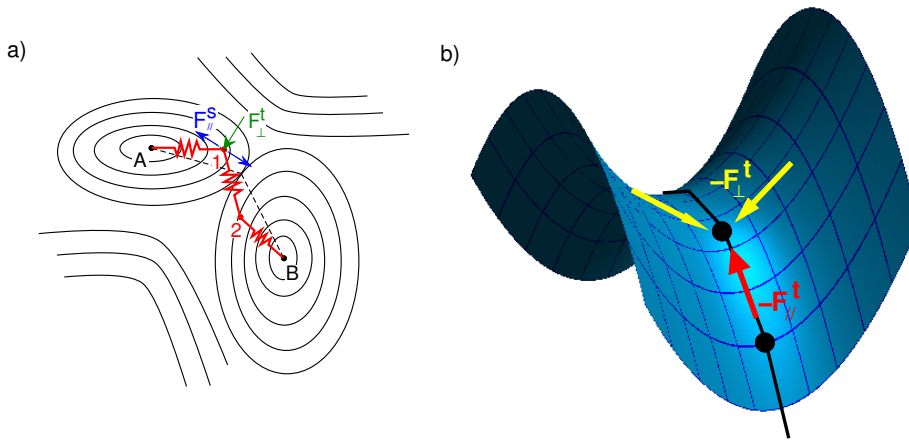


Figure 2.10: a) Schematic representation of the nudged elastic band method, to find the minimum-energy path between equilibrium states A and B. The lines represent isoenergy hypersurfaces. On each image, the true force act only on a plane perpendicular to the band local tangent, whereas the spring forces act only along the direction of the local tangent. b) Climbing-image forces acting on the image closest to the saddle point. The spring forces are removed, and the parallel component of the true force is reversed, in order to push the image towards the saddle point.

Calculation of attempt frequencies

In Eq. 2.2, the attempt frequency ν is an effective frequency associated with the lattice vibrations. In the harmonic approximation, each atom of the lattice can be

seen as a body connected to its neighbors throughout a spring, forming a three-dimensional spring network. Such a system is therefore characterized by a number of vibrational (phonon) modes that affect the defect vibrational properties, and the transition rates consequently [88].

The phonon spectrum can be calculated by diagonalizing the dynamical matrix, which is defined as [91]:

$$\Phi_{ij} = \frac{1}{\sqrt{m_i m_j}} \frac{\partial^2 E}{\partial r_i \partial r_j} = \frac{1}{\sqrt{m_i m_j}} \frac{\partial F_i}{\partial r_j}. \quad (2.50)$$

Each element of the matrix is obtained by performing a small displacement r_j of atom j , and measuring the force F_i acting on atom i . In an N -atom system, the matrix has size $(3N - 3) \times (3N - 3)$, because each atom has three degrees of freedom, and the total energy is translational invariant in a supercell with periodic boundary conditions. The displacement must be sufficiently small to remain within the harmonic approximation, and sufficiently large not to be affected by the numerical noise on the force measurement. In practice, this type of calculation can be done in *ab initio* codes in an automated fashion, as the code can determine the least amount of displacements needed to calculate the whole matrix, based on the supercell symmetries. A high level of accuracy on the residual forces in the relaxed supercell is required. The accuracy can be improved by performing several displacements of different amplitudes for each atom, and by interpolating the force with the least-squares method.

The eigenvalues of the matrix are the lattice phonon modes. Following Vineyard's theory [92], the attempt frequency of a defect can be determined as:

$$\nu = \prod_{j=1}^{3N-3} \nu_j^R / \prod_{j=1}^{3N-4} \nu_k^S, \quad (2.51)$$

where ν_j^R are the phonon modes in the relaxed defect supercell, and ν_j^S are those of the saddle-point configuration. In the latter configuration, one degree of freedom is missing, as it corresponds to the mode for the motion of the jumping atom in the saddle-point direction, which is constrained.

Frozen-phonon calculations are also used in Paper II to determine the vacancy formation entropy in pure iron. In this case, following the work of Mishin *et al.* [93], the formation entropy can be obtained from the phonon modes of the undefected cell ν_j^U and those of the relaxed defect cell ν_j^R :

$$\frac{S_v^f}{k_B} = - \left[\sum_{j=1}^{3N-6} \ln \nu_j^R - \frac{N-2}{N-1} \sum_{j=1}^{3N-3} \ln \nu_j^U \right], \quad (2.52)$$

where N is here the number of atoms in the undefected supercell.

2.8 Kinetic Monte Carlo methods

The aim of the second part of the thesis is to model the microstructure evolution of RPV alloys under irradiation. Long-term evolution can be simulated either by mean-field rate theory (MFRT) models, or by kinetic Monte Carlo (KMC) methods. MFRT is an analytical method featuring a set of balance equations that describe the concentration of defects and clusters of different size. Although their solution is fairly straight forward, the main setback is the absence of spatial inhomogeneities and correlations, which have been shown to be a significant feature in clustering phenomena [50].

On the other hand, KMC is a method that provides a solution to the Master equation (Eq. 2.20) with a stochastic approach. The evolution of the system is simulated by randomly choosing among a set of transitions between possible states, based on probability distribution functions built on the known transition rates. Each event is therefore characterized by a frequency ω_i , corresponding to the thermally-resolved barrier of Eq. 2.2. The simulation time is advanced after each step with the residence-time algorithm [94]:

$$\delta t = \frac{-\ln r}{\sum_i \omega_i}, \quad (2.53)$$

where r is a random number between 0 and 1. In KMC, spatial correlations and the overall geometry of the system are correctly represented. One of the main drawbacks is the large computational power needed, especially when the system falls into trapping configurations. For instance, this occurs when the frequency of one event is much larger than that of the other events (e.g. solute atoms with a low migration barrier).

Two types of KMC are employed in this work: atomistic (AKMC) and object KMC (OKMC). The main difference between the two methods lies in the entities performing the transitions. In AKMC, single species (atoms and defects) perform the jumps. In this way, the elementary atomic mechanisms are reproduced and the diffusion phenomena can be studied in details, although this yields a slower evolution. Conversely, in OKMC the evolution is driven by the transitions of user-defined objects, which can be for instance single defects, impurities, or their clusters. For this reason, OKMC belongs to the category of *coarse-grained methods* [95]. The possible events that can occur in an OKMC simulation are also defined by the user, and normally entail object migration, dissociation, aggregation (coarsening of smaller objects into bigger ones), or annihilation of opposite types of defects. This allows for longer time scales to be reached, because the motion of a big object, which would require a large amount of AKMC steps, occurs in OKMC with a single step. OKMC methods are therefore suitable to simulate microstructure evolution of RPV steels, as they allow to match the real time scales. In Paper V, a hybrid AKMC-OKMC model is presented. In this model, the evolution follows the usual AKMC algorithm. However, copper clusters above a critical size are treated in an OKMC fashion when they contain a vacancy, and they can migrate as a whole

object until the vacancy is emitted. Such approach represents an adequate tradeoff between simulation speed and accuracy of the elementary atomistic mechanisms.

The only physical input that determines the reliability of the simulation is given by the transition rates of each event, which must therefore be as accurate as possible. This subject is treated in the following sections.

Transition rates in AKMC models

As discussed in Section 2.1, the defect jump frequencies depend on the LAE around the defect. In a dilute binary alloy, it is fairly easy to obtain the jump frequencies for all the possible configurations. However, the task becomes prohibitive as soon as some complexity is added (e.g. concentrated alloys, multicomponent alloys, or multiple defects), because of the fast-increasing number of LAE configurations.

The usual approach is to calculate migration barriers of a given configuration based on a cohesive model that is used to describe the energy of the system in that configuration. The whole model reliability depends then on the accuracy of the cohesive model. Interatomic potentials or cluster-expansion methods are the most common choices for such cohesive models [96, 50]. In particular, it is customary to build up pair-interaction models, where all properties of the alloy are described by effective atomic-pair interactions [97, 98, 40]. Such models need to be fitted on *ab initio* and experimental data in order to ensure their reliability.

Once the cohesive model is defined, the migration barrier can be obtained by means of different approaches. The most common one is the use of the final-to-initial-state-energy (FISE) formula [96]:

$$E^{\text{mig}} = E_0^{\text{mig}} + \frac{E_f - E_i}{2}, \quad (2.54)$$

(Fig. 2.11a) where E_f and E_i mark respectively the energy of the final and initial state, and are determined by the cohesive model. The attempt frequencies are usually assigned the value of the Debye frequency in iron (6 THz) [67]. This model then assumes that the energy barrier depends mostly on the energy difference between equilibrium end-states, neglecting in this way any effect by the LAE on the saddle-point properties. In Paper II, it is shown that the LAE effects are actually non-negligible and can affect the global solute-transport tendencies. Therefore, the FISE model is likely to be inaccurate in the reproduction of such tendencies. Moreover, it is also somewhat unphysical because it assumes *a priori* the knowledge of the final state, whereas this is actually unknown in reality. More advanced methods, allowing for the on-the-fly calculation of saddle-point energies, are available (e.g. the dimer method [99], or the NEB method based on DFT or other cohesive models), but are usually computationally demanding and their application for long-term evolution simulation is therefore impractical [50]. As an alternative to the FISE approach, it is possible to obtain the saddle-point energy by means of broken-bond models [100, 50]. In this way, the migration barrier is computed inde-

pendently of the final state, but the broken-bond model still has to be fitted on *ab initio* or experimental data.

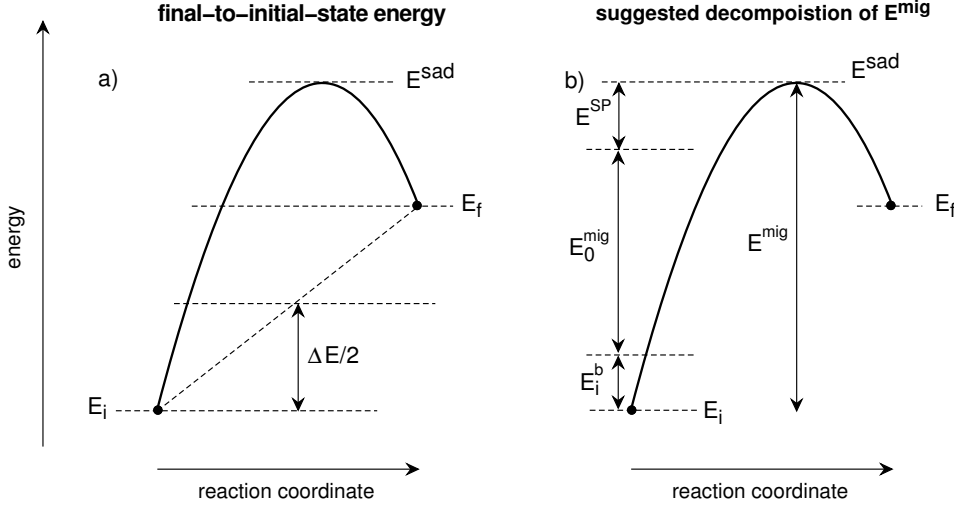


Figure 2.11: a) Schematic representation of the common energy model for the prediction of unknown energy barriers [96]. b) Decomposition of the migration barrier in a thermodynamic contribution (the binding energy E_i^b) and a kinetic contribution (E^{SP}), suggested in this work.

Finding the correct migration barriers corresponding to a given LAE is therefore crucial to reproduce the correct solute-transport behavior of defects in KMC models. For instance, the cohesive model used for the simulation of cluster formation in FeMnNiCu alloys [40] was tested in this work by calculating the transport coefficients of a dilute binary alloy by means of Eq. 2.12, but did not yield any vacancy-drag tendency. Conversely, the implementation of the exact set of *ab initio* jump frequencies yielded transport coefficients in perfect agreement with the SCMF method (as is discussed in Paper IV). The atomistic processes leading to cluster formation simulated by means of this pair-interaction model [40] are therefore likely to be inaccurate.

The model can be improved by applying the cluster-expansion method to the saddle-point energies [96]. In other words, a way to circumvent the inaccuracy of the migration barrier prediction may be to aim at building a cohesive model for the saddle-point energy landscape. For this purpose, it would be beneficial to separate the kinetic component from the thermodynamic component of the migration barrier in the way suggested in Paper II:

$$E^{\text{mig}} = E^{\text{SP}} + E_0^{\text{mig}} + E_i^b, \quad (2.55)$$

(Fig. 2.11b) where E_i^b is the total binding energy of non-iron species (impurities and defects) in the LAE. E^{SP} represents hence the perturbation from the background saddle-point energy due to the presence of non-iron objects in the LAE. It might be advantageous to build two separate cohesive models for E_i^b and E^{SP} .

In Paper IV, a simple cohesive model is used to calculate the properties of vacancy-MnNi clusters in FeMnNi dilute alloys. It is based on the sum of pair binding energies between non-iron objects X_j as follows:

$$\Delta E = E^f - E^i = \sum_{j=1}^{N_{\text{obj}}} \left[\left(E_{V,X_j}^{\text{b,f}} - E_{V,X_j}^{\text{b,i}} \right) + \left(E_{\text{AT},X_j}^{\text{b,f}} - E_{\text{AT},X_j}^{\text{b,i}} \right) \right], \quad (2.56)$$

where AT marks the migrating atomic species. The migration barriers are then obtained with the FISE formula (Eq. 2.54). The binding energies at 1nn and 2nn are calculated *ab initio*. The purpose is to build a simple model that can yield the correct solute-transport tendencies, which are related, although not exclusively, to the thermodynamic interactions. However, the saddle-point interactions is still neglected, and the flux-coupling tendencies turn to be still underestimated with respect to the SCMF predictions. An alternative solution to this migration-barrier issue is presented in the following section.

Artificial neural networks

Paper V investigates an alternative approach to the prediction of migration barriers. Based on the work of Castin [101, 102, 103, 104], the migration barriers of unknown LAE configurations can be predicted by using artificial intelligence, more precisely by performing a non-linear regression based on an *artificial neural network* (ANN). This method has been successfully applied to simulate copper precipitation in FeCu alloys, and has proved to be both physically reliable and computationally efficient [105, 106, 107].

The main idea is to build a network that can "learn" to predict migration barriers based on a set of known examples. In this way, the network can provide reliable predictions when the LAE appearing during the simulation is not part of the set of known examples. The accuracy of the ANN predictions is checked by means of another set of known barriers. The ANN in this case can therefore be seen as an extension of a polynomial fitting procedure, where the coefficients of the polynomial are obtained by minimizing the least-squares error.

Neural networks are a broad range of methods that find application in several fields, such as data mining, pattern recognition and classification, data processing, non-linear control, and many others [108]. For instance, a relevant application for the purposes of this project is the prediction of radiation-induced hardening of RPV steels from a large database of RPV mechanical tests [109]. Neural networks represent a computational framework in which the solution to a problem is learned from a set of examples, taking inspiration from the information-processing mechanisms of the human brain. In the brain, electric signals are processed by neurons, connected

to other neurons through a thick and highly parallelized network of synapses. In each neuron the information processing is relatively slow, but the high degree of parallelism allows the brain to achieve a high processing power [110]. Most importantly, neurons can modify their responses after being exposed to external signals, a process that is usually referred to as "learning".

For the application of interest in this work, the ANN is a non-linear mathematical function that transforms a set of inputs (the LAE chemical composition and the type of migrating atom) into an output (the migration barrier). The transformation occurs through a set of weight parameters, which are obtained by training on a known set of data. One of the most common types of ANN, which is also employed here, is the *multilayer perceptron*, an example of which is schematically depicted in Fig. 2.12. In this example, the network consists of an input layer, a hidden layer, and an output layer, each of them containing one or several nodes. Each node is a simple processing unit (the neuron of the ANN) that receives some input signals and emits an output signal. The hidden structure can be made of several layers in series. Each node is connected to other nodes by synapses. In so-called *feedforward* models, the most common ones, the signal is allowed to proceed only forward. This means that each node receives an input only from previous layers, and sends the output only to following layers [110, 104].

The mathematical structure of a given hidden node j is the following:

$$\begin{cases} y_j &= \phi(v_j) \\ v_j &= w_j^0 + \sum_{i=1}^N w_{ji}x_i \end{cases}, \quad (2.57)$$

where the index i marks the N inputs coming into node j , x_i is the input value, y_j the output of the node, and v_j the *internal activity*. w_{ji} and w_j^0 are the weights (synapses) that can be determined by training the network. ϕ can be any non-linear function, which is usually bounded in order to prevent the formation and amplification of excessively large signals. The same structure characterizes as well the output node. Several techniques exist to design the most appropriate architecture, which consists in finding the optimal number of hidden layers, nodes, and synapses [104]. The architecture utilized in Paper V is a single-hidden layer network, and is described in details in [103].

Training the algorithm then consists in finding proper values for the synapses that minimize the error made on the training data set. This training set has to be carefully planned, in order to make it as much diverse and inclusive as possible. If the network is "taught" to predict barriers only in a restricted range of conditions, it would provide completely wrong predictions when the conditions are considerably different. For instance, an elementary but useful example is that the evolution of a concentrated alloy cannot be reproduced by an ANN that has been trained only on migration barriers calculated in the dilute alloy.

For the purposes of this work the ANN represents an efficient, high-speed non-linear regression method in the large database set of migration barriers in different LAE's. It allows for the extraction of hidden knowledge from this database, and

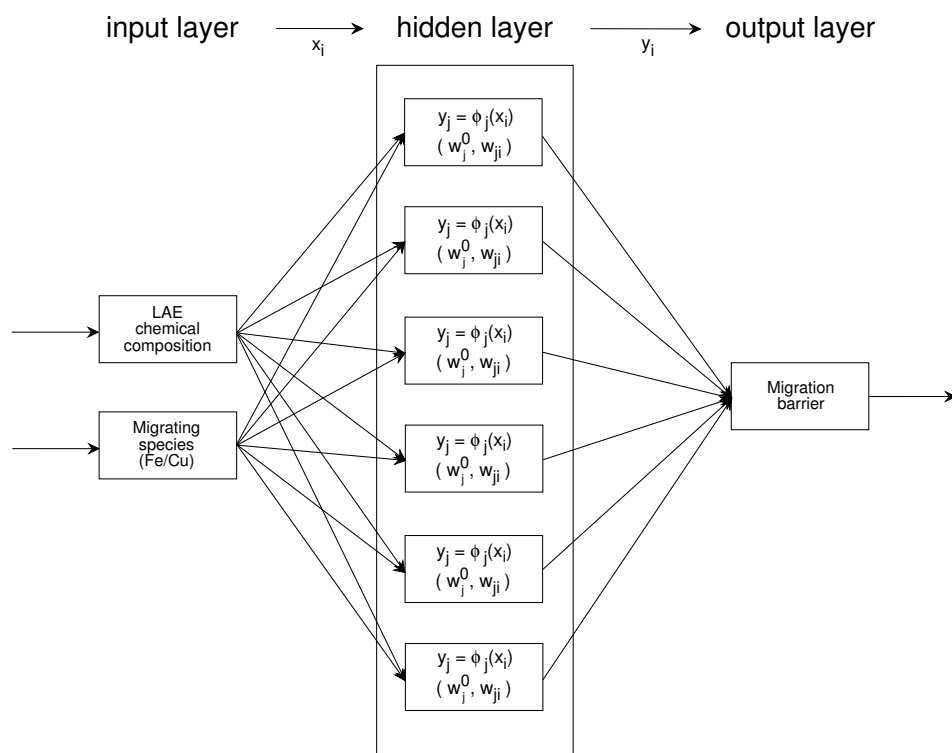


Figure 2.12: Example of artificial neural network with one hidden layer and 6 hidden nodes, applied to the calculation of migration barriers as functions of two input data: the type of migrating species, and the composition of the local atomic environment (LAE). Each node j is characterized by the parameters w_j^0 and w_{ji} , which are obtained by training the network on a set of known migration barriers.

is able to provide accurate predictions when new LAE's are encountered. The application to prediction of migration barriers is hence very promising and can represent a valuable aid to microstructure-evolution models.

The main setback is surely the need for a large amount of migration barriers to be used for training and validation. In [103] 10^4 barriers were calculated by means of the NEB method applied on an interatomic potential. This method allows large amounts of energy barriers to be calculated rather inexpensively, but obviously relies on the properties (and the reliability) of the potential used. In this work, the ANN training is performed for the first time with DFT-NEB calculated migration barriers. Thanks to the ever-increasing computational power of modern supercomputers, it is now feasible to perform large amounts of NEB simulations with DFT, which is to date the most reliable cohesive model that one can use to calculate alloy

properties.

In the particular application to thermal aging in FeCu alloys, it is shown in Paper V how the set of known migration barriers can be limited to 2000 configurations, without invalidating the ANN predictive capabilities. This set has to be carefully planned in order to provide the ANN network with the most diverse and inclusive set of configurations, which sample as well as possible all the LAE's that the defect may encounter during the simulation. For this reason, three types of LAE were distinguished and sampled (Fig. 1 of Paper V): a perfectly random alloy, a vacancy jump in the vicinity of small-sized Cu clusters, and vacancy transitions inside and across the surface of large Cu clusters. The latter LAE type uncovers another issue in this ANN-DFT approach. DFT-NEB calculations become in fact very computationally demanding in supercells larger than 250 atoms. Therefore, at the current state very large clusters cannot be treated with DFT. This matter is discussed in more details in Paper V.

Transition rates in OKMC models

OKMC codes need to be parameterized by providing the transition rates for all events that are included in the model, mainly activation energies and prefactors for migration and dissociation of clusters of any composition and size. Other parameters might be needed, depending on the objects and the events included in the model, such as dissociation patterns (possible emission of different objects), object interaction radii, and sink strengths [95].

The stability (dissociation) and mobility (migration) parameters can be obtained by *ab initio* calculations for small-sized clusters, or with molecular-dynamics (MD) simulations and AKMC simulations for larger sized ones [95]. In this work, such parameters are obtained by means of dedicated AKMC simulations. Again, the reliability of these parameters depend on the cohesive model and migration-barrier prediction method that is used in the AKMC model. In Paper IV, the cohesive model is provided by Eq. 2.56, whereas in Paper V the migration-barrier prediction is performed with the ANN.

The algorithm to calculate the cluster parameters is quite straight forward [105, 106]. Provided that a reliable AKMC kinetic model is available, a cluster of a given size, composition, and at a given temperature is placed in the centre of a simulation cell with periodic boundary conditions. During the simulation, the cluster evolves with the usual AKMC algorithm until it dissociates, i.e. when it emits at least one of its constituents. This procedure is repeated N times in order to gather enough statistical data.

At the end of each experiment, the following quantities are recorded: the cluster trajectory, the relative distance covered by the cluster (i.e. the free path \vec{R}_j), and the dissociation time τ . The average dissociation time can be obtained as $\bar{\tau} = \sum_N \tau_j / N$. The diffusion coefficient can be inferred with two alternative procedures:

1. from the square of the free path of each simulation, using Einstein's definition

[58]:

$$D = \frac{1}{N} \sum_{j=1}^N \frac{|\vec{R}_j|^2}{6\tau_j}; \quad (2.58)$$

2. in case the mean free path is too short (for unstable or immobile clusters), the trajectories from several simulations are lashed together, to form a unique long trajectory. The latter is then divided in segments corresponding to time intervals of increasing size. The diffusion coefficient can hence be computed as a function of the size of the time interval, with Eq. 2.58. By doing this operation, a plot such as the one in Fig. 2.13a is obtained. The diffusion coefficient is then taken as the average D in the convergence (flat) zone [106].

The second method is more accurate, because when the distance covered in one simulation is too short, correlation effects might be lost, as the cluster has no time to possibly repeat back-and-forth jumps. Therefore, the diffusion coefficient might be overestimated. Finally, the mean free path is obtained either as an average of the free paths \vec{R}_j in each simulation: $\delta = 1/N \sum_j |\vec{R}_j|$, or by inversion of Eq. 2.58: $\delta = \sqrt{6D\tau}$.

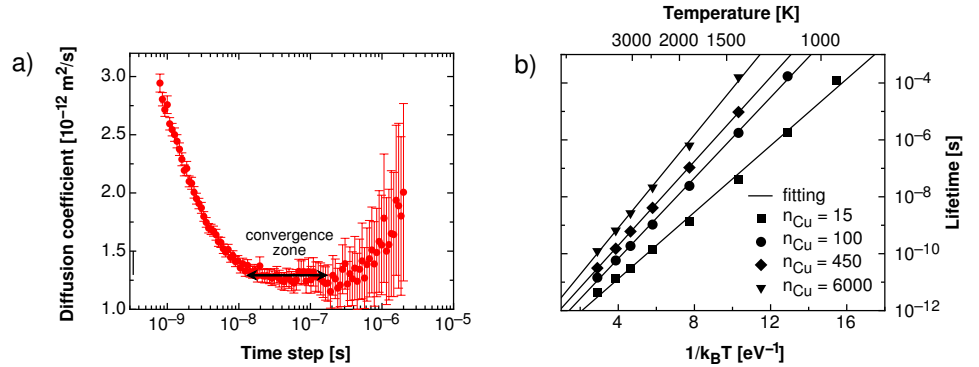


Figure 2.13: a) Example of calculation of diffusion coefficient (for a divacancy cluster) by lashing several trajectories from different KMC simulations and using the time step as a variable parameter. The diffusion coefficient is taken as the average in the convergence zone. b) Example of copper-cluster lifetime fitting in the Arrhenius domain. The slope of the straight line yields the cluster dissociation energy.

The last step consists in deriving the dissociation energy, migration energy, and relative prefactors by performing a linear regression in the Arrhenius domain of the quantities $\bar{\tau}$ and D calculated at different temperatures, as is shown for instance

in Fig. 2.13b. The dissociation energy E^{dis} and prefactor τ_0 are therefore obtained as:

$$\tau(T) = \tau_0 \exp\left(\frac{E^{\text{dis}}}{k_{\text{B}}T}\right), \quad (2.59)$$

whereas the migration energy E^{mig} and prefactor D_0 are given by:

$$D(T) = D_0 \exp\left(-\frac{E^{\text{mig}}}{k_{\text{B}}T}\right). \quad (2.60)$$

The quantities E^{dis} , E^{mig} , τ_0 , and D_0 for each cluster size and composition are therefore the main parameters used in the OKMC simulations.

Gray-alloy approach

One of the main scopes of this project is to provide the theoretical background for the introduction of solute-transport mechanisms in OKMC simulations. This is not an easy task. It requires the knowledge of stability and mobility properties of a large variety of defect-solute clusters, and the complexity increases with the number of chemical species to be simulated in the alloy. Even simple solute-transport mechanisms (as for instance vacancy-solute coupled pairs) are still not included in the existing OKMC models, to the author's knowledge. The systematic solute-transport investigation performed by this work allows to build the foundation for the implementation of direct solute transport in OKMC models. For instance, in Paper IV the stability and mobility parameters of solute-vacancy pairs are calculated by AKMC simulations parameterized with the exact *ab initio* migration barriers.

In an existing OKMC model [111, 49] for the microstructure simulation of FeMnNi alloys, the presence of impurities was treated with a *gray-alloy* approach, and successfully applied to reproduce experimental results. Here, this model is used to simulate the long-term evolution of Ringhals steels. For this reason, a short presentation is provided here. Full details can be found in the aforementioned references.

The OKMC model describes the evolution of vacancy- and interstitial-cluster populations under neutron irradiation. In addition to defect clusters, the model contains also carbon traps, dislocations and grain boundaries, as to reproduce as closely as possible the microstructure of a real alloy. Traps (C atoms and C_2V complexes) are modeled as immobile objects that can block defect clusters with an assigned cluster size-dependent binding energy. Their concentration is adjusted in order to match the actual carbon content in the matrix. Sinks are represented as spherical objects with the proper size and density to match the sink strength corresponding to the experimental dislocation density. Finally, grain boundaries are included by instantly removing an object when the total distance covered from the beginning of the simulation has reached the mean experimental grain radius.

The approach is defined as *gray alloy* because the chemical impurities (Mn and Ni) are not explicitly present in the code, but their effect is introduced by modifying the mobility parameters of defect clusters. The interstitial mobility reduction was based on the work of Terentyev *et al.* on FeCr alloys [33], where an MD-based analytical model was derived to describe the slowdown of interstitial clusters due to the presence of Cr solute atoms in the alloy. Analogous MD simulations have shown a similar effect by Mn impurities [112]. For this reason, the model described in [49] included the effect of Mn only, but it has been here modified in order to introduce a similar effect of Ni impurities. Recent DFT calculations [44] have shown that the binding energy of a Ni solute (E_b^{Ni}) with an interstitial loop is actually stronger than that of a Mn solute (E_b^{Mn}), which strongly suggests a similarity in the way they interfere with the loop mobility. Therefore, the diffusion coefficient of an interstitial loop of size n is defined as:

$$\frac{D_n^{\text{FeMnNi}}}{D_n^{\text{Fe}}} = \exp \left[-\frac{n \ell (E_b^{\text{Mn}} + E_b^{\text{Ni}})}{k_B T} \right], \quad (2.61)$$

where D_n^{FeMnNi} is the diffusion coefficient of a loop of size n in the multicomponent alloy, and D_n^{Fe} is that of the corresponding cluster in pure-iron (which can be found in [111]). $\ell = 9$ is an effective interaction range (in atomic-position units), and $E_b^{\text{Mn/Ni}}$ are the binding energy of one Mn or Ni solute atom with a loop (here attractive interactions are assigned a positive sign).

On the other hand, the effect of Mn and Ni on vacancy impurities is not precisely known, and a first measurement of such parameters is provided in Paper IV. Therefore, in this gray-alloy OKMC model, vacancies are postulated to be considerably slowed down in an FeMnNi alloy up to a given size ($n < 10$), and completely immobilized above this size. This choice was made in order to fit the experimental measurement of vacancy-cluster density [49]. Although not yet proved, this assumption has been retained for the OKMC simulations of the Ringhals RPV steels presented in Chapter 4.

Chapter 3

Results I: Solute-transport mechanisms

3.1 Vacancy-assisted transport

In this section, the focus is on solute-transport tendencies arising from vacancy diffusion, to which Paper I and II are dedicated. The main goal is to identify the intrinsic impurity-transport mechanisms (inverse Kirkendall or vacancy drag, see Section 2.1), first for the main RPV chemical constituents observed in the radiation-induced nanofeatures (Paper I), and then for all transition-metal impurities (Paper II). As was discussed in the introduction, vacancy drag can possibly intervene as a growth mechanism for solute clusters, and be partially responsible for impurity segregation at grain boundaries or dislocations.

The possibility of vacancy drag is therefore here investigated as a function of temperature. In Paper I, a network of 26 frequencies (Fig. 2.2) is developed to describe the effect of the impurity within the 5nm distance. The migration barriers for each transition are calculated by DFT, and the SCMF vacancy method is applied to obtain the transport coefficients [63]. The SCMF solution is achieved based on the computer code developed in [76], although the kinetic model is here extended in order to cover the 5nm distance. This represents the first complete analytical model able to investigate flux coupling without approximations in alloys characterized by long-ranged interactions. It provides a considerable advancement with respect to the available multifrequency models [113, 114] that were limited to 2nm interactions only and did not feature a full description of kinetic correlations.

The main conclusions of Paper I are here drawn and discussed. Fig. 3.1 shows the solute-vacancy binding energies (left panel) and the wind factor (right panel). The latter is given by L_{BV}/L_{BB} , where $L_{BV} = -(L_{AB} + L_{BB})$ ($A=Fe$, $B=solute$, $V=vacancy$), and is positive when drag occurs. In the opposite case, the vacancy and solute fluxes are opposite to each other.

All solutes characterized by a binding interaction with vacancies are subjected

to vacancy drag at low temperature, where correlations are enhanced by the Boltzmann factor $\exp(E^b/k_B T)$. Therefore, Cu, Mn, Ni, P, and Si are expected to be dragged by vacancies, below a threshold temperature close to the Curie temperature¹ in iron (1043 K [67]). At RPV temperature ($\approx 300^\circ\text{C}$) the coupling tendency is strong and suggests that such impurities can be carried by vacancies towards sinks, as for instance nucleated clusters, grain boundaries, or dislocations. Cr represents an exception, as it interacts only weakly with vacancies and is therefore not subjected to drag. This is in agreement with the lack of segregation of Cr atoms on solute-rich clusters [36, 37, 20, 38].

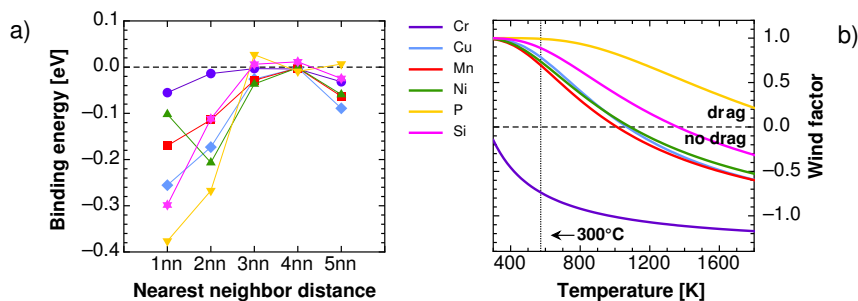


Figure 3.1: a) Solute-vacancy binding energy as a function of the nearest neighbor (nn) distance (negative signs stand for attractive interactions). b) Wind factor L_{BV}/L_{BB} as a function of temperature. Vacancy drag occurs for positive values of the ratio.

The convergence of the flux-coupling tendencies with the extent of the thermodynamic interactions is also investigated in Paper I. Fig. 3.2 shows the wind factor for Cr and Ni impurities, for different thermodynamic models (1nn, 2nn, and 5nn), compared to a study [115] based on previous multifrequency models. Whereas for Cr the predictions of all models are alike, the predictions for Ni drag differ considerably. Because of the strong 2nn Ni-vacancy interaction, the 1nn model fails in reproducing the correct flux-coupling tendency, which is the reason why the predictions of [115] were incorrect. The 2nn model shows that Ni is dragged by vacancies. On the other hand, the extension to the 5nn shell is not essential. These results are confirmed also for the other impurities. Large differences between 1nn and 2nn models are consistently found, whereas the largest change of the 5nn model is seen only for Cu (namely, a mismatch of 150 K on the drag transition temperature, due to a non-negligible 5nn solute-vacancy binding interaction). Therefore, it can be concluded that any kinetic study in bcc alloys must include the effects of interactions to at least the 2nn distance.

¹The Curie temperature marks the transition between the ferromagnetic and the paramagnetic state.

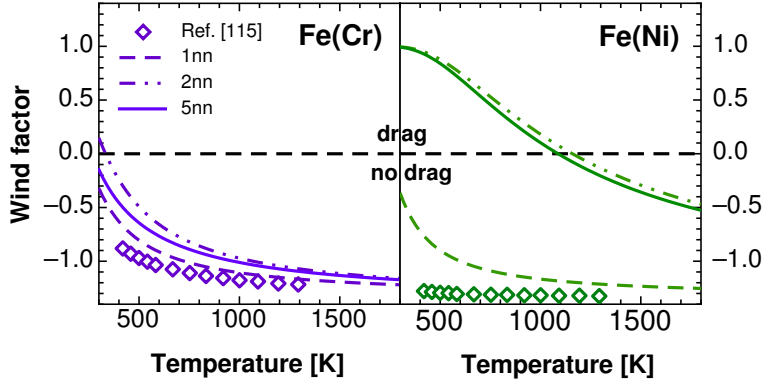


Figure 3.2: Wind factor for Cr and Ni impurities, as a function of temperature, obtained by using different thermodynamic models, with interaction ranges set to 1nn, 2nn, and 5nn. The blank markers refer to the results of a previous work [115].

Vacancy drag seems therefore to appear systematically at low temperatures. In order to investigate the origin of such flux-coupling tendencies, the method is extended in Paper II to include a wider range of impurities, encompassing all transition metals from Group IV to Group XII, as well as a few elements from the 3p row (Al, Si, and P). This is to achieve three main objectives.

1. Search for possible trends across the transition-metal groups, in order to investigate in detail the link between flux-coupling tendencies, defect properties (binding energies, migration energies, and attempt frequencies), and electronic-structure properties.
2. Verify the assumption according to which a 2nn solute-vacancy interaction is necessary for vacancy drag to arise, as advanced by previous studies [116, 117]. This statement is motivated by the necessity for the vacancy to visit 2nn sites during the drag path, as shown in Fig. 2.3.
3. Provide reliable predictions of solute diffusion coefficients at low temperatures, not accessible by experiments, and for impurities for which experimental diffusion coefficients are not available. The comparison with high-temperature experimental diffusion coefficients also allows for a model validation.

Following the findings of Paper I, the range of thermodynamic interactions is set to the 2nn distance. The main results are reported in Fig. 3.3. All properties, with the exception of the 2nn binding energy, are characterized by common trends: bell-shaped curves for 4d and 5d elements, and M-shaped (or W-shaped) curves for the 3d ones. The latter shape is caused by the atypical behavior of Mn. Such

common trends are determined by interactions at the electronic level between impurity atoms and vacancies, both for what concerns the relaxed equilibrium states, and the saddle-point configurations. Since the drag threshold temperature (Fig. 3.3c) has a very similar shape, it is possible to state that flux-coupling tendencies are driven by such electronic interactions occurring both at equilibrium and during migration. It is thus evident that the apparently atypical behaviors of Cr (weak interaction and no drag) and Ni (strong 2nn binding energy) are not exceptions, but are part of consistent trends.

Fig. 3.3c shows that the early transition metals, which have a 2nn repulsive interaction with vacancies, are also subjected to drag. This proves that vacancy drag is a more general phenomenon than expected, and given its solute electronic origin it is likely to arise also for impurity diffusion in other metallic matrices. The results can also explain the behavior of Mo impurities in RPV steels. As can be seen in the APT maps of [20], Mo is never to be found in solute-rich clusters, in spite of its non-negligible concentration (see Table 1.1). According to this work, since the drag threshold temperature for Mo is very close to the RPV operation temperature, Mo impurities are expected to undergo very weak drag tendencies, which can explain why they are not transported to solute-rich clusters.

Solute jump frequencies (Fig. 3.3b) are directly related to the diffusion activation energy (Eq. 2.5), and are shown to be controlled by the solute compressibility. This leads to the curious effect that large solutes can migrate faster, which was already observed in the Ni matrix [120]. This effect is only partially compensated for by lower solute attempt frequencies and stronger correlations. The total activation energy is therefore mainly influenced by the solute migration barrier, the solute-vacancy 1nn binding energy, and the correlation factor. The slowdown effect due to correlations can be quite relevant: for instance, Fig. 3.3d shows the very low magnitude of the correlation factor, especially for the early transition metals.

The method allows for the prediction of solute diffusion coefficients (shown in Fig. 11 of Paper II and in the Supplemental Material of the same paper). Because of magnetic effects, the shape of the diffusion coefficients is not linear in the Arrhenius plot. For this reason, the fitting to obtain the typical diffusion parameters (the activation energy Q and the prefactor D_0) is temperature dependent. The fitting results in the range 400-800 K are shown in Table 3.1. In agreement with experiments, Co is predicted to be a slow diffuser, i.e. a solute with a lower mobility with respect to self diffusion. In addition, this work predicts that Re, Os, and Ir are also expected to be slow diffusers, although no experiments are available to confirm or disprove this prediction. Finally, the comparison with the available experimental data yields an outstanding agreement for center-band elements, and an increasing mismatch for elements towards the band end (with a maximal mismatch of a factor 30). The prediction exceeds in all cases the experimental values, and the mismatch seems to affect the prefactor only (with the notable exception of Mn, for which the activation energy is in complete disagreement). The bell shape of the mismatch (Fig. 3.3f) seems to indicate the effect of some quantities (possibly some entropic effects) that are missing or are not well caught by the assumptions of this model. A

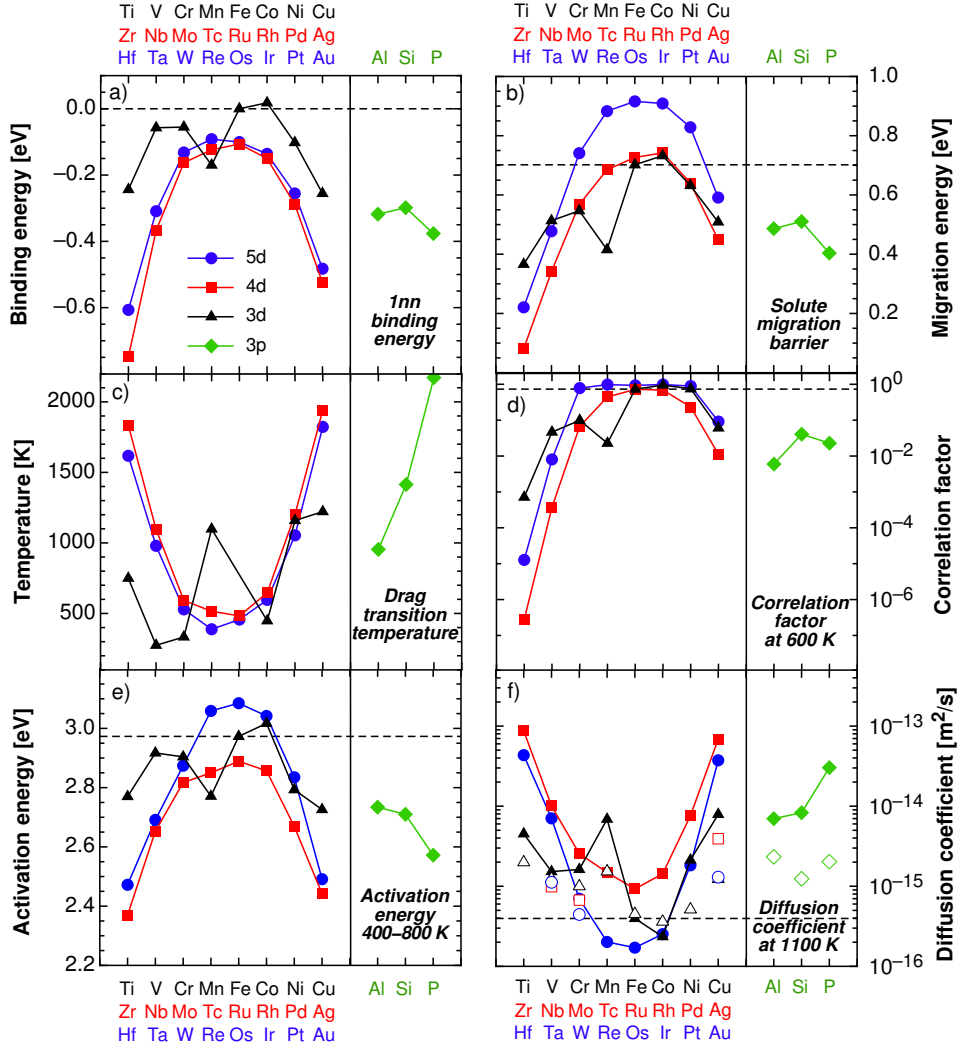


Figure 3.3: Dependence of several properties in bcc Fe on the number of electrons in the outermost shell of the solute: a) 1nn solute-vacancy binding energy; b) solute migration energy; c) threshold temperature from drag to non-drag regime; d) correlation factor f_B (Eq. 2.5) calculated at 600 K; e) solute-diffusion activation energy Q obtained from fitting in the temperature range 400-800 K; f) solute diffusion coefficient calculated at 1100 K (solid lines) compared with experimental measurements at 1100 K (blank markers) [118, 119]. The dashed lines represent the corresponding values in pure iron.

way to correct these predictions can therefore be to adjust the prefactor based on the mismatch with experiments at high temperature. Such values, when available, are provided in Table 3.1.

3.2 Interstitial-assisted transport

The solute-transport tendencies analyzed in the previous section need to be complemented with the analysis of solute transport via dumbbell mechanism, which is the main object of Paper III. Since under irradiation self-interstitial atoms (dumbbells in Fe) are produced with vacancies in equal amounts, in steady-state conditions there is an equal flux of vacancies and interstitials towards sinks. For this reason, dumbbell motion can strongly contribute to solute transport. Moreover, dumbbell-solute correlations can strongly affect the mobility of single dumbbells as well as that of small dumbbell clusters, as highlighted by several works [33, 35, 49]. Discussing such correlations in the dilute limit (one dumbbell and one solute) can be beneficial to understand correlations in more complex systems.

The method used here is analogous to that of vacancies. The thermodynamic range for solute-defect interactions is set to the 2nn distance, as inferred from the interaction extent predicted by DFT (Fig. 4 of Paper III). Based on this cutoff range, a multifrequency network in the LAE around the solute is built (Fig. 2 of Paper III). The corresponding migration barriers are obtained with the DFT-NEB method, and the SCMF theory is applied in order to analyze the solute-transport properties. The existing SCMF model for interstitial diffusion in dilute alloys [64] is extended in order to include longer-ranged interactions, thanks to the aid of a computer code purposely developed. The combination of vacancy (Paper I) and interstitial (Paper III) transport coefficients yields then global RIS tendencies, which are presented in the next section. Experimental benchmarking is in this case more cumbersome, mainly because of the lack of interstitials in thermal equilibrium due to their large formation energy [59]. At any rate, it is qualitatively achieved in Paper III by comparing with resistivity recovery experiments [121, 122, 123] and RIS experimental observations in ferritic alloys [124, 125].

A highlight on the main results is provided in Fig. 3.4. The stability of the mixed dumbbell favors the possibility of solute transport. P, Mn, and Cr solutes are carried by dumbbells, whereas Si, Cu, and Ni solutes are not. This tendency is pronounced for P, Mn (strong binding) and Cu, Ni (strong repulsion), while for Cr and Si the interaction is weak and the overall tendency is affected by the mixed-dumbbell jump frequency and all other jump frequencies in the LAE. Namely, the high migration barrier for the Fe-Si mixed dumbbell impedes Si transport, whereas Cr transport is made possible by the low barrier for the migration of the Fe-Cr dumbbell.

This yields the ratio of partial diffusion coefficients shown in Fig. 3.4b. The transport of P and Mn atoms is very efficient, and is dominant over the vacancy mechanism. This is therefore likely to be the main mechanism leading to segrega-

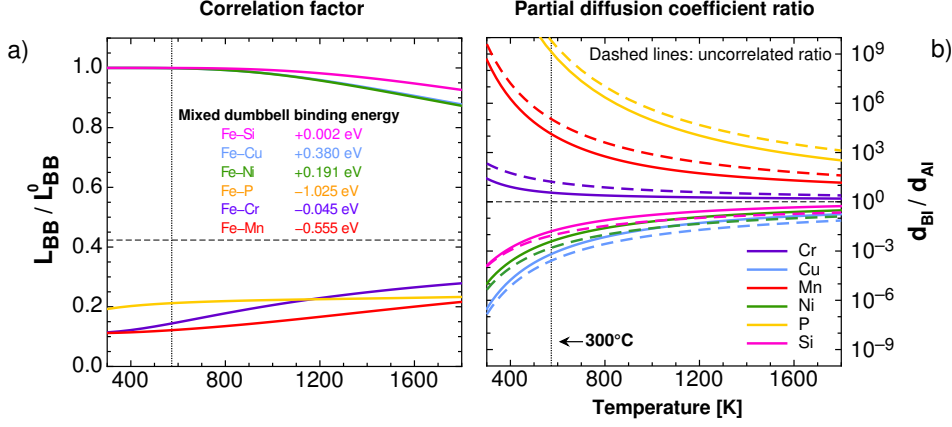


Figure 3.4: a) Correlation factor for dumbbell-assisted solute diffusion as a function of temperature, and DFT mixed-dumbbell binding energies (negative values stand for attractive interactions). The dashed line marks the value of the geometric correlation factor $f_0 = 0.42$ [58] for dumbbell diffusion in bcc crystals. b) Ratio of solute-to-iron partial diffusion coefficients (Eq. 2.17), as a function of temperature. Solute transport by a dumbbell mechanism occurs when the ratio is larger than unity. The dashed lines represent the same quantity when kinetic correlations are not taken into account (i.e. $d_{BI}/d_{AI} = l_{BB}^0/l_{AA}^0$).

tion of Mn and P atoms on solute clusters and sinks. It is worthwhile reminding, anyway, that P impurities can also move independently on an interstitial sublattice, and by continuous interchange between substitutional and foreign-interstitial position [57]. This could hence yield an even faster P migration via a general interstitial mechanism. Conversely, Cr transport is weaker and opposed to the vacancy tendency: there is thus a competition between the depletion tendency due to vacancy diffusion, and the enrichment tendency due to dumbbell diffusion.

The dumbbell-solute correlation factors, corresponding to the f_B factor of Eq. 2.5, are shown in Fig. 3.4a. This factor is small for Cr, Mn, P and close to unity for the other solutes. In the latter case, solute motion by mixed-dumbbell migration occurs very rarely, and the direction of two consecutive jumps is completely uncorrelated. In the former case, correlations slow down the motion of both solutes and interstitials. This is clearly visible in the uncorrelated PDC ratios shown in Fig. 3.4b (dashed lines). The effect is anyway relevant only for Cr. In this sense, the extension of this model to at least two solutes in the dumbbell LAE would lead to much stronger trapping effects, as was discussed in previous works [56, 33, 57].

Finally, it is worth mentioning that the results in terms of solute mobility and dumbbell-solute correlations are very similar to those obtained with the previous model [64], but the extension provided in this work is necessary to ensure that

the results are actually converged. The only relevant difference is seen in the L_{AB} coefficient (Fig. 12 of Paper III), which is quite different from the prediction of the previous model. At any rate, the effect on solute transport is completely negligible because the off-diagonal coefficient for P and Mn is almost null.

In conclusion, for the impurities here investigated solute transport occurs when the mixed dumbbell is stable. In this case, the diffusion coefficient is dominated by the L_{BB} coefficient, because correlations with iron atoms are negligible. If the mixed dumbbell is not stable, no solute transport occurs. In the latter case, the calculation of PDC ratios can still be of interest if they happen to be of the same order of magnitude of the PDC ratio for vacancies, as is the case for some of the impurities discussed in the next section. It should be anyway mentioned that there might exist cases where the mixed dumbbell is unstable, but its migration energy is sufficiently low to compensate for the repulsive binding energy. In such cases, solute transport would be due to kinetics. This possibility could be investigated by extending this study to other impurities. Finally, it is worth pointing out that the L_{AB} coefficient is always positive, as opposed to the vacancy L_{AB} that can change sign. This entails that no mechanism of flux reversal (solute flowing in the opposite direction with respect to self interstitials in the bulk) can arise.

3.3 Radiation-induced segregation tendencies

The vacancy and dumbbell transport coefficients can be combined to analyze the steady-state RIS tendencies in the dilute limit by means of Eq. 2.19. This discussion summarizes the analysis included in Paper III. Fig. 3.5a compares the magnitudes of the partial diffusion coefficient ratios for the two types of mechanisms. Each PDC ratio is shown by setting the other ratio to one, in order to obtain a depletion tendency for positive values, and an enrichment tendency for negative values, in agreement with Eq. 2.19. In Fig. 3.5b are shown the global RIS tendencies, including the magnitude prefactor. The prefactor is calculated in this case by assuming that, at steady state, $c_I/c_V = D_V/D_I = l_{AA}^{V,0}/l_{AA}^{I,0}$, which corresponds to most of the temperature and sink-density regimes discussed in [74]. It is also assumed that there is no bias in the absorption of vacancies and interstitials.

The vacancy mechanism is dominant for Ni, Cu, and Si, because the dumbbell mechanism is inactive (and the PDC ratio is almost null). Therefore, solute enrichment occurs as long as vacancy drag is ongoing, and depletion when vacancy drag terminates. This entails that, under vacancy drag, no interstitial mechanism is able to counterbalance the enrichment due to vacancies, as the interstitial PDC ratio is always positive. Just above the drag threshold temperature, the solute is slower than iron regarding vacancy diffusion, and enrichment would be expected. However, the incoming flux of Fe-Fe dumbbells counterbalances this effect, because more iron atoms are added to the sink.

For Mn and P impurities, both mechanisms lead to solute enrichment, but the interstitial contribution is dominant. P and Mn are therefore preferentially

transported by dumbbells. The enrichment tendency is very strong and independent of temperature, in agreement with the heavy segregation well known for P [126, 31, 57, 20] and recently observed for Mn [46].

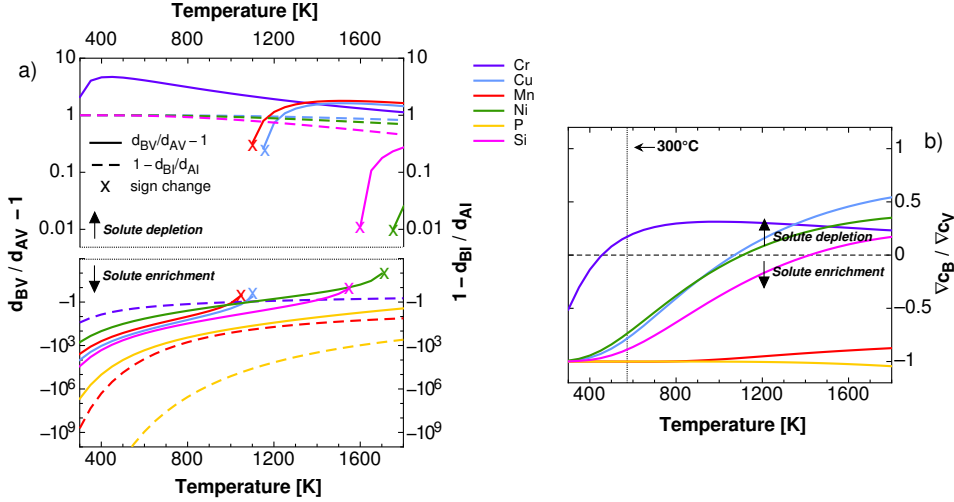


Figure 3.5: a) Partial diffusion coefficient ratio for vacancy- (solid lines) and interstitial-assisted (dashed lines) diffusion as a function of temperature. The ratios are renormalized in order to have solute depletion in the above panel, and solute depletion below. The sign change for a few curves is marked with 'X'. b) Global radiation-induced segregation tendencies as functions of temperature (Eq. 2.19). The concentration gradient ratio is explained in Fig. 2.5.

The case of Cr is surely the most interesting. Here, the contributions to RIS by vacancy and interstitial diffusion are opposite, namely vacancies lead to solute depletion, and interstitials to solute enrichment. The balance yields a switchover at around 460 K. This is in qualitative agreement with previous RIS models [125] and with RIS experimental observation in Fe-Cr alloys [124], in which a switchover was observed at 650 °C. The quantitative disagreement can be explained by the high Cr concentration in the experimental samples ($\approx 8\%$), for which a dilute-limit model is clearly unsuitable. This fine balance between vacancy and interstitial contributions is likely to be sensitive to experimental conditions (irradiation, sink density, local strains, and so on) and can hence explain the vast range of clashing Cr RIS tendencies observed in ferritic alloys [127, 128, 129, 130]. The other impurities consistently enrich in the low-temperature range. This is also in qualitative agreement with the experimental observations [124], where enrichment for Cu, Ni, Si was observed in the range 300 to 700 °C.

For the other transition-metal impurities (those of Paper II), the RIS tendencies can be qualitatively discussed, although the interstitial transport coefficients have

not been calculated. Since for these impurities the mixed dumbbell is considerably unstable [116], the dumbbell PDC ratio is expected to be small. For vacancy-dragged impurities, the vacancy mechanism is thus expected to be dominant, and the enrichment-to-depletion switchover temperature should be close to that of the drag switchover. In the absence of vacancy drag, the vacancy and dumbbell PDC ratios might be of comparable magnitudes. In the latter case, obtaining the full set of interstitial transport coefficients is necessary for any conclusion about RIS to be drawn.

Table 3.1 summarizes the transport properties for each of the analyzed impurities. When available, both vacancy and interstitial mechanisms are included in the balance, otherwise RIS tendencies due to vacancies only (with $d_{BI}/d_{AI} = 1$) are shown.

3.4 Effect of strain on interstitial transport

Strain fields next to solute clusters, grain boundaries, and dislocations can modify solute-defect interactions, diffusion rates, and flux correlations. For this reason, the steady-state RIS tendencies discussed in the previous section can be strongly affected as soon as the defect approaches a sink. This effect appears in both the defect properties and the transport coefficients. The SCMF method can be applied also to strained alloys, as was done for vacancy diffusion in NiSi alloys [79]. The amount of needed kinetic equations is increased by the reduced level of symmetry due to strain, and the use of computer codes such as the one mentioned in the previous section becomes necessary to analyze this complex symmetry.

Here is presented a preliminary study about the effect of elementary strains (Fig. 2.9) on solute-transport properties by dumbbells in FeCr. This is achieved by computing the defect elastic dipole with DFT and by applying linear elasticity theory [78, 77] to obtain the change of dumbbell formation energy, dumbbell-solute binding energy, and pure and mixed dumbbell migration energy, according to Eqs. 2.35, 2.36, and 2.37. Furthermore, it is assumed that the PDC ratio can be approximated by the ratio of mixed-to-pure-dumbbell jump frequency (Eq. 2.38). This entails that all correlation effects, namely the effect of strains on the transport coefficients, are neglected. In future works, the effect on correlations will be introduced by means of the SCMF theory.

The stability of the mixed dumbbell is strongly affected by hydrostatic strain, and the mixed dumbbell becomes unstable above $\varepsilon = 0.5\%$. For this reason, the fraction of mixed dumbbells in the system with respect to the total dumbbell population (shown in Fig. 3.6a) becomes negligible for positive strain values (i.e. in tensile regions). For the other elementary strain types, the effect is more limited because of the compensation given by dumbbells in different orientations (e.g. a tetragonal strain can have opposite effects on $\langle 110 \rangle$, $\langle 011 \rangle$, and $\langle 101 \rangle$ dumbbells).

Tetragonal strains have little effect on the PDC ratio at 300 °C, as can be seen in Fig. 3.6b. On the other hand, the other strain types can yield a non-negligible

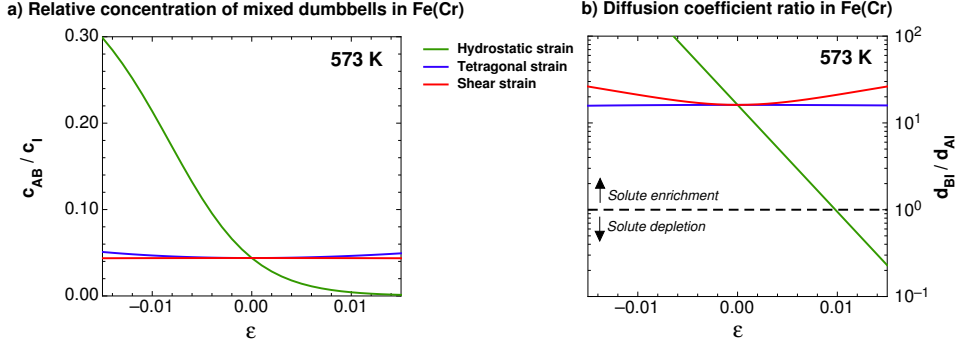


Figure 3.6: Effects of elementary strains ϵ on a) the fraction of mixed dumbbells in the total dumbbell population, and b) the ratio of partial diffusion coefficients for interstitial transport in FeCr. The elementary-strain types are shown in Fig. 2.9.

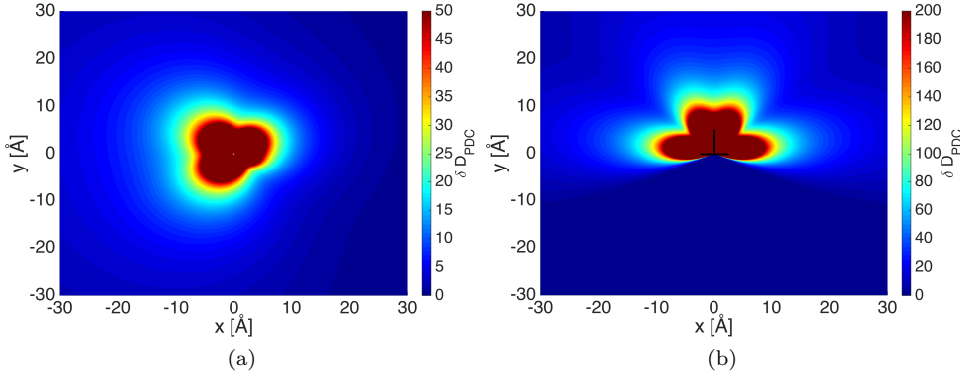


Figure 3.7: Variation of the interstitial partial diffusion coefficient (PDC) ratio $D_{PDC} = d_{BV}/d_{AI}$ for Cr transport in the elastically isotropic strain field of a) a screw dislocation, and b) an edge dislocation (Eqs. 2.41 and 2.42) with Burger's vector $\vec{b} = \frac{1}{2}a_0\langle 111 \rangle$. The variation is calculated with respect to the PDC ratio in the absence of strain: $\delta D_{PDC} = D_{PDC}(\epsilon) - D_{PDC}(0)$. The dislocation core radius is set to $r_0 = 3b$. The solute enrichment tendency is more pronounced in the regions marked in red, which correspond to the compressive regions of the dislocation strain field.

Table 3.1: Summary of diffusion and flux-coupling properties for several impurities in Fe: 1nn and 2nn solute-vacancy binding energy (E_{xV}^b), solute migration energy (E_x^{mig}) and attempt frequency (ν_x), transition temperature (TT) from drag to non-drag regime, solute-diffusion activation energy (Q) and prefactor (D_0) obtained by fitting in the temperature range 400-800 K, diffusion-coefficient mismatch with experimental values (D_x/D_{exp}) at 1100 K [118, 119], transition temperature from enrichment to depletion RIS tendency, and dominant RIS mechanism at 600 K.

	$E_{xV}^{b,1nn}$ [eV]	$E_{xV}^{b,2nn}$ [eV]	E_x^{mig} [eV]	ν_x [THz]	Drag TT [K]	Q [eV]	D_0 [cm ² /s]	D_x/D_{exp} at 1100 K	RIS TT [K]	Dominant mech. at 600 K
3p elements										
Al	-0.32	+0.02	0.49	5.1	954	2.73	10.0	3.0	986 ^(V)	vacancy
Si	-0.30	-0.11	0.51	3.5	1360	2.71	11.9	6.7	1420 ^(V+1)	vacancy
P	-0.38	-0.27	0.40	2.2	2172	2.57	10.4	14.9	enrichment	dumb/foreign
3d elements										
Ti	-0.24	+0.17	0.37	8.2	750	2.77	9.2	2.3	767 ^(V)	vacancy
V	-0.06	+0.08	0.51	10.1	274	2.92	19.5	1.2	281 ^(V)	vac/dumb ^(*)
Cr	-0.06	-0.01	0.55	9.7	262	2.90	19.4	1-1.8	457 ^(V+1)	vac/dumb
Mn	-0.17	-0.11	0.42	5.6	1011	2.77	18.2	-	enrichment	dumbbell
Fe	-	-	0.70	10.8	-	2.97	8.4	0.9-2.0	-	-
Co	+0.02	-0.10	0.73	8.9	448	3.02	8.1	0.6-0.7	enrichment by V	vac/dumb ^(*)
Ni	-0.10	-0.21	0.63	9.6	1087	2.79	6.6	4.1	1109 ^(V+1)	vacancy
Cu	-0.26	-0.17	0.51	4.3	1068	2.73	13.5	6.4-8.5	1071 ^(V+1)	vacancy
4d elements										
Zr	-0.75	+0.07	0.08	3.4	1834	2.37	2.7	-	1876 ^(V)	vacancy
Nb	-0.37	+0.15	0.34	5.8	1096	2.65	6.2	10.2	1121 ^(V)	vacancy
Mo	-0.16	+0.11	0.57	8.9	593	2.82	9.9	3.8	608 ^(V)	vac/dumb ^(*)
Tc	-0.12	+0.04	0.68	12.2	515	2.85	8.2	-	539 ^(V)	vac/dumb ^(*)
Ru	-0.11	-0.02	0.73	10.8	483	2.89	7.9	-	550 ^(V)	vac/dumb ^(*)
Rh	-0.15	-0.10	0.74	13.1	646	2.86	8.6	-	726 ^(V)	vacancy
Pd	-0.29	-0.19	0.64	9.6	1202	2.67	5.8	-	1283 ^(V)	vacancy
Ag	-0.52	-0.23	0.45	3.7	1942	2.44	5.2	17.5	2043 ^(V)	vacancy
5d elements										
Hf	-0.61	+0.16	0.22	3.6	1618	2.47	4.1	-	1656 ^(V)	vacancy
Ta	-0.31	+0.18	0.48	6.0	973	2.69	6.7	6.3	1004 ^(V)	vacancy
W	-0.13	+0.14	0.74	6.9	529	2.87	5.1	1.6-2.4	605 ^(V)	vac/dumb ^(*)
Re	-0.09	+0.06	0.88	11.2	388	3.06	11.0	-	enrichment by V	vac/dumb ^(*)
Os	-0.10	-0.01	0.92	11.9	457	3.08	12.1	-	enrichment by V	vac/dumb ^(*)
Ir	-0.14	-0.09	0.91	11.3	596	3.04	11.4	-	enrichment by V	vac/dumb ^(*)
Pt	-0.26	-0.19	0.83	11.6	1054	2.83	9.1	-	1383 ^(V)	vacancy
Au	-0.48	-0.27	0.59	5.6	1822	2.49	4.6	28.8	1952 ^(V)	vacancy

^(V) Only the vacancy mechanism is considered.

^(V+1) Both the vacancy and dumbbell mechanisms are considered.

^(*) The possible presence of a dominant mechanism needs to be verified by computing the dumbbell transport coefficients.

perturbation. Namely, shear strain always increases Cr mobility, while in the case of large tensile strains ($> 1\%$) Cr transport by dumbbells can be interrupted, and the enrichment tendency can turn into depletion (here the vacancy contribution to the RIS balance is neglected). These results show that the effect of strain fields can be relevant, and in cases where the RIS tendency is borderline (as is the case for Cr in Fe), local effects can lead to strong changes in the observed segregation tendencies.

As a further example, the variation of the interstitial PDC ratio in the elastically isotropic strain field of a screw and an edge dislocation is shown in Fig. 3.7. The

unstrained value of the PDC ratio is taken as reference. In both cases, the Cr enrichment tendency is enhanced, more prominently in the compressive regions. It is known that the dumbbell flux is preferentially directed towards dislocation tensile regions [131]. Hence, for edge dislocations the strain effect on solute segregation is likely to be small, because in the tensile region (for negative y -values in Fig. 3.7b) the PDC ratio is not affected. On the other hand, the enrichment tendency is more evenly distributed around a screw dislocation. For this reason, the strain effects are expected to be more important. When the strain-dependent variation of the transport coefficients is also included, this method can be useful to determine full 2-D segregation profiles and predict the segregation behavior in a vast range of experimental conditions.

Chapter 4

Results II: Kinetic Monte Carlo simulations

The atomistic phenomena involved in solute precipitation and in the long-term microstructure evolution of irradiated alloys can be simulated by means of KMC methods. As was discussed in Section 2.8, the simulation reliability depends on the correct modeling of transition and event rates. The aim of this chapter is to discuss reliable KMC models that can reproduce the solute-transport tendencies highlighted in the previous chapter. For this purpose, the first application of an ANN based on *ab initio* calculations is presented (Section 4.3). In addition, the properties of a wide range of vacancy-solute clusters are calculated by means of AKMC simulations, with the aim of providing the necessary parameters to implement OKMC simulations with explicit solute transport (Section 4.2). Finally, the evolution of the Ringhals RPV steels is simulated by means of a gray-alloy OKMC model (Section 4.4).

4.1 Vacancy drag in AKMC simulations

In a recent work, the evolution of RPV model alloys (ternary FeMnNi, and quaternary FeMnNiCu) was simulated by means of a pair interaction-based AKMC model [40]. The authors showed the formation of two classes of precipitates, Cu-rich (CRP's) and Mn-Ni-rich (MNP's) clusters. It was suggested that the formation of MNP's would be driven by self-interstitial atoms, which can carry Mn impurities via a mixed-dumbbell mechanism and can be trapped by Ni impurities in a 1nn solute-interstitial configuration. On the other hand, the precipitation of copper clusters would be driven by vacancy drag of copper atoms. The possibility of vacancy drag of Mn and Ni impurities was mentioned, but not investigated.

The conclusions drawn in [40] on the diffusion mechanisms can be verified based on the solute-transport tendencies obtained in Chapter 3, according to which Mn, Ni, and Cu solutes are dragged by vacancies at RPV temperature (≈ 300 °C).

The transport coefficients in AKMC simulations can be calculated by means of Eq. 2.12, and then compared with the ones obtained with the SCMF method. This is achieved here by following the evolution of one solute atom and one vacancy in a 432-atom simulation cell, and applying the FISE approach to the cohesive model of [40]. The results (triangles in Fig. 4.1) show that this KMC parameterization fails in reproducing the correct vacancy mechanism, as no vacancy drag is present. Hence, in this model the mechanisms leading to clustering, and consequently the predicted cluster composition, might be partly incorrect. Conversely, the same AKMC simulations performed with the *ab initio* jump frequencies (circles in Fig. 4.1) are in perfect agreement with the SCMF method.

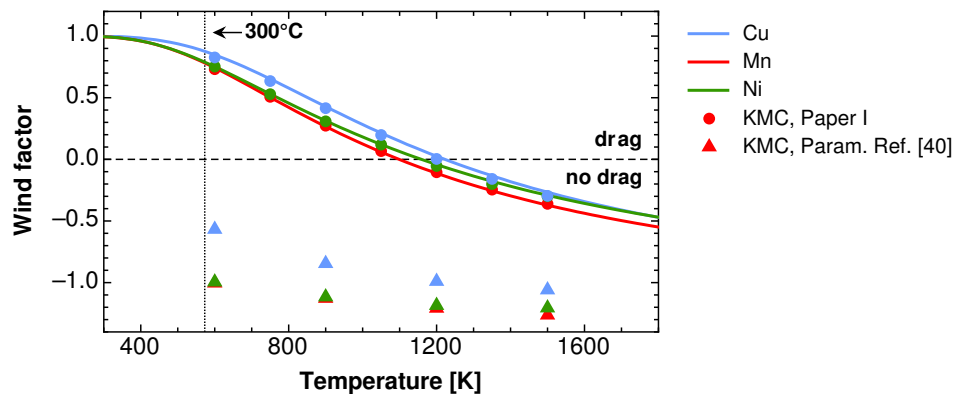


Figure 4.1: Wind factor for Cu, Mn, and Ni impurities in Fe, obtained with the SCMF method (lines), and by AKMC simulations based on DFT-computed jump frequencies (circles) or on the pair-interaction model of [40] (triangles).

It is therefore necessary to find a better strategy to predict migration barriers, in order to ensure that the correct transport mechanisms are modeled. This is even more important when calculating the mobility properties of vacancy-solute clusters, as parameters for OKMC simulations. The ideal solution is represented by the direct implementation of *ab initio*-computed jump frequencies, which is feasible only in the case of single point defect-solute pairs, thanks to the limited amount of configurations to be considered.

For instance, the properties of single vacancy-solute pairs are investigated in the first part of Paper IV, by using the jump frequencies obtained for the vacancy-transport study of Paper I. The lifetimes, diffusion coefficients and mean free paths of vacancy-Mn, vacancy-Ni, and vacancy-Cu pairs are obtained with the AKMC algorithm explained in Section 2.8, and the results are shown in Fig. 4.2. Due to the strong binding energy, the vacancy-Cu pair is characterized by a higher stability than Mn and Ni. On the other hand, the lower migration barrier for the vacancy-Mn exchange enhances the mobility of the vacancy-Mn pair, which has an effective

migration energy lower than that of a monovacancy. The combination of these two factors yields a long-ranged transport of Cu atoms, and of Mn atoms to a lesser extent, whereas the transport of Ni atoms is short-ranged. The previous KMC model [40] (empty markers in Fig. 4.2) considerably underestimated the transport capabilities of single vacancies, as the mean free paths were considerably lower. Vacancy transport was therefore not only occurring with the incorrect mechanism (absence of vacancy drag), but was also less efficient than the DFT-based prediction.

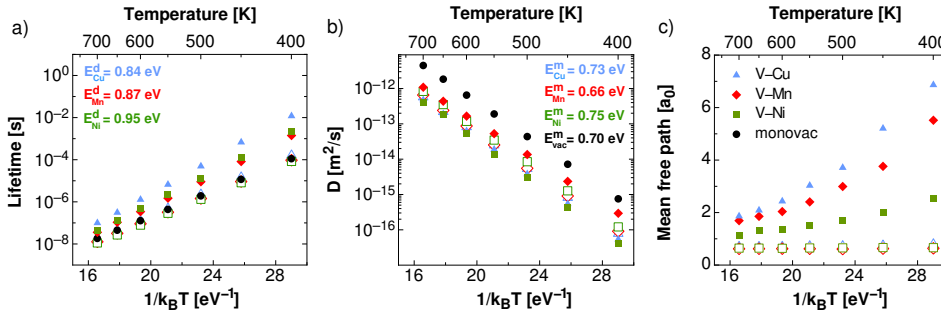


Figure 4.2: a) Average lifetime and dissociation energies E^d , b) diffusion coefficient and migration energies E^m , and c) mean free path of vacancy-solute pairs, obtained with AKMC simulations based on DFT-computed migration barriers. The monovacancy lifetime is here defined as the inverse of the vacancy jump frequency ω_0 . The empty markers are obtained with the AKMC simulations based on the cohesive model of [40].

4.2 Stability and mobility of vacancy-solute clusters

The dataset shown in Fig. 4.2 and in Paper IV can be directly implemented in OKMC simulations to describe solute transport by single vacancies. This dataset should be complemented with the stability and mobility properties of mixed dumbbells, which can be obtained with analogous AKMC simulations based on DFT-computed jump frequencies. Furthermore, the stability, mobility, and solute-transport capabilities of defect clusters should also be known. For this purpose, the properties of vacancy-Mn-Ni clusters are investigated in Paper IV.

The direct use of *ab initio*-computed jump frequencies is prohibitive for multi-defect and multi-solute systems, because of the large amount of LAE configurations. On the other hand, the pair-interaction model in [40] is inadequate because of the lack of vacancy drag. In Paper IV, this issue is addressed with a cohesive model based on DFT-computed binding energies between vacancies and solutes (Eq. 2.56), with the aim of enhancing the vacancy-solute correlations with respect to the previous pair-interaction model. With this simplified cohesive model, the properties of small vacancy-Mn-Ni clusters are obtained for clusters containing up

to four vacancies and two solute atoms of each type. A selection of the results is shown in Fig. 4.3. The panels above gather the properties of single vacancy-solute pairs, as obtained with the model based on Eq. 2.56 (full markers), and with the accurate DFT model (the same as in Fig. 4.2, here in empty markers). The results show that in this simplified binding energy-based cohesive model solute-vacancy correlations are still underestimated, more considerably in the case of vacancy-Mn pairs because of the wrong diffusion-coefficient prediction. The migration-barrier prediction provided by Eq. 2.56 is therefore not sufficiently accurate to fully describe the correct diffusion mechanism.

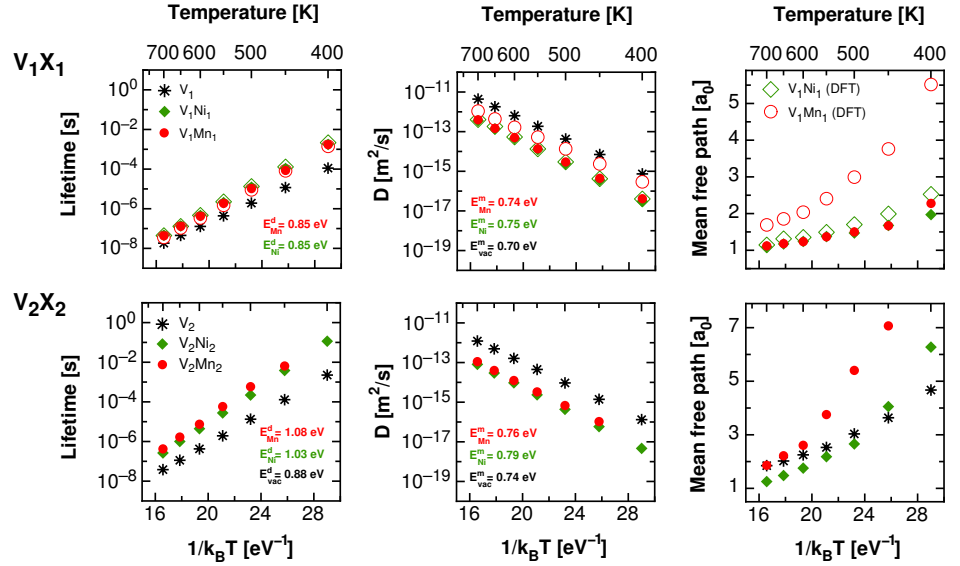


Figure 4.3: Lifetime, diffusion coefficient and mean free path of vacancy-solute pairs (above), and vacancy-solute clusters containing two vacancies and two solute atoms (below), obtained with AKMC simulations based on the simplified cohesive model of Eq. 2.56. E^d and E^m mark the dissociation and migration energies, respectively. The empty markers refer to the results obtained with the DFT-based AKMC simulations.

In the bottom panels of Fig. 4.3 are shown the properties of two-vacancy clusters containing two solute atoms, as well as the dissociation and migration energies. According to this model, the addition of solute atoms to a di-vacancy increases the stability and reduces the mobility of the complex. Moreover, the overall solute-transport capability is quite marked, especially for what concerns Mn impurities. In the gray-alloy OKMC simulations in [49], small vacancy clusters were postulated to be considerably slowed down by Mn and Ni impurities: for instance, the migration energy of a di-vacancy was increased from 0.62 eV [107] to 1.20 eV [49]. This

4.3. ANN-KMC SIMULATIONS OF THERMAL AGING IN FECU ALLOYS 67

assumption, although unjustified, was necessary to yield the correct microstructure evolution of the model FeMnNi alloy. One of the purposes of Paper IV is then to attempt to verify this assumption. Fig. 4.3 shows that a slowdown effect is present, although not to the extent postulated by [49]. Since solute-vacancy correlations are not fully caught, it is possible that the slowdown effect is here underestimated. However, the vacancy-cluster mobility might be reduced as well because of complex interactions between clusters, impurities, and carbon traps. This issue should be further investigated in future works.

In spite of the limitations of the cohesive-energy model, the dataset obtained in Paper IV represents a good starting point for the introduction of solute transport by small vacancy clusters in OKMC simulations of FeMnNi alloys. It is also possible to obtain these properties with a slightly different approach, which can be directly used in gray-alloy OKMC simulations. In this case, the focus is on pure vacancy clusters, and their stability and mobility is calculated in a simulation cell containing a random distribution of Mn and Ni impurities. Under the same AKMC algorithm, the cluster is free to evolve until one or more vacancies are emitted. The results of a few simulations are provided in Fig. 4.4, where are shown the properties of a di-vacancy in an alloy with an increasing Mn content, for two values of the Ni concentration. The mobility of the vacancy cluster is not dramatically reduced by the presence of Mn impurities. On the other hand, the introduction of Ni impurities is much more impactful on both the dissociation and the migration energy. The overall vacancy-cluster mobility is therefore considerably reduced by nickel, to an extent that is closer to the assumptions of [49]. This effect is at any rate partially counterbalanced by an increase of the prefactor D_0 (here not shown). The approach in Fig. 4.4 allows for the definition of the cluster properties (lifetime, diffusion coefficient, and mean free path) as continuous functions of the solute concentration, which can be therefore varied without the explicit introduction of the chemical impurities. Such data can be directly used in a gray-alloy OKMC simulation. Consistently with the results of Fig. 4.3, it is possible to conclude that according to this model Mn and Ni impurities are not sufficient to explain the partial immobilization of vacancy clusters postulated by [49].

4.3 ANN-KMC simulations of thermal aging in FeCu alloys

The KMC models discussed so far are not able to describe the proper solute-transport tendencies and correlations, because of the lack of a reliable migration-barrier prediction. The ANN approach described in Section 2.8 represents a solution to this issue, as it provides a regression scheme for a more reliable on-the-fly calculation of migration barriers in unknown atomic configurations. In Paper V, an ANN has been purposely trained, for the first time, on *ab initio*-computed migration barriers, as opposed to previous works [103, 107] where an interatomic potential was used. This method is very promising because it maintains the physical properties of the cohesive model chosen for training (DFT in this case), and is therefore ca-

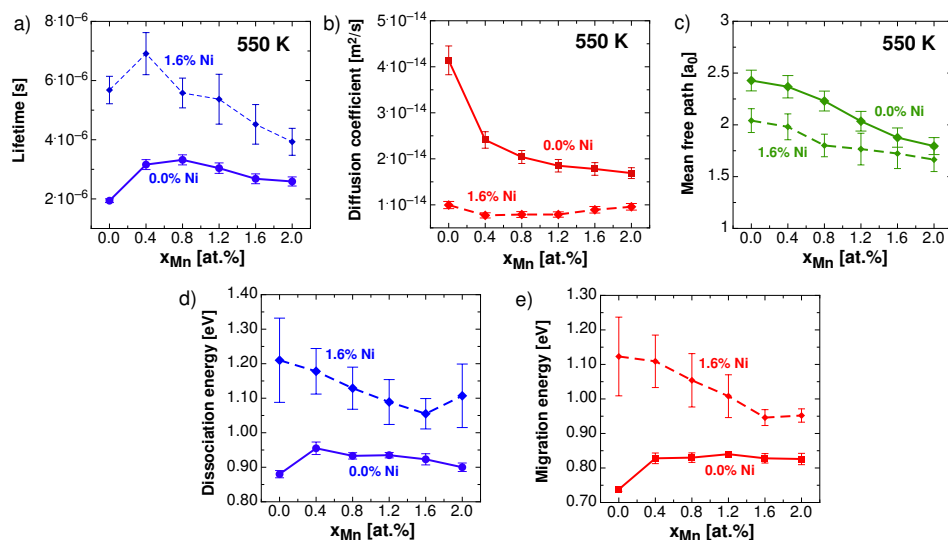


Figure 4.4: Variation of a) lifetime, b) diffusion coefficient, and c) mean free path of a two-vacancy cluster in an FeMnNi alloy, as a function of the solute concentration, at 550 K. The AKMC simulations are based on the cohesive model described by Eq. 2.56. d) Dissociation energy and e) migration energy of the same cluster, as obtained after Arrhenius fitting in the temperature range 400-700 K.

pable of transferring the correct solute-defect correlations and transport properties from DFT to the KMC simulation. In principle, alloys of any chemical complexity can be modeled, simply by extending the set of configurations used for training, as opposed to the development of interatomic potentials [132, 41] which become overly complicated with the increasing amount of chemical elements involved.

Here, the feasibility of such an approach is proven, by testing on the rather well-known case of copper precipitation in thermally-aged FeCu alloys. This is the same system chosen for the first ANN application to migration-barrier predictions [103]. 2000 DFT-NEB migration barriers are employed for training and validation. In the overall, the DFT calculations required a total computational effort of about three million core-hours, which is surely a non-negligible but feasible amount. After the ANN training, the properties of Cu clusters containing one vacancy are obtained by means of AKMC simulations. Finally, the evolution of FeCu alloys is simulated with a hybrid AKMC-OKMC approach described in the Section 2.8, where the AKMC transition rates are provided by the ANN, and the OKMC rates are based on the aforementioned copper-cluster properties.

Some of the Cu-cluster properties are shown in Fig. 4.5. In Fig. 4.5a are reported the diffusion coefficients with increasing cluster size, at different temperatures and in comparison with previous AKMC simulations [97] based on an

ab initio-based pair interaction model. It should be noticed that in this kind of AKMC simulations, the simulation time needs to be rescaled based on the real vacancy concentration, which strongly depends on the binding energy between the vacancy and the Cu cluster. For the sake of simplicity, in Fig. 4.5a the time is rescaled by fitting the results obtained for the Cu monomer to the Cu diffusion coefficient calculated in Paper II, and the curves as functions of cluster size are shifted accordingly. This simplified procedure neglects the effect of the increasing vacancy-cluster binding energy with size. The latter would lead to a higher equilibrium vacancy concentration, hence to a lower the simulation time and a larger cluster diffusivity with respect to the obtained results.

One of the main findings in [97] was that large copper clusters ($n \approx 100$) are not only mobile, but are even more mobile than clusters of smaller sizes. This entails that direct coagulation of large precipitates should play an important role in thermal aging, as was confirmed subsequently by the first ANN-based work [103]. According to the results obtained here with the DFT-ANN method, the diffusion coefficient does not increase with cluster size. However, because of the increasing cluster stability, the mean free path does increase with size, as is shown in Fig. 4.5b, and the effect gradually fades with increasing temperature. This occurs because, according to DFT, vacancy and copper atoms are strongly correlated, and the vacancy thus stays longer inside the copper cluster, rather than around its surface. Hence, the DFT-ANN method yields an increasing mobility with cluster size in terms of longer distances covered, rather than in terms of diffusion coefficient. The mobility of large-sized clusters plays therefore still an important role, although it occurs more slowly. It should be mentioned, anyway, that introducing the aforementioned effect of the vacancy-cluster binding energy in the time rescaling would reduce the mismatch between these results and those in [97]. It is also interesting to observe the arising of "magic numbers" characterized by a sudden drop of the cluster mobility. They correspond to particularly stable cluster configurations, where the clusters atoms fill a full shell of nearest-neighbor positions: for instance, $n = 15$ corresponds to a cluster with one atom in the centre and 14 atoms fully covering the 1nn and 2nn shells.

The thermal-aging evolution of a Fe-1.34%Cu alloy (from Paper V) obtained with the hybrid KMC approach is shown in Fig. 4.6. The simulation time is rescaled based on the real vacancy concentration (obtained by means of Eq. 2.1), as well as on the time spent by the vacancy next to copper atoms, according to the procedure explained in [103]. The microstructure evolution is generally well reproduced, although it is seemingly anticipated with respect to the experimental behavior. This might be due to the effect of entropic contributions. For instance the copper attempt frequency is here assumed to be equal to that of iron (6 THz), although it was found in Paper II to be more than two times smaller. Moreover, in the simulation of a low-Cu alloy (shown in Paper V), the cluster density is greatly overestimated. This is probably related to the specific DFT method (PAW-PBE) chosen for the training set of migration barriers, which is known to underestimate the solubility limit of Cu in Fe [116, 133]. This confirms the ability of the ANN

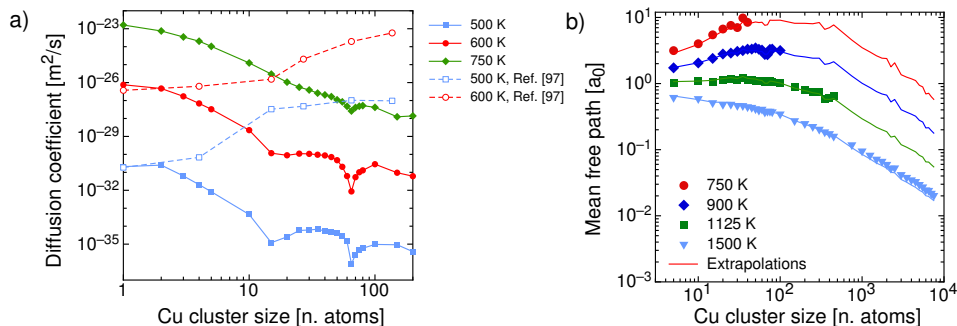


Figure 4.5: (a) Diffusion coefficient and (b) mean free path of copper clusters containing one vacancy, with increasing cluster size, obtained with AKMC simulations based on the DFT-ANN approach. The dashed lines refer to the results of a previous AKMC model [97]. The extrapolated curves are obtained by fitting the corresponding diffusion coefficients D and lifetimes τ at high temperatures, and calculating the mean free path as $\sqrt{6D\tau}$.

approach to transfer the physical information of the used cohesive model (also the incorrect parts) into the KMC simulation. In this specific case, the choice of another DFT method would be useful to obtain results more in agreement with experiments. The model might also be improved by splitting the thermodynamic and kinetic descriptions. For instance, two separate ANN networks can act in parallel: the first one for the prediction of the end-state equilibrium energies, and the second one for the prediction of saddle-point energies, both based on DFT data. This approach will be investigated in future works.

In general, this work demonstrates the feasibility of the DFT-ANN approach and its potential advantages for a consistent and efficient prediction of migration barriers in KMC simulations. The increasing computational power of modern supercomputers will allow for the calculation of larger sets of DFT migration barriers, which will in turn lead to the application of this approach to alloys of increasing chemical complexity, including several solute species, multiple defects, and interstitial-type defects.

4.4 Microstructure evolution of Ringhals steels

This thesis has thoroughly investigated the transport of solutes by point defects, and provides solute-defect cluster parameters for direct application in OKMC simulations of RPV microstructure evolution. Although an OKMC code featuring the explicit presence and transport of chemical impurities is still not available, the gray-alloy approach [49] can be applied to perform the first microstructure-evolution simulations of the Ringhals RPV steels. The microstructure analysis performed so

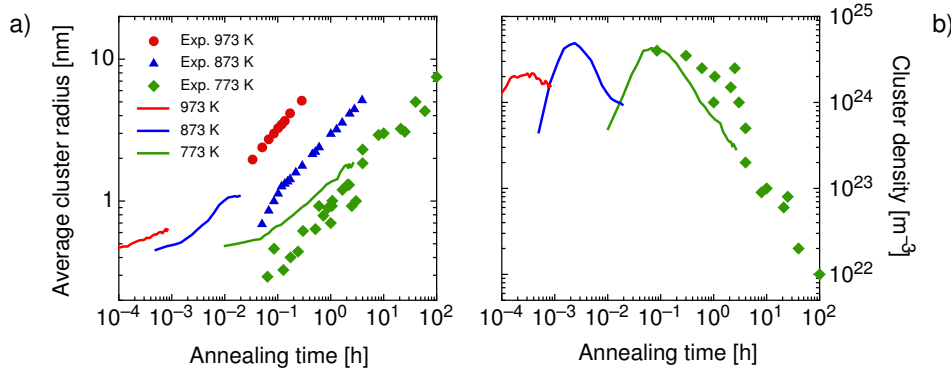


Figure 4.6: Simulation of thermal-aging evolution of a Fe-1.34%Cu alloy, by means of a hybrid AKMC-OKMC model based on the DFT-ANN parameterization: a) average radius, and b) total number density of copper clusters. The experimental data refer to various APT and SANS characterizations (the references can be found in Paper V).

far on surveillance samples consists in the APT characterization of solute clusters by [20], and the electron-microscope observations by [25] and [26], according to which no large defect clusters are observed. These gray-alloy simulations can give a first insight into the atomistic phenomena occurring in these specific RPV steels, which are characterized by a simultaneously high concentration of manganese and nickel.

The experimental data needed for the OKMC simulations are summarized in Table 4.1. The relevant conditions of one of the last surveillance samples removed by Ringhals unit R4 are compared to those of the FeMnNi model alloy [134] simulated in [49]. The damage dose and flux are expressed in terms of displacements per atom (dpa), and are calculated based on the vessel irradiation history [135]. The simulations are performed with the chemical composition indicated by [20]. The Mn and Ni concentrations affect only the mobility of interstitial clusters, whereas the mobility of vacancy clusters is kept fixed to the values assumed in the previous work [49]. The amount of carbon in the matrix was measured by means of internal friction, and it was found mainly in the form of C₂V complexes [136]. The latter are therefore assumed to be the only type of traps in the system. Unfortunately, the average dislocation density and grain size are not available. For this reason, they are assumed to be equal to the model alloy. All other parameters and assumptions are unchanged with respect to the model-alloy case and can be found in [49].

The results are shown in Fig. 4.7, in terms of density and average size of vacancy clusters (above) and interstitial clusters (below). They are also compared with the model FeMnNi alloy [49]. Experimentally, vacancy clusters can be observed by PAS and TEM, the latter only above a size threshold of about 45 vacancies [49].

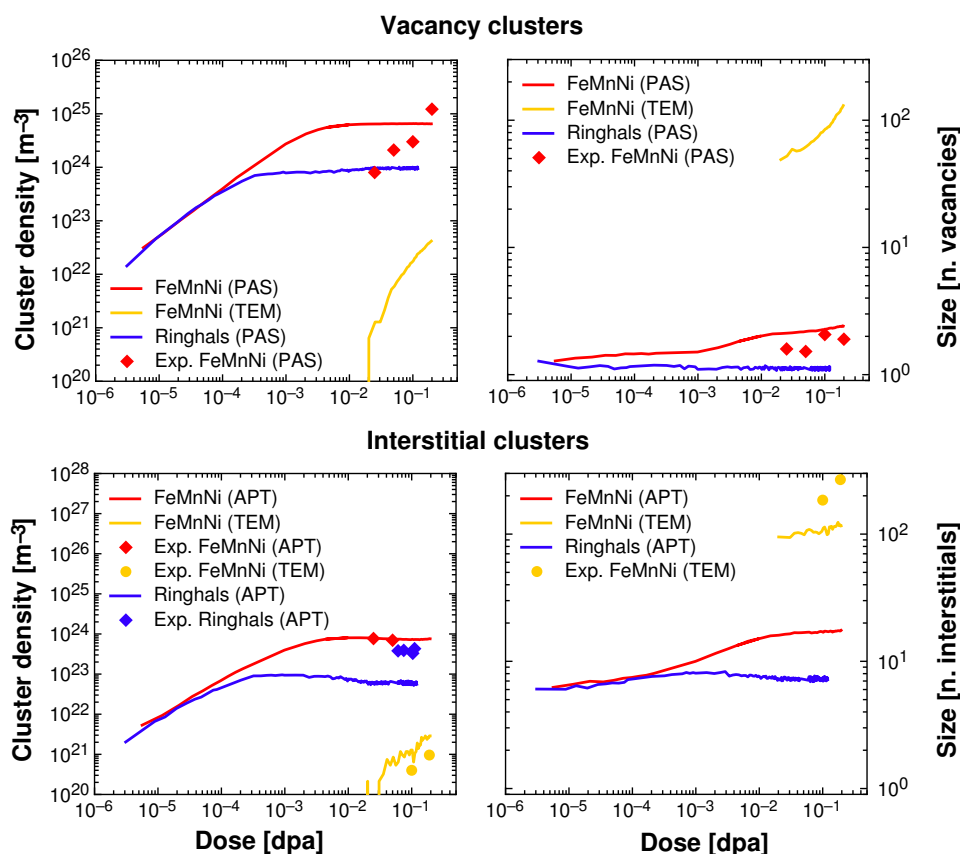


Figure 4.7: Simulated microstructure evolution of Ringhals RPV steels with an OKMC gray-alloy approach, compared with the simulated evolution of a model FeMnNi alloy [134, 49]. For vacancy clusters, the curves marked with TEM refer to TEM-visible clusters larger than 45 vacancies, whereas those marked with PAS refer to the whole vacancy-cluster population. For interstitial clusters, the threshold for TEM-visible objects is 90 interstitials. The curves marked with APT refer to the population of invisible interstitial clusters, assumed to correspond to the solute-cluster population. The experimental points for the Ringhals samples are taken from [20], whereas those of the model FeMnNi alloy are to be found in [49].

Table 4.1: Experimental characterization of the model FeMnNi alloy [134, 49] and of one of Ringhals surveillance capsules [15, 20], employed in the OKMC simulations of Fig. 4.7.

	FeMnNi model alloy [134]	Ringhals welds (R4, capsule U) [20]
Composition [at.%]	1.2% Mn, 0.7% Ni	1.37% Mn, 1.58% Ni
Irradiation temperature [°C]	290 [49]	284 [20]
Neutron flux [n/cm ² s]	$9.5 \cdot 10^{13}$ [134]	$1.5 \cdot 10^{11}$ [20]
Dpa flux [dpa/s]	$1.4 \cdot 10^{-7}$ [49]	$2.7 \cdot 10^{-10}$ [135]
Dpa dose [dpa]	0.2 [49]	0.11 [135]
Carbon in matrix [at ppm]	134 [49]	100 [136]
Dislocation density [m ⁻²]	$7 \cdot 10^{13}$ [134]	not available
Average grain size [μm]	88 [134]	not available

TEM can also observe large interstitial clusters, above approximately 90 interstitials [49], but the smaller ones are invisible. However, if MNP's form on immobilized interstitial clusters, APT solute-cluster density should correspond to the density of invisible loops. This was for instance the case in the model alloy (Fig. 4.7c), where the two densities matched perfectly.

The OKMC simulations on Ringhals welds (blue lines in Fig. 4.7) show, consistently with the electron-microscope observations, that at such low dose-rate levels no TEM-visible defect clusters are formed. The average size of vacancy clusters remains close to one vacancy throughout the whole simulation. This occurs because the lower dose rate allows the defects to flow towards the sinks before a new primary-damage event occurs. However, it can be observed in Fig. 4.7c that the density of interstitial clusters does not match the APT solute-cluster density. This might suggest either a fault in the model parameterization, or that solute precipitates form not only on interstitial clusters, but also on vacancy clusters, possibly trapped by carbon atoms.

Given the missing information about dislocation density and grain size, more simulations are performed by modifying such parameters and verifying their effect on the evolution of the interstitial-cluster population. Firstly, the grain size has been reduced by up to two orders of magnitude, but no major effects have been found. Furthermore, the bias factor has been modified according to the bias calculations in bcc iron performed in [131], setting Z_I/Z_V to 1.2, with respect to $Z_I/Z_V = 2.5$ used in [49] and in Fig. 4.7. With this new bias factor, the predicted cluster density match the APT solute-cluster population (Fig. 4.8a). Finally, the dislocation density has been increased up to $\rho_D = 3 \cdot 10^{14} \text{ m}^{-2}$, since ρ_D in Ringhals welds is expected to be higher than in the model alloy. The results depicted in Fig. 4.8b show that this parameter leads to a further improvement, although the effect is smaller than that of the dislocation bias.

This first microstructure-evolution simulations of the Ringhals RPV steels confirm therefore that the observed solute clusters are likely to form on invisible in-

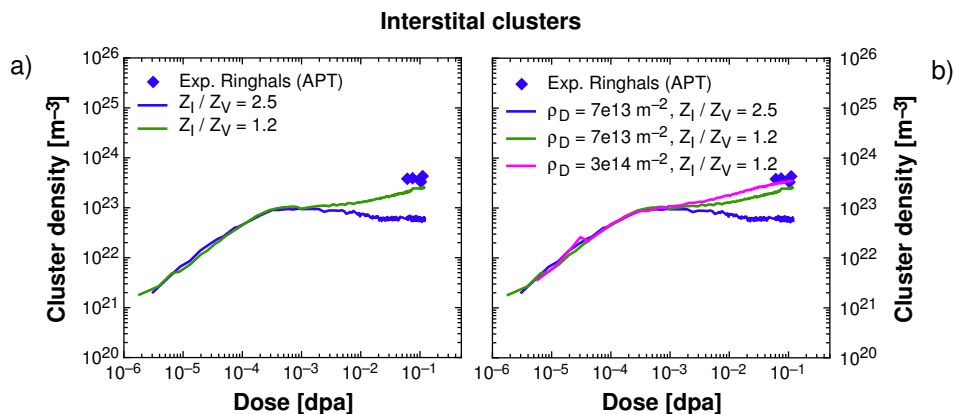


Figure 4.8: OKMC-simulated microstructure evolution of Ringhals RPV steels, where a) the dislocation defect-absorption bias ratio Z_I/Z_V has been modified from 2.5 to 1.2 match that of previous calculations [131], and b) the dislocation density ρ_D has been varied as a parametric quantity. The experimental APT measurements were performed in [20].

terstitial loops. However, it is difficult to assess the reason why the modified bias factor, outcome of an accurate modeling work [131], yields the correct evolution of the Ringhals steels, but not that of the model FeMnNi alloy. In order to perform a more accurate simulation, more microstructure characterization of the Ringhals surveillance samples is needed, namely the missing information regarding dislocation density and grain size, as well as PAS measurements of the vacancy-cluster density. When more experimental information is available, the parameterization of the gray-alloy model will need to be revised, in order to yield the correct evolution of both the model alloy and the RPV steel. Moreover, the assumption concerning the largely reduced vacancy-cluster mobility is still to be fully justified with more investigations of vacancy-Mn-Ni cluster properties (possibly with an ANN approach). As a further step, the model will be greatly improved when the chemical impurities are introduced explicitly, and solute-transport mechanisms by point defects and defect clusters are properly modeled. This will allow for an ultimate verification of the dynamics of the clustering process, as well as for an investigation of the actual role of vacancy clusters in the evolution of solute precipitates. Once ready, this model will be able to predict the evolution of RPV steels even beyond the timeframe covered nowadays by surveillance programs.

Chapter 5

Conclusions

The primary objective of this thesis was the investigation of the atomistic-level mechanisms leading to the formation of embrittling solute-rich clusters in low-copper reactor pressure vessel (RPV) steels. Given the apparent lack of thermodynamic driving forces inducing solute precipitation, it has been suggested [37, 40, 45] that such clusters nucleate on interstitial loops immobilized by manganese impurities, and grow collecting other impurities carried by incoming point defects. This mechanism is only possible if the point defects are able to transport solute atoms along. No experimental evidence of such a mechanism has emerged yet, because of the small size of these loops, but the gathering of solutes around loop-shaped objects has been recently observed [46].

The first part of the thesis consisted therefore in a systematic investigation of impurity-transport mechanisms in ferritic alloys, with the aim of proving from a modeling standpoint the actual possibility for such a mechanism to occur. This was achieved by combining *ab initio* calculations of atomic transition rates with a mean-field atomistic diffusion model that allows for an accurate analysis of solute-defect flux-coupling tendencies. The results show that all impurities observed in the embrittling nanostructures (mainly Mn, Ni, and Si, but also Cu and P) are dragged by vacancies. Impurity drag by vacancies is found to be a common phenomenon occurring in iron (and likely as well in other metals) for all solutes characterized by a binding interaction with vacancies. It was also found that manganese and phosphorus impurities can diffuse via a dumbbell mechanism, which makes them considerably prone to radiation-induced segregation. The model predicts also a consistent enrichment of the aforementioned solutes on grain boundaries and dislocations, in agreement with the experimental evidence [124]. These flux-coupling tendencies prove therefore that the suggested dynamic formation mechanism can indeed take place under the vessel operating conditions.

The second part focused on the development of kinetic Monte Carlo (KMC) models able to closely reproduce the impurity-transport properties uncovered in the first part. Introducing explicit solute-transport mechanisms in KMC simu-

lations requires the determination of stability and mobility parameters of defect-solute clusters. This was here achieved for vacancy-manganese-nickel clusters by performing atomistic KMC simulations with different parameterizations. Such simulations showed that manganese and nickel impurities can effectively reduce the mobility of vacancy clusters, although not to the extent postulated in a previous work [49]. In order to include the correct correlations and transport tendencies, a new approach was here suggested for an accurate on-the-fly prediction of migration barriers. This approach featured an artificial neural network based on *ab initio* calculations. The first application to thermal aging in FeCu alloys showed the arising of strong vacancy-copper correlations, and produced a thermal-aging evolution close to the experimental one, within the limitations of the chosen DFT method. Finally, the microstructure evolution simulation of Ringhals RPV steels showed that large defect clusters are not expected to form, in agreement with the microstructure characterizations [25, 26]. According to this preliminary model, it is possible that the observed solute clusters form around small interstitial loops, but the obtained loop population is not sufficient to account for all solute clusters observed by atom-probe tomography [20]. The mismatch can be due to the limitations of the model, but might also suggest that immobilized vacancy clusters (i.e. small voids) act as nucleation centers for solute clusters, in a mechanism analogous to that of immobilized interstitial loops.

Based on these achievements, the following future developments are suggested.

1. Extend the calculation of transport coefficients to concentrated Fe-X binary alloys and to multicomponent alloys, in order to describe the effect on the transport properties of inhomogeneous concentration fields and of synergies among impurities. The effect of external strains should also be investigated more carefully, in order to analyze the variation of such coefficients next to large defects (e.g. dislocation lines).
2. Implement in a computer code the computational framework for the calculation of transport coefficients by interstitials in concentrated alloys [60], and extend the self-consistent mean-field model to describe the transport properties of small interstitial clusters.
3. Introduce solute-transport mechanisms by defects in kinetic Monte Carlo simulations, in order to prove that solute clusters can form on interstitial loops. This must be achieved by completing the dataset of solute-defect cluster properties, for both vacancy- and interstitial-type clusters.
4. Pursue the development of *ab initio*-based artificial neural networks for the accurate prediction of migration barriers in further systems relevant for RPV alloys, such as an FeMnNi model alloy. This approach can be used also for the determination of defect-solute cluster properties mentioned in the previous point.

5. Improve the simulations of microstructure evolution of Ringhals RPV steels by introducing the transport of solutes explicitly and refining the simulation parameters. For this purpose, further microstructure characterization is needed in order to provide the missing microstructural information (part of this effort is already ongoing). This would allow to tune the simulation with the best parameterization, and can potentially provide a powerful tool to simulate the evolution of this steel beyond the lifetime covered by the surveillance program. In addition, it would allow for the investigation of flux effects, especially if combined with accelerated-irradiation experiments. This would help in assessing the reliability of surveillance samples, which are exposed to a higher flux than the actual one received by the RPV.

This thesis provides an important contribution to the general ongoing effort to understand embrittling phenomena in ferritic steels at the atomistic level, and represents a step forward towards an ultimate modeling tool of microstructure evolution of irradiated ferritic alloys. The microstructure evolution can then be linked with the macroscopic change of mechanical properties, by analyzing the interaction between dislocations and e.g. solute clusters. This can be achieved with atomistic techniques such as molecular dynamics [34] and dislocation dynamics [137], but a wide multi-disciplinary effort is still needed in order to reach a satisfactory and inclusive prediction of hardening and embrittlement in RPV steels.

The methods here described can be of interest for a much broader range of materials and applications. The combined *ab initio*-mean field approach is indeed useful for the determination of impurity diffusion mechanisms, flux-coupling tendencies and solute diffusion coefficients in a wide variety of alloys under irradiation. It can be also applied to investigate the kinetics of alloys under metallurgical processing, where it is important to know and control the microstructure evolution at different temperatures. In addition, the introduction of neural networks in microstructure-evolution simulations can combine their powerful regression capabilities with density-functional theory, which represents to date the most accurate cohesive model available. The increasing computational power will allow in the near future for the extension of this approach to complex alloys such as RPV steels, as well as to other materials of interest for Generation-IV and fusion applications.

Bibliography

- [1] R. E. H. Sims, H. H. Rogner, and K. Gregory, “Carbon emission and mitigation cost comparisons between fossil fuel, nuclear and renewable energy resources for electricity generation,” *Energy Policy*, vol. 31, pp. 1315–1326, 2003.
- [2] D. Maisonnier, I. Cook, S. Pierre, L. Boccaccini, L. Di Pace, L. Giancarli, P. Norajitra, and A. Pizzuto, “DEMO and fusion power plant conceptual studies in Europe,” *Fusion Engineering and Design*, vol. 81, pp. 1123–1130, 2006.
- [3] T. Abram and S. Ion, “Generation-IV nuclear power: A review of the state of the science,” *Energy Policy*, vol. 36, pp. 4323–4330, 2008.
- [4] V. H. M. Visschers and M. Siegrist, “Fair play in energy policy decisions: Procedural fairness, outcome fairness and acceptance of the decision to rebuild nuclear power plants,” *Energy Policy*, vol. 46, pp. 292–300, 2012.
- [5] N. M. A. Huijts, E. J. E. Molin, and L. Steg, “Psychological factors influencing sustainable energy technology acceptance: A review-based comprehensive framework,” *Renewable and Sustainable Energy Reviews*, vol. 16, pp. 525–531, 2012.
- [6] “Investigation of long-term safety in the Swedish nuclear power industry and measures owing to the accident at Fukushima Dai-ichi,” Tech. Rep. SSM2010-1557-10, Strålsäkerhetsmyndigheten (Swedish Radiation Safety Authority), 2013.
- [7] S. L. Dudarev, J. L. Boutard, R. Lässer, M. J. Caturla, P. M. Derlet, M. Fivel, C.-C. Fu, M. Y. Lavrentiev, L. Malerba, M. Mrovec, D. Nguyen-Manh, K. Nordlund, M. Perlado, R. Schäublin, H. Van Swygenhoven, D. Terentyev, J. Wallenius, D. Weygand, and F. Willaime, “The EU programme for modelling radiation effects in fusion reactor materials: An overview of recent advances and future goals,” *Journal of Nuclear Materials*, vol. 386-388, pp. 1–7, 2009.

- [8] B. D. Wirth, K. Nordlund, D. G. Whyte, and D. Xu, “Fusion materials modeling: Challenges and opportunities,” *MRS Bulletin*, vol. 36, pp. 216–222, 2011.
- [9] M. L. Grossbeck, “Effect of Radiation on Strength and Ductility of Metals and Alloys,” in *Comprehensive Nuclear Materials* (R. J. M. Konings, T. R. Allen, R. E. Stoller, and S. Yamanaka, eds.), pp. 99–122, Amsterdam: Elsevier, 2012.
- [10] P. J. Maziasz and J. T. Busby, “Properties of Austenitic Steels for Nuclear Reactor Applications,” in *Comprehensive Nuclear Materials* (R. J. M. Konings, T. R. Allen, R. E. Stoller, and S. Yamanaka, eds.), pp. 267–283, Amsterdam: Elsevier, 2012.
- [11] C. English and J. Hyde, “Radiation Damage of Reactor Pressure Vessel Steels,” in *Comprehensive Nuclear Materials* (R. J. M. Konings, T. R. Allen, R. E. Stoller, and S. Yamanaka, eds.), pp. 151–180, Amsterdam: Elsevier, 2012.
- [12] F. A. Garner, “Radiation Damage in Austenitic Steels,” in *Comprehensive Nuclear Materials* (R. J. M. Konings, T. R. Allen, R. E. Stoller, and S. Yamanaka, eds.), pp. 33–95, Amsterdam: Elsevier, 2012.
- [13] “Integrity of reactor pressure vessels in nuclear power plants: assessment of irradiation embrittlement effects in reactor pressure vessel steels,” Tech. Rep. NP-T-3.11, International Atomic Energy Agency, 2009.
- [14] P. Efsing, J. Roudén, and M. Lundgren, “Long term irradiation effects on the mechanical properties of reactor pressure vessel steels from two commercial PWR plants,” in *Effects of Radiation on Nuclear Materials: 25th Volume* (T. Yamamoto, ed.), pp. 52–68, West Conshohocken: ASTM International, 2012.
- [15] P. Efsing, C. Jansson, G. Embring, and T. Mager, “Analysis of the Ductile-to-Brittle Transition Temperature Shift in a Commercial Power Plant with High Nickel Containing Weld Material,” *Journal of ASTM International*, vol. 4, pp. 1–12, 2007.
- [16] B. Z. Margolin, V. A. Nikolayev, E. V. Yurchenko, Y. A. Nikolayev, D. Y. Erak, and A. V. Nikolayeva, “Analysis of embrittlement of WWER-1000 RPV materials,” *International Journal of Pressure Vessels and Piping*, vol. 89, pp. 178–186, 2012.
- [17] H. Hein, E. Keim, J. May, and H. Schnabel, “Some recent research results and their implications for RPV irradiation surveillance under long term operation,” in *IAEA Technical Meeting on Degradation of Primary Components of Pressurised Water Cooled Nuclear Power Plants: current issues and future challenges, 5-8 November 2013, Vienna, Austria*, 2013.

- [18] A. Kryukov, R. K. Nanstad, and M. Brumovsky, "Common comparison of the irradiation embrittlement of WWER/PWR reactor pressure vessel steels," *Nuclear Engineering and Design*, vol. 273, pp. 175–180, 2014.
- [19] World Nuclear Association, "Nuclear Power in Sweden." <http://www.world-nuclear.org/info/Country-Profiles/Countries-0-S/Sweden/>, 2015. [Online, accessed on 21 October 2015].
- [20] M. K. Miller, K. A. Powers, R. K. Nanstad, and P. Efsing, "Atom probe tomography characterizations of high nickel, low copper surveillance RPV welds irradiated to high fluences," *Journal of Nuclear Materials*, vol. 437, pp. 107–115, 2013.
- [21] US Nuclear Regulatory Commission, "Regulatory guide 1.99, rev. 2," pp. 1–10, 1988.
- [22] P. Efsing, J. Roudén, and P. Nilsson, "Flux Effects on Radiation Induced Aging Behaviour of Low Alloy Steel Weld Material with High Nickel and Manganese Content," in *Effects of radiation on nuclear materials: 26th volume* (M. Kirk and E. Lucon, eds.), pp. 119–134, West Conshohocken: ASTM International, 2014.
- [23] M. G. Burke, R. J. Stofanak, T. J. Williams, K. Wilford, J. M. Hyde, H. Thompson, R. M. Boothby, C. A. English, W. L. Server, and P. Efsing, "Complementary LEAP & SANS evaluation of surveillance-irradiated low-Cu/high-Ni welds." Presented at IGRDM, December 4-9, Santa Barbara, USA, 2011.
- [24] P. D. Styman, J. M. Hyde, D. Parfitt, K. Wilford, M. G. Burke, C. A. English, and P. Efsing, "Post-irradiation annealing of Ni–Mn–Si-enriched clusters in a neutron-irradiated RPV steel weld using Atom Probe Tomography," *Journal of Nuclear Materials*, vol. 459, pp. 127–134, 2015.
- [25] W. Karlson, "Analytical TEM examination of RPV weld metal microstructure," Tech. Rep. VTT-R-01951-10, VTT Technical Research Centre of Finland, 2010.
- [26] M. G. Burke, T. N. Nuhfer, J. J. Haugh, and P. Efsing, "Characterization of irradiation damage in high Ni-Mn welds with low Cu: HREM characterization." Presented at IGRDM, December 4-9, Santa Barbara, USA, 2011.
- [27] H. Thompson, "Post-irradiation annealing behaviour of surveillance-irradiated low-Cu/high-Ni welds." Presented at IGRDM, December 4-9, Santa Barbara, USA, 2011.
- [28] G. R. Odette and R. K. Nanstad, "Predictive Reactor Pressure Vessel Steel Irradiation Embrittlement Models: Issues and Opportunities," *JOM Journal of the Minerals Metals and Materials Society*, vol. 61, pp. 17–23, 2009.

- [29] M. Lambrecht, E. Meslin, L. Malerba, M. Hernandez-Mayoral, F. Bergner, P. Pareige, B. Radiguet, and A. Almazouzi, “On the correlation between irradiation-induced microstructural features and the hardening of reactor pressure vessel steels,” *Journal of Nuclear Materials*, vol. 406, pp. 84–89, 2010.
- [30] D. Terentyev, L. Malerba, G. Bonny, A. T. Al-Motasem, and M. Posselt, “Interaction of an edge dislocation with Cu–Ni–vacancy clusters in bcc iron,” *Journal of Nuclear Materials*, vol. 419, pp. 134–139, 2011.
- [31] G. R. Odette and G. E. Lucas, “Embrittlement of nuclear reactor pressure vessels,” *JOM Journal of the Minerals Metals and Materials Society*, vol. 53, pp. 18–22, 2001.
- [32] M. K. Miller and K. F. Russell, “Embrittlement of RPV steels: An atom probe tomography perspective,” *Journal of Nuclear Materials*, vol. 371, pp. 145–160, 2007.
- [33] D. Terentyev, L. Malerba, and A. V. Barashev, “On the correlation between self-interstitial cluster diffusivity and irradiation-induced swelling in Fe–Cr alloys,” *Philosophical Magazine Letters*, vol. 85, pp. 587–594, 2005.
- [34] D. Terentyev, X. He, G. Bonny, A. Bakaev, E. Zhurkin, and L. Malerba, “Hardening due to dislocation loop damage in RPV model alloys: Role of Mn segregation,” *Journal of Nuclear Materials*, vol. 457, pp. 173–181, 2015.
- [35] K. Yabuuchi, M. Saito, R. Kasada, and A. Kimura, “Neutron irradiation hardening and microstructure changes in Fe–Mn binary alloys,” *Journal of Nuclear Materials*, vol. 414, pp. 498–502, 2011.
- [36] M. K. Miller, K. F. Russell, M. A. Sokolov, and R. K. Nanstad, “APT characterization of irradiated high nickel RPV steels,” *Journal of Nuclear Materials*, vol. 361, pp. 248–261, 2007.
- [37] E. Meslin, B. Radiguet, P. Pareige, and A. Barbu, “Kinetic of solute clustering in neutron irradiated ferritic model alloys and a French pressure vessel steel investigated by atom probe tomography,” *Journal of Nuclear Materials*, vol. 399, pp. 137–145, 2010.
- [38] P. B. Wells, T. Yamamoto, B. Miller, T. Milot, J. Cole, Y. Wu, and G. R. Odette, “Evolution of manganese–nickel–silicon-dominated phases in highly irradiated reactor pressure vessel steels,” *Acta Materialia*, vol. 80, pp. 205–219, 2014.
- [39] G. R. Odette and G. E. Lucas, “Recent progress in understanding reactor pressure vessel steel embrittlement,” *Radiation Effects and Defects in Solids*, vol. 144, pp. 189–231, 1998.

- [40] R. Ngayam-Happy, C. S. Becquart, C. Domain, and L. Malerba, "Formation and evolution of MnNi clusters in neutron irradiated dilute Fe alloys modelled by a first principle-based AKMC method," *Journal of Nuclear Materials*, vol. 426, pp. 198–207, 2012.
- [41] G. Bonny, D. Terentyev, A. Bakaev, E. E. Zhurkin, M. Hou, D. Van Neck, and L. Malerba, "On the thermal stability of late blooming phases in reactor pressure vessel steels: an atomistic study," *Journal of Nuclear Materials*, vol. 442, pp. 282–291, 2013.
- [42] E. Meslin, B. Radiguet, and M. Loyer-Prost, "Radiation-induced precipitation in a ferritic model alloy: An experimental and theoretical study," *Acta Materialia*, vol. 61, pp. 6246–6254, 2013.
- [43] G. Bonny, D. Terentyev, E. E. Zhurkin, and L. Malerba, "Monte Carlo study of decorated dislocation loops in FeNiMnCu model alloys," *Journal of Nuclear Materials*, vol. 452, pp. 486–492, 2014.
- [44] C. Domain. Private communication, 2015.
- [45] L. Malerba, "Advances in modelling nanostructural evolution in iron alloys: what do models tell about late blooming phases?." Presented at the LONGLIFE final workshop, 15-16 January 2015, Dresden, Germany (available online at: http://projects.tecnatom.es/webaccess/LONGLIFE/index.php?option=com_docman&task=cat_view&gid=242&Itemid=19).
- [46] B. Radiguet, S. Cammelli, E. Meslin, M. Hernandez-Mayoral, and P. Pareige, "Effect of neutron fluence on radiation-induced microstructure of low Cu RPV steels." Presented at TMS, March 15-19, Orlando, USA, 2015.
- [47] Y. Nagai, Z. Tang, M. Hasegawa, T. Kanai, and M. Saneyasu, "Irradiation-induced Cu aggregations in Fe: An origin of embrittlement of reactor pressure vessel steels," *Physical Review B*, vol. 63, p. 134110, 2001.
- [48] Y. Nagai, K. Takadate, Z. Tang, H. Ohkubo, H. Sunaga, H. Takizawa, and M. Hasegawa, "Positron annihilation study of vacancy-solute complex evolution in Fe-based alloys," *Physical Review B*, vol. 67, p. 224202, 2003.
- [49] M. Chiapetto, L. Malerba, and C. S. Becquart, "Nanostructure evolution under irradiation in FeMnNi alloy: A "grey alloy" object Monte Carlo model," *Journal of Nuclear Materials*, vol. 462, pp. 91–99, 2015.
- [50] C. S. Becquart and C. Domain, "Modeling Microstructure and Irradiation Effects," *Metallurgical and Materials Transactions A*, vol. 42, pp. 852–870, 2010.

- [51] S. Bugat, A. Zeghadi, and G. Adjanor, “A not-so-short description of the PERFECT platform,” *Journal of Nuclear Materials*, vol. 406, pp. 166–174, 2010.
- [52] R. L. Klueh and A. T. Nelson, “Ferritic/martensitic steels for next-generation reactors,” *Journal of Nuclear Materials*, vol. 371, pp. 37–52, 2007.
- [53] F. Danoix, E. Bémont, P. Maugis, and D. Blavette, “Atom Probe Tomography I. Early Stages of Precipitation of NbC and NbN in Ferritic Steels,” *Advanced Engineering Materials*, vol. 8, pp. 1202–1205, 2006.
- [54] Z. Mao, C. K. Sudbrack, K. E. Yoon, G. Martin, and D. N. Seidman, “The mechanism of morphogenesis in a phase-separating concentrated multicomponent alloy,” *Nature Materials*, vol. 6, pp. 210–216, 2007.
- [55] C. L. Fu, M. Krčmar, G. S. Painter, and X.-Q. Chen, “Vacancy Mechanism of High Oxygen Solubility and Nucleation of Stable Oxygen-Enriched Clusters in Fe,” *Physical Review Letters*, vol. 99, p. 225502, 2007.
- [56] C. Domain and C. S. Becquart, “Diffusion of phosphorus in α -Fe: An ab initio study,” *Physical Review B*, vol. 71, p. 214109, 2005.
- [57] E. Meslin, C.-C. Fu, A. Barbu, F. Gao, and F. Willaime, “Theoretical study of atomic transport via interstitials in dilute Fe-P alloys,” *Physical Review B*, vol. 75, p. 094303, 2007.
- [58] A. R. Allnatt and A. B. Lidiard, *Atomic Transport in Solids*. Cambridge University Press, 2003.
- [59] C. Domain and C. S. Becquart, “Ab initio calculations of defects in Fe and dilute Fe-Cu alloys,” *Physical Review B*, vol. 65, p. 024103, 2001.
- [60] V. Barbe and M. Nastar, “Phenomenological coefficients in a concentrated alloy for the dumbbell mechanism,” *Philosophical Magazine*, vol. 86, pp. 3503–3535, 2006.
- [61] A. Seeger, “Lattice Vacancies in High-Purity α -Iron,” *Physical Status Solidi A*, vol. 167, pp. 289–311, 1998.
- [62] A. D. Le Claire, “Solute diffusion in dilute alloys,” *Journal of Nuclear Materials*, vol. 69-70, pp. 70–96, 1978.
- [63] M. Nastar, “A mean field theory for diffusion in a dilute multi-component alloy: a new model for the effect of solutes on self-diffusion,” *Philosophical Magazine*, vol. 85, pp. 3767–3794, 2005.
- [64] V. Barbe and M. Nastar, “Phenomenological coefficients in a dilute BCC alloy for the dumbbell mechanism,” *Philosophical Magazine*, vol. 87, pp. 1649–1669, 2007.

- [65] T. R. Anthony, “Atom Currents Generated by Vacancy Winds,” in *Diffusion in Solids: Recent Developments* (A. S. Nowick and J. J. Burton, eds.), pp. 353–378, New York: Academic Press, 1975.
- [66] M. Nastar and F. Soisson, “Radiation-Induced Segregation,” in *Comprehensive Nuclear Materials* (R. J. M. Konings, T. R. Allen, R. E. Stoller, and S. Yamanaka, eds.), pp. 471–496, Amsterdam: Elsevier Inc., 2012.
- [67] C. Kittel, *Introduction to Solid State Physics*. Wiley, 8th ed., 2004.
- [68] N. Sandberg, Z. Chang, L. Messina, P. Olsson, and P. Korzhavyi, “Modeling of the magnetic free energy of self-diffusion in bcc Fe,” *Physical Review B*, vol. 92, p. 184102, 2015.
- [69] A. D. Le Claire, “Correlation effects in diffusion in solids,” in *Physical Chemistry: an advanced treatise* (H. Eyring, ed.), New York: Academic Press, 1970.
- [70] L. Onsager, “Reciprocal relations in irreversible processes. II.,” *Physical Review*, vol. 38, pp. 2265–2279, 1931.
- [71] A. R. Allnatt and E. L. Allnatt, “Computer simulation of phenomenological coefficients for atom transport in a random alloy,” *Philosophical Magazine A*, vol. 49, pp. 625–635, 1984.
- [72] E. Clouet and M. Nastar, “Classical nucleation theory in ordering alloys precipitating with $L1_2$ structure,” *Physical Review B*, vol. 75, p. 132102, 2007.
- [73] W. G. Wolfer, “Drift Forces on Vacancies and Interstitials in Alloys with Radiation-Induced Segregation,” *Journal of Nuclear Materials*, vol. 114, pp. 292–304, 1983.
- [74] R. Sizmann, “The effect of radiation upon diffusion in metals,” *Journal of Nuclear Materials*, vol. 69, pp. 386–412, 1978.
- [75] T. Garnier, *Transfert des propriétés thermodynamiques et cinétiques de l'échelle atomique à l'échelle macroscopique pour la simulation des transformations de phase diffusives*. PhD thesis, Université Paris Sud, 2012.
- [76] T. Garnier, M. Nastar, P. Bellon, and D. R. Trinkle, “Solute drag by vacancies in body-centered cubic alloys,” *Physical Review B*, vol. 88, p. 134201, 2013.
- [77] C. Varvenne, F. Bruneval, M.-C. Marinica, and E. Clouet, “Point defect modeling in materials: Coupling ab initio and elasticity approaches,” *Physical Review B*, vol. 88, p. 134102, 2013.
- [78] D. J. Bacon, D. M. Barnett, and R. O. Scattergood, “Anisotropic continuum theory of lattice defects,” *Progress in Materials Science*, vol. 23, pp. 51–262, 1980.

- [79] T. Garnier, V. R. Manga, D. R. Trinkle, M. Nastar, and P. Bellon, “Stress-induced anisotropic diffusion in alloys: Complex Si solute flow near a dislocation core in Ni,” *Physical Review B*, vol. 88, p. 134108, 2013.
- [80] D. Hull and D. J. Bacon, *Introduction to dislocations*. Oxford: Butterworth-Heinemann, 2011.
- [81] J. Roesler, H. Harders, and M. Baeker, *Mechanical behaviour of engineering materials*. Berlin: Springer-Verlag, 2006.
- [82] R. G. Parr and W. Yang, *Density-Functional Theory of Atoms and Molecules*. Oxford: Oxford University Press, 1989.
- [83] N. M. Harrison, “An Introduction to Density Functional Theory,” in *Computational Materials Science* (R. Catlow and E. Kotomin, eds.), pp. 1–26, Amsterdam: IOS Press, 2003.
- [84] W. Kohn and L. J. Sham, “Quantum Density Oscillations in an Inhomogeneous Electron Gas,” *Physical Review*, vol. 137, pp. A1697–A1705, 1965.
- [85] J. P. Perdew, J. A. Chevary, S. H. Vosko, K. A. Jackson, M. R. Pederson, D. J. Singh, and C. Fiolhais, “Atoms, molecules, solids, and surfaces: Applications of the generalized gradient approximation for exchange and correlation,” *Physical Review B*, vol. 46, pp. 6671–6687, 1992.
- [86] J. P. Perdew, K. Burke, and Y. Wang, “Generalized gradient approximation for the exchange-correlation hole of a many-electron system,” *Physical Review B*, vol. 54, pp. 16533–16539, 1996.
- [87] P. E. Blöchl, “Projector Augmented-Wave Method,” *Physical Review B*, vol. 50, pp. 17953–17979, 1994.
- [88] N. W. Ashcroft and N. D. Mermin, *Solid state physics*. Belmont: Brooks/Cole, Cengage Learning, 1976.
- [89] H. Jonsson, G. Mills, and K. W. Jacobsen, “Nudged Elastic Band Method for Finding Minimum Energy Paths of Transitions,” in *Classical and quantum dynamics in condensed phase simulations* (B. J. Berne, G. Ciccotti, and D. F. Coker, eds.), World Scientific, 1998.
- [90] G. Henkelman, B. P. Uberuaga, and H. Jonsson, “A climbing image nudged elastic band method for finding saddle points and minimum energy paths,” *The Journal of Chemical Physics*, vol. 113, pp. 9901–9904, 2000.
- [91] G. E. Lucas and R. Schaublin, “Vibrational contributions to the stability of point defects in bcc iron: A first-principles study,” *Nuclear Instruments and Methods in Physics Research Section B: Beam Interactions with Materials and Atoms*, vol. 267, pp. 3009–3012, 2009.

- [92] G. H. Vineyard, "Frequency factors and isotope effects in solid state rate processes," *Journal of Physics and Chemistry of Solids*, vol. 3, pp. 121–127, 1957.
- [93] Y. Mishin, M. R. Sørensen, and A. F. Voter, "Calculation of point-defect entropy in metals," *Philosophical Magazine A*, vol. 81, pp. 2591–2612, 2001.
- [94] A. B. Bortz, M. H. Kalos, and J. L. Lebowitz, "A new algorithm for Monte Carlo simulation of Ising spin systems," *Journal of Computational Physics*, vol. 17, pp. 10–18, 1975.
- [95] C. S. Becquart, A. Barbu, J.-L. Bocquet, M. J. Caturla, C. Domain, C.-C. Fu, S. I. Golubov, M. Hou, L. Malerba, C. J. Ortiz, A. Soudi, and R. E. Stoller, "Modeling the long-term evolution of the primary damage in ferritic alloys using coarse-grained methods," *Journal of Nuclear Materials*, vol. 406, pp. 39–54, 2010.
- [96] C. S. Becquart and C. Domain, "Introducing chemistry in atomistic kinetic Monte Carlo simulations of Fe alloys under irradiation," *Physical Status Solidi B*, vol. 247, pp. 9–22, 2010.
- [97] F. Soisson and C.-C. Fu, "Cu-precipitation kinetics in α -Fe from atomistic simulations: Vacancy-trapping effects and Cu-cluster mobility," *Physical Review B*, vol. 76, p. 214102, 2007.
- [98] E. Vincent, C. S. Becquart, and C. Domain, "Microstructural evolution under high flux irradiation of dilute Fe-CuNiMnSi alloys studied by an atomic kinetic Monte Carlo model accounting for both vacancies and self interstitials," *Journal of Nuclear Materials*, vol. 382, pp. 154–159, 2008.
- [99] G. Henkelman and H. Jónsson, "A dimer method for finding saddle points on high dimensional potential surfaces using only first derivatives," *The Journal of Chemical Physics*, vol. 111, pp. 7010–7022, 1999.
- [100] F. Soisson and C.-C. Fu, "Atomistic simulations of copper precipitation and radiation induced segregation in α -iron," *Solid State Phenomena*, vol. 139, pp. 107–112, 2008.
- [101] N. Castin, R. Pinheiro Domingos, and L. Malerba, "Use of computational intelligence for the prediction of vacancy migration energies in atomistic kinetic monte carlo simulations," *International Journal of Computational Intelligence Systems*, vol. 1, pp. 340–352, 2008.
- [102] N. Castin, L. Malerba, G. Bonny, and M. I. Pascuet, "Modelling radiation-induced phase changes in binary FeCu and ternary FeCuNi alloys using an artificial intelligence-based atomistic kinetic Monte Carlo approach," *Nuclear Instruments and Methods in Physics Research Section B: Beam Interactions with Materials and Atoms*, vol. 267, pp. 3002–3008, 2009.

- [103] N. Castin and L. Malerba, “Calculation of proper energy barriers for atomistic kinetic Monte Carlo simulations on rigid lattice with chemical and strain field long-range effects using artificial neural networks,” *The Journal of Chemical Physics*, vol. 132, p. 074507, 2010.
- [104] N. Castin, *Atomistic kinetic Monte Carlo simulation of precipitation and segregation in metals for nuclear applications, using a novel methodology based on artificial neural networks*. PhD thesis, Université Libre de Bruxelles, 2011.
- [105] N. Castin, M. I. Pascuet, and L. Malerba, “Modeling the first stages of Cu precipitation in α -Fe using a hybrid atomistic kinetic Monte Carlo approach,” *The Journal of Chemical Physics*, vol. 135, p. 064502, 2011.
- [106] M. I. Pascuet, N. Castin, C. S. Becquart, and L. Malerba, “Stability and mobility of Cu–vacancy clusters in Fe–Cu alloys: A computational study based on the use of artificial neural networks for energy barrier calculations,” *Journal of Nuclear Materials*, vol. 412, pp. 106–115, 2011.
- [107] N. Castin, M. I. Pascuet, and L. Malerba, “Mobility and stability of large vacancy and vacancy-copper clusters in iron - An atomistic kinetic Monte Carlo study,” *Journal of Nuclear Materials*, vol. 429, pp. 315–324, 2012.
- [108] C. M. Bishop, *Neural networks for pattern recognition*. Oxford: Oxford University Press, 1995.
- [109] N. Castin, L. Malerba, and R. Chaouadi, “Prediction of radiation induced hardening of reactor pressure vessel steels using artificial neural networks,” *Journal of Nuclear Materials*, vol. 408, pp. 30–39, 2011.
- [110] C. M. Bishop, “Neural networks and their applications,” *Review of Scientific Instruments*, vol. 65, p. 1803, 1994.
- [111] V. Jansson and L. Malerba, “Simulation of the nanostructure evolution under irradiation in Fe-C alloys,” *Journal of Nuclear Materials*, vol. 443, pp. 1–12, 2013.
- [112] N. Anento, N. Castin, A. Serra, and L. Malerba, “Assessment of stability and mobility of SIA and vacancy clusters in target ternary alloy,” Tech. Rep. D1-3.16, PERFORM 60 FP7 project (grant agreement no. FP7-232612), 2013.
- [113] P. Y. Serruys and G. Brebec, “Détermination des rapports de fréquences de saut de la facune par électromigration dans les alliages binaires cubiques centrés dilués,” *Philosophical Magazine A*, vol. 46, pp. 661–675, 1982.
- [114] Y. Okamura and A. R. Allnatt, “Calculations of phenomenological coefficients for matter transport by the matrix method of random walk theory,” *Journal of Physics C: Solid State Physics*, vol. 16, p. 1841, 1983.

- [115] S. Choudhury, L. Barnard, J. D. Tucker, T. R. Allen, B. D. Wirth, M. Asta, and D. Morgan, “Ab-initio based modeling of diffusion in dilute bcc Fe-Ni and Fe-Cr alloys and implications for radiation induced segregation,” *Journal of Nuclear Materials*, vol. 411, pp. 1–14, 2011.
- [116] P. Olsson, T. P. C. Klaver, and C. Domain, “Ab initio study of solute transition-metal interactions with point defects in bcc Fe,” *Physical Review B*, vol. 81, p. 054102, 2010.
- [117] C. S. Becquart and C. Domain, “Solute–point defect interactions in bcc systems: Focus on first principles modelling in W and RPV steels ,” *Current Opinion in Solid State & Materials Science*, vol. 16, pp. 115–125, 2012.
- [118] A. D. Le Claire and G. Neumann, “Impurity diffusion in iron group metals,” in *Diffusion in Solid Metals and Alloys* (H. Mehrer, ed.), pp. 1–10, Berlin: Springer-Verlag, 2001.
- [119] G. Neumann and C. Tuijn, “Self-diffusion and impurity diffusion in group VIII metals,” in *Self-diffusion and impurity diffusion in pure metals: handbook of experimental data*, Oxford: Elsevier, 2011.
- [120] A. Janotti, M. Krčmar, C. L. Fu, and R. C. Reed, “Solute Diffusion in Metals: Larger Atoms Can Move Faster,” *Physical Review Letters*, vol. 92, p. 085901, 2004.
- [121] F. Maury, P. Lucasson, A. Lucasson, F. Faudot, and J. Bigot, “A study of irradiated FeCr alloys: deviations from Matthiessen’s rule and interstitial migration,” *Journal of Physics F - Metal Physics*, vol. 17, pp. 1143–1165, 1987.
- [122] F. Maury, A. Lucasson, P. Lucasson, P. Moser, and F. Faudot, “Interstitial migration in irradiated iron and iron-based dilute alloys. II. Interstitial migration and solute transport in FeNi, FeMn and FeCu dilute alloys,” *Journal of Physics: Condensed Matter*, vol. 2, pp. 9291–9307, 1990.
- [123] H. Abe and E. Kuramoto, “Interaction of solutes with irradiation-induced defects of electron-irradiated dilute iron alloys,” *Journal of Nuclear Materials*, vol. 271, pp. 209–213, 1999.
- [124] J. P. Wharry and G. S. Was, “A systematic study of radiation-induced segregation in ferritic–martensitic alloys,” *Journal of Nuclear Materials*, vol. 442, pp. 7–16, 2013.
- [125] J. P. Wharry and G. S. Was, “The mechanism of radiation-induced segregation in ferritic–martensitic alloys,” *Acta Materialia*, vol. 65, pp. 42–55, 2014.

- [126] R. G. Faulkner, S. H. Song, P. E. J. Flewitt, M. Victoria, and P. Marmy, “Grain boundary segregation under neutron irradiation in dilute alloys,” *Journal of Nuclear Materials*, vol. 255, pp. 189–209, 1998.
- [127] G. Gupta, Z. Jiao, A. N. Ham, J. T. Busby, and G. S. Was, “Microstructural evolution of proton irradiated T91,” *Journal of Nuclear Materials*, vol. 351, pp. 162–173, 2006.
- [128] Z. Lu, R. G. Faulkner, N. Sakaguchi, and H. Kinoshita, “Effect of hafnium on radiation-induced inter-granular segregation in ferritic steel,” *Journal of Nuclear Materials*, vol. 351, pp. 155–161, 2006.
- [129] E. A. Marquis, S. Lozano-Perez, and V. De Castro, “Effects of heavy-ion irradiation on the grain boundary chemistry of an oxide-dispersion strengthened Fe–12wt.% Cr alloy,” *Journal of Nuclear Materials*, vol. 417, pp. 257–261, 2011.
- [130] E. A. Marquis, R. Hu, and T. Rousseau, “A systematic approach for the study of radiation-induced segregation/depletion at grain boundaries in steels,” *Journal of Nuclear Materials*, vol. 413, pp. 1–4, 2011.
- [131] Z. Chang, D. Terentyev, and N. Sandberg, “Anomalous bias factors of dislocations in bcc iron,” *Journal of Nuclear Materials*, vol. 461, pp. 221–229, 2015.
- [132] G. J. Ackland, D. J. Bacon, A. F. Calder, and T. Harry, “Computer simulation of point defect properties in dilute Fe-Cu alloy using a many-body interatomic potential,” *Philosophical Magazine A*, vol. 75, pp. 713–732, 1997.
- [133] O. I. Gorbatov, *Theoretical investigation of copper precipitation in steel*. PhD thesis, KTH Royal Institute of Technology, Stockholm, 2015.
- [134] M. Hernandez-Mayoral and D. Gómez-Briceño, “Transmission electron microscopy study on neutron irradiated pure iron and RPV model alloys,” *Journal of Nuclear Materials*, vol. 399, pp. 146–153, 2010.
- [135] J. Roudén and P. Efsing. Private communication, 2015.
- [136] M. Konstantinovic. Private communication, 2015.
- [137] G. Monnet, “Investigation of precipitation hardening by dislocation dynamics simulations,” *Philosophical Magazine*, vol. 86, pp. 5927–5941, 2006.

Paper I

Exact *ab initio* transport coefficients in bcc Fe-*X* (*X*=Cr, Cu, Mn, Ni, P, Si) dilute alloysLuca Messina,^{1,*} Maylise Nastar,² Thomas Garnier,^{2,3} Christophe Domain,⁴ and Pär Olsson¹¹*KTH Royal Institute of Technology, Reactor Physics, 106 91 Stockholm, Sweden*²*CEA, DEN, Service de Recherches de Métallurgie Physique, F-91191 Gif-sur-Yvette, France*³*Department of Materials Science and Engineering, University of Illinois, Urbana-Champaign, Illinois 61801, USA*⁴*Département Matériaux et Mécanique des Composants, EDF-R&D, Les Renardières, F-77250 Moret sur Loing, France*

(Received 13 February 2014; revised manuscript received 2 September 2014; published 22 September 2014)

Defect-driven diffusion of impurities is the major phenomenon leading to formation of embrittling nanoscopic precipitates in irradiated reactor pressure vessel (RPV) steels. Diffusion depends strongly on the kinetic correlations that may lead to flux coupling between solute atoms and point defects. In this work, flux coupling phenomena such as solute drag by vacancies and radiation-induced segregation at defect sinks are systematically investigated for six bcc iron-based dilute binary alloys, containing Cr, Cu, Mn, Ni, P, and Si impurities, respectively. First, solute-vacancy interactions and migration energies are obtained by means of *ab initio* calculations; subsequently, self-consistent mean field theory is employed in order to determine the exact Onsager matrix of the alloys. This innovative multiscale approach provides a more complete treatment of the solute-defect interaction than previous multifrequency models. Solute drag is found to be a widespread phenomenon that occurs systematically in ferritic alloys and is enhanced at low temperatures (as for instance RPV operational temperature), as long as an attractive solute-vacancy interaction is present, and that the kinetic modeling of bcc alloys requires the extension of the interaction shell to the second-nearest neighbors. Drag occurs in all alloys except Fe(Cr); the transition from dragging to nondragging regime takes place for the other alloys around (Cu, Mn, Ni) or above (P, Si) the Curie temperature. As far as only the vacancy-mediated solute migration is concerned, Cr depletion at sinks is foreseen by the model, as opposed to the other impurities which are expected to enrich up to no less than 1000 K. The results of this study confirm the current interpretation of the hardening processes in ferritic-martensitic steels under irradiation.

DOI: [10.1103/PhysRevB.90.104203](https://doi.org/10.1103/PhysRevB.90.104203)

PACS number(s): 61.82.Bg, 66.30.J-, 61.72.Yx, 31.15.A-

I. INTRODUCTION

Solute diffusion in alloys is predominantly mediated by defect-driven mechanisms, that is through vacancy exchange and interstitial migration. Especially in irradiated materials, the defect concentrations can be considerably larger than in thermal equilibrium and solute diffusion can then be strongly enhanced or even induced. According to the binding or repulsive nature of the interaction between solutes and point defects (PD), kinetic correlations can arise and solute-PD coupled fluxes can lead to an acceleration of thermodynamic-driven diffusion (radiation-enhanced effect) or to the net flux of solute atoms even in the absence of thermodynamic driving forces for the solute (radiation-induced effect). Flux coupling is of great importance in any metallurgical process in which an accurate microstructural characterization of the material is needed, as for instance in phase transformations during heat treatments [1,2]. A precise description of the diffusion mechanisms is essential for a correct modeling of driven systems because both phase transitions and stationary states depend on the alloy diffusion properties. In addition, flux coupling is fundamental for understanding the nanostructural and microstructural evolution of irradiated materials. For instance, it plays a key role in radiation-induced segregation (RIS) of solute atoms at sinks. Recently, a systematic experimental RIS study of several irradiated ferritic-martensitic alloys in the low-temperature regime showed that many impurities consistently enrich at grain boundaries [3]. It is mentioned

that this behavior can be explained in terms of balance between vacancy- and interstitial-mediated diffusion. This issue can be analyzed and solved if the transport coefficients (or Onsager matrix) of the system are known [4].

An important example of irradiated alloys is represented by reactor pressure vessels (RPV) steels, whose integrity is affected by the microstructural changes induced by the neutron-induced defect population. In particular, hardening and consequent embrittlement due to the formation of nanofeatures inside the steel is regarded as the most serious concern for the reactor lifetime. These nanofeatures consist of matrix damage (small voids and dislocation loops) or defect-impurity clusters. They originate from the PD produced by incident neutrons and their interaction with the alloy constituents. Both types of damage hinder the movement of dislocations and consequently increase the RPV ductile-to-brittle transition temperature (DBTT). In particular, Mn-Ni-Si-rich precipitates have been recently observed in RPV surveillance tests to be the cause of a further unexpected DBTT shift [5,6]. Intergranular segregation of impurities such as phosphorus is, among others, a secondary but non-negligible embrittling phenomenon occurring under irradiation [7]. The investigation of the phenomena inducing solute clustering even in undersaturated conditions has been carried on since the early stages of nuclear power plant operation, but is still missing an exhaustive explanation.

RPV-like steels are usually body-centered-cubic (bcc) ferritic dilute alloys, with varying concentrations of Cu, Mn, Ni, Si, P, Cr and other minor impurities [8,9]. Although they have been extensively studied, a systematic investigation of flux coupling is still missing. This work aims at covering this

*messina@kth.se

gap. The issue is tackled with model binary alloys, in order to identify the inherent transport properties of each solute species in bcc iron. Six alloys are selected for this purpose (Fe- X , with $X = \text{Cu, Mn, Ni, P, Si, and Cr}$), in reference to the solute atoms that are usually observed in nanoclusters [5,10]. In addition to those, Cr is of great interest mainly for the upcoming Generation IV reactor vessels and other structural materials, although in nondilute concentrations.

A very small number of experimental studies are devoted to binary model alloys. The observation of irradiated iron dilute alloys seems to indicate that a strong kinetic correlation between vacancies and Mn, Si, Ni, Cu, and P solute atoms is the trigger for solute-vacancy cluster agglomeration and accelerated void growth [11]. A strong kinetic correlation between PD and Mn solute atoms was also advanced as cause for the formation of Mn-rich clusters observed around dislocation loops [12,13], and in such cases the contribution of vacancy versus interstitial diffusion is still to be determined.

Such issues can be properly assessed by computing the transport coefficients (L_{ij}). From these quantities, flux coupling between different atomic species can be easily inferred. In a near equilibrium system, the flux of each species can be written as

$$J_i = - \sum_{j=1}^N \frac{L_{ij}}{k_B T} \nabla \mu_j, \quad (1)$$

or in other words as a linear combination of the thermodynamic driving forces $\nabla \mu_j$ acting on all species, including PD. The L_{ij} coefficients are therefore expressions of the kinetic response of the system to an external solicitation and allow for a clear separation between thermodynamic and kinetic properties of the alloy. Moreover, the off-diagonal coefficients $L_{ij, i \neq j}$ emphasize the kinetic coupling that may appear between fluxes of different atomic species, for instance, between solvent and solute atoms, which would be missed by “traditional” diffusion coefficients.

The L_{ij} 's can be inferred from experimentally measured tracer diffusion coefficients with Darken's [14] or Manning's [15] theories, but none of them are able to provide an accurate estimation of the crucial off-diagonal coefficients, nor to allow such coefficients to be negative. Alternatively, the L_{ij} 's can be obtained starting from microscopic jump frequencies that can be computed either with interatomic potentials [16–18] or through density functional theory (DFT) calculations [19–22]. Such frequencies can be then used as parameters for atomistic Monte Carlo simulations [23] or analytical multifrequency models [24]. Monte Carlo simulations can be effective but become computationally demanding when complex solute-defect interactions are present. On the other hand, the analytical models developed in the so-called multifrequency framework that are available in the literature take into account only first-nearest neighbor (1nn) solute-vacancy interactions (SVI), or second-nearest neighbor (2nn) interactions to a partial extent [25,26]. In the latter case, the flux coupling prediction capability is considerably hampered by strong approximations in the microscopic jump rates. Later on, a more general and flexible self-consistent mean field (SCMF) method was developed, initially for vacancy-mediated diffusion in concentrated ideal solid solutions [27], then in nonideal

alloys [28], and finally for interstitial diffusion [29,30]. Its main advantage is to yield exact transport coefficients in dilute alloys; moreover, it can be extended to any range of solute-defect interactions, its self-consistency being ensured by an appropriate choice of the amount of unknowns. The reliability of the SCMF theory is assured by its perfect agreement with Monte Carlo simulations in generic AB alloys, for both vacancy- [28] and interstitial-mediated diffusion [29]. More recently, it was successfully employed to analyze the conditions for the onset of vacancy drag in bcc [31] and fcc [32] alloys. These works have highlighted the importance of the nearest-neighbor shells beyond the first one for a correct prediction of flux coupling, as opposed to many studies where only 1nn interactions were considered [33,34].

On the modeling side, flux coupling was investigated for the Fe(P) system by molecular dynamics simulations based on an interatomic potential [16]. In this case, it was shown that a strong kinetic correlation with both vacancies and interstitials lets P migrate quickly to PD sinks. Furthermore, kinetic Monte Carlo (KMC) simulations of the Fe(Cu) system confirmed the possibility of Cu-vacancy drag at low temperatures. To the authors' knowledge, the only referenced case in which a full set of transport coefficients was derived for the Fe- X dilute alloys object of this work was a study on the Fe(Cr) and Fe(Ni) systems by Choudhury *et al.* [22]. They applied an approximated multifrequency model where 2nn SVI were only partially considered, and concluded that no solute drag was expected for either solute. Solute-drag phenomena are known to be strongly related to attractive solute-vacancy binding energies. Calculations of such binding energies in Fe dilute alloys [35] corroborate this conclusion in Fe(Cr) alloy, but not in Fe(Ni). Indeed, the prediction of no drag effect in Fe(Ni) is in contradiction with the idea that binding SVI at first- and second-nn sites lead to solute-drag phenomena.

In this work, the SCMF method is applied to dilute ferritic alloys in order to provide an exact prediction of the flux coupling tendencies between solutes and defects. The Onsager matrix is computed for each of the selected dilute alloys from a set of DFT-computed jump frequencies. The obtained phenomenological coefficients are then used to discuss solute drag as function of temperature, to predict RIS tendencies and to obtain solute diffusion coefficients for the sake of comparison with experimental values. Only the case of vacancy-mediated diffusion is considered, and the issue of interstitial-mediated diffusion is left for a future work.

The paper is organized as follows. The following section is dedicated to the first-principles computation of solute-vacancy interaction energies and jump frequencies. The focus is then moved to the mean field treatment of the obtained jump frequencies in the SCMF framework. Finally, the computed L_{ij} 's, vacancy drag, diffusion coefficients, and RIS tendencies are shown in the last section and are analyzed in terms of physical implications on the RPV microstructural evolution.

II. AB INITIO STUDY

A. Definition of jump frequencies

The phenomenological coefficients related to vacancy-mediated diffusion can be derived in terms of microscopic

vacancy jump frequencies. These jump rates depend on the activation energy that is needed for one surrounding atom to move into a vacant site. In the framework of transition state theory, a jump frequency ω_{ij} for an atom moving from site j to a vacant site i is defined as [36]

$$\omega_{ij} = v_{ij} \exp\left(-\frac{E_{ij}^{\text{mig}}}{k_B T}\right). \quad (2)$$

The attempt frequency v_{ij} is related to the lattice vibrational modes, whereas the energy barrier E_{ij}^{mig} depends on the type of moving atom and the local chemical environment around the moving atom-vacancy pair. In a binary dilute alloy, solvent and solute atoms are characterized by different migration barriers, and the corresponding jump frequencies are referred to as ω_0 and ω_2 , in accordance to LeClaire's nomenclature [24]. Moreover, if a strong solute-vacancy interaction exists, the jump rates of the solvent atoms in the vicinity of the solute-vacancy pair are considerably affected.

The set of jump frequencies that need to be calculated depends on the spatial extent of the SVI. For instance, for bcc dilute alloys, Le Claire [24] showed that four jump types are needed if only the 1nn SVI is considered, or nine jump types when the 2nn SVI is introduced. However, the 2nn analytical models derived from Le Claire's framework [25,26] are approximated to such an extent that the flux coupling tendency is considerably underestimated, as explained in the following section.

In principle, nothing is limiting the spatial extent of the SVI, but in practice the range must be limited in order to have a finite set of jump frequencies. The choice of a cutoff distance depends not only on the extent of the SVI, but also on the kinetics of the targeted phenomenon: in the case of solute drag by vacancies, the paths leading to a possible drag mechanism are multifold and can involve distances beyond the 2nn position [31]. Moreover, some of the impurities of interest present a non-negligible SVI at the fifth-nearest-neighbor (5nn) distance [37]. Hence, the interaction shell was extended in this work to 5nn sites, which entails the definition of 12 forward-backward jump types, as shown in Fig. 1.

Ab initio calculations based on DFT represent an accurate way of obtaining zero-temperature interaction energies, migration barriers, and attempt frequencies. Finite-temperature effects, such as the influence of magnetic disordering on ω_{ij} , must be explicitly introduced in order to extrapolate the diffusion properties to higher temperatures, as was done for instance in [38]. Other approaches, such as the development of alloy interatomic potentials, can be pursued. Such potentials are, however, fitted either on *ab initio* data or experiments. Therefore, they are valid only for the specific system they were developed for and need a cutoff distance beyond which the interatomic interactions are set to null. On the other hand, in DFT calculations there is no assumption on the potential range. Therefore, the SVI trends as function of nn distance must be investigated in order to estimate at which distance they become negligible.

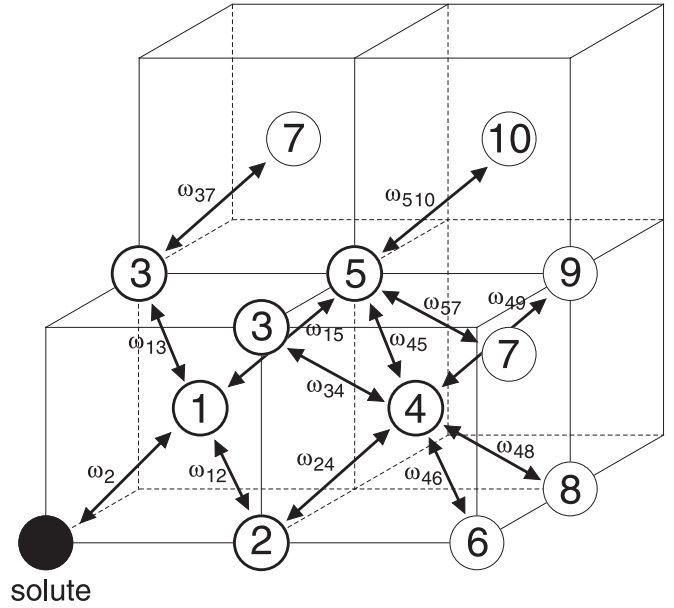


FIG. 1. Network of the 12 Fe-V jump frequencies affected by the presence of a solute atom, for solute-vacancy interactions extending to the 5nn distance. The solute-vacancy exchange is labeled with ω_2 , while ω_0 represents the unaffected Fe-V jump frequency (not shown).

B. *Ab initio* methodology

The first-principles calculations in this work were performed with the Vienna *ab initio* simulation package (VASP) [39–41]. As part of the *ab initio* procedure, the supercell relaxation allowed for the determination of solute-vacancy binding energies, which represents a partial hint of whether a solute atom is likely to follow a vacancy during the diffusion process.

DFT is employed in order to compute the bulk properties in pure iron and a full set of SVI energies and migration barriers for the Fe(Cr), Fe(Cu), Fe(Mn), Fe(Ni), Fe(P), and Fe(Si) dilute binary alloys. The calculations were performed on a plane-wave basis, employing the pseudopotentials developed within the projector augmented wave (PAW) method [42,43]. The exchange correlation function was described through the Perdew-Burke-Ernzerhof (PBE) parametrization [44] of the generalized gradient approximation (GGA). All calculations were spin polarized and the Vosko-Wilk-Nusair (VWN) algorithm [45] was used for the spin interpolation of the correlation potential. The Brillouin zone was sampled with the Monkhorst-Pack scheme.

The simulations were carried out on a 128-atom bcc supercell with full periodic boundary conditions. A plane-wave cutoff of 300 eV and a $3 \times 3 \times 3$ k -point mesh were chosen, in accordance with the convergence tests of a previous study [46]. The defects were introduced allowing for atomic relaxations but restraining the cell shape and volume. In pure iron, the vacancy formation enthalpy is computed as $E_v^{\text{form}} = E(N-1) - (N-1)/N \cdot E(N)$, where $E(N)$ is the energy of the undefected supercell and $E(N-1)$ that of the system containing a vacant site. The further introduction of a solute atom yields the solute-vacancy binding energy (at the

TABLE I. Bulk properties (computed or adopted in this work), compared with experiments and previous calculations.

Quantity	This work	Previous calculations	Experiments
Lattice parameter a_0	2.831 Å	2.83 Å ^a , 2.86 Å ^b	2.86 Å ^k
Vacancy formation enthalpy H_v^f	2.18 eV	2.20 eV ^c , 2.02 eV ^d , 2.16 eV ^e	1.60 eV ^l , 2.0 eV ^m
Vacancy migration energy E_v^{mig}	0.70 eV	0.67 eV ^c , 0.65 eV ^d	0.55 eV ⁿ
Ferromagnetic activation energy Q_v^F	2.88 eV	2.87 eV ^e , 2.67 eV ^d	2.95 eV ^o , 2.88 eV ^l
Vacancy formation entropy S_v^f	4.1k _B ^e	1.5–2.0k _B ^f , 2.1k _B ^g , <5 k _B ^h	
Attempt frequency ν_0^*	6 THz	91.5 THz ⁱ , 4.9 THz ^j	

^aReference [35].^bReference [57].^cReference [59].^dReference [58].^eReference [61].^fReference [63].^gReference [62].^hReference [64].ⁱReference [67].^jReference [19].^kReference [56].^lReference [65].^mReference [66].ⁿReference [68].^oReference [60].

Xnn distance):

$$E_{V, Xnn}^b = E_{1V, \text{Isol}(Xnn)}^{N-2} - E_{1V}^{N-1} - E_{\text{Isol}}^{N-1} + E^N, \quad (3)$$

where the terms on the right-hand side are the energies of the supercell, respectively, with one substitutional solute atom and one vacancy, with only one vacancy, with only one solute atom and without any defect.

The nudged elastic band (NEB) method [47,48], implemented with three images and the climbing-image algorithm [49], was employed for the evaluation of the system energy at the saddle point for all jump configurations. In the climbing-image algorithm, three images are sufficient for an accurate evaluation of the saddle-point energy [50] since all barriers here investigated are of single-hump shape. The migration barriers are defined as energy difference between the saddle point and the initial state. Each NEB simulation yields the migration energy of a forward jump ($E_{ij}^{\text{mig}} = E_{\text{sad}}^{ij} - E_{\text{relax}}^i$) and its backward counterpart ($E_{ji}^{\text{mig}} = E_{\text{sad}}^{ij} - E_{\text{relax}}^j$). The uncertainty related to the computed binding energies and migration barriers is estimated to about 5 meV.

The standard potentials available in the VASP library were employed for all involved chemical elements. Concerning the calculations in the Fe(Mn) alloy, it was previously reported that some NEB simulations did not converge to a physically meaningful magnetic state [37] and led to anomalously high migration barriers (>1 eV) [51]. A similar issue was encountered in the Fe(Si) alloy. Once more, the system was successfully driven to the correct global minimum with the use of linear mixing in the starting guess of the charge dielectric function, as opposed to using the Kerker model [52,53].

The jump frequency prefactor ν_i^* might also be computed *ab initio*, by means of frozen phonon calculations and the application of Vineyard's theory [36]. The same calculations

allow as well for the computation of the vacancy formation entropy [54]. However, this is beyond the scope of this work since the drag tendencies are weakly affected by the attempt frequency value [55], as long as the latter is the same for all jump types. Hence, the attempt frequency is assumed to be the same for all kind of jumps and of the same order of magnitude of the Debye frequency in iron: 6 THz [56].

C. *Ab initio* results

The bulk properties of pure iron are reported in Table I. The computed equilibrium lattice parameter is consistent with previous VASP calculations [35,57]. The total vacancy diffusion activation energy in pure iron of 2.88 eV is in line with previous DFT calculations [58,59] and close to the experimental value of 2.95 eV [60]. The vacancy formation entropy was computed with DFT by Lucas *et al.* [61]. Their larger value of 4.1k_B with respect to previous calculations [62,63] is anyway consistent with the total value for formation and migration entropy of 5k_B found in another study [64]. However, the entropy of migration is neglected in this work.

The binding energies obtained by supercell relaxation with the VASP code are reported in Fig. 2. The solutes are ordered from the strongest binding (P) to the weakest (Cr). It is evident that all solutes, with the exception of Cr, present a strong binding character with vacancies, which confirms the findings of previous DFT calculations [35]. As already argued in the same reference, the binding character for the transition metals in the 3d group is most likely caused by a strong magnetic coupling. For the oversized impurities (Cu, Mn, Ni), the strong interaction arises also because of strain relief in the matrix.

The general agreement with previous computations and experimental data is quite satisfactory. A minor difference

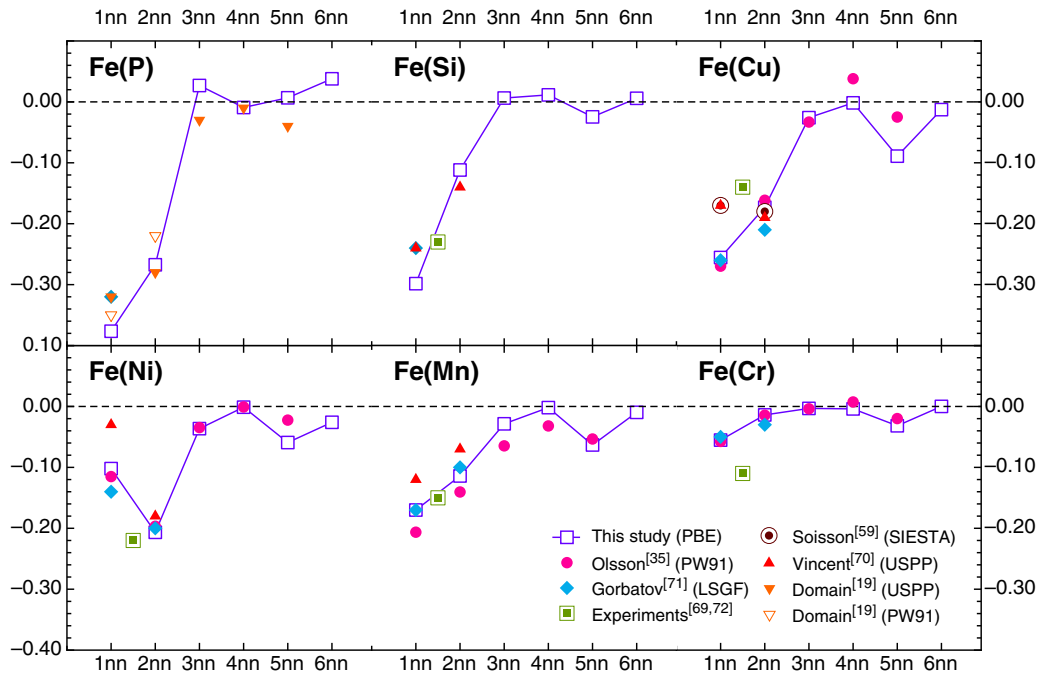


FIG. 2. (Color online) *Ab initio* solute-vacancy binding energies (in eV) obtained by supercell relaxation, compared with previous calculations [19,35,59,70,71] and experiments [69,72]. Negative energies stand for attractive interactions.

is related to Cu, for which previous computations performed with the ultrasoft pseudopotential (USPP) yielded a stronger interaction at 2nn than 1nn. Concerning the experimental measurements, the 1nn and 2nn can not be distinguished in bcc crystals, due to their similar relative distance. Furthermore, the Cr experimental value that is shown in Fig. 2 represents the upper bound of the interaction energy [69] and is therefore in agreement with this work's calculations.

The interaction is strong up to the 2nn distance, beyond which it abruptly drops to zero. This is due to the relatively short distance between second-nearest neighbors in bcc crystals, with respect, for instance, to that in the fcc structure. The anomalous behavior shown by Ni, namely, the stronger 2nn interaction, was also observed for cobalt [35]. The reason is to be investigated by a more in-depth analysis of the magnetic coupling that is beyond the scope of this paper. In general, the binding character of the solute-vacancy interaction is a hint that dragging by vacancies is likely to occur, although it is not possible to state *a priori* its strength and temperature dependence.

In some cases (Cu, Mn, Ni), there exists a weak attraction between solute and vacancy at the 5nn distance. This residual interaction is caused by elastic interactions among the atoms lying on the close-packed $\langle 111 \rangle$ direction, as the next atom in line (10nn) is also characterized by a slightly higher binding energy than the 9nn or 11nn (not shown in the graph). In order to investigate the effect of this non-negligible interaction, the thermodynamic model for the computation of the transport coefficients was therefore extended to the 5nn. Models neglecting the 2nn interaction are likely to yield unreliable results, given the strong 2nn interaction in most of the studied alloys.

The following step is the calculation of the migration barriers for the network of $12 + 2$ jump frequencies (for each

impurity) described in Fig. 1. Table II shows the energy barriers obtained via NEB calculations. They are also compared to previous computations performed with different DFT parameters [19,22,50,51] and with DFT calculations performed with the SIESTA code [59]. In addition, the same migration barriers are represented in Fig. 3 as function of the solute-vacancy distance. As expected, the migration barriers approach the background value ω_0 as the solute-vacancy distance increases, since the interaction fades out with distance.

Generally speaking, the attractive binding energy leads to an increment of the dissociative migration barriers and to a decrement of the associative counterparts. The effect is more prominent when the binding energy is stronger (P, Si), whereas all values are close to ω_0 in the Cr case. A higher solute-vacancy association rate than dissociation means in physical terms that the probability for a vacancy to abandon the interaction area around the solute is small. Nevertheless, at least another ω_{ij} frequency is necessary for the vacancy to turn around the solute and yield a net displacement, as observed in the *AB* model alloy [31]. Therefore, the calculation of transport coefficients is unavoidable if one is to investigate the possibility of vacancy drag.

In most cases, the agreement with previous calculations is good. The only remarkable exception is represented by the ω_2 frequency for Mn. The much higher value of 1.03 eV previously reported by Vincent *et al.* [51] and applied to their KMC model was affected by the problematic convergence of the Mn magnetic state, as the same authors mentioned. It can be observed that all here-studied impurities are characterized by a higher migration frequency, if one assumes the attempt frequency ν_2^* to be comparable to ν_0^* . In this regards, the result of Ni is in partial contradiction with the findings of Choudhury *et al.* [22], who observed a higher solute migration barrier than that of pure iron. This inconsistency can be related to

TABLE II. *Ab initio* migration barriers (in eV) computed in this study and comparison with previous DFT calculations (in square brackets), according to the jump frequency nomenclature described in Fig. 1.

	P	Si	Cu	Ni	Mn	Cr
ω_0				0.70 [0.67] ^a , [0.68] ^b , [0.65] ^c		
ω_2	0.40 [0.34] ^d , [0.31] ^e	0.51 [0.44] ^f	0.51 [0.59] ^b , [0.56] ^f	0.63 [0.68] ^a , [0.70] ^f	0.42 [1.03] ^f	0.53 [0.58] ^a , [0.62] ^g
ω_{12}, ω_{21}	0.68 [0.60] ^d	0.57 [0.56] ^d	0.74 [0.65] ^f	0.55 [0.64] ^b , [0.64] ^b	0.72 [0.60] ^f	0.64 [0.55] ^a , [0.69] ^a
ω_{13}, ω_{31}	0.68 [0.92] ^d	0.58 [0.59] ^d	0.89 [0.84] ^f	0.58 [0.70] ^b , [0.67] ^f	0.74 [0.70] ^a , [0.69] ^f	0.51 [0.56] ^b , [0.70] ^a
ω_{15}, ω_{51}	0.86 [0.68] ^d	0.47 [0.34] ^d	0.82 [0.65] ^f	0.55 [0.63] ^b , [0.62] ^f	0.67 [0.53] ^b , [0.63] ^f	0.50 [0.62] ^a , [0.59] ^a
ω_{24}, ω_{42}	0.74 [0.68] ^d	0.48 [0.37] ^d	0.71 [0.74] ^b	0.58 [0.55] ^b	0.75 [0.74] ^b	0.57 [0.55] ^b
ω_{34}, ω_{43}	0.66	0.69	0.68	0.67	0.69	0.67
ω_{37}, ω_{73}	0.69	0.70	0.69	0.69	0.69	0.68
ω_{45}, ω_{54}	0.66	0.65	0.67	0.70	0.68	0.77
ω_{46}, ω_{64}	0.68	0.63	0.65	0.66	0.67	0.68
ω_{48}, ω_{84}	0.69	0.67	0.69	0.69	0.70	0.70
ω_{49}, ω_{94}	0.69	0.71	0.69	0.72	0.70	0.70
ω_{57}, ω_{75}	0.69	0.68	0.68	0.65	0.71	0.63
$\omega_{510}, \omega_{105}$	0.67	0.66	0.68	0.65	0.70	0.64

^aReference [22], PAW-PBE.

^bReference [59], SIESTA.

^cReference [58], PAW-PW91.

^dReference [19], USPP.

^eReference [16], interatomic potential.

^fReference [51], PAW-PW91.

^gReference [50], PAW-PBE.

their smaller supercell size (54 atoms). It is worth noticing that a higher solute-vacancy exchange frequency does not necessarily entail a faster impurity diffusion, as the $D_{\text{sol}}/D_{\text{Fe}}$ ratio depends on the drag tendency as well.

III. COMPUTATION OF THE TRANSPORT COEFFICIENTS

A. Manipulation of jump frequencies

For practical reasons, the long-ranged SVI must be cut off at a finite distance in order to limit the amount of equations of the analytical mean field model. In a dilute alloy, this entails the distinction between an interacting area around the solute atom and the background. The former is represented by the ensemble of atoms located at a distance from the solute within the chosen interaction range. The solute-vacancy pair is regarded as associated (i.e., there exists a non-null SVI) when the vacancy is inside the interaction area, or dissociated otherwise.

Once the cutoff is introduced, the binding energy beyond this distance must be set to null ($E_{\infty}^b = 0$). This implies a manipulation of the DFT-computed jump frequencies, in order to fulfill the detailed balance requirements [73]. According to the detailed balance principle, each elementary transition must be balanced by its reverse process in thermodynamic

equilibrium conditions. In general, this means that the forward and backward transitions between two states i and j occur at the same rate:

$$\omega_{ij}^{(0)} p_i^{(0)} = \omega_{ji}^{(0)} p_j^{(0)}, \quad (4)$$

where the probability p of each state depends upon the energy of the state through the classic Boltzmann factor $\exp(-E/k_B T)$. In the specific case of atom-vacancy exchange, all couples of forward-backward jumps (ω_{ij}, ω_{ji}) are bound to this condition. Since the energy of the initial and final configurations can be expressed in terms of binding energy difference

$$\frac{\omega_{ij}}{\omega_{ji}} = \exp\left(-\frac{E_j^b - E_i^b}{k_B T}\right), \quad (5)$$

it follows that $E_i^b - E_j^b = E_j^{\text{mig}} - E_i^{\text{mig}}$, if the attempt frequencies are assumed to be the same for all jumps.

The practical consequence on the set of DFT-computed migration barriers is that any sequence of jumps starting from the same i nn position and leading to a dissociation must occur at the same rate:

$$\frac{\omega_{\infty i}}{\omega_{i\infty}} = \frac{\omega_{\infty j}}{\omega_{j\infty}} \frac{\omega_{ji}}{\omega_{ij}} = \frac{\omega_{\infty l}}{\omega_{l\infty}} \frac{\omega_{lk}}{\omega_{kl}} \frac{\omega_{ki}}{\omega_{ik}} = \dots \quad (i, j, k, l \leq \hat{R}), \quad (6)$$

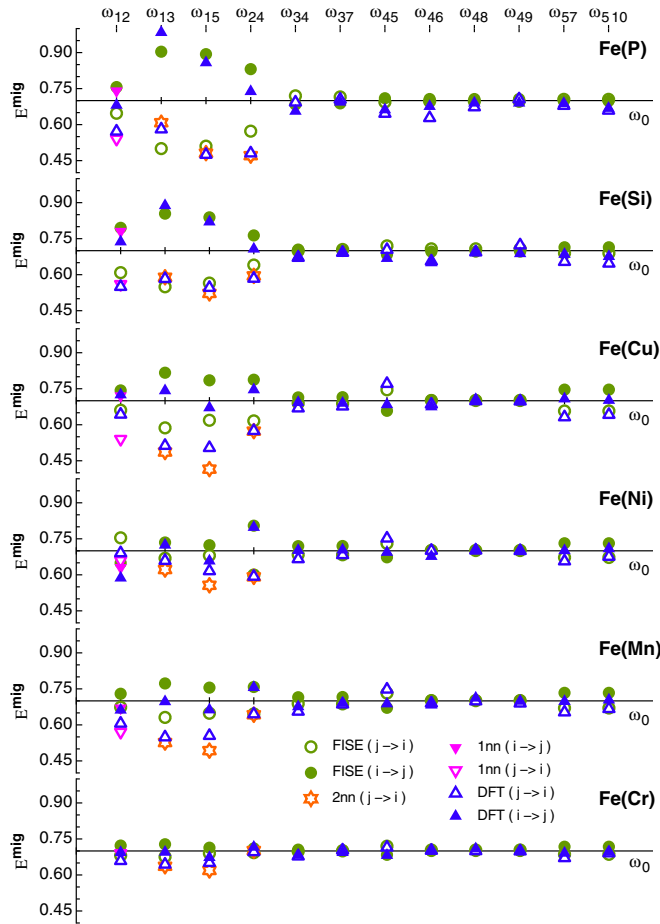


FIG. 3. (Color online) Migration barriers (in eV) for Fe-V jumps of type ω_{ij} , where i is the initial nn position of the vacancy with respect to the solute, and j the distance after the jump. Backward jumps (from configuration j to i) are shown with blank symbols. DFT-calculated values are compared to those obtained with the final-initial-state energy (FISE) approach. The modified barriers for the 1nn and 2nn sets are also shown.

where the jump chain can consist of several jumps ($i \rightarrow \infty$, $i \rightarrow j \rightarrow \infty$, $i \rightarrow k \rightarrow l \rightarrow \infty$, and so on). The ∞ symbol marks any nn distance beyond the interaction zone.

The set of DFT migration barriers is therefore modified in order to comply to the requirement of null binding energy beyond \hat{R} . The most straightforward way is to keep the *ab initio* computed saddle-point energy constant and let the associative frequencies of type $\omega_{\infty i}$ ($i \leq \hat{R}$) change, so that $E_{\infty i}^{\text{mig}}$ is decreased exactly by the binding energy that is to be neglected. For instance, setting $E_3^b = 0$ makes the activation energy of the jump ω_{31} decrease by the DFT value of E_3^b . It is clear that this approach has little effect on the interaction physics as long as the binding energies to be neglected are small. Given the non-negligible values of E_5^b , cutting the thermodynamic range to the 2nn would lead to a considerable modification of the backward frequencies. For this reason, the cutoff range was set on the 5nn distance, resulting in the jump frequency network shown in Fig. 1.

Several range cutoffs were explored, leading to three distinct frequency sets, whose performances are compared in terms of drag predictability.

(a) 5nn set: All DFT jump frequencies are introduced. The backward frequencies are modified according to the procedure described above, so that the binding energies beyond the 5nn are null.

(b) 2nn set: Only frequencies related to the 1nn and 2nn are considered ($\omega_{12}, \omega_{13}, \omega_{15}, \omega_{24}$). The backward frequencies are modified in the same fashion in order to set the binding energies beyond 2nn to zero. By comparing the 2nn set to the 5nn set, the influence of E_5^b in terms of vacancy drag can be determined. This model represents a considerable advancement with respect to the most advanced existing 2nn models [25,26], as the latter assume the backward jumps ω_{31} , ω_{51} , and ω_{42} to occur at the background frequency ω_0 . As a consequence, the associative tendency of the vacancy-solute pair is seriously underestimated.

(c) 1nn set: The thermodynamic SVI is truncated to the first nn sites. The frequencies involved are ω_{12}, ω_{13} , and ω_{15} . In this case, a unique $\omega_{1\infty}$ frequency is calculated as $7\omega_{1\infty} = 3\omega_{12} + 3\omega_{13} + \omega_{15}$ (and analogously for $\omega_{\infty 1}$). Many analytical models available in the literature (for instance, the 4-frequency model in [24]) are limited to the 1nn; it is therefore interesting to analyze the accuracy of such a simple model in terms of solute diffusion by vacancies.

In addition to the 1nn, 2nn, and 5nn sets, a further set was derived from the DFT database by using the final-initial-state energy approximation. FISE is an alternative model that is very often employed to predict migration barriers, when DFT calculations are not available for all atomic configurations. It was used in the past under different names [31,74,75], as it is the most commonly employed model in atomistic kinetic Monte Carlo (AKMC) simulations.

The amount of migration barriers computed in this work makes it possible to assess the reliability of the FISE approach and the consequences in terms of vacancy-drag predictability. In this model, the migration barrier E_{ij}^{mig} between configurations i and j depends on a reference migration barrier and the energy difference between the final and initial states:

$$E_{ij}^{\text{mig}} = E_0^{\text{mig}} + \frac{E_j - E_i}{2}. \quad (7)$$

E_0^{mig} usually depends on the jumping species: ω_0 for the host atom and ω_2 for the solute. The model always ensures fulfillment of the detailed balance condition. The energy of the end states can be computed through *ab initio* relaxations (this work) or many available broken bond models, whereas the reference migration barrier E_0^{mig} can be obtained through several methods (for an extensive review of such methods, see [76]). In the case of concentrated alloys, more advanced models allow for the local chemical environment around the jumping atom at the saddle point to be taken into account (see for instance [50]).

The main issue related to the use of this simple model is that in reality the energy of the arriving state is not known *a priori*. In order to assess its reliability in terms of jump frequency prediction and diffusion modeling, a set of jump frequencies is computed based on the DFT initial- and final-state energies obtained in this work. E_0^{mig} is given by the unperturbed Fe-V

migration barrier (0.70 eV). Applying Eq. (7) entails that all forward-backward migration barriers are shifted so that they are symmetric with respect to ω_0 .

The four sets of jump frequencies are shown in Fig. 3 for each impurity. It is made a distinction between forward (full symbols) and backward (blank symbols) jumps, in order to emphasize the lower probability for dissociation jumps. It can be observed that the FISE migration barriers based on DFT-computed end-state energies are in most cases in disagreement with the NEB values inside the interaction shell, whereas they agree quite well beyond the ω_{24} jump type.

B. Finite-temperature magnetic model

In order to allow for a comparison with diffusion experiments, which are usually performed at relatively high temperatures, magnetic disordering must be taken into account. It is here assumed that the magnetic transition to the paramagnetic state leads to a progressive reduction of the self-diffusion activation energy $Q_0^F = E_v^{\text{form}} + E_v^{\text{mig}}$. The reduction is proportional to the magnetic excess enthalpy H^{mag} [77]:

$$Q(T) = Q_0^F - \alpha H(T). \quad (8)$$

The normalized coefficient $H(T) = 1 - H^{\text{mag}}(T)/H^{\text{mag}}(0)$ is defined so that $H = 0$ at 0 K and $H = 1$ in a perfectly disordered state. The model yielding the excess enthalpy H^{mag} is described in [78]. Short-range ordering is represented as residual magnetization above the Curie temperature. From this definition it follows that $\alpha = Q_0^F - Q_0^P$, where Q_0^P is the activation energy in fully paramagnetic state. Such a value can be inferred from experiments or computed with first-principles methods. In this work, $Q_0^P = 2.26$ eV is taken from the *ab initio* calculations by Chang *et al.* [77]. It is worth noticing that this magnetic effect appears as the same multiplicative factor in all Onsager coefficients. It therefore does not affect the drag coefficient given by the ratio L_{BV}/L_{BB} . Although this magnetic model was devised only for self-diffusion in pure iron and fitted to self-diffusion experiments, it is assumed that the presence of one solute atom has a negligible effect on the magnetic transition.

C. SCMF model

The sets of jump frequencies are used as input parameters for the calculation of the transport coefficients, in the framework of the self-consistent mean field (SCMF) theory. The interested reader can find in [27,28,31] further details about the SCMF model and its solution.

One of the main features of the SCMF method is the distinction between thermodynamic and kinetic interatomic interactions. The former determine the probability of a certain crystal configuration to occur in thermodynamic equilibrium conditions, and correspond to the binding energies shown in Fig. 2. As already discussed, a range cutoff has to be imposed in practice and is differently chosen in the aforementioned frequency sets.

The kinetic interactions are fictitious interactions that are introduced in the Hamiltonian of the system in order to describe the probability perturbation of a certain configura-

tion in near-equilibrium conditions. At equilibrium they are null by definition. The amount of introduced interactions depends on a cutoff range that is analogous to the previous cutoff, but is now referred to the kinetic interactions. The kinetic interaction shell must necessarily include the thermodynamic shell in order to properly describe the system thermodynamically.

The choice of the kinetic shell is strictly related to the vacancy migration paths. The migration paths that are outside the kinetic interaction shell are in fact not considered in the mean field model. On the other hand, the ability of a vacancy to drag a solute atom depends on its possibility to turn around the solute between two consecutive solute-vacancy exchanges. The vacancy may follow different paths. It was shown in [31] that, in bcc crystals, paths beyond the 1nn and 2nn positions are also important for such phenomenon (for instance, the 2nn-4nn-3nn-4nn path). It is therefore evident that any kinetic model being limited to the 1nn or 2nn would miss out some of the possible drag patterns.

In that work, the extent of the interaction shell reached the 3nn of 3nn sites (referred to as the 3nn3nn model). Since in this work the thermodynamic interactions are cut off at the 5nn distance, the kinetic model is extended to the 5nn(1nn)^k sites. The truncation at the *k*th shell implies that the calculation is exact for sequences of maximum *k* jumps [31]. In another work [32] it was shown that in the case of a 3nn(1nn)^k approximation in fcc crystals, the error decreases exponentially with *k*. The result is confirmed in this work for the 5nn(1nn)^k approximation in bcc crystals by performing convergence tests. A truncation to *k* = 2 leads to a relative error of less than 0.01% in the computation of the L_{AB} coefficient (which is the most sensitive one) with respect to *k* = 3. For this reason, the approximation adopted in this work for the 5nn frequency sets is 5nn(1nn)², hence 1nn of 1nn of (1nn, 2nn, 3nn, 4nn, 5nn). Conversely, the kinetic models for the 2nn and 1nn frequency sets are, respectively, 3nn3nn and 1nn1nn, for the sake of consistency with the thermodynamic assumptions.

As a benchmark for the obtained transport coefficients, AKMC simulations were performed, limitedly to a 2nn(1nn)^k kinetic model, by using the LAKIMOCA code [57]. In the AKMC framework, the phenomenological coefficients are obtained with the Kubo-Green formula [23]

$$L_{ij} = \frac{\Delta \vec{R}_i \cdot \Delta \vec{R}_j}{6Vt}, \quad (9)$$

where $\Delta \vec{R}_i$ is the total displacement of all atoms of species *i* in time *t* and *V* is the system volume. With such a definition, the Onsager coefficients are expressed in (ms)⁻¹ units.

The simulation box contains 432 sites disposed in a 6 × 6 × 6 bcc cell, with one solute atom and one vacancy. As a single solute atom is present in the box, no solute-solute interaction takes place and the dilute limit behavior is simulated even though the nominal concentration of 0.23% might seem not representative of a dilute alloy. Convergence is reached after 3 × 10¹⁰ atomic jumps and the atomic paths are sampled every 5000 steps, hence after approximately 10 jumps in average for each atom.

D. Applications of the Onsager matrix

An accurate computation of the Onsager matrix allows for the investigation of several different properties of the system that rely on the coupling between different diffusion fluxes. In this work, the L_{ij} 's are employed for the determination of the vacancy drag factor L_{BV}/L_{BB} , the solute tracer diffusion coefficients D_B^* , and the RIS tendency.

In a dilute binary alloy, a solute atom can diffuse in the opposite direction than that of vacancies (inverse Kirkendall), or in the same direction (vacancy drag). Solute drag by vacancies is a common phenomenon that can occur, under certain conditions, in several types of alloy [31]. Contrary to a common misconception, the conventional thermodynamic SVI is not the only ingredient determining the possibility of vacancy drag. For instance, it is shown in [31] that in alloys with no thermodynamic interactions, drag can still occur if the set of jump frequencies in the interaction zone allows the vacancy to complete a path around the solute. It depends in fact in an intricate manner on the several jump frequencies involved inside and across the interaction zone. For such a reason, a prediction of solute drag exclusively based on interaction energies is likely to fail.

In this work, solute drag was investigated following the approach of Anthony [79], i.e., by calculating the ratio L_{BV}/L_{BB} , where $L_{BV} = -(L_{AB} + L_{BB})$. In this framework, the ratio is positive when drag occurs, or negative otherwise.

Given the impossibility of measuring the full Onsager matrix by experiments, a way to benchmark the model is to compare with measured solute tracer diffusion coefficients D_B^* , which can be directly derived from the L_{BB} coefficient. In a dilute alloy, the solute tracer and intrinsic diffusion coefficients coincide. Hence, a unique diffusion coefficient can be defined [73]:

$$D_B^* = D_B = \frac{L_{BB}}{nC_B}, \quad (10)$$

where n is the number of atoms per atomic volume and C_B the solute concentration.

The coefficients of the Onsager matrix can also be used to derive RIS tendencies in multicomponent alloys. In the particular case of dilute alloys, RIS phenomena in dilute alloys are easier to describe thanks to the reduced amount of jump frequencies involved and the clear definition of the solute-vacancy interaction. Consequently, the derivation of the L_{ij} coefficients through the SCMF method guarantees a high degree of accuracy in the RIS prediction.

A continuous model relying on the knowledge of the Onsager coefficients [4,80] is here applied. When defect and chemical fluxes are in dynamic equilibrium, the following relationship between chemical and defect concentration gradients near defect sinks can be derived:

$$\frac{\nabla C_B}{\nabla C_V} = \frac{C_A C_B d_{AV} d_{AI}}{(C_A d_{AI} D_B + C_B d_{BI} D_A)} \left(\frac{d_{BV}}{d_{AV}} - \frac{d_{BI}}{d_{AI}} \right), \quad (11)$$

where C_i represents the equilibrium concentration of species (or defect) i , D_i the intrinsic diffusion coefficient, and d_i the partial diffusion coefficients that depend on the L_{ij} :

$$d_{AV} = \frac{L_{AA}^V + L_{AB}^V}{C_A C_V}, \quad d_{BV} = \frac{L_{AB}^V + L_{BB}^V}{C_B C_V}. \quad (12)$$

Similar partial diffusion coefficients are defined for interstitial mediated diffusion [a detailed description of the terms in Eq. (11) can be found in [4], and a misprint in the same equation has been corrected here]. Since this work is limited to vacancy diffusion, a precise evaluation of the ratio $\nabla C_B/\nabla C_V$ is not achievable. However, the RIS trends solely due to vacancies can be qualitatively inferred by the ratio d_{BV}/d_{AV} , as long as the analogous ratio d_{BI}/d_{AI} is set equal to 1.

As far as vacancy diffusion is concerned, there exists a clear correlation between diffusion mechanism and RIS tendency. If vacancy drag occurs, d_{BV} is negative (while d_{AV} is always positive): only solute enrichment at PD sinks is possible, as the solute atoms follow the vacancies migrating towards the sinks. In the case of inverse Kirkendall mechanism, the partial diffusion coefficient ratio is always positive, but enrichment of B can still occur if $d_{BV} < d_{AV}$, i.e., if the solute moves slower than the matrix atoms. In this specific case, the L_{AB} coefficient can be negative but is always greater than -1 . Finally, solute depletion at sinks occurs when $d_{BV} > d_{AV}$.

1. Dilute limit and vacancy concentration

The transport coefficients are derived in the dilute limit ($C_B \rightarrow 0$). $L_{AB} = l_{AB} C_B$ and $L_{BB} = l_{BB} C_B$ are directly proportional to C_B , as second- and higher-order terms in C_B are neglected. Concerning the L_{AA} coefficient, there is also a zero-order term: $L_{AA} = L_{AA}^0 - l_{AA} C_B$ (where l_{AA} expresses the effect of the A - B correlation). Therefore in the dilute limit, the drag factor L_{BV}/L_{BB} , the solute tracer coefficient D_B^* and the partial coefficient d_{BV} are independent from the solute concentration. As well, a first-order expansion of d_{BV} implies that the ratio d_{BV}/d_{AV} is properly defined at zero order only: $d_{BV}/d_{AV} = (l_{AB} + l_{BB})/L_{AA}^0$.

The vacancy concentration is assumed to be that of the thermodynamic equilibrium (i.e., nonirradiated) conditions

$$C_V^{eq} = \exp\left(-\frac{H_V^f}{k_B T}\right) \exp\left(\frac{S_V^f}{k_B}\right). \quad (13)$$

The effect of irradiation would be to increase the number of vacancies of the system, and increase at the same extent the transport coefficients, which are proportional to C_V . The drag and RIS tendencies given by the partial diffusion coefficient ratio would not change (although the RIS effect would increase in magnitude). As for the comparison to experimental diffusion coefficients, they are always performed in nonirradiated conditions.

E. Results and discussion

1. Onsager coefficients and vacancy drag

The obtained Onsager coefficients are shown in Fig. 4 (exclusively for the 5nn model), where the solute concentration C_B is assumed to be 1% and the equilibrium vacancy concentration is given by Eq. (13). The magnetic correction is not applied. It is worth observing that the L_{AB} coefficient deviates from the Arrhenius behavior because of the strong correlations between vacancy and solute flux. Therefore, extrapolation from the high-temperature regime to the low-temperature one would lead to an error estimable up to two orders of magnitude.

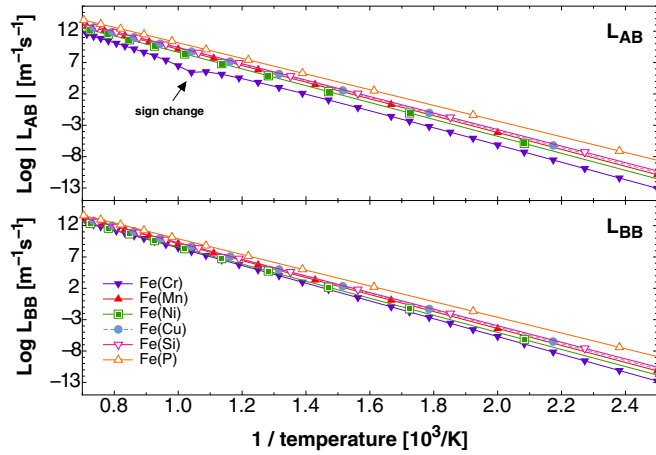


FIG. 4. (Color online) Off-diagonal (L_{AB}) and solute (L_{BB}) Onsager coefficients, obtained with the SCMF method in the 5nn model for each binary alloy and a solute concentration of 1%. L_{AB} is negative for all solutes except Cr, in which case $L_{AB} > 0$ for $T > 970$ K.

In the dilute limit ($C_B \rightarrow 0$), L_{AA} approaches L_{AA}^0 and is independent from the solute species, as it represents the uncorrelated part of the Fe-Fe transport coefficient. L_{AA}^0 (not shown in Fig. 4) is characterized by a perfect Arrhenius temperature dependence, where the prefactor is 2.6×10^{24} (ms) $^{-1}$ and the slope is $Q = 1.25$ eV. L_{BB} is always positive as it should be according to the second law of thermodynamics, and is directly related to the solute diffusion coefficient. L_{AB} determines the sign of the wind factor, hence the dragging behavior. It can be observed that in all cases except Cr the L_{AB} coefficients are negative. This does not necessarily entail solute drag: if $L_{AB} > -1$, species A and B move in the same direction under a gradient of vacancy chemical potential.

The magnitude of the L_{AB} coefficient is larger in the systems where the SVI are stronger. Only when the critical condition $L_{AB} = -L_{BB}$ (or equivalently $L_{BV} = 0$) is reached, solute drag arises. For this reason, the ratio L_{BV}/L_{BB} (wind factor) is shown in Fig. 5 as function of temperature. In this plot, the different sets of frequencies are shown, as well as the Lakimoca results and previous calculations of the wind factor for the Fe(Cr) [22], Fe(Ni) [22], and Fe(Cu) [20,81] alloys.

There exists a minor difference between the 2nn and 5nn models, which implies that in these alloys it is completely acceptable to limit the interaction shell to the 2nn, even with the modifications to the backward frequencies imposed by the detailed balance condition. The largest discrepancy is in the Fe(Cu) system, where the strongest 5nn interaction is present: $\Delta(L_{BV}/L_{BB}) < 0.2$. Furthermore, the results of the 2nn model are perfectly reproduced by the KMC simulations, which confirms the reliability of the SCMF method. In the case of Fe(Cu), vacancy drag was already predicted by a KMC study based on *ab initio* migration barriers [20], and the results match perfectly with the 2nn model of this study. It is worthwhile noticing that the available 2nn multifrequency models before SCMF [25,26] are not suitable for flux coupling analysis because they underestimate the associative probability and yield wrong wind factors. This was clear in [37], where the application of such an approximated model was not conclusive for the Fe(Cu) and Fe(Mn) systems. It is also important to

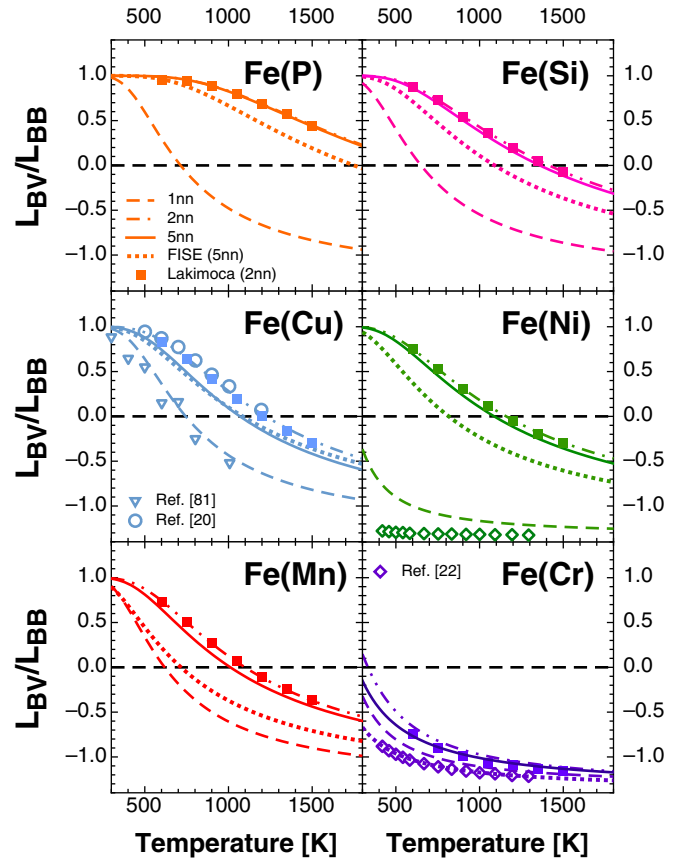


FIG. 5. (Color online) Solute-drag factors $L_{BV}/L_{BB} = -(1 + L_{AB}/L_{BB})$ obtained with the SCMF method (lines) and with Monte Carlo simulations (dots) for each binary alloy, with several jump frequency sets (1nn, 2nn, 5nn, and FISE). Drag occurs for values greater than 0. The 2nn-model curve overlaps with the 5nn-model one for Fe(P). Results of previous works are also shown for Fe(Cr) [22], Fe(Ni) [22], and Fe(Cu) [20,81].

remember from [31] that the 3nn interaction gives a quite considerable contribution, so it should not be neglected *a priori*. Nevertheless, in this work the 3nn binding energy is always quite small; moreover, many of the transition-metal impurities in iron do not have a strong 3nn interaction, therefore, a complete 2nn model is suitable for solute-drag prediction.

On the other hand, the 1nn model (dashed lines) is clearly unsuitable. The drag tendency is considerably underestimated, which marks the importance of the 2nn SVI in bcc crystals. The 1nn model is often used for modeling impurity diffusion because of its simplicity, but it evidently leads to wrong conclusions. For instance, in [22] it was deduced that no drag would occur in Fe(Ni). This conclusion is wrong because of the overly approximated model. Furthermore, solute drag in dilute Fe(Cu) was predicted in a Monte Carlo study based on a broken bond model developed for both Fe- and Cu-rich phases to simulate Cu precipitation, but the predicted drag tendency was weaker [81].

Finally, it can be observed that in most cases the drag tendency is surprisingly well reproduced by the set of frequencies calculated in the FISE approximation, in spite of

TABLE III. 1nn and 2nn binding energies (E_{Xnn}^b), transition temperature between drag and nondrag regime (T_{crit}) and wind factor at RPV operational temperature [$L_{BV}/L_{BB}(573\text{ K})$] for the different alloys. The solute atoms are ordered according to T_{crit} of the 2nn model.

	P	Si	Cu	Ni	Mn	Cr
Binding energies [eV]						
E_{1nn}^b	-0.38	-0.30	-0.26	-0.10	-0.17	-0.06
E_{2nn}^b	-0.27	-0.11	-0.17	-0.21	-0.11	-0.01
Model: 5nn						
T_{crit} [K]	$\approx 2100^a$	1360	1068	1087	1011	262
$L_{BV}/L_{BB}(573\text{ K})$	0.99	0.89	0.78	0.74	0.70	-0.74
Model: 2nn						
T_{crit} [K]	$\approx 2130^a$	1414	1223	1159	1099	333
$L_{BV}/L_{BB}(573\text{ K})$	0.99	0.91	0.88	0.79	0.78	-0.62
Model: 1nn						
T_{crit} [K]	714	650	744	$\approx 225^a$	619	$\approx 220^a$
$L_{BV}/L_{BB}(573\text{ K})$	0.38	0.19	0.44	-0.98	0.12	-0.89
Model: 5nn (with FISE approximation)						
T_{crit} [K]	1750	1090	1085	816	716	$\approx 10^a$
$L_{BV}/L_{BB}(573\text{ K})$	0.97	0.75	0.74	0.43	0.28	-1.02

^aLinearly extrapolated data.

the disagreement with the DFT-computed migration barriers inside the interaction shell. Exceptions are given by the Fe(Mn) and Fe(Cr) alloys, for which the FISE predictions are more inaccurate. At any rate, KMC simulations based on FISE seem to be suitable for modeling vacancy-solute behavior, provided that the cohesive model is reliable. FISE may therefore represent a good choice for calculations in multicomponent alloys, where the amount of jump frequencies is very large and cannot be fully computed with *ab initio* methods.

In general, it stands out that vacancy drag is a common phenomenon occurring in all alloys and favored by low temperatures. This work shows that the conclusions of [31] for a general *AB* alloy apply also to the real dilute alloys here studied. A strong binding SVI (as for instance in FeP) has the effect of shifting the curve towards the low-temperature side. The limit for all curves at high temperatures corresponds to the case of an ideal alloy with no interactions; from Manning's theory [15], the theoretical L_{BV}/L_{VV} ratio is -1.388 , which is approached at lower temperatures in the 1nn model. The SCMF theory in the 5nn(1nn)² kinetic model yields a value of -1.371 , in slightly better agreement than the 3nn3nn model [31] since more paths around the solute atom are available for the vacancy.

There is a clear trend between binding SVI and drag, as visible in Table III. The solutes are ordered from the strongest binding (P) to the weakest (Cr). One can see in the 2nn and 5nn models that the critical temperature (under which drag occurs) decreases as the binding tendency becomes weaker. Longer-ranged interactions, even though not remarkably visible in Fig. 5, are in some cases unexpectedly important for the critical temperature. For instance, in Fe(Cu), where the E_5^b is the largest, the drag tendency is weakened because of the higher frequency of the dissociative jump ω_{45} and T_{crit} is hence 15% lower. The wind factor at 573 K, which is approximately the operational temperature of RPV steels, follows the same trend. In every system, the 1-2 orbital is activated for solute drag and

$|E_2^b| < |E_1^b|$. In this specific case, $|E_1^b|$ determines T_{crit} and the amplitude of the drag effect. Conversely, the Fe(Ni) system is exceptional since $|E_2^b| > |E_1^b|$ and consequently T_{crit} and the wind factor are not determined by $|E_1^b|$ only. Evidently, the 2nn SVI is fundamental for a correct description of this alloy. On the other hand, in the 1nn model there is no clear relationship between binding tendency and critical temperature or wind factor, which clearly shows the unreliability of that model. As for the FISE-computed set of frequencies, the general trend is respected but the drag effect is slightly underestimated.

In conclusion, vacancy drag is an expectable phenomenon at RPV operational temperature. Even though vacancy mobility is rather small, radiation-enhanced and induced phenomena are likely to occur because of the strong drag tendency. Such tendency progressively fades out at temperatures that are close to the Curie temperature in pure iron (1043 K), therefore closer to the temperatures at which diffusion experiments are usually performed. At any rate, it is undoubtedly an important diffusion mechanism at RPV temperature, in competition with possible interstitial-mediated diffusion.

2. Diffusion coefficients and RIS

The comparison with experimental solute tracer diffusion coefficients allows for a validation of the model. As shown by Eq. (10), D_B is directly proportional to the L_{BB} coefficient. The latter is directly related to the solute-vacancy exchange frequency ω_2 , however, it is also affected by correlation effects. It can be observed in Fig. 4, for instance, that Si and Cu are characterized by a higher diffusion coefficient than Mn, although their migration barrier for the solute-vacancy exchange is considerably higher (0.51 eV versus 0.42 eV). Vacancy drag has therefore the effect of enhancing solute diffusion. It is also important mentioning that in the 1nn model the L_{BB} coefficient (and therefore the D_B coefficient) is strongly underestimated, which is consistent with the lack

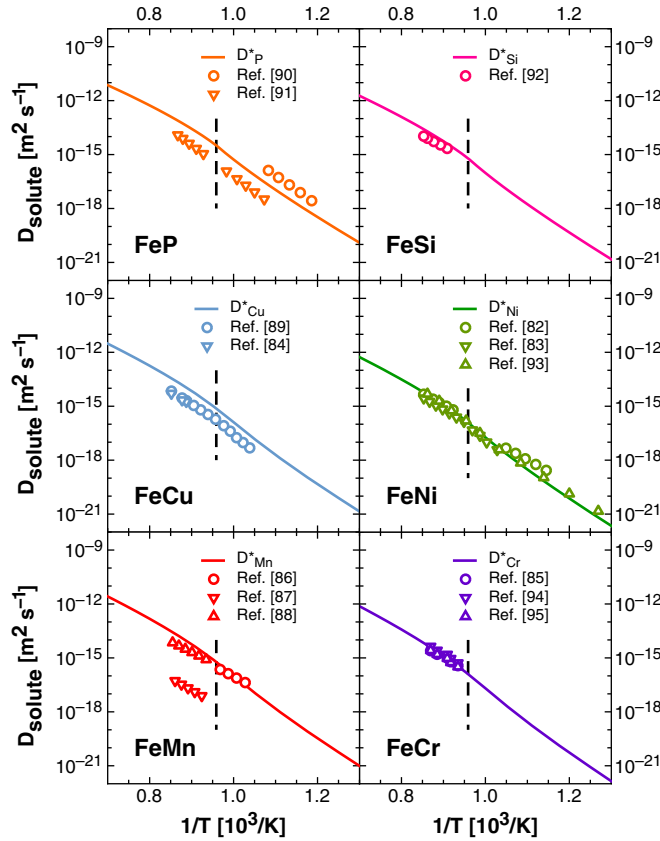


FIG. 6. (Color online) Comparison of solute tracer diffusion coefficients computed with the SCMF method in the 5nn model with experiments [82–95]. The dashed line marks the magnetic order-disorder transition.

of drag predictive capability of this model. No substantial differences are observed between the 2nn and 5nn models.

The solute tracer diffusion coefficients D_B^* are shown in Fig. 6. In order to compare with experimental measurements, the effect of the magnetic transition is taken into account. It is worthwhile noticing that in nonirradiated diffusion experiments, the interstitial concentration is always very low compared to that of vacancies. In spite of the arbitrariness introduced by the attempt frequency and vacancy formation entropy that were taken from previous calculations, the activation energies are in quite good agreement, especially at low temperatures (Ni, P), at which the magnetic correction is small. The magnetic transition seems also to be well reproduced for Si, Cu, and Cr. The only remarkable disagreement is represented by the activation energy and magnetic transition of the D_{Mn}^* coefficient. The mismatch could depend on the complex magnetic behavior of Mn in Fe, which might not be well reproduced by the rudimentary model here applied that was developed for pure iron.

Given the overall agreement between calculated and experimental values, it can be concluded that in the dilute limit the presence of a solute atom does not invalidate the bulk-iron magnetic model, except possibly the case of Fe(Mn). A more refined model, such as [38], would yield visible effects on the drag tendency and the diffusion coefficient slopes only in nondilute alloys. It is also worth mentioning that the attempt

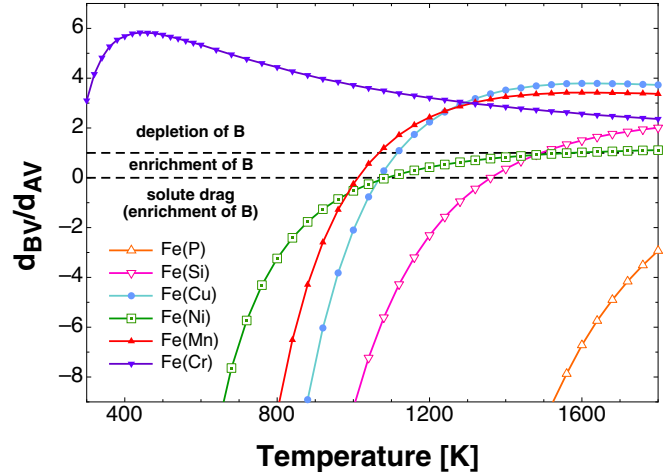


FIG. 7. (Color online) RIS tendencies [Eq. (12)] computed with the SCMF method in the 5nn model, for the Fe-X binary alloys. Solute drag (and subsequent enrichment at sinks) takes place when the ratio is negative; in the opposite case, enrichment holds as long as the ratio is smaller than 1.

frequency value in pure iron affects only the magnitude of the calculated diffusion coefficients. It would influence the drag tendency if it strongly depended on the relative distance between vacancy and solute atom, which is considered here to be unlikely. Even in this case, it was shown in [55] that the quantitative effect on T_{crit} would be limited.

The RIS tendencies can be discussed by looking at Fig. 7, where the partial diffusion coefficient ratio d_{BV}/d_{AV} is shown for all binary alloys in the 5nn model. Only the contribution from the vacancy mechanism is considered. The ratio of partial diffusion coefficients due to interstitial mechanism is set to 1 and the prefactor of Eq. (11) is assumed to be always positive.

With the exception of Cr, the solutes show a common trend. Vacancy drag obviously entails solute enrichment, as the vacancy concentration gradient is negative at sinks. Therefore, solute enrichment is expected at low temperatures and depletion at high temperatures, in agreement with the experimental trends observed in [3]. Furthermore, there exists a temperature interval in which the solute diffuses through the inverse Kirkendall mechanism, but since d_{BV} is smaller than d_{AV} the solvent atoms are moving away from the grain boundary and thus solute enhancement still occurs. An analogous trend is visible even in the Fe(Cr) system, but at such low temperatures it would never occur in reality.

In conclusion, as far as vacancy diffusion is concerned, all solutes except for Cr are expected to enrich at grain boundaries at RPV operational temperature since they move through vacancy drag. At a relatively high temperatures, Cu and Mn switch from enrichment to depletion, while Ni, P, and Si are always in the enrichment regime (the crossover for Si occurs above 1400 K). At any rate, the effective enrichment or depletion tendency has to be completed by adding the contribution given by interstitials and by the intrinsic diffusion coefficients appearing in Eq. (11).

IV. CONCLUSIONS

The main goal of this study was to perform a systematic and complete analysis of transport and diffusion properties of six different solute species (Cr, Cu, Mn, Ni, P, and Si) in bcc iron-based dilute alloys, with the aim of investigating flux coupling phenomena between solute species and monovacancies, in particular vacancy drag and RIS. A new multiscale approach is developed, where DFT-computed jump frequencies are combined with a self-consistent mean field method that allow for the longer-ranged solute-vacancy interactions to be correctly taken into consideration.

It was shown that vacancy drag is a widespread phenomenon occurring systematically in real binary alloys characterized by non-negligible solute-vacancy interactions, i.e., all Fe(X) alloys except Fe(Cr). This result, especially in the case of Fe(Mn) and Fe(Ni), is in contrast with previous computations [22] based on the available multifrequency models, which are unsuitable for vacancy drag prediction as they do not treat correctly the crucial 2nn SVI. The drag strength is affected by the complex combined effect of thermodynamic and kinetic interactions. As a general trend, vacancy drag is stronger in the low-temperature regime (<1000 K), including RPV operational temperature (≈ 573 K), while the inverse Kirkendall mechanism is dominant at high temperature. The crossover temperature lies always close to or above the Curie temperature and is higher in those alloys where the SVI are stronger, whereas in the Fe(Cr) alloy the crossover occurs at room temperature. The results are supported by a very good agreement with Monte Carlo simulations and experimental solute tracer diffusion coefficients. Concerning the RIS profiles, all model alloys with the exception of Fe(Cr) show the same trend: solute enrichment at low temperature and depletion at high temperature. This trend is in great agreement with the experiments performed in real multi-component ferritic-martensitic alloys [3]; however, synergetic

effects between solute atoms are here neglected. Depletion of Cr should occur if the only vacancy mechanism were in action. At any rate, the drag and RIS results are to be further investigated with the calculation of transport coefficients for interstitial-mediated diffusion, which is expected to be relevant in Fe(Cr), Fe(Mn), and Fe(P) [19,35].

Since the drag character is strong at RPV temperature, it is likely that solute drag contributes to the formation of embrittling solute-defect clusters in RPV steels, although other diffusion mechanisms may also play a key role (diffusion via single interstitials, small loops, or voids). The described model represents a powerful tool for predicting diffusion properties. It combines accurate first-principles calculations with the SCMF framework in order to obtain exact transport coefficients, especially in the low-temperature regime which is usually not accessible by experiments but is extremely important for many applications. The obtained sets of *ab initio* migration barriers represent as well a useful database for mean field modeling or AKMC simulations of ferritic steels.

ACKNOWLEDGMENTS

This work contributes to the Joint Programme on Nuclear Materials (JPNM) of the European Energy Research Alliance (EERA). It was accomplished thanks to the financial support from Vattenfall AB, Göran Gustafsson Stiftelse, and the European Commission, in the framework of the MatISSE project under Grant No. 604862. The high-performance computing resources were provided by the Swedish National Infrastructure for Computing (SNIC) and by the Swiss National Supercomputing Centre (CSCS) through the PRACE-2IP project (No. FP7 RI-283493). Furthermore, the authors acknowledge L. Malerba, F. Soisson, N. Sandberg, and Z. Chang for the valuable discussions.

-
- [1] F. Danoix, E. Bémont, P. Maugis, and D. Blavette, *Adv. Eng. Mater.* **8**, 1202 (2006).
 - [2] Z. Mao, C. K. Sudbrack, K. E. Yoon, G. Martin, and D. N. Seidman, *Nat. Mater.* **6**, 210 (2007).
 - [3] J. P. Wharry and G. S. Was, *J. Nucl. Mater.* **442**, 7 (2013).
 - [4] M. Nastar and F. Soisson, *Comprehensive Nuclear Materials* (Elsevier, New York, 2012), Chap. 1.18, pp. 471–496.
 - [5] M. K. Miller, K. A. Powers, R. K. Nanstad, and P. Efsing, *J. Nucl. Mater.* **437**, 107 (2013).
 - [6] H. Hein, E. Keim, J. May, and H. Schnabel, in IAEA Technical Meeting on Degradation of Primary Components of Pressurised Water Cooled Nuclear Power Plants: Current Issues and Future Challenges, 5–8 November 2013, Vienna, Austria (unpublished).
 - [7] M. K. Miller and K. F. Russell, *J. Nucl. Mater.* **371**, 145 (2007).
 - [8] P. Auger, P. Pareige, S. Welzel, and J. C. Van Duysen, *J. Nucl. Mater.* **280**, 331 (2000).
 - [9] P. Efsing, C. Jansson, G. Embring, and T. Mager, *J. ASTM Int.* **4**, 1 (2007).
 - [10] S. C. Glade, B. D. Wirth, G. R. Odette, and P. Asoka-Kumar, *J. Nucl. Mater.* **351**, 197 (2006).
 - [11] Y. Nagai, K. Takadate, Z. Tang, H. Ohkubo, H. Sunaga, H. Takizawa, and M. Hasegawa, *Phys. Rev. B* **67**, 224202 (2003).
 - [12] K. Yabuuchi, M. Saito, R. Kasada, and A. Kimura, *J. Nucl. Mater.* **414**, 498 (2011).
 - [13] E. Meslin, B. Radigue, and M. Loyer-Prost, *Acta Mater.* **61**, 6246 (2013).
 - [14] L. S. Darken, *Trans. Metall. Soc. AIME* **175**, 41 (1948).
 - [15] J. R. Manning, *Metall. Trans. B* **1**, 499 (1970).
 - [16] G. J. Ackland, M. I. Mendeleev, D. J. Srolovitz, S. Han, and A. V. Barashev, *J. Phys.: Condens. Matter* **16**, S2629 (2004).
 - [17] E. Meslin, C.-C. Fu, A. Barbu, F. Gao, and F. Willaime, *Phys. Rev. B* **75**, 094303 (2007).
 - [18] D. A. Terentyev, L. Malerba, and M. Hou, *Phys. Rev. B* **75**, 104108 (2007).
 - [19] C. Domain and C. S. Becquart, *Phys. Rev. B* **71**, 214109 (2005).
 - [20] A. V. Barashev and A. C. Arokiam, *Philos. Mag. Lett.* **86**, 321 (2006).

- [21] J. D. Tucker, R. Najafabadi, T. R. Allen, and D. Morgan, *J. Nucl. Mater.* **405**, 216 (2010).
- [22] S. Choudhury, L. Barnard, J. D. Tucker, T. R. Allen, B. D. Wirth, M. Asta, and D. Morgan, *J. Nucl. Mater.* **411**, 1 (2011).
- [23] A. R. Allnatt and E. L. Allnatt, *Philos. Mag. A* **49**, 625 (1984).
- [24] A. D. Le Claire, *J. Nucl. Mater.* **69-70**, 70 (1978).
- [25] P. Y. Serruys and G. Brebec, *Philos. Mag. A* **46**, 661 (1982).
- [26] Y. Okamura and A. R. Allnatt, *J. Phys. C: Solid State Phys.* **16**, 1841 (1983).
- [27] M. Nastar, V. Y. Dobretsov, and G. Martin, *Philos. Mag. A* **80**, 155 (2000).
- [28] M. Nastar, *Philos. Mag.* **85**, 3767 (2005).
- [29] V. Barbe and M. Nastar, *Philos. Mag.* **86**, 3503 (2006).
- [30] V. Barbe and M. Nastar, *Philos. Mag.* **87**, 1649 (2007).
- [31] T. Garnier, M. Nastar, P. Bellon, and D. R. Trinkle, *Phys. Rev. B* **88**, 134201 (2013).
- [32] T. Garnier, D. R. Trinkle, M. Nastar, and P. Bellon, *Phys. Rev. B* **89**, 144202 (2014).
- [33] A. Barbu and A. B. Lidiard, *Philos. Mag. A* **74**, 709 (1996).
- [34] A. C. Arokiam, A. V. Barashev, D. J. Bacon, and Y. N. Osetsky, *Phys. Rev. B* **71**, 174205 (2005).
- [35] P. Olsson, T. P. C. Klaver, and C. Domain, *Phys. Rev. B* **81**, 054102 (2010).
- [36] G. H. Vineyard, *J. Phys. Chem. Solids* **3**, 121 (1957).
- [37] L. Messina, Z. Chang, and P. Olsson, *Nucl. Instrum. Methods Phys. Res., Sect. B* **303**, 28 (2013).
- [38] O. Senninger, E. Martínez, F. Soisson, M. Nastar, and Y. Bréchet, *Acta Mater.* **73**, 97 (2014).
- [39] G. Kresse and J. Hafner, *Phys. Rev. B* **47**, 558 (1993).
- [40] G. Kresse and J. Hafner, *Phys. Rev. B* **49**, 14251 (1994).
- [41] G. Kresse and J. Hafner, *J. Phys.: Condens. Matter* **6**, 8245 (1994).
- [42] P. E. Blöchl, *Phys. Rev. B* **50**, 17953 (1994).
- [43] G. Kresse and D. Joubert, *Phys. Rev. B* **59**, 1758 (1999).
- [44] J. P. Perdew, K. Burke, and Y. Wang, *Phys. Rev. B* **54**, 16533 (1996).
- [45] S. H. Vosko, L. Wilk, and M. Nusair, *Can. J. Phys.* **58**, 1200 (1980).
- [46] P. Olsson, C. Domain, and J. Wallenius, *Phys. Rev. B* **75**, 014110 (2007).
- [47] G. Mills, H. Jonsson, and G. K. Schenter, *Surf. Sci.* **324**, 305 (1995).
- [48] H. Jonsson, G. Mills, and K. W. Jacobsen, in *Classical and Quantum Dynamics in Condensed Phase Simulations*, edited by B. J. Berne, G. Ciccotti, and D. F. Coker (World Scientific, Singapore, 1998).
- [49] G. Henkelman, B. P. Uberuaga, and H. Jonsson, *J. Chem. Phys.* **113**, 9901 (2000).
- [50] D. Costa, Ph.D. thesis, Université de Sciences et Technologies USTL Lille 1, 2012.
- [51] E. Vincent, C. S. Becquart, and C. Domain, *J. Nucl. Mater.* **351**, 88 (2006).
- [52] P. Pulay, *Chem. Phys. Lett.* **73**, 393 (1980).
- [53] G. P. Kerker, *Phys. Rev. B* **23**, 3082 (1981).
- [54] Y. Mishin, M. R. Sørensen, and A. F. Voter, *Philos. Mag. A* **81**, 2591 (2001).
- [55] T. Garnier, V. R. Manga, D. R. Trinkle, M. Nastar, and P. Bellon, *Phys. Rev. B* **88**, 134108 (2013).
- [56] C. Kittel, *Introduction to Solid State Physics*, 8th ed. (Wiley, Hoboken, NJ, 2004).
- [57] C. Domain, C. S. Becquart, and L. Malerba, *J. Nucl. Mater.* **335**, 121 (2004).
- [58] C. Domain and C. S. Becquart, *Phys. Rev. B* **65**, 024103 (2001).
- [59] F. Soisson and C.-C. Fu, *Phys. Rev. B* **76**, 214102 (2007).
- [60] L. Malerba, G. J. Ackland, C. S. Becquart, G. Bonny, C. Domain, S. L. Dudarev, C. C. Fu, D. Hepburn, M. C. Marinica, P. Olsson, R. C. Pasianot, J. M. Raulot, F. Soisson, D. Terentyev, E. Vincent, and F. Willaime, *J. Nucl. Mater.* **406**, 7 (2010).
- [61] G. Lucas and R. Schäublin, *Nucl. Instrum. Methods Phys. Res., Sect. B* **267**, 3009 (2009).
- [62] R. D. Hatcher, R. Zeller, and P. H. Dederichs, *Phys. Rev. B* **19**, 5083 (1979).
- [63] S. S. Pohlong and P. N. Ram, *J. Phys.: Condens. Matter* **10**, 10901 (1999).
- [64] A. Seeger, *Phys. Status Solidi A* **167**, 289 (1998).
- [65] H.-E. Schaefer, K. Maier, M. Weller, D. Herlach, A. Seeger, and J. Diehl, *Scr. Metall.* **11**, 803 (1977).
- [66] L. De Schepper, D. Segers, L. Dorikens-Vanpraet, M. Dorikens, G. Knuyt, L. M. Stals, and P. Moser, *Phys. Rev. B* **27**, 5257 (1983).
- [67] J. Wallenius, P. Olsson, C. Lagerstedt, N. Sandberg, R. Chakarova, and V. Pontikis, *Phys. Rev. B* **69**, 094103 (2004).
- [68] A. Vehanen, P. Hautojärvi, J. Johansson, J. Yli-Kauppila, and P. Moser, *Phys. Rev. B* **25**, 762 (1982).
- [69] A. Möslang, E. Albert, E. Recknagel, A. Weidinger, and P. Moser, *Hyperfine Interact.* **15**, 409 (1983).
- [70] E. Vincent, C. S. Becquart, and C. Domain, *Nucl. Instrum. Methods Phys. Res., Sect. B* **228**, 137 (2005).
- [71] O. I. Gorbatov, P. A. Korzhavyi, A. V. Ruban, B. Johansson, and Y. N. Gornostyrev, *J. Nucl. Mater.* **419**, 248 (2011).
- [72] M. Doyama, *Trans. Jpn. Inst. Met.* **25**, 808 (1986).
- [73] A. R. Allnatt and A. B. Lidiard, *Atomic Transport in Solids* (Cambridge University Press, Cambridge, UK, 2003).
- [74] A. Senhaji, G. Treglia, B. Legrand, N. T. Barrett, C. Guillot, and B. Villette, *Surf. Sci.* **274**, 297 (1992).
- [75] E. Vincent, C. S. Becquart, and C. Domain, *Nucl. Instrum. Methods Phys. Res., Sect. B* **255**, 78 (2007).
- [76] C. S. Becquart and C. Domain, *Phys. Status Solidi B* **247**, 9 (2010).
- [77] Z. Chang, N. Sandberg, and P. A. Korzhavyi (private communication).
- [78] B. Jonsson, *Z. Metallkd.* **83**, 349 (1992).
- [79] T. R. Anthony, in *Diffusion in Solids: Recent Developments*, edited by A. S. Nowick and J. J. Burton (Academic, New York, 1975), pp. 353–378.
- [80] W. G. Wolfer, *J. Nucl. Mater.* **114**, 292 (1983).
- [81] F. Soisson and C.-C. Fu, *Solid State Phenom.* **139**, 107 (2008).
- [82] K. Hirano, M. Cohen, and B. L. Averbach, *Acta Metall.* **9**, 440 (1961).
- [83] R. J. Borg and D. Lai, *Acta Metall.* **11**, 861 (1963).
- [84] S. J. Rothman, *J. Appl. Phys.* **39**, 5041 (1968).
- [85] A. W. Bowen and G. M. Leak, *Metall. Trans.* **1**, 2767 (1970).
- [86] K. Nohara and K. Hirano, *Proc. Int. Conf. Sci. Tech. Iron Steel* **7**, 11 (1970).
- [87] V. Imer and M. Feller-Kniepmeier, *J. Phys. Chem. Solids* **33**, 2141 (1972).
- [88] J. S. Kirkaldy, P. N. Smith, and R. C. Sharma, *Metall. Mater. Trans. B* **4**, 624 (1973).
- [89] G. Salje and M. Feller-Kniepmeier, *J. Appl. Phys.* **48**, 1833 (1977).

- [90] G. Luckman, R. A. DiDio, and W. R. Graham, *Metall. Trans. A* **12**, 253 (1981).
- [91] T. Matsuyama, H. Hosokawa, and H. Suto, *Trans. Jpn. Inst. Met.* **24**, 589 (1983).
- [92] D. Bergner, Y. Khaddour, and S. Lörx, in *Diffusion in Metals and Alloys*, edited by F. J. Kedves and D. L. Beke (Trans Tech Publications, Switzerland, 1991), p. 1407.
- [93] J. Čermák, M. Lübbehusen, and M. Mehrer, *Z. Metallkd.* **80**, 213 (1989).
- [94] K. Hirano and Y. Iijima, in *Diffusion in Metals and Alloys*, edited by F. J. Kedves and D. L. Beke (Trans Tech Publications, Switzerland, 1991), p. 1039.
- [95] C. G. Lee, Y. Iijima, T. Hiratani, and K. Hirano, *Mater. Trans., JIM* **31**, 255 (1990)

Paper II

Systematic electronic-structure investigation of substitutional impurity diffusion and flux coupling in bcc iron

Luca Messina,^{1,*} Maylise Nastar,² Nils Sandberg,^{1,3} and Pär Olsson¹

¹*KTH Royal Institute of Technology, Reactor Physics, SE-106 91 Stockholm, Sweden*

²*CEA, DEN, Service de Recherches de Métallurgie Physique, F-91191 Gif-sur-Yvette, France*

³*Swedish Radiation Safety Authority, Solna Strandväg 96, SE-171 16 Stockholm, Sweden*

The diffusion properties of a wide range of impurities (transition metals and Al, Si, and P) in ferritic alloys are here investigated by means of a combined *ab initio*-atomic diffusion theory approach. The flux-coupling mechanisms and the solute diffusion coefficients are inferred from electronic-structure calculations of solute-defect interactions and microscopic jump frequencies. All properties except the second nearest-neighbor binding energy are found to have a characteristic bell shape as a function of the d-band filling for the 4d and 5d series, and an M-shape for the 3d row because of the out-of-trend behavior of Mn. The solute jump frequencies are governed by compressibility, which makes diffusion of large solutes faster, although this effect is partially compensated for by lower attempt frequencies and larger correlations with the vacancy. Diffusion coefficients are predicted in a wide temperature range, far below the experimentally-accessible temperatures. In accordance with experiments, Co is found to be a slow diffuser in iron, and the same behavior is predicted for Re, Os, and Ir impurities. Finally, flux-coupling phenomena depend on the iron jump frequencies next to a solute atom, which are mainly controlled by similar electronic interactions to those determining the binding energies. Vacancy drag and solute enrichment at sinks systematically arise below a solute-dependent temperature threshold, directly correlated with the electronic-level interactions at the equilibrium and the saddle-point states. Early transition metals with repulsive second nearest-neighbor interactions also diffuse via vacancy drag, although they show a lower temperature threshold than the late metals. This confirms that drag is the most common solute-vacancy coupling mechanism in iron at low temperatures, and this is likely to be confirmed as well for impurity diffusion in other transition metals.

INTRODUCTION

Ferritic and ferritic-martensitic (F/M) alloys are widely used in many industrial applications. They consist of body-centered cubic (bcc) iron alloys with varying concentrations of several impurities, most of which are purposely included in order to improve the alloy mechanical properties. Impurity diffusion plays a crucial role in determining such properties during fabrication, processing, and operation. Correlations with crystal defects can severely affect the diffusion process and hence the material macroscopic behavior. The effects in irradiated materials are even greater, because of the strongly increased concentration of vacancies and self-interstitial atoms (SIA). For instance, the arising of solute drag by vacancies has been shown to be among the main causes for radiation-enhanced or -induced solute precipitation [1–3], as well as for solute segregation at defect sinks [4–6], which in turn are responsible for hardening and embrittlement [7, 8]. Solute-defect correlations can also substantially affect defect migration. As an example, the swelling-rate reduction in FeCr alloys with increasing Cr content has been ascribed to the strong correlation between Cr atoms and self-interstitial loops: diffusion of SIA's is slowed down by the correlation with solutes, and the recombination with vacancies is therefore enhanced [9]. A similar effect has been postulated for Mn impurities [10, 11].

Kinetic correlations between solutes and vacancies can

lead to vacancy drag, i.e. to a coupled flux of solutes and vacancies in the same direction, as opposed to the inverse-Kirkendall diffusion mechanism [12]. Recent studies in dilute iron alloys have shown that vacancy drag can systematically arise in a wide range of conditions [13–15]. These studies are based upon the calculation of transport coefficients through the self-consistent mean-field (SCMF) method [16], which proved to be considerably more accurate than the traditional multifrequency models [17–19]. SCMF theory was applied for a systematic investigation of vacancy drag in bcc and face-centered cubic (fcc) alloys. [13, 20] In these works, the authors highlighted the predominant role of kinetic correlations over thermodynamic interactions in controlling and determining the arising of vacancy drag. This entails that the character of solute-vacancy interactions is not sufficient for an accurate prediction of flux coupling, but a full kinetic characterization of each single alloy is necessary. However, the conclusions therein are based on simple thermodynamic models, which are not necessarily representative of the behavior of "real" alloys. Such kind of kinetic studies can be performed with a higher accuracy if *ab initio* methods are applied in the calculation of microscopic jump frequencies, on which the SCMF method relies.

Several examples of *ab initio*-based studies of impurity diffusion in bcc iron can be found in the literature [21–24]. However, such studies cover a limited set of impurities and do not treat flux-coupling phenomena. Flux

coupling was more extensively investigated in [15, 25], limitedly to some impurities that are of importance for the microstructure evolution of reactor-pressure vessel (RPV) F/M steels. By means of a combined *ab initio*-SCMF approach, vacancy drag was found to systematically occur for most impurities (Cu, Mn, Ni, P, Si) below a solute-dependent temperature threshold that is usually above 1000 K. [15] This could be directly linked to the observed formation of solute precipitates, even in the apparent absence of thermodynamic driving forces [3, 8].

Flux coupling is a complex kinetic phenomenon that depends on a large set of jump frequencies, for which clear physical trends have not been identified yet. The coupling strength and the threshold temperature could be correlated to first and second nearest-neighbor (nn) solute-vacancy interactions only in a qualitative way in [13]. However, the variation of the 2nn solute-vacancy binding energy from one solute to another, as well as its effective impact on flux coupling, are not totally understood. The presence of a 2nn binding interaction in bcc crystals is usually regarded as a necessary condition for vacancy drag to take place [26, 27]; however, it was shown in [13] that vacancy drag can occur even in the presence of some repulsive interactions, either at 1nn or 2nn. Our objective is hence to improve our understanding of the binding energies, the jump frequencies and flux coupling in dilute Fe(X) alloys by studying these properties at the electronic scale. Group-specific trends have already been evidenced for the cohesive energy, the bulk modulus and the equilibrium atomic volume [28], for the solute-vacancy binding energies in Fe [26], for the solute-vacancy [27] and divacancy binding energies [29] in W, and for solute diffusion in Ni [30, 31]. While the variation of many physical properties across the transition metal series have a simple bell-shaped behavior with a maximum approximately in the middle of the series, 2nn binding energies have a linear behavior in contrast to the parabolic trend [26, 29]. It is then interesting to investigate the effect of this anomalous trend on diffusion properties.

In addition, transport coefficients allow for an accurate first-principle-based calculation of low-temperature solute tracer diffusion coefficients. The latter are essential quantities for the modeling of radiation-response phenomena, but are usually not accessible experimentally below 750 °C. Recently, thanks to an advanced atom-probe technique [32], it was possible to improve the spatial resolution and accurately measure diffusion coefficients at temperatures stretching down to 550 °C. However, many applications of irradiated materials require the knowledge of solute diffusion coefficients at lower temperatures, since the increased defect population accelerates diffusion phenomena that would otherwise be very slow. Given the lack of low-temperature data, diffusion coefficients are usually extrapolated from high-temperature measurements. In ferritic alloys, however,

the extrapolation is normally based on a limited temperature range in the ferromagnetic (FM) region, and can therefore lead to errors of several orders of magnitude. Conversely, the transport coefficients calculated in this work, combined with a proper magnetic-transition model, allow for a reliable estimation of solute diffusion coefficients for all the transition metals (TM), over a wide range of temperatures.

This work presents therefore an electronic study of vacancy-assisted diffusion for all TM impurities in iron-based dilute alloys. Other solutes (Al, Si, and P) are also included in this analysis, since they are often present in many types of F/M steels, for a total of 26 impurities. For each binary alloy, microscopic jump frequencies are computed with an *ab initio* method. The trends of binding energies, migration barriers, and attempt frequencies as functions of the d-band filling are discussed. Afterwards, the transport coefficients are obtained with the SCMF method, and are used to determine the arising of vacancy drag and solute segregation tendencies, as well as to provide diffusion coefficients in the low-temperature range. The several recurrent trends revealed by this systematic study allow for a deeper understanding of the physics of impurity diffusion in iron.

METHODOLOGY

Mean-field model

The kinetic analysis of this work is based on the calculation of transport coefficients (L_{ij}). The latter describe the kinetic response of the system to a thermodynamic driving force, and can be expressed as:

$$J_i = - \sum_{j=1}^N \frac{L_{ij}}{k_B T} \nabla \mu_j, \quad (1)$$

where J_i is the flux of species i and $\nabla \mu_j$ is the chemical potential gradient of species j . The off-diagonal terms L_{ij} ($i \neq j$) describe the correlation between the fluxes of i and j .

The transport coefficients (also called the Onsager coefficients) are obtained here in the framework of the SCMF theory [16]. In this theory, an alloy is described through a set of kinetic pair interactions, which embody a small perturbation from the thermodynamic equilibrium state. Such kinetic interactions are calculated by solving the corresponding kinetic equations in steady-state conditions. A detailed explanation of this method can be found in [13, 16], and its extension to non-homogeneous driving forces is introduced in [33].

The key-input parameters for the SCMF theory are the atomic jump frequencies in the local atomic environment (LAE) around the solute-vacancy pair. In analogy with the regular multifrequency models [17–19], the size

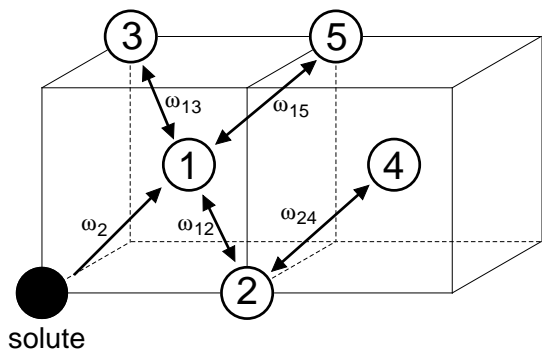


FIG. 1: 9-frequency model enforced in this work for the calculation of the transport coefficients, in a 2nn thermodynamic model. The numbers in the circles mark the possible nearest-neighbor positions of the vacancy before the jump.

of the LAE (and therefore the amount of jump types to be distinguished) is determined by a cutoff distance R , beyond which all thermodynamic interactions are neglected. Once R is defined, the jumps to be distinguished are those occurring within or across the borders of the LAE. In [15] the cutoff radius was set to the 5nn, and the results showed that, in those binary alloys, a cutoff to the 2nn is necessary and sufficient to provide an acceptable description of flux coupling and diffusion coefficients. 1nn models in bcc are not suitable because the 2nn site plays a relevant role in vacancy-solute coupled diffusion, whereas the cutoff extension to the 5nn only slightly improved the results, to the cost of a considerable increase of the computational time. For this reason, the cutoff radius is set in this work to the 2nn, leading to the typical 9-frequency configuration depicted in Fig. 1. It is worth pointing out that in precedent 2nn multifrequency models the kinetic interactions are not fully accounted for, whereas the application of SCMF theory yields the correct flux-coupling tendencies, as was shown in [15].

Each migration is modeled as a thermally-activated event with frequency:

$$\omega_{ij} = \nu_x \exp\left(-\frac{E_{ij}^{\text{mig}}}{k_B T}\right). \quad (2)$$

The migration energies E_{ij}^{mig} and attempt frequencies ν_{Fe} , ν_x are obtained by means of Density Functional Theory (DFT) *ab initio* calculations. Given the high computational cost required by attempt frequency DFT calculations, the attempt frequencies for iron jumps in the vicinity of a solute atom ($\omega_{ij} \neq \omega_0, \omega_2$) are assumed to be equal to ν_{Fe} .

The SCMF method requires the transition rates to be calculated in conditions of thermodynamic equilibrium, and in such conditions each elementary transition must

be balanced by its reverse process (detailed-balance principle). A manipulation of the DFT migration barriers is therefore necessary. It is achieved by adding the DFT-computed binding energy E_z^b to each migration barrier of type E_{zy}^{mig} , with $z > R$ and $y \leq R$, so to set E_z^b to zero. For instance, since DFT yields $E_3^b(\text{Mo}) = -0.02$ eV (attractive), the migration energy of the jump ω_{31} is lowered by 0.02 eV in order to remove this residual interaction at 3nn. Clearly, this procedure has little effect on the results as long as the residual interactions beyond R are small. [15]

Once the set of jump frequencies is obtained, the transport coefficients are computed in the SCMF framework with the 3nn3nn kinetic model, which includes the kinetic interactions among atoms within the 3nn of 3nn sites (with respect to the vacancy initial and final position). The matrix formulation of this model is to be found in the appendix of [13]. The vacancy-drag coefficient is defined as L_{xv}/L_{xx} , with $L_{xv} = -(L_{\text{Fe},x} + L_{xx})$. This coefficient is positive under vacancy-drag conditions, and negative otherwise. The radiation-induced segregation (RIS) tendency due to vacancy-mediated diffusion is analyzed in terms of partial diffusion coefficient (PDC) ratio [34], which can be written in the dilute limit as:

$$\frac{d_{xv}}{d_{\text{Fe},v}} = \frac{l_{\text{Fe},x} + l_{xx}}{L_{\text{Fe},\text{Fe}}^0}, \quad (3)$$

where $l_{\text{Fe},x} = L_{\text{Fe},x}/c_x$ and $l_{xx} = L_{xx}/c_x$. $L_{\text{Fe},\text{Fe}}^0$ is the uncorrelated, solute-independent part of the $L_{\text{Fe},\text{Fe}}$ coefficient, and c_x is the atomic solute concentration. The PDC ratio enters the general RIS balance equation [15]:

$$\frac{\nabla c_x}{\nabla c_v} = \frac{c_{\text{Fe}} c_x d_{\text{Fe},v} d_{\text{Fe},i}}{(c_{\text{Fe}} d_{\text{Fe},i} D_x + c_x d_{x,i} D_{\text{Fe}})} \left(\frac{d_{xv}}{d_{\text{Fe},v}} - \frac{d_{x,i}}{d_{\text{Fe},i}} \right), \quad (4)$$

where the indices v and i stand for vacancies and interstitials, respectively. The definition of the interdiffusion coefficients D_{Fe} , D_x can be found in [34]. Here, the amplitude prefactor is neglected and the PDC ratio for interstitials is set to 1. This is equivalent to neglecting the enrichment or depletion tendency induced by interstitial transport, which might be significant for solutes that form stable dumbbells such as P, Mn, and Cr [21, 26].

The solute tracer diffusion coefficient is calculated as

$$D_x^* = \frac{L_{xx}}{n c_x}, \quad (5)$$

where n is the iron atomic density. This coefficient can be equivalently expressed as [35]:

$$D_x^* = a_0^2 c_v f_x \omega_2 \exp\left(-\frac{E_{1nn}^b}{k_B T}\right), \quad (6)$$

where c_v is the vacancy concentration, f_x the solute diffusion correlation factor, and E_{1nn}^b the 1nn solute-vacancy interaction energy (taken as positive when repulsive and

negative otherwise). The correlation factor takes into account the probability that atomic jumps do not occur randomly in each direction because of geometric reasons as well as solute-vacancy correlations. Therefore, the whole effect of kinetic correlations on solute diffusion is included in this factor. The correlation factor f_x corresponding yielded by SCMF theory is provided in the appendix as a function of the jump frequencies. Contrary to the commonly used Le Claire's formula [17], this expression does not assume that $\omega_{42} = \omega_0$, thus allowing for a more accurate calculation of f_x . The tracer self-diffusion coefficient can be obtained with the same methodology, by introducing a "mock" solute atom with null binding energy and jump frequency ω_0 .

The vacancy concentration c_v is here taken to be that of non-irradiation thermodynamic-equilibrium conditions:

$$c_v = c_v^{eq} = \exp\left(-\frac{E_v^f}{k_B T}\right) \cdot \exp\left(\frac{S_v^f}{k_B}\right), \quad (7)$$

for the sake of consistency with diffusion experiments. The formation enthalpy and entropy E_v^f and S_v^f are obtained as well via DFT calculations. The variation of E_v^f due to the solute concentration can be neglected in the dilute-limit calculation of vacancy-solute flux coupling. In irradiated materials, the vacancy concentration is fixed by the external irradiation and the dynamic balance with other defects. At any rate, since each transport coefficient is proportional to c_v , the flux-coupling tendencies here obtained are not affected by an increased vacancy population.

As to account for the effects of ferro- to paramagnetic (PM) transition in iron, a finite-temperature model inspired by the work of Sandberg *et al.* [36] is here adopted. The total vacancy diffusion activation energy in pure iron $Q_0^F = E_v^f + E_v^m$ decreases proportionally to the magnetic excess enthalpy H^{mag} :

$$Q(T) = Q_0^F - \alpha H(T) \quad (8)$$

with $\alpha = Q_0^F - Q^P$ and $H(T) = 1 - H^{\text{mag}}(T)/H^{\text{mag}}(0 \text{ K})$. Q^P is the vacancy diffusion activation energy in a fully PM state ($Q^P = 2.26 \text{ eV}$ according to recent *ab initio* calculations [36]). The magnetic excess enthalpy is calculated by means of the Hillert-Jarl model [37], reported in the appendix. Eq. 8 was developed for self-diffusion in iron, but can be also applied to solute diffusion, under the assumption that one solute atom has a negligible effect on the correlation between the magnetic state and vacancy migration properties. The minor electronic contribution to the activation energy treated in [36] is here neglected. The vacancy mobility, and hence the self- and solute diffusion coefficients, are increased by the temperature-dependent factor $\exp[\alpha H(T)]$ shown in Fig. 2. The same figure reports as well the value of the factor $H(T)$. The discontinuity at the Curie temperature is due

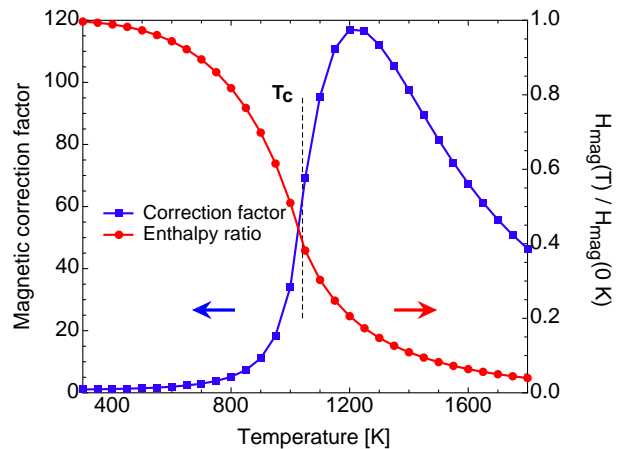


FIG. 2: (blue squares) Correcting factor $\exp[\alpha H(T)]$ to self- and solute diffusion coefficients due to the finite-temperature magnetic transition. (red circles) Relative excess magnetic enthalpy obtained with the Hillert-Jarl model [37]. $T_C = 1043 \text{ K}$ marks the Curie temperature in iron.

to the two different Hillert-Jarl expressions for the magnetic excess enthalpy used in the FM and PM regions. Short-range ordering is represented by the residual magnetic enthalpy above the Curie temperature.

Ab initio method

The DFT calculations are performed with the Vienna *ab initio* simulation package (VASP) [38–40] on a plane-wave basis, by making use of projector augmented wave (PAW) pseudopotentials [41, 42]. The exchange-correlation function is modeled with the Perdew-Burke-Ernzerhof (PBE) parameterization [43] of the generalized gradient approximation. The plane-wave cutoff is set to 300 eV and the Brillouin zone is sampled with a $3 \times 3 \times 3$ k-point mesh. Unless otherwise specified, the calculations are performed in a 127-atom supercell, allowing for atomic relaxations but restraining the cell shape and volume. Standard potentials from the VASP library are employed for all the elements included in this study. The migration barriers are calculated with the nudged-elastic band (NEB) method [44, 45] and the climbing image algorithm [46], using 3 intermediate images. In this way, the migration barriers can be determined to an accuracy of 5 meV or less. More details can be found in [15].

The vacancy formation and migration energies in pure iron were calculated in [15] and are here unchanged. The solute-vacancy binding energy for a given *inn* configuration is obtained as:

$$E_{\text{inn}}^b = E_{v+x(\text{inn})}^{N-2} - E_v^{N-1} - E_x^{N-1} + E^N, \quad (9)$$

where the terms on the right-hand side refer to the su-

percell energy with a vacancy and a solute atom, one vacancy, one solute atom, and with no defects nor solutes, respectively.

The vacancy formation entropy and the attempt frequencies for iron and solute migration are determined by means of DFT frozen-phonon calculations. In the framework of transition-state theory (TST), the vacancy formation entropy in pure iron is obtained from the vibrational frequencies of the defected (I) and undefected (U) supercell [47]:

$$\frac{S_v^f}{k_B} = - \left[\ln \left(\prod_{k=1}^{3N-3} \nu^I \right) - \frac{N}{N+1} \ln \left(\prod_{k=1}^{3(N+1)-3} \nu^U \right) \right], \quad (10)$$

and the attempt frequency of a given migration event is derived from the vibrational frequencies of the initial (I) and saddle-point (S) configurations [48]:

$$\nu_x = \frac{\prod_{k=1}^{3N-3} \nu_k^I}{\prod_{k=1}^{3N-4} \nu_k^S}. \quad (11)$$

N is the number of atoms (127 in a $4 \times 4 \times 4$ supercell), and the index k scans through the degrees of freedom of the system. The vibrational frequencies are computed in the quasi-harmonic approximation by diagonalizing the Hessian matrix. Each element k_{ij} of this matrix is given by the derivative of the force on atom i with respect to a small displacement of atom j in one of the three spacial directions:

$$k_{ij} = \frac{1}{\sqrt{m_i m_j}} \frac{\partial F_i}{\partial r_j}. \quad (12)$$

Four displacements of ± 0.015 and ± 0.030 Å are applied on each atom in each direction, and the force is interpolated with the least-square method. Given the extreme sensibility with respect to the force convergence criterion, the initial and undefected configurations are relaxed so that the force on each atom is lower than 0.001 eV/Å. This value is one order of magnitude higher than in similar calculations performed by Lucas *et al.* [49]. Tests on 15-atom cells with varying cutoff and k-point mesh size confirmed that the vibrational properties are quite well converged at 0.001 eV/Å. With this fixed force-convergence criterion, the phonon calculations in pure iron are run in simulation cells of increasing size, in order to check the box-size effect. For this purpose, simulation cells of 15, 53, 127 and 249 atoms are used, and the k-point mesh is adjusted accordingly ($7 \times 7 \times 7$ for 15 atoms, $5 \times 5 \times 5$ for 53 atoms, and $3 \times 3 \times 3$ for 127 and 249 atoms), with a fixed cutoff energy of 350 eV. Because of the large computational cost, the solute attempt frequencies are calculated in a 53-atom supercell only. At the moment, the same computation-time limitation prevents the possibility of calculating the attempt frequency of pure Fe in a 249-atom cell.

RESULTS AND DISCUSSION

Bulk-iron properties

The bulk properties of iron obtained or adopted in this work are listed in Table I. The lattice parameter and the vacancy activation energy in FM state were already shown to be in agreement with experiments and previous DFT calculations [15]. The PM activation energy was DFT calculated in [36], as an average over a set of several randomly-assigned spin configurations, so to simulate the PM state.

The phonon-related quantities (S_v^f and ν_{Fe}) are calculated in simulation cells of increasing size, and in both cases they reach an acceptable convergence. Based on these values it is possible to assess the accuracy of the calculations to less than $\pm 0.2 k_B$ and ± 1 THz, respectively. The obtained vacancy formation entropy of $4.6 k_B$ is larger than early calculations using semi-empirical potentials (SEP) and ranging between 1.5 and $2.6 k_B$ [50–52]. It is however in better agreement with previous DFT calculations ($S_v^f = 4.08 k_B$) [49], confirming the qualitative difference between DFT and SEP. In addition, this value is also compatible with the estimation provided in [53] based on a TST-based analysis of self-diffusion data. According to this analysis, the sum of the vacancy formation and migration entropy should be lower than $5 k_B$. As for the attempt frequency, the calculated value is in very good agreement with recent DFT calculations (12 THz) [54].

Solute-vacancy interactions

The calculated solute-vacancy interaction energies are shown in Fig. 3. They are in good agreement with previous calculations [23, 26, 55, 56] performed with various first-principle methods, and with the experimental values listed in [15, 26]. With the exception of the 2nn, the interaction is always attractive, reaching particularly strong values at the two ends of the band. Three types of 1nn-2nn solute-vacancy interactions can be therefore distinguished: binding-repulsive (early TM's), binding-binding (late TM's), and weak interactions (the metals in between, except Mn). To the second category belong also P and Si, whereas Al can be included into the first class. According to the traditional assumptions, the early TM's should not be dragged by vacancies because of the 2nn repulsion, in spite of the (in some cases) very strong 1nn binding interaction. The diffusion behavior of the early TM's is therefore suitable for confirming or disproving this theory.

Co and Ni are anomalous as they are characterized by a higher binding energy at 2nn than 1nn. Such anomalies, repeatedly found in past works [26, 56], can now be explained thanks to the peculiar shape of the 2nn group

TABLE I: Bulk properties in pure iron, computed or adopted in this work.

Quantity	Value			
Lattice parameter a_0	2.831 Å ^a			
Vacancy formation enthalpy E_v^f	2.18 eV ^a			
Vacancy migration energy E_v^{mig}	0.70 eV ^a			
Ferromagnetic activation energy Q_v^F	2.88 eV ^a			
Paramagnetic activation energy Q_v^P	2.26 eV ^b			
Entropic quantities (this work)	15 at.	53 at.	127 at.	249 at.
Vacancy formation entropy S_v^f [k_B]	4.90	4.54	4.83	4.62
Attempt frequency ν_{Fe} [THz]	4.19	10.8	11.6	—
Vacancy diffusion prefactor D_{Fe}^0 [cm^2/s]	0.45	0.81	1.16	—

^a Reference [15].

^b Reference [36].

trend, i.e. a somewhat linear descent from repulsion to attraction. Similar calculations of solute-vacancy interactions in bcc tungsten also showed an anomalous 2nn d-band trend, as well as a separation in behavior between early and late TM's.[27]

On the other hand, the group trends of the other nn interactions follow a parabolic curve for 4d and 5d metals, and an M-shaped curve for the 3d series. Such shapes are observed in many TM properties such as cohesive energy [57], bulk modulus [57], solute size factor in Fe [26], or solute migration energy in Ni [30], and will reappear as well in the diffusion properties presented in the later sections of this paper. The parabolic trend was shown to be associated with the second moment of the density of states (DOS), in the framework of a tight-binding model [28, 58]. Conversely, the behavior of the 3d metals in Fe is strongly affected by magnetic interactions, which are absent in the 4d and 5d series [26]. In particular, the M-shape is determined by the atypical behavior of Mn. This was shown to be also the case for interactions in a Ni matrix [30]. While Ti and V show an analogous behavior to the early 4d and 5d TM solutes, and Cu that of a late TM solute, one can note that the 3d solutes with significant magnetic coupling diverge from the 4d and 5d trends. Namely, the antiferromagnetic solutes (Cr, Mn) have a purely binding behavior, to an extent that clearly depends on the magnetic moment. On the other hand, the FM solutes (Co, Ni) are strongly bound at 2nn only, and their behavior tends to the late TM's trend as the magnetic moment decreases.

Solute-defect interactions are usually explained according to strain-relief arguments: oversized atoms are expected to bind in compressed positions (1nn, 3nn, 5nn) and repulse in tensile ones (2nn, 4nn). However, the 2nn interaction of the late metals contradicts this rule. According to [26], this has an electronic origin: the late elements perturb the charge distribution around the vacancy in a different fashion with respect to the early elements.

In order to rule out the size-strain effects, the elec-

tronic contribution to the total binding energy is also shown in Fig. 3 for 1nn, 2nn, and 5nn (empty markers). As can be seen in the figure, such contribution is clearly the dominant factor, as has already been shown for some of the impurities. [55] The difference between the electronic contribution and the total interaction increases with solute size, again in agreement with [55]. On the other hand, the size effect seems to be negligible for the 3d metals, which are fairly close-matched in size with Fe. The interaction is driven by electronic bonds also for the p elements, as was already mentioned for P. [21]

The effect of ionic relaxations cannot be rationalized with simple size arguments. For instance, the 1nn interaction becomes stronger for Zr and Hf, and increasingly weaker for the other elements. This is surely due to additional effects of the electronic rearrangement after relaxation, and might also be affected by the larger substitution energy of the late TM's [26]. Moreover, the linear trend of the 2nn interaction has a clear electronic origin, and the total energy is systematically more binding than the electronic contribution, in spite of the tensile character of the 2nn strain field [26]. Following the tight-binding model of [28], the linear shape of the 2nn interaction is caused by the contribution of higher-than-second moments of the DOS, which in turn can be related to a strong angular character of the electronic interactions. Such character might also explain the deviation from the trend of the large-sized elements (Zr, Hf on one side and Ag, Au on the other side). It is worth mentioning that some anomalies in the properties of Ag and Au have already been observed [26].

Fig. 3 shows as well a residual interaction at 3nn and especially at 5nn. In the latter case, the iron atom between the solute and the vacancy might be playing an important role. This is in disagreement with previous DFT-PW91 calculations [26], which yielded negligible 3nn and 5nn interactions. However, additional testing of such potentials confirms this residual interaction. Since the impact is larger for large solutes, the box-size effect was also estimated in a 249-atom supercell for some selected

cases, but it showed to be no larger than 0.02 eV. This proves that indeed the large-sized solutes are characterized by a long-ranged interaction with vacancies, which is dominated by electronic effects of the second-moment type. This finding suggests that, for such solutes, a 2nn diffusion model might not suffice to fully describe the solute-vacancy kinetic interactions.

Migration barriers

The solute migration barriers (for jump ω_2) as functions of the d-band filling are depicted in Fig. 4, alongside the corresponding attempt frequencies. The group trends have very similar shapes to those of the 1nn binding energy: a parabolic function for the 4d and 5d elements, and an M-shaped curve for the 3d ones. These shapes suggest that large solutes diffuse faster, as their migration barrier is lower. On the other hand, also the small solutes (P and Si) have a lower barrier. This general trend is very similar to that of solute migration barriers in a nickel matrix [30]. Although the effect is partially compensated by the opposite trend in the attempt frequencies, it can be also observed in the experimental diffusion data of solutes in Fe (see Fig. 12).

That large atoms are faster is surely counterintuitive, as one would expect smaller atoms to induce less strain in the crystal and have therefore an easier way while migrating. Janotti *et al.* [30] explained this phenomenon in terms of solute compressibility. They demonstrated that the saddle-point energy is not much affected by the misfit strain, but is instead dominated by how much the solute can be compressed at the saddle-point position. This was also the case for solute migration in Al [59], and holds here as well in an iron matrix, because of the electronic origin of this effect. Band-center solutes are less compressible because of the presence of directional bonds, which are not there for the band-end solutes. For comparison, the experimental bulk moduli of each element (in the pure material) are reported in the above-left panel of Fig. 4. It is clear that the shapes of the migration barrier trends for all the TM series are correlated with the solute bulk moduli, or their compressibilities. The lower compressibility of the 5d row with respect to the 4d row is the cause for the systematically higher migration barriers of 5d metals, in spite of the similar chemical properties, and the difference increases towards the centre. From a tight-binding standpoint, the parabolic behavior of the bulk modulus, and as a consequence of the migration barrier, is determined by the DOS second moment. As was the case for the Ni matrix [30], the saddle-point distance between the migrating solute and the 1nn iron atoms is only weakly dependent on the solute type, which confirms the low influence of the size factor. The asymmetry of the curve, which was observed as well in Ni, can be attributed to the higher substitution energy [26]

and to the lower cohesive energy [57] of the late TM's. Certainly, the size factor that is commonly proposed as argument to explain interactions and migration barriers, provides a negligible contribution. For what concerns the 3d metals, the crossing with the 4d and 5d curves is observed for both the bulk modulus and E_2^{mig} , but their behavior cannot be explained by compressibility only. It is most likely affected by complex magnetic interactions. For the same reasons as the binding energy case, the peculiar electronic interactions of Mn determine the local minimum and the M-shape of the 3d trend.

A few elements are characterized by a higher migration barrier than Fe, namely Co, Ru, Rh, and all 5d metals from W to Pt. However, as will be discussed in the next sections, this does not entail necessarily a slower diffusion than self-diffusion. On the other hand, a few early TM's, especially Zr, have very small migration barriers (0.08 eV). The behavior of this solute tends to the limiting case of yttrium, whose binding with a vacancy is so strong that it is not located in a substitutional position, rather it relaxes towards the middle of two vacant spaces. The "migration barrier" of Y is so low (below 0.01 eV) that the diffusion mechanism is no more an exchange with a monovacancy, but rather a migration of the whole Y-vac complex [60]. The Zr-vacancy configuration is very stable, since Zr relaxes quite far into the middle of the vacant space (0.4 Å, or 16% of the 1nn distance), and the probability of vacancy escape is negligible (the escape barriers for ω_{12} , ω_{13} , and ω_{15} are much higher than ω_2 , and the re-association barriers ω_{31} and ω_{51} are much lower than ω_0). This suggests that the vacancy is actually trapped next to a Zr solute up to high temperatures, and diffusion could take place with a mechanism similar to that of Y, in which case the diffusion model here applied would be inaccurate.

The iron migration barriers in the vicinity of a solute atom are shown in Fig. 5, according to the jump-frequency nomenclature of Fig. 1. For these jumps, the iron attempt frequency is assumed to be independent from the LAE of the migrating atom. In general, it is possible to observe a very strong association tendency (low migration barriers for the reverse jumps ω_{31} and ω_{51}) and also a strong resistance against dissociation for the early TM's (high barriers for the ω_{12} and ω_{13} jumps). Given also the low solute migration barriers, very strong solute-vacancy correlations are expected for the early TM's. For Co, the lack of 1nn interaction and the combination of the iron jump frequencies show that the Co-vac 2nn configuration can represent a trapping configuration, which makes Co diffusion in iron considerably more difficult.

The group trends can be explained by separating the saddle-point energy properties from the binding energy influence. For this purpose, the saddle-point (SP) contribution to the total migration barrier can be isolated by removing the initial-state binding energy in the following

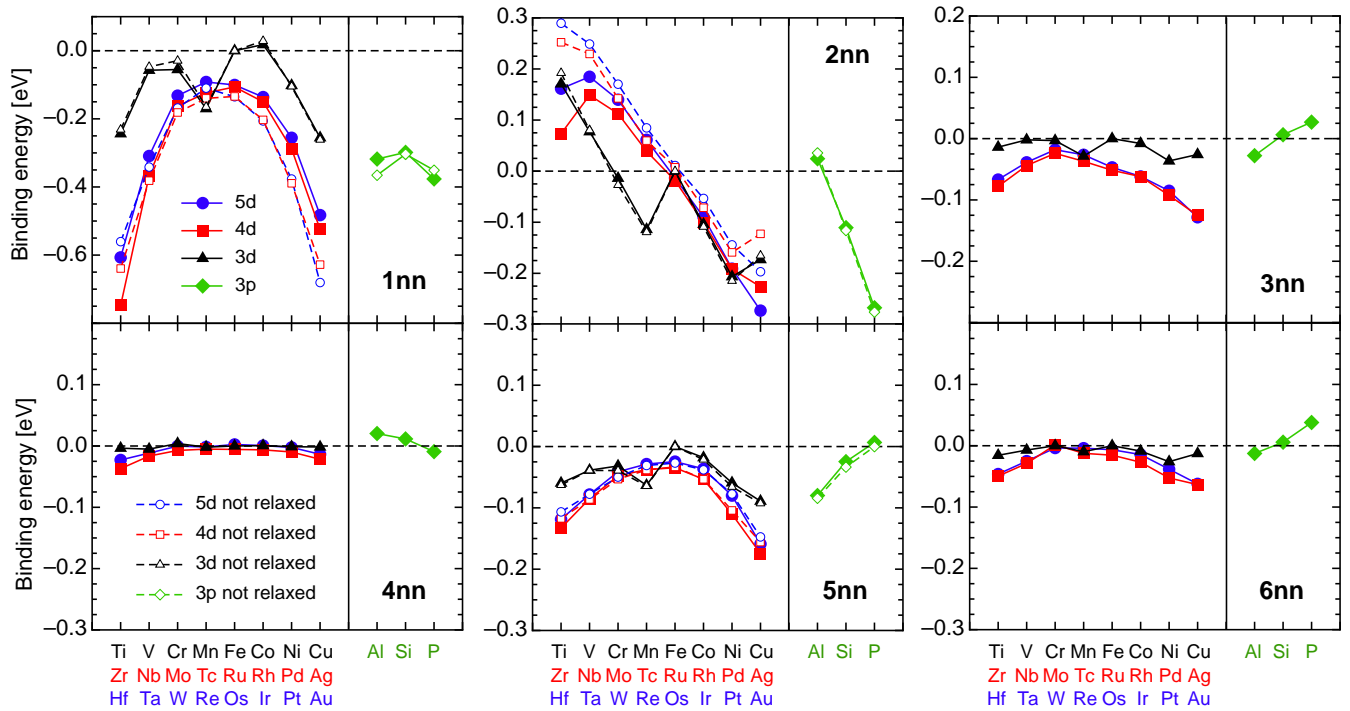


FIG. 3: DFT-calculated solute-vacancy interaction energies in iron (full symbols), and computed by neglecting the relaxation of the cell due to the solute presence (open symbols). Negative values stand for attractive interactions

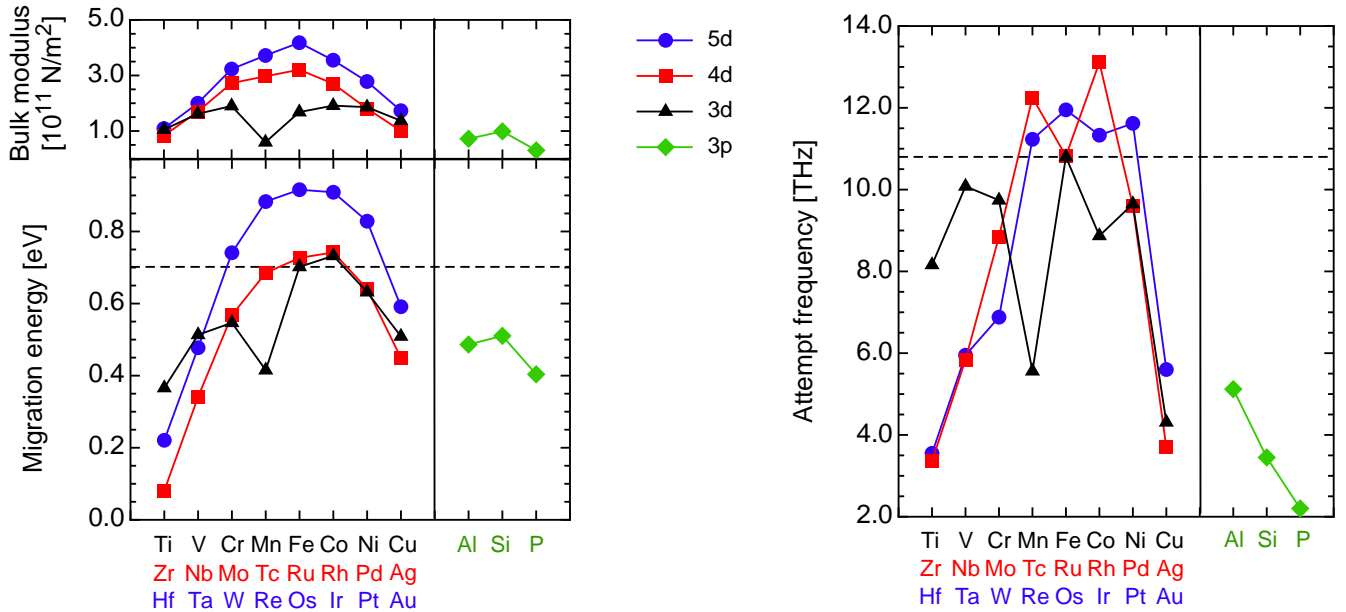


FIG. 4: DFT-computed solute migration barriers and attempt frequencies (ω_2). In the above-left panel, experimental bulk moduli of the pure elements [57]. The dashed lines represent the values in pure Fe.

way:

$$E_{ij}^{\text{SP}} = E_{ij}^{\text{mig}} - E_0^{\text{mig}} - E_i^{\text{b}}, \quad (13)$$

where $E_0^{\text{mig}}=0.70$ eV is the migration energy in pure iron. E_{ij}^{SP} embodies therefore the deviation from the saddle-

point energy in pure Fe, due to the interactions of the solute with the hopping vacancy. Moreover, since $E_{ij}^{\text{mig}} - E_{ji}^{\text{mig}} = E_j^{\text{b}} - E_i^{\text{b}}$ due to the detailed-balance principle, it is easy to derive that $E_{ij}^{\text{SP}} = E_{ji}^{\text{SP}}$.

E_{ij}^{SP} is shown for each jump type in the middle panels

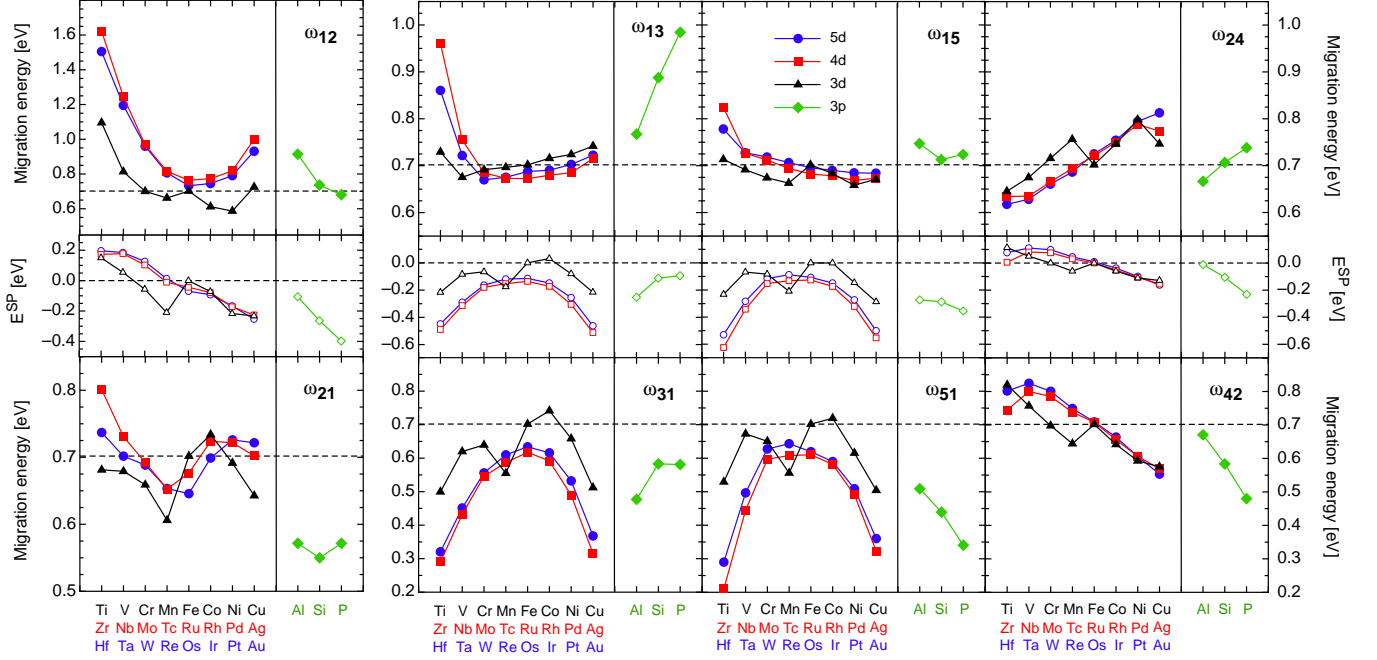


FIG. 5: DFT-computed iron migration barriers ω_{ij} in the vicinity of a solute atom, according to the jump-frequency nomenclature of Fig. 1. The dashed lines mark the values in pure Fe (ν_{Fe}). In the middle panels, the saddle-point contribution to each migration barrier, obtained by removing the initial-state binding energy and the pure-Fe vacancy migration barrier ($E_{ij}^{\text{SP}} = E_{ji}^{\text{SP}}$).

of Fig. 5. The trends show a smooth variation with the d-band filling that closely resembles that of the binding energies. Namely, E_{13}^{SP} and E_{15}^{SP} are very similar to the 1nn binding energy, whereas E_{12}^{SP} and E_{24}^{SP} are remarkably close to $E_{2\text{nn}}^{\text{b}}$. Even the magnitude of E_{12}^{SP} matches that of $E_{2\text{nn}}^{\text{b}}$, while the magnitudes of the other jumps are dampened. This suggests that the saddle-point electronic interactions are similar to those occurring in the corresponding end states, and that the 2nn interaction dominates for the transitions to and from the 2nn configuration. Such interactions progressively fade out for saddle-points that are further away from the solute.

The final shapes of the migration energy trends are then determined by the combination of the SP trends and the binding energy ones. For the ω_{13} and ω_{15} jumps, the 1nn binding energy contribution is opposed, leading to values close to the background ω_0 , with the exception of the early TM's for which the 1nn binding energy is very strongly attractive. The situation is more complex for the ω_{12} and ω_{21} jumps. For the former, the superposition of SP and 1nn binding energy yields smooth trends with very high barriers, whereas for the latter the 2nn binding energy contribution has opposite sign and causes a very sharp-cornered behavior. These jumps, which are very important for vacancy drag, are therefore determined by a complex balance between SP properties and binding energies.

Attempt frequencies

The solute attempt frequencies (for the ω_2 jump) are shown in Fig. 4. The results refer to calculations in 53-atom cells only, because of the high computational cost required. However, the attempt frequencies for Fe and Al were computed in 127-atom cells as well. It was found that in both cases the attempt frequency in the bigger simulation cell is about 10% larger. For this reason, the values shown in Fig. 4 are considered to be affected by an uncertainty of $\pm 10\%$.

The shapes of the group trends are again similar to those found previously for binding energies and migration barriers, although the behavior is here more irregular. The 3d row is M-shaped once again because of the odd behavior of Mn, whereas the expected parabolic behavior of the other rows is disturbed by some numerical noise (5d) and the out-of-trend value of Ru.

In general, it is evident that solutes with a low migration barrier are also characterized by a lower attempt frequency. This compensation effect is in qualitative agreement with the Meyer-Neldel rule (MNR), which was reported for the first time to describe conduction processes in disordered materials [61], and has thereafter been observed for several thermally-activated processes, not limited to condensed-matter physics [62]. For what concerns diffusion phenomena, the MNR has been successfully applied to surface self-diffusion [63] and adatom diffusion

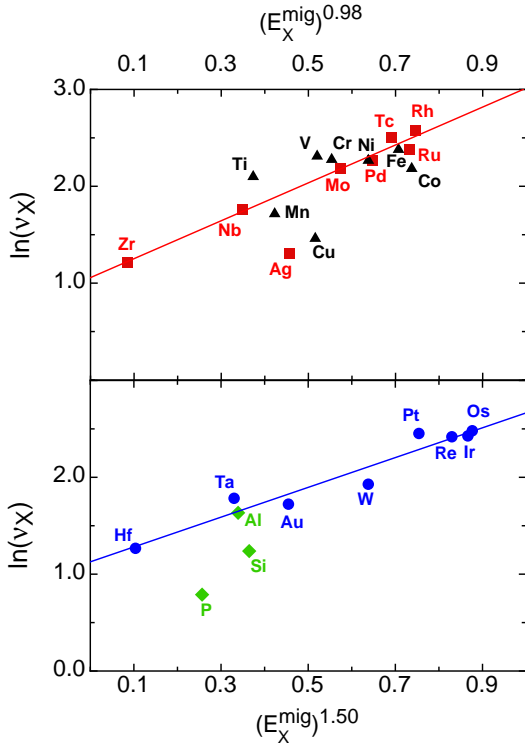


FIG. 6: Meyer-Neldel plot of migration energies versus attempt frequencies for 3d and 4d metals (above), and 5d metals and 3p elements (below). The fitting lines for the 4d and 5d elements are obtained with the least-square method.

[64] in Cu. In both cases, the activation energies and the prefactors were obtained by means of molecular dynamics simulations and were found to be linked by the following relationship:

$$\nu_x = \nu_0 \exp\left(\frac{E_x^{\text{mig}}}{\epsilon_0}\right)^\alpha, \quad (14)$$

where the process-dependent constants ν_0 and ϵ_0 , as well as the exponent α , were used as fitting parameters. ϵ_0 is also referred to as the Meyer-Neldel energy (MNE) [62]. Hence, according to the MNR, when plotting $(E_x^{\text{mig}})^\alpha$ versus $\ln(\nu)$, the data should lie on a straight line. For migration processes, the exponent α determines what types of phonons are involved. According to some phenomenological models [65, 66], an exponent α between 0.5 and 1 implies the main contribution by acoustic phonons.

It is therefore interesting to investigate if solute migration in an iron matrix can be also quantitatively described by Eq. 14. The fitting could not be performed on the whole set of data, but it was at any rate successful on the single rows individually. The fitting results are shown in Fig. 6. An exponent $\alpha = 0.98$ was found to fit best the 4d elements and some of the 3d elements, whereas $\alpha = 1.5$ was found to describe well the 5d row. The fitting could not be performed on the 3p elements,

because of the limited amount of data points. The fitting led to the same $\nu_0 = 3$ THz for both rows, but with a different MNE, namely $\epsilon_0 = 0.52$ eV (4d) and $\epsilon_0 = 0.73$ (5d). Such values are considerably higher than the Debye temperature in iron (0.04 eV), and also larger than what reported by previous works ($\epsilon_0 = 0.074$ eV) [63, 64]. In addition, the difference is similar to the difference in solute migration energy between the 4d and 5d elements. In some models [62], the ratio $E_x^{\text{mig}}/\epsilon_0$ is claimed to be related to the mean number of excitations that are necessary for a solute jump. Here, this quantity is seemingly constant between the 4d and 5d series. Finally, the noble metals Ag and Cu are found to lie out of the trend (the 4d fitting was performed by neglecting the Ag data point). Therefore, it can be concluded that this set of data can be also quantitatively fitted into the MNR, although with some exceptions, in particular the 3d elements and the noble metals. The higher exponents found here with respect to the Cu diffusion studies [63, 64] might indicate that solute diffusion is actually guided by local optical modes, which are strongly related to the solute-vacancy chemical bonding.

Solute-vacancy drag

The vacancy drag tendencies as functions of temperature are shown in Fig. 7a. The wind factor L_{xv}/L_{xx} is positive when drag occurs, and negative otherwise. As was already highlighted for some impurities [15], all curves are S-shaped, going from vacancy drag at low temperature to the inverse Kirkendall mechanism at high temperature. The flux-coupling strength determines the transition temperature, shifting the curve along the temperature axis.

It is possible to observe a strong correlation between drag tendencies and 1nn and 2nn binding energies. Solutes with 1nn and 2nn attractive characters with vacancies are dragged up to higher temperatures, with a smooth transition; conversely, solutes with a 1nn binding interaction and a 2nn repulsive one are characterized by a sharper transition and a lower transition temperature. This proves that vacancy drag can occur also in presence of a repulsive 2nn interaction, contrary to previous statements [26, 27], as a consequence of the combination of the ω_{ij} jump frequencies. In addition, vacancy drag does not occur for weakly-interacting elements such as Cr and V, whereas Co is dragged below 450 K, in spite of the absence of a 1nn binding interaction. Hence, vacancy drag, although minimal, can occur even thanks to attractive 2nn interactions only. It is possible therefore to conclude that the 1nn binding interaction is surely the dominant factor, if present, but does not represent a necessary condition for vacancy drag. Conversely, a binding 2nn interaction can considerably extend the vacancy drag range, but a repulsive one is definitely negligible if paired

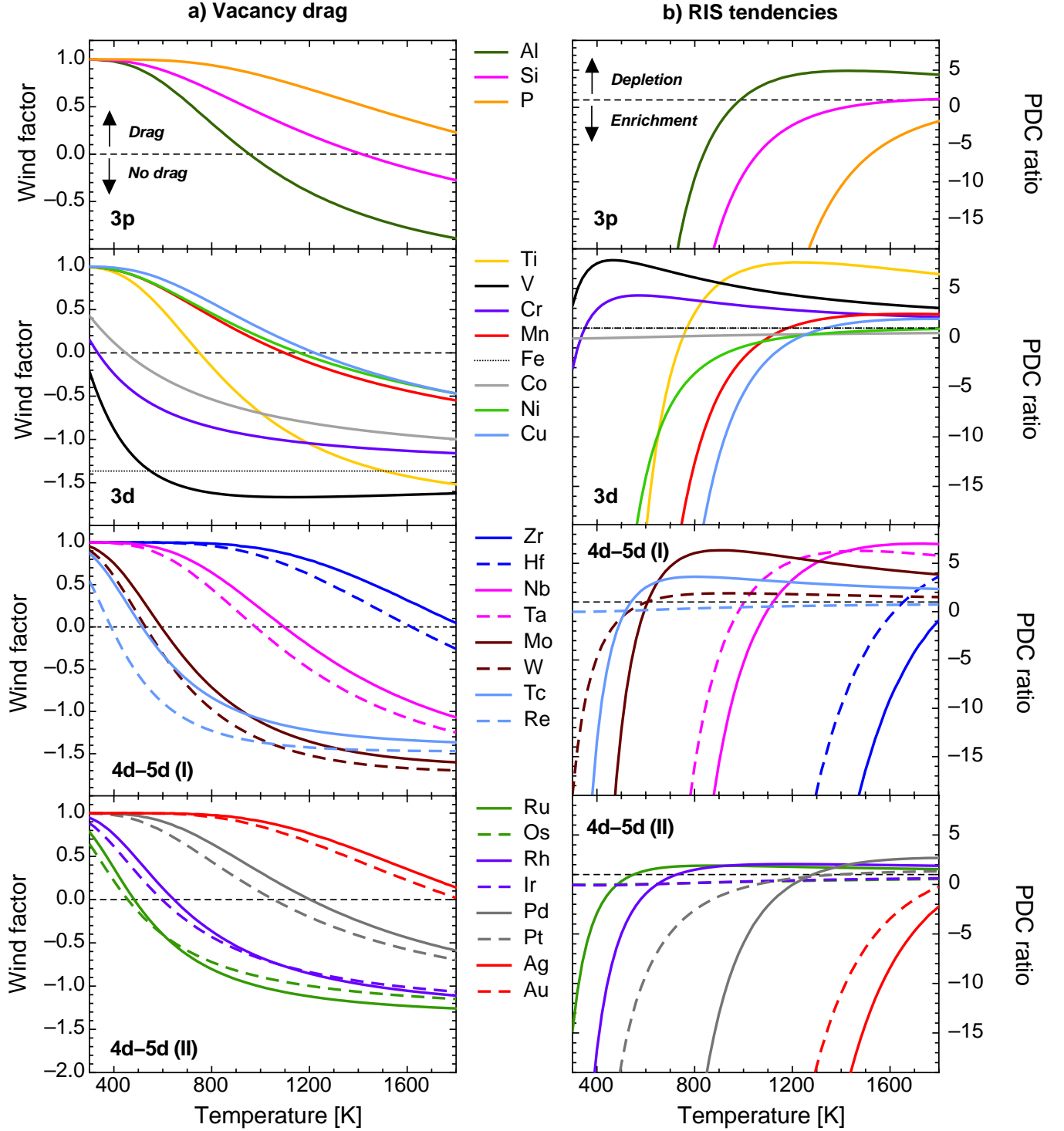


FIG. 7: a) Solute-vacancy drag tendencies as functions of temperature for the Fe(x) dilute binary alloys. Drag occurs for positive values of the wind factor. b) Ratio of solute-to-iron partial diffusion coefficients (PDC) as defined in Eq. 3. Solute enrichment (via vacancy mechanism) occurs for values of this ratio smaller than unity (the solute is slower than Fe) or negative (vacancy drag). The lines of Ir and Os are perfectly superposed.

with an attractive 1nn one.

For the 4d and 5d elements, the curves of Fig. 7a are coupled in order to show that elements with the same number of electrons in the outermost d-band are also characterized by very similar flux-coupling behaviors, thanks to the similar binding-energy trends. Drag is systematically stronger for the 4d metals, because of the stronger 1nn binding. It is worthwhile noticing that the drag tendency is completely independent from the solute jump frequency. It is also necessary to point out that the (already strong) drag tendency of the band-end elements is most likely underestimated because of the 5nn solute-vacancy interaction, which is neglected in this SCMF model.

The group trends of the wind factor at 600 K and of the transition temperature are shown in Fig. 8a and 8c, respectively. Because of the strong correlation with the binding energy, the trends are very similar: a parabolic shape for the 4d and 5d TM's, and a W-shaped curve for the 3d metals. Flux coupling for Mn is considerably stronger than its neighbors on the periodic table. The only exception is represented by Cu, for which the transition temperature is markedly lower than the other noble metals. Conversely, the neighboring solute (Ni) matches the drag tendency of the corresponding metals (Pd and Pt). This is a direct consequence of the anomaly observed in the 2nn binding energy for the noble metals (Fig. 3), which is reflected onto a lower ω_{24} barrier (Fig. 5). This anomaly implies a higher escape frequency from 2nn in FeCu, and therefore a weaker drag tendency. In a previous study [15], this anomaly was erroneously ascribed to the stronger Ni-vacancy 2nn interaction with respect to the 1nn one, but the systematic approach of this work clarifies that the exception is actually represented by Cu. It is also remarkable that a seemingly small difference in the ω_{24} frequency, which is often disregarded in flux-coupling studies, has such a large effect on the Cu drag transition temperature (600 K lower than Ag, Au).

The effect of the 2nn binding is visible in Fig. 8c, as the transition temperatures are slightly higher for the late TM's than the early ones. In order to take into account the effect of both the 2nn binding energy and the saddle point, this asymmetry is discussed in terms of a combination of jump frequencies. In first approximation, the drag tendency depends on the ratio $\omega_{12}/(\omega_{13} + \omega_{15})$, as ω_{12} allows the vacancy to turn around the solute, whereas ω_{13} and ω_{15} cause the pair to dissociate. It can be observed from Fig. 5 that such ratio is lower for the early TM's and higher for the late ones.

In conclusion, vacancy drag is the most common solute-diffusion mechanism at low temperatures for all impurities except Cr and V. Any low-temperature model assuming an inverse Kirkendall mechanism and neglecting flux coupling is therefore likely not to yield the correct transport properties. The found strong correlation with 1nn and 2nn interaction energies confirms that drag ten-

dencies can indeed be qualitatively inferred from such energies, although the Onsager matrix must be always calculated in order to determine the strength and extent of vacancy drag. However, transport properties are in first place determined by kinetics, or in other words by the saddle-point properties. It was shown in Fig. 5 that such properties show the same trends as the binding energies, which justifies why it is possible to correlate the flux-coupling tendencies with thermodynamic interactions. Moreover, given the electronic origin of both trends that was discussed in the previous sections, it is also expected to find similar vacancy-drag tendencies in other bcc transition metals, confirming that vacancy drag might be a widespread phenomenon not limited only to iron-based dilute alloys.

RIS tendencies

In irradiated materials, flux coupling can produce RIS at defect sinks because of the permanent production of defects. When vacancy drag occurs, vacancies diffusing to sinks carry solute atoms, causing the solute species to enrich for instance on grain boundaries or dislocations [34]. In the absence of drag, instead, the solute and matrix atoms diffuse away from the sink surface at a relative speed given by the PDC ratio (Eq. 3): if this ratio is smaller than 1, solute atoms are slower and enrichment still occurs, whereas depletion is observed in the opposite case.

The RIS tendencies due to vacancy-diffusion only (thus assuming a neutral contribution from SIA's and neglecting the prefactor of Eq. 4) are shown in Fig. 7b as functions of temperature. It is possible to distinguish two types of behavior. Most elements switch from an enrichment tendency due to drag at low temperature, to a depletion tendency in the high-temperature range, passing through a short interval of enrichment without drag. This is not uncommon: switch of RIS tendency from enrichment to depletion as a function of temperature has been observed, for instance, in FeCr alloys [5]. On the other hand, a few elements, namely Co, Re, Os, and Ir, are slower than Fe at any temperature and hence enrichment always occurs, independently from the flux-coupling sign. Such elements are the "slow diffusers" in Fe, and the reason for their behavior is discussed in the next section.

For the "fast diffusers", the trends are obviously correlated to vacancy drag. The early TM's, with a repulsive 2nn interaction, are characterized by a sharp transition from enrichment to depletion, whereas the late TM's have a smoother transition and a higher switchover temperature. The weakly-interacting elements such as Cr and V deplete at all temperatures because of the absence of drag. An analogous shift between corresponding 4d and 5d metals can be observed, for the same reason that was

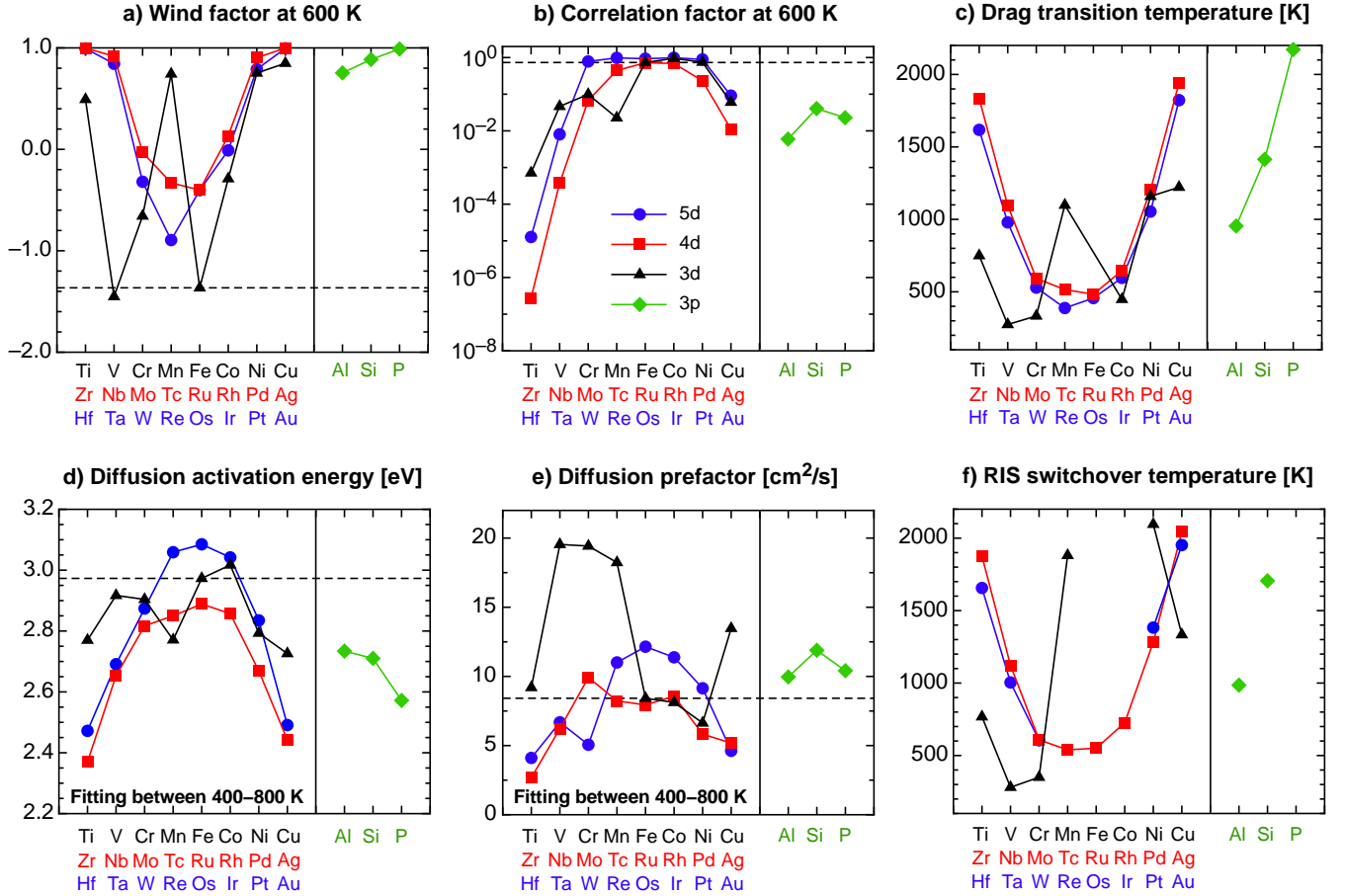


FIG. 8: Group trends of a) the wind factor at 600 K, b) the solute-diffusion correlation factor at 600 K, d) the solute diffusion activation energy and e) prefactors corresponding to a least-square fitting between 400 and 800 K, the transition temperatures c) from drag to non-drag tendencies, and f) from RIS enrichment to depletion tendencies. In the latter, the elements with a temperature-independent enrichment tendency are not shown. The dashed lines represent the values for pure Fe.

mentioned for the drag tendency.

The switchover temperature as a function of the d -band filling is shown in Fig. 8f. Elements that are consistently enriched are not shown (for P the switchover temperature is very high). In spite of the missing elements, it is possible to recognize the same curve shapes, which are closely related to the vacancy drag trends of Fig. 8c. Again, Cu has an exceptionally low critical temperature because of the same aforementioned anomalies. On the other hand, the critical temperature for Ni is much higher than the corresponding metals (Pd, Pt), in spite of comparable drag tendencies. This is related to a non-trivial combination of the ω_{ij} frequencies, which highlights the importance of kinetics in solute-diffusion modeling.

The outcome of this flux-coupling study can be applied to several observations of solute transport in irradiated ferritic and F/M alloys. For instance, vacancy drag can explain the nucleation of solute clusters containing Mn,

Ni on pre-existing Cu clusters [8, 67], interstitial loops [3, 68, 69] and dislocations [70], as well as the formation of Cu-vacancy clusters [71]. In RPV surveillance materials, precipitation of impurities such as Mn, Ni, Si, Cu, and P was observed with atom-probe tomography [8], and can also be explained by vacancies dragging solute atoms towards small sinks such as invisible interstitial loops, as suggested in [3, 11]. In these clusters, however, no Mo is found, in spite of its non-negligible concentration. This work shows that the drag transition temperature of Mo (593 K) is very close to that of RPV operation (573 K), hence confirming the weakness of the flux coupling with respect to the other mentioned impurities. In addition, several experiments have shown the segregation of P [8, 70] and Mn [69] on grain boundaries and dislocations, as well as the enrichment profiles at grain boundaries of other elements such as Si, Ni, Cu, and Cr [5]. The Cr RIS tendency cannot be comprehensively discussed here because of the stability of the Fe-

Cr mixed dumbbell, which suggests that the interstitial contribution to the RIS tendency cannot be neglected. As for Si, Ni, and Cu, the bell-shaped enrichment tendencies observed in [5] as functions of temperature are compatible with the trends of Fig. 7b. At low temperature, there should be strong vacancy drag and therefore a marked enrichment tendency according to this work's model; however, at such temperatures defects are very slow, and defect recombination is enhanced. Therefore, even in steady-state conditions no RIS occurs and no change of solute concentration is found. With increasing temperature, the enrichment tendency decreases due to the PDC ratio, whereas defect mobility is enhanced, consistently with the experimental observations. However, this represents only a secondary effect, as RIS is mostly dampened and eventually stopped by the vanishing difference between point defect saturation and the corresponding equilibrium values.

Solute-vacancy correlations

The solute correlation factor f_x appearing in Eq. 6 accounts for the solute "slowing down" due to the probability of performing two consecutive exchanges with a neighboring vacancy (forward and backward), which do not contribute to an effective displacement of the solute atom. In a non-interacting bcc alloy (or in a pure bcc metal), this corresponds to the geometric factor $f_0=0.727$ [17]. f_x can range from 0 to 1, and tends to f_0 as temperature increases, since correlations are smoothed by the Boltzmann factor $1/k_B T$.

The correlation factors are here obtained by means of Eq. 17 and are shown for each solute group in Fig. 8b at 600 K. The temperature-dependent factors are provided for each solute in the Supplemental Material [72]. It should be pointed out that the correction provided by Eq. 17 with respect to the previously available formula [17] does not significantly affect the value of the solute-diffusion coefficients.

Once again, the group trends are M-shaped for the 3d metals and bell-shaped for the 4d and 5d metals. The top of the curves is flat, because the correlation factor cannot exceed 1. These trends are clearly correlated to the solute migration barrier, which is characterized by the same shape and the same type of asymmetry. The very low migration barriers of the early TM's make the correlation factor (and hence the solute diffusion coefficient) decrease by several order of magnitudes, and this effect grows stronger at low temperatures, up to 10^{-13} for Zr at 300 K. The compensation provided by the solute attempt frequency is secondary, and negligible at low temperatures. Solute-vacancy correlations can therefore make solute diffusion considerably slower, as the solute can effectively "trap" the vacancy in a 1nn position. Moreover, they introduce deviations from the Arrhenius

behavior at low temperatures, contributing to the inaccuracy of extrapolations from high-temperature diffusion data.

This qualitative description can be completed by comparing ω_2 with the other jump frequencies. The correlation strength can be connected with the probability of the complementary jumps to ω_2 , namely the jumps leading to a dissociation of the solute-vacancy pair at 1nn. One can define an average dissociation frequency ω_{1*} as:

$$\omega_{1*} = \frac{1}{7} (3\omega_{12} + 3\omega_{13} + \omega_{15}) , \quad (15)$$

where the average is weighed upon the available dissociation paths. The ratio ω_{1*}/ω_2 represents therefore the probability of escaping the 1nn configuration and allowing the vacancy to access the paths around the solute atom to produce a net solute displacement. In Fig. 9, the calculated correlations factors at 600 K are compared to the ω_{1*}/ω_2 ratio at the same temperature. The astounding match between the two highlights that solute-vacancy correlations are indeed controlled by this frequency ratio, in accordance to Manning's early formulation of f_x . [73] For the early TM's, hence, the strong correlation is not determined only by the low migration barrier, but is enhanced by the high barriers for the ω_{12} and ω_{13} jumps, which is not the case for the late TM's. It can be therefore concluded that solute-vacancy correlations are stronger for the band-end elements, and particularly strong for the early ones, because of the combined effect of low solute migration barriers, high 1nn solute-vacancy binding energy and the saddle-point electronic interactions.

With the same argument it is possible to explain why some elements, such as Co, Ni, and the middle-row elements of the 4d and 5d bands, show a "negative correlation", i.e. their correlation factor is above the geometric factor f_0 . For these elements, the ω_{1*}/ω_2 ratio is larger than 1, which entails that in the 1nn configuration the vacancy has a larger probability to escape than to exchange with the solute. Hence the correlation factor approaches 1 because the vacancy tends to "avoid" the solute, or anyway not to undergo repeated exchanges. This efficiency of the diffusion process from a kinetic standpoint is anyway counterbalanced by thermodynamics, since for these elements the 1nn binding energy is small and thus so is the probability to have a vacancy next to the solute, which is a necessary condition for solute diffusion to occur. On the other hand, for the strongly-correlated solutes the ω_{1*}/ω_2 ratio is very small and the vacancy does not have the possibility to leave the solute, therefore impeding solute diffusion because the vacancy is trapped and cannot move.

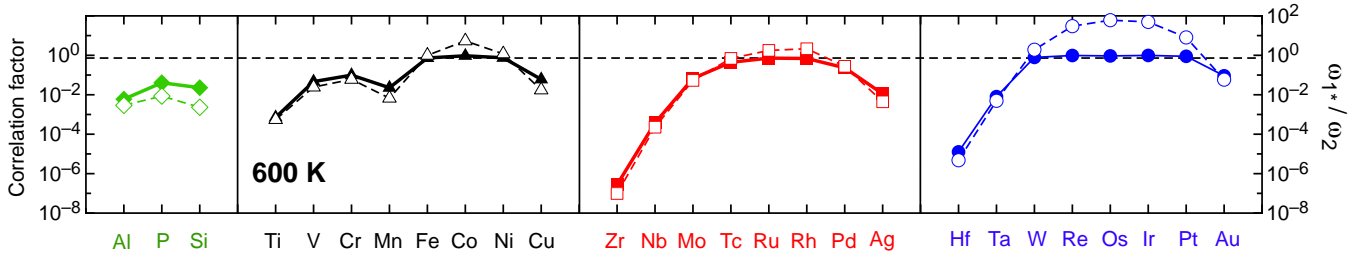


FIG. 9: Solute-diffusion correlation factors (full symbols) and ratio of average 1nn dissociation frequency ω_{1*} to solute jump frequency ω_2 at 600 K. The correlation factor cannot assume values larger than 1. The dashed line marks the the correlation factor value in pure Fe ($f_0=0.727$).

Solute diffusion coefficients

The self- and solute diffusion coefficients, obtained by means of Eq. 5, are shown respectively in Fig. 10 and 11 for the impurities for which experimental measurements are available, and are compared with experimental measurements [32, 74, 75] and previous calculations [21–24]. For the sake of consistency with the solute attempt-frequency calculations, the diffusion coefficients are calculated with the values for S_v^f and ν_{Fe} obtained in 53-atom cells. Each diffusion coefficient is corrected with the magnetic factor of Fig. 2, in order to account for the effects of the FM-to-PM transition. Because of the magnetic-related non-Arrhenius behavior, the fitting in the FM region is extremely sensitive to the chosen temperature range. In order to provide values of Q and D_0 for low-temperature applications, the fitting results in the temperature range 400-800 K are reported in Fig. 8d (Q) and 8e (D_0). The numerical values of Q and D_0 , as well as the solute diffusion coefficients in the temperature range (800-1800 K) for all solutes are to be found in the Supplemental Material [72].

There is an overall satisfactory agreement with experiments. The perfect match with self-diffusion measurements proves the quality of the magnetic model, which did not entail any fitting procedure. The solute diffusion coefficients are also well matched with experiments, for what concerns the activation energy Q (i.e. the slope in the Arrhenius plot) and the change of slope across the Curie temperature, with the exception of Mn. The accuracy in the Q value confirms the reliability of this model in the prediction of low-temperature solute diffusion coefficients. Moreover, the comparison with previous calculations in iron with Al [23], P [21], Cu [22], Mo [24], and W [24] solute atoms shows that the values obtained in this work are always in better agreement with experiments, although the difference with the calculations in [24] is minimal. The mismatch for Mn diffusion shows the inadequacy of the pure-Fe magnetic model for this peculiar system. In order to properly describe solute diffusion across the Curie temperature, the direct effect of magnetism on the solute PM activation energy should be

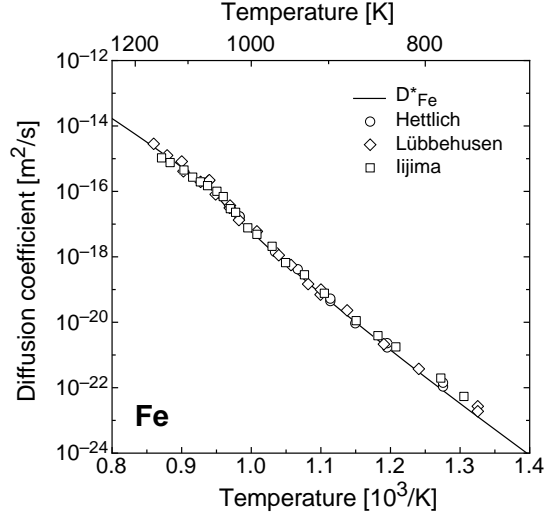


FIG. 10: Tracer self-diffusion coefficient calculated in this work, and comparison to experimental measurements [75].

carefully modeled, hence calling for further investigations of the Mn solute magnetic behavior in Fe.

On the other hand, for a few solutes the agreement in the diffusion prefactor is not as satisfactory. The prefactor is consistently overestimated, although the difference is in most cases limited, and it does not exceed one order of magnitude, approximately. In Fig. 12, the diffusion coefficients here calculated are compared to experimental measurements at 1100 K. It can be observed that the mismatch is small for the middle TM's (except Mn) and progressively increases towards the band ends, which might suggest the presence of a systematic error. This error might be due to the assumption $\nu_{ij} = \nu_{Fe}$ for all iron jumps, or to the inadequacy of a 2nn thermodynamic model for the large-sized solutes, which are characterized by a non-negligible 5nn interaction. It is also worthwhile mentioning that some entropic contributions, such as the binding entropy or the electronic entropy, are here neglected. The effect of lattice expansion at non-zero temperature might also play a role, although this effect

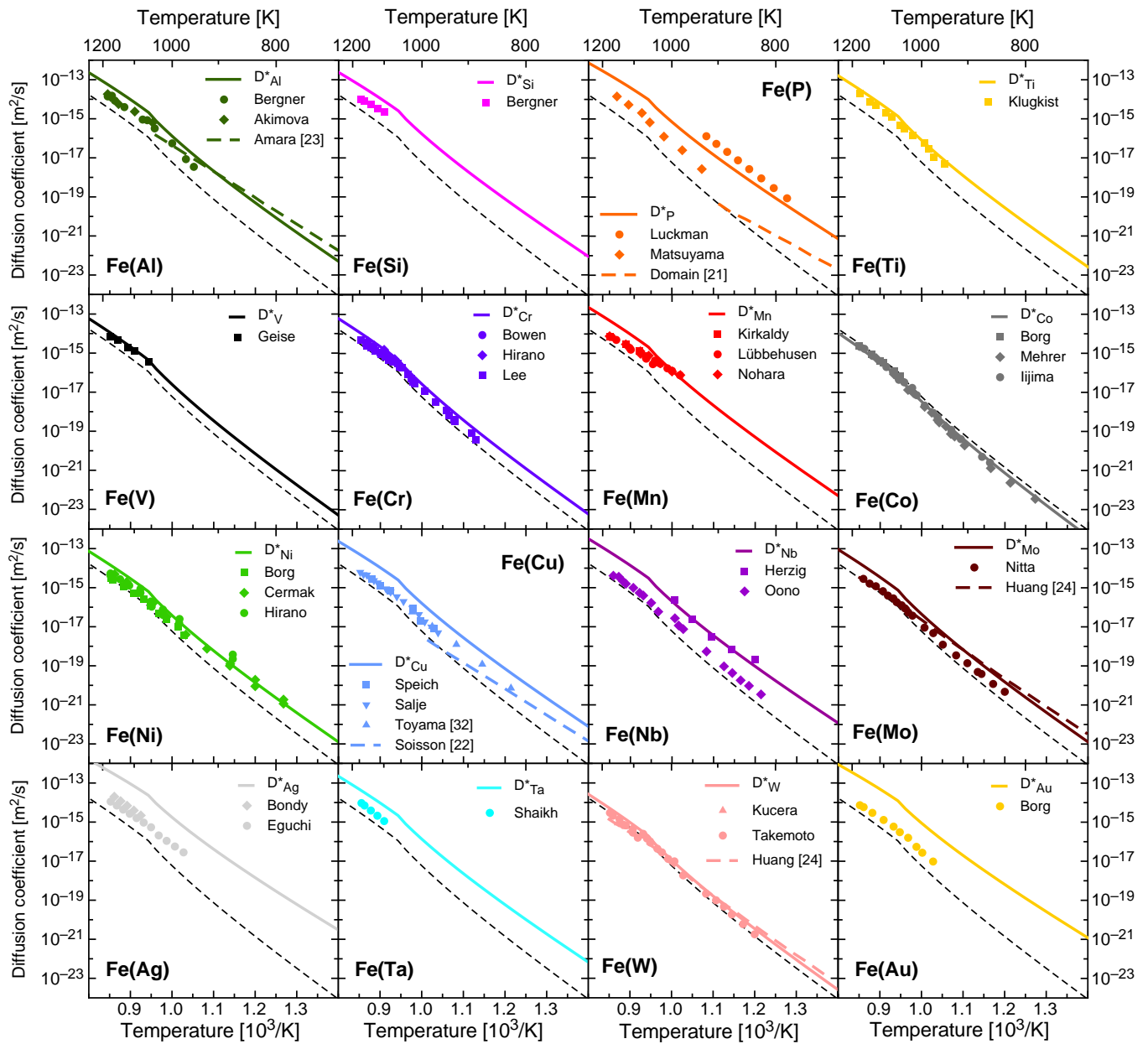


FIG. 11: Solute tracer diffusion coefficients calculated in this work, and comparison to experimental measurements [32, 74, 75] and previous calculations [21–24].

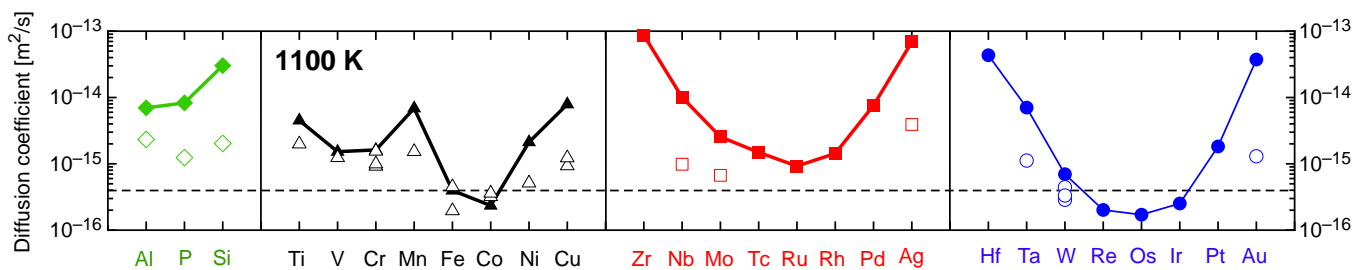


FIG. 12: Solute tracer diffusion coefficients at 1100 K, as calculated in this work (full symbols) and from experimental measurements (open symbols) [32, 74, 75].

would be temperature dependent. Since the mismatch affects the prefactor only, the accuracy of the calculated solute diffusion coefficients at any temperature can be improved by simply shifting the curve down by the mismatch factor, inferable for instance from Fig. 12. The mismatch values can also be found in the Supplemental Material [72].

The activation energies shown in Fig. 8d follow the same group trends observed for many other quantities in this work. These trends, which are also visible in the experimental coefficients of Fig. 12, are analogous to those obtained for solute diffusion in Ni [30] and Al [59]. Since they are mainly determined by the solute migration barrier trends of Fig. 4, it is possible to state that the activation energy for solute diffusion is controlled by the saddle-point interactions discussed in the previous section. However, the Q curve is more symmetric than E^{mig} because of the compensation effect given by the correlation factor, and to a smaller extent by the attempt frequency, in accordance with the MNR. As previously discussed, solute-vacancy correlations are stronger for the early TM's and reduce the diffusion coefficient by several orders of magnitude, especially at low temperature. As a consequence, the effective activation energy of the late TM's is comparable to that of the early TM's.

On the contrary, the D_0 trends are not trivial to explain, as they are affected by f_x and the less smooth behavior of the solute attempt frequency (Fig. 4b). However, the usual M-shaped and bell-shaped trends can be obtained by applying the aforesaid correction to the prefactor, based on the mismatch with the experiments (under the assumption that the mismatch is bell-shaped also for solutes with missing experimental measurements).

Among all TM impurities, Co is the only one known to be a slower diffuser than Fe. This exception, which is well caught by the calculations in this work, might be mistakenly ascribed to the larger migration barrier of Co (0.73 eV) with respect to Fe (0.70 eV). However, this is also the case for other impurities such as Ru, Rh, W, Re, Os, Ir, Pt (Fig. 4). It was suggested that such behavior might be due to kinetic correlations [56]. This can be checked by analyzing the ratio of solute to self-diffusion coefficient [35]:

$$\frac{D_x^*}{D_{\text{Fe}}^*} = \frac{f_x \nu_x}{f_0 \nu_0} \exp \left[-\frac{(\Delta E^{\text{mig}} + E_{1\text{nn}}^{\text{b}})}{k_B T} \right], \quad (16)$$

where $\Delta E^{\text{mig}} = E_2^{\text{mig}} - E_0^{\text{mig}}$. Since the solute attempt frequencies are not very different from ν_{Fe} , the D_x^*/D_{Fe}^* ratio is controlled by the exponential term and the correlation factor f_x . Moreover, since $f_x < 1$, the exponential term dominates if f_x is larger than f_0 . Since the correlation factor for all the aforementioned impurities is close to unity, the exponential term is dominant and kinetic correlations play a minor role. Then, the ratio of Eq. 16 is lower than 1 if $\Delta E^{\text{mig}} > -E_{1\text{nn}}^{\text{b}}$. In other words, the 1nn

binding energy counteracts the higher solute migration barrier, because it increases the probability of having a vacancy next to the solute. Therefore, Ru, Rh, W, and Pt are faster diffusers than Fe because their 1nn binding energy is larger than ΔE^{mig} , as is confirmed by experiments for W. On the other hand, Co is a slow diffuser because the 1nn interaction is very weakly repulsive. Therefore, the low Co diffusivity is due to the (missing) thermodynamic interaction with a vacancy at 1nn rather than to kinetic correlations. Analogously, this model predicts that Re, Os and Ir are slow diffusers as well, although no experiments have been yet performed to confirm this prediction. The method proposed in this work is therefore useful to predict the diffusion coefficients of impurities for which experimental measurements are missing, and to provide such quantities in low temperature ranges that are not accessible by experiments.

CONCLUSIONS

The aim of this work was to investigate impurity diffusion in bcc iron with a systematic approach to all the 3d, 4d, and 5d solutes, as well as Al, Si, and P. This was achieved by combining electronic structure calculations of solute-vacancy interactions, jump frequencies and attempt frequencies with an accurate mean-field computation of transport coefficients. From the latter were inferred solute-vacancy flux-coupling tendencies, correlations and diffusion coefficients.

Remarkably, the variation of almost all properties with respect to the d-band filling follows similar trends: the properties of 4d and 5d impurities are bell-shaped, whereas 3d elements are influenced by magnetic interactions and show consistently an M- (or W-)shaped trend because of the peculiar behavior of Mn. Such common trends are all determined by the character of electronic interactions between the solute and the neighboring atoms next to a vacancy. Common size-factor (misfit-strain) arguments are shown to play only a minor role, in agreement with calculations in other matrices. The main exception to the general trends is represented by the 2nn binding energy, which varies linearly along the d-band. Similar interactions are also found at the saddle point of a migrating iron atom next to a solute. The migration barriers are therefore determined by the combination of saddle-point interactions and binding energies. Conversely, the solute migration barriers are governed mainly by the compressibility of the corresponding solid: large atoms are also more compressible and can hence migrate faster. However, this is partially compensated by two effects: a lower attempt frequency, in accordance with the Meyer-Neldel compensation law, and stronger correlations lowering the diffusion coefficient by several orders of magnitude. The combination of high migration barrier and low 1nn binding energy makes cobalt a "slow

diffuser” in iron, and the same behavior is predicted for other impurities (namely Re, Os, and Ir), although experimental measurements for these solutes are still missing.

Vacancy drag is found to be the dominant flux-coupling mechanism at low temperature for almost all impurities. Contrary to common beliefs, drag can occur also for impurities with repulsive 2nn interactions with vacancies, as the 1nn binding energy is the dominant factor. The common origin of binding energies and saddle-point interactions allows the coupling tendencies to be qualitatively analyzed from binding-energy trends only, although a quantitative analysis must rely on the transport coefficient calculation. Finally, drag causes a clear solute-enrichment tendency at defect sinks, and a switchover to depletion across a large range of temperatures. Conclusions about RIS tendencies are to be corroborated by the analysis of dumbbell transport.

In conclusion, this systematic investigation has revealed the common electronic origins of flux-coupling and solute-diffusion trends, contributing to a deeper understanding of impurity-diffusion mechanisms in metals and providing a reliable, *ab initio*-based kinetic database of diffusion properties. Such common origins are seemingly solute-dependent rather than matrix-dependent, suggesting that similar trends might arise as well in other transition metals. This work has also yielded solute diffusion coefficients in good agreement with experiments, providing ready-to-use low-temperature values that are not experimentally viable, and even for the missing impurities. The provided database of diffusion properties represents therefore a valuable contribution that can be employed in the modeling of a vast range of diffusion-controlled aging phenomena.

ACKNOWLEDGMENTS

This work has received funding from the Euratom research and training programme 2014-2018 under the grant agreement No 661913 (SOTERIA). The paper reflects only the authors’ view and the European Commission is not responsible for any use that may be made of the information it contains. It contributes to the Joint Program on Nuclear Materials (JPNM) of the European Energy Research Alliance (EERA). This work was also funded by Vattenfall AB and Göran Gustafsson Stiftelse. The high-performance computing resources were provided by the Swedish National Infrastructure for Computing (SNIC). Furthermore, the authors acknowledge C. Marinica, F. Willaime, and B. Legrand for the fruitful discussions.

* messina@kth.se

- [1] S. C. Glade, B. D. Wirth, G. R. Odette, and P. Asoka-Kumar, *J. Nucl. Mat.* **351**, 197 (2006).
- [2] M. Hernández-Mayoral and D. Gómez-Briceño, *J. Nucl. Mat.* **399**, 146 (2010).
- [3] E. Meslin, B. Radiguet, and M. Loyer-Prost, *Acta Mater.* **61**, 6246 (2013).
- [4] Y. Nishiyama, K. Onizawa, M. Suzuki, J. W. Andereg, Y. Nagai, T. Toyama, M. Hasegawa, and J. Kameda, *Acta Mater.* **56**, 4510 (2008).
- [5] J. P. Wharry and G. S. Was, *J. Nucl. Mat.* **442**, 7 (2013).
- [6] T. Toyama, Y. Nagai, A. Al Mazouzi, M. Hatakeyama, M. Hasegawa, T. Ohkubo, E. Van Walle, and R. Gerard, *Mater. Trans., JIM* **54**, 2119 (2013).
- [7] G. R. Odette and R. K. Nanstad, *JOM* **61**, 17 (2009).
- [8] M. K. Miller, K. A. Powers, R. K. Nanstad, and P. Efsing, *J. Nucl. Mat.* **437**, 107 (2013).
- [9] D. Terentyev, L. Malerba, and A. V. Barashev, *Philos. Mag. Lett.* **85**, 587 (2005).
- [10] M. Lambrecht and A. Almazouzi, *J. Nucl. Mat.* **385**, 334 (2009).
- [11] K. Yabuuchi, M. Saito, R. Kasada, and A. Kimura, *J. Nucl. Mat.* **414**, 498 (2011).
- [12] A. R. Allnatt and A. B. Lidiard, *Atomic Transport in Solids* (Cambridge University Press, Cambridge, 2003).
- [13] T. Garnier, M. Nastar, P. Bellon, and D. R. Trinkle, *Phys. Rev. B* **88**, 134201 (2013).
- [14] T. Garnier, V. R. Manga, D. R. Trinkle, M. Nastar, and P. Bellon, *Phys. Rev. B* **88**, 134108 (2013).
- [15] L. Messina, M. Nastar, T. Garnier, C. Domain, and P. Olsson, *Phys. Rev. B* **90**, 104203 (2014).
- [16] M. Nastar, *Philos. Mag.* **85**, 3767 (2005).
- [17] A. D. Le Claire, in *Physical chemistry: an advanced treatise*, edited by H. Eyring (Academic Press, New York, 1970).
- [18] P. Y. Serruys and G. Brebec, *Philos. Mag. A* **46**, 661 (1982).
- [19] Y. Okamura and A. R. Allnatt, *J. Phys. C: Solid State Phys.* **16**, 1841 (1983).
- [20] T. Garnier, D. R. Trinkle, M. Nastar, and P. Bellon, *Phys. Rev. B* **89**, 144202 (2014).
- [21] C. Domain and C. S. Becquart, *Phys. Rev. B* **71**, 214109 (2005).
- [22] F. Soisson and C.-C. Fu, *Phys. Rev. B* **76**, 214102 (2007).
- [23] H. Amara, C.-C. Fu, F. Soisson, and P. Maugis, *Phys. Rev. B* **81**, 174101 (2010).
- [24] S. Huang, D. L. Worthington, M. Asta, V. Ozolins, G. Ghosh, and P. K. Liaw, *Acta Mater.* **58**, 1982 (2010).
- [25] S. Choudhury, L. Barnard, J. D. Tucker, T. R. Allen, B. D. Wirth, M. Asta, and D. Morgan, *J. Nucl. Mat.* **411**, 1 (2011).
- [26] P. Olsson, T. P. C. Klaver, and C. Domain, *Phys. Rev. B* **81**, 054102 (2010).
- [27] C. S. Becquart and C. Domain, *Curr. Opin. Solid State Mater. Sci.* **16**, 115 (2012).
- [28] M. Nastar and F. Willaime, *Phys. Rev. B* **51**, 6896 (1995).
- [29] L. Ventelon, F. Willaime, C.-C. Fu, M. Heran, and I. Ginoux, *J. Nucl. Mat.* **425**, 16 (2012).
- [30] A. Janotti, M. Krčmar, C. L. Fu, and R. C. Reed, *Phys. Rev. Lett.* **92**, 085901 (2004).
- [31] M. Krčmar, C. Fu, A. Janotti, and R. C. Reed, *Acta Mater.* **53**, 2369 (2005).
- [32] T. Toyama, F. Takahama, A. Kuramoto, and H. Takamizawa, *Scripta Mater.* **83**, 5 (2014).

- [33] M. Nastar, Phys. Rev. B **90**, 144101 (2014).
- [34] M. Nastar and F. Soisson, *Comprehensive Nuclear Materials* (Elsevier Inc., New York, 2012) Chap. 1.18, pp. 471–496.
- [35] A. D. Le Claire, J. Nucl. Mat. **69-70**, 70 (1978).
- [36] N. Sandberg, Z. Chang, L. Messina, P. Olsson, and P. Korzhavyi, “Modeling of the magnetic free energy of self-diffusion in bcc Fe,” To be published.
- [37] B. Jonsson, Z. Metallkd. **83**, 349 (1992).
- [38] G. Kresse and J. Hafner, Phys. Rev. B **47**, 558 (1993).
- [39] G. Kresse and J. Hafner, J. Phys.: Condens. Matter **6**, 8245 (1994).
- [40] G. Kresse and J. Hafner, Phys. Rev. B **49**, 14251 (1994).
- [41] P. E. Blöchl, Phys. Rev. B **50**, 17953 (1994).
- [42] G. Kresse and D. Joubert, Phys. Rev. B **59**, 1758 (1999).
- [43] J. P. Perdew, K. Burke, and Y. Wang, Phys. Rev. B **54**, 16533 (1996).
- [44] G. Mills, H. Jonsson, and G. K. Schenter, Surf. Sci. **324**, 305 (1995).
- [45] H. Jonsson, G. Mills, and K. W. Jacobsen, in *Classical and quantum dynamics in condensed phase simulations*, edited by B. J. Berne, G. Cicciotti, and D. F. Coker (World Scientific, 1998).
- [46] G. Henkelman, B. P. Uberuaga, and H. Jonsson, J. Chem. Phys. **113**, 9901 (2000).
- [47] Y. Mishin, M. R. Sørensen, and A. F. Voter, Philos. Mag. A **81**, 2591 (2001).
- [48] G. H. Vineyard, J. Phys. Chem. Solids **3**, 121 (1957).
- [49] G. E. Lucas and R. Schäublin, Nucl. Instrum. Methods Phys. Res. B **267**, 3009 (2009).
- [50] R. D. Hatcher, R. Zeller, and P. H. Dederichs, Phys. Rev. B **19**, 5083 (1979).
- [51] S. S. Pohlson and P. N. Ram, J. Phys.: Condens. Matter **10**, 10901 (1999).
- [52] J. Wallenius, P. Olsson, C. Lagerstedt, N. Sandberg, R. Chakarova, and V. Pontikis, Phys. Rev. B **69**, 094103 (2004).
- [53] A. Seeger, Phys. Status Solidi A **167**, 289 (1998).
- [54] M.-C. Marinica, M. Athènes, and F. Willaime, *High temperature properties of vacancy and interstitial type defects in tungsten.*, Tech. Rep. WP13-MAT-01-IREMEV-01-03 (EFDA, 2014).
- [55] T. Ohnuma, N. Soneda, and M. Iwasawa, Acta Mater. **57**, 5947 (2009).
- [56] O. I. Gorbатов, P. A. Korzhavyi, A. V. Ruban, B. Johansson, and Y. N. Gornostyrev, J. Nucl. Mat. **419**, 248 (2011).
- [57] C. Kittel, *Introduction to Solid State Physics*, 8th ed. (Wiley, New York, 2004).
- [58] F. Willaime, A. Satta, and M. Nastar, Int. J. Quantum Chem. **77**, 927 (2000).
- [59] N. Sandberg and R. Holmestad, Phys. Rev. B **73**, 014108 (2006).
- [60] A. Claisse and P. Olsson, Nucl. Instrum. Methods Phys. Res. B **303**, 18 (2013).
- [61] W. Meyer and H. Neldel, Z. Tech. Phys. **12**, 588 (1937).
- [62] A. Yelon, B. Movaghar, and R. S. Crandall, Rep. Prog. Phys. **69**, 1145 (2006).
- [63] G. Boisvert, L. J. Lewis, and A. Yelon, Phys. Rev. Lett. **75**, 469 (1995).
- [64] M.-C. Marinica, C. Barreteau, D. Spanjaard, and M.-C. Desjonquères, Phys. Rev. B **72**, 115402 (2005).
- [65] D. Emin, Phys. Rev. Lett. **32**, 303 (1974).
- [66] A. Yelon, B. Movaghar, and H. M. Branz, Phys. Rev. B **46**, 12244 (1992).
- [67] P. B. Wells, T. Yamamoto, B. Miller, T. Milot, J. Cole, Y. Wu, and G. R. Odette, Acta Mater. **80**, 205 (2014).
- [68] E. Meslin, M. Lambrecht, M. Hernández-Mayoral, F. Bergner, L. Malerba, P. Pareige, B. Radiguet, A. Barbu, D. Gómez-Briceno, A. Ulbricht, and A. Almazouzi, J. Nucl. Mat. **406**, 73 (2010).
- [69] B. Radiguet, S. Cammelli, E. Meslin, M. Hernández-Mayoral, and P. Pareige, “Effect of neutron fluence on radiation-induced microstructure of low Cu RPV steels,” Private communication.
- [70] M. K. Miller, K. F. Russell, M. A. Sokolov, and R. K. Nanstad, J. Nucl. Mat. **361**, 248 (2007).
- [71] Y. Nagai, K. Takadate, Z. Tang, H. Ohkubo, H. Sunaga, H. Takizawa, and M. Hasegawa, Phys. Rev. B **67**, 224202 (2003).
- [72] See Supplemental Material.
- [73] J. R. Manning, Phys. Rev. B **4**, 1111 (1971).
- [74] H. Bakker, H. P. Bonzel, C. M. Bruff, M. A. Dayananda, W. Gust, J. Horváth, I. Kaur, G. V. Kidson, A. D. Le Claire, Mehrer, H, G. E. Murch, G. Neumann, N. Stolica, and N. A. Stolwijk, in *Diffusion in Solid Metals and Alloys, Landolt-Börnstein, New Series, Group III, Vol. 26*, edited by H. Mehrer (Springer, Berlin, 1990).
- [75] G. Neumann and C. Tuijtm, *Self-diffusion and impurity diffusion in pure metals: handbook of experimental data* (Elsevier, Oxford, 2011).
- [76] M. Hillert and M. Jarl, Calphad **2**, 227 (1978).

APPENDIX A: Correlation factor

The correlation factor f_x appearing in Eq. 6 can be expressed as a function of the atomic jump frequencies, in a multifrequency framework such as for instance the ones defined in [35]. Different expressions are available, depending on the extent of the solute-vacancy interactions and consequently of the amount of jump frequencies to be considered. The most complete one [17] includes 1nn and 2nn interactions, but was developed under the assumption $\omega_{42} = \omega_0$.

Thanks to the SCMF theory, it is possible to provide a more accurate expression of f_x in a bcc dilute binary alloy with 1nn and 2nn solute-vacancy interactions, removing the $\omega_{42} = \omega_0$ assumption. It reads:

$$f_x = 1 - \frac{2\omega_2}{2\omega_2 + 3\omega_{12} + 3\omega_{13} + \omega_{15} - \frac{\omega_{12}\omega_{21}}{\omega_{21} + \omega_{24}} - \frac{\omega_{15}\omega_{51}}{\omega_A} - \frac{\omega_{C1}\omega_{C2}}{\omega_B} + \frac{2\omega_B \left(\omega_{13} + k\omega_{15} + \frac{\omega_0 \omega_{C1}(1+k)}{\omega_B} \right) \left(\omega_{31} + k\omega_{51} + \frac{\omega_0 \omega_{C2}(1+k)}{\omega_B} \right)}{\omega_B (3\omega_0 + \omega_{31} - k\omega_A - 2k^2\omega_A) - 2\omega_0^2(1+k)^2}}, \quad (17)$$

where the following factors are introduced:

$$\omega_A = \omega_{51} + 7\omega_0 - \frac{2\omega_0^2}{\omega_{42} + 7\omega_0}; \quad (18)$$

$$\omega_B = \omega_{42} + 7\omega_0 - \frac{\omega_{24}\omega_{42}}{\omega_{21} + \omega_{24}} - \frac{\omega_0^2}{\omega_A}; \quad (19)$$

$$\omega_{C1} = \frac{\omega_{12}\omega_{24}}{\omega_{21} + \omega_{24}} + \frac{\omega_0\omega_{15}}{\omega_A}; \quad (20)$$

$$\omega_{C2} = \frac{\omega_{21}\omega_{42}}{\omega_{21} + \omega_{24}} + \frac{\omega_0\omega_{51}}{\omega_A}; \quad (21)$$

$$k = \frac{\omega_0^2}{\omega_A(\omega_{42} + 7\omega_0)}. \quad (22)$$

The correction provided by this new expression is expected to be relevant when the association frequency ω_{42} is considerably different from ω_0 , which is not the case for the dilute alloys investigated in this work. At any rate, larger differences with respect to the previous Le Claire's formula [17] are also obtained at very low temperatures.

APPENDIX B: Magnetic excess enthalpy

The magnetic excess enthalpy due to the magnetic transition in iron is here calculated by means of the

Hillert-Jarl phenomenological model [76]. According to this model, $H^{\text{mag}}(T)$ is expressed by:

$$H^{\text{mag}}(T) = RT_C \ln(B + 1)f(\tau), \quad (23)$$

where R is the gas constant, $T_C = 1043$ K the Curie temperature in iron [57], B the magnetic moment (2.22 Bohr magnetons in iron [57]) and $\tau = T/T_C$. The function $f(\tau)$ has two different expressions in the FM and PM regions, respectively:

$$f(\tau) = \begin{cases} \frac{1}{A} \left[\frac{79}{140P} - \frac{474}{497} \left(\frac{1-P}{P} \right) \left(\frac{\tau^4}{2} + \frac{\tau^{10}}{15} + \frac{\tau^{16}}{40} \right) \right], & \text{if } \tau < 1 \\ \frac{1}{A} \left[\frac{\tau^{-4}}{2} + \frac{\tau^{-14}}{21} + \frac{\tau^{-24}}{60} \right], & \text{if } \tau \geq 1 \end{cases}. \quad (24)$$

P is a geometry factor equal to 0.40 for bcc crystals, whereas the parameter A is equal to

$$A = \frac{518}{1125} + \frac{11692}{15975} \left(\frac{1-P}{P} \right). \quad (25)$$

Finally, the factor $H(T)$ appearing in Eq. 8 is normalized with respect to the magnetic excess enthalpy at 0 K, which can be obtained by setting $\tau = 0$:

$$H^{\text{mag}}(0) = RT_C \ln(B + 1) \frac{1}{A} \frac{79}{140P}. \quad (26)$$

Solute-vacancy correlation factors and tracer diffusion coefficients in bcc iron

Luca Messina,^{1,*} Pär Olsson,¹ and Maylise Nastar²

¹*KTH Royal Institute of Technology, Reactor Physics, 106 91 Stockholm, Sweden*

²*CEA, DEN, Service de Recherches de Métallurgie Physique, F-91191 Gif-sur-Yvette, France*

In the following table and figures are reported the solute correlation factors f_x as functions of temperature (Fig. 1), each solute diffusion coefficient in the range 800–1800 K (Fig. 2) and the fitted activation energies Q and prefactor D_0 in the range 400–800 K (Table I). In the latter are also included the ratios between the calculated diffusion coefficient and the experimental measurement (when available) at 1100 K. Since the inaccuracy in the calculations are limited mainly to D_0 , the mismatch between calculations and experiment can be employed to correct the calculated D_0 and hence obtain an improved estimation of the diffusion coefficient.

TABLE I: Activation energy Q and diffusion prefactor D_0 for impurity diffusion in iron, obtained by fitting in the temperature range 400–800 K. The mismatch between predicted values and experimental measurements is calculated at 1100 K.

	Q [eV]	D_0 [cm ² /s]	D_x/D_x^{exp}		Q [eV]	D_0 [cm ² /s]	D_x/D_x^{exp}
Al	2.73	9.96	3.0	Zr	2.37	2.67	-
Si	2.71	11.9	6.7	Nb	2.65	6.22	10.2
P	2.57	10.4	14.9	Mo	2.82	9.93	3.8
Ti	2.77	9.20	2.3	Tc	2.85	8.23	-
V	2.92	19.5	1.2	Ru	2.89	7.94	-
Cr	2.90	19.4	1-1.8	Rh	2.86	8.57	-
Mn	2.77	18.2	-	Pd	2.67	5.83	-
Fe	2.97	8.42	0.9-2.0	Ag	2.44	5.18	17.5
Co	3.02	8.12	0.6-0.7	Hf	2.47	4.11	-
Ni	2.79	6.63	4.1	Ta	2.69	6.68	6.3
Cu	2.73	13.5	6.4-8.5	W	2.87	5.06	1.6-2.4
				Re	3.06	11.0	-
				Os	3.08	12.1	-
				Ir	3.04	11.4	-
				Pt	2.83	9.14	-
				Au	2.49	4.62	28.8

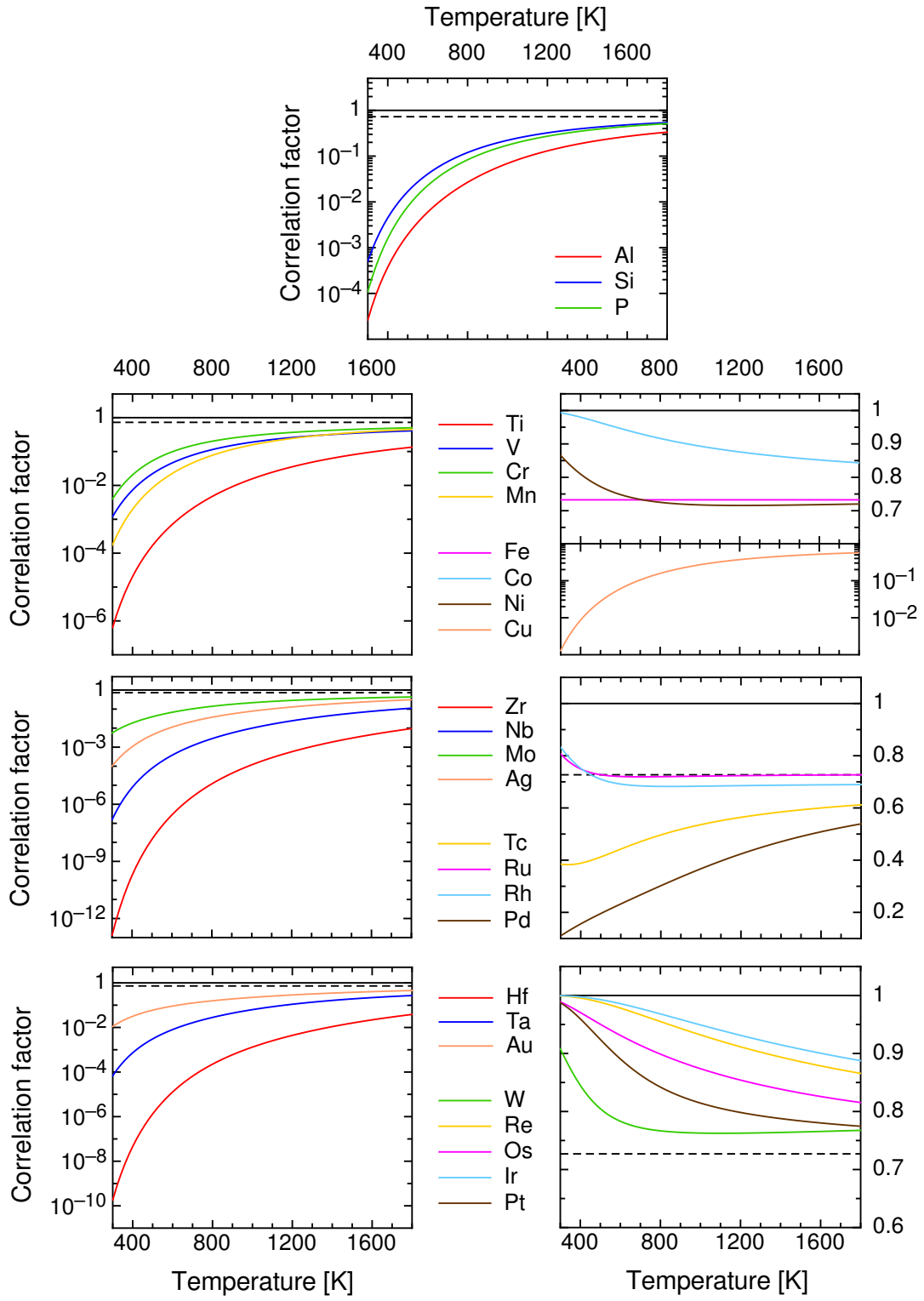


FIG. 1: Solute correlation factors f_x as functions of temperature. The dashed lines refer to the value in pure iron ($f_0 = 0.727$).

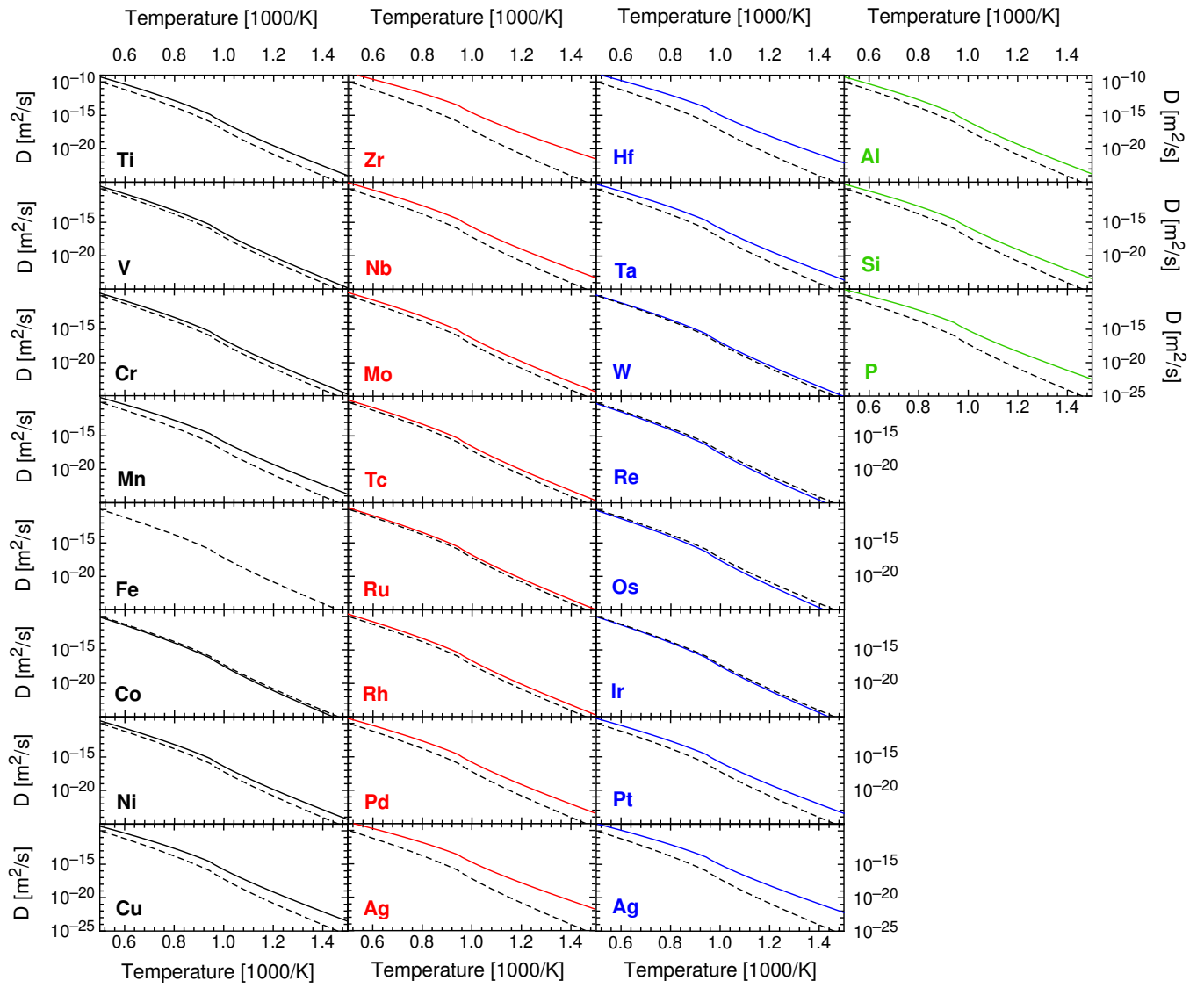


FIG. 2: Solute tracer diffusion coefficients in iron, as functions of temperature. The dashed lines represent the self-diffusion coefficient in pure iron.

Paper III

Ab initio-based investigation of solute-dumbbell transport and radiation induced segregation in Fe- X ($X = \text{Cr}, \text{Cu}, \text{Mn}, \text{Ni}, \text{P}, \text{Si}$) dilute alloys.

Luca Messina,^{1,*} Maylise Nastar,² and Pär Olsson¹

¹*KTH Royal Institute of Technology, Reactor Physics, SE-106 91 Stockholm, Sweden*

²*CEA, DEN, Service de Recherches de Métallurgie Physique, F-91191 Gif-sur-Yvette, France*

(Dated: November 16, 2015)

In this work are analyzed the solute-transport mechanisms due to coupling with dumbbell-type defects in iron alloys, for selected impurities, by combining *ab initio* calculations of defect transition rates with a mean-field treatment yielding the transport coefficients of the alloy. Average radiation-induced segregation tendencies are determined based on these results and the vacancy-diffusion tendencies derived in a previous study. A new mathematical framework allows for such tendencies to be expressed in terms of vacancy-solute and dumbbell-solute flux-coupling, as well as the relative efficiency of the two mechanisms. The results show that P, Mn, and Cr to a lesser extent are transported by dumbbells thanks to the combination of high mixed-dumbbell stability and mobility, whereas Cu, Ni, and Si impurities are not. For the latter impurities the vacancy mechanism is dominant, which entails solute enrichment at low temperature and depletion above the drag transition temperature. For P and Mn, the mixed-dumbbell mechanism is dominant and leads to consistent enrichment at defect sinks, independently of temperature. Finally, the RIS tendency for Cr is the outcome of a balance between enrichment due to dumbbells and depletion due to vacancies, leading to a switchover between enrichment and depletion at 460 K. The results are in qualitative agreement with resistivity-recovery experiments and experimental RIS observations in ferritic alloys.

INTRODUCTION

Atomic transport in materials plays a key role in driving the evolution of structural properties during fabrication, processing, and operation. For instance, solute diffusion determines the final microstructure during phase transformations in heat treatments [1, 2], and the knowledge of the atomistic diffusion mechanisms is necessary to obtain the desired microstructure. Moreover, the microstructure evolution of irradiated materials is controlled by atomic diffusion. Irradiation introduces high concentrations of point defects in the alloy, and when defect fluxes are coupled to atomic fluxes, solutes migrate to defect sinks, causing radiation-induced segregation (RIS) on grain boundaries or dislocations [3]. Moreover, flux coupling can enhance or even induce solute precipitation. An example is given by reactor pressure vessel (RPV) ferritic-martensitic steels, where RIS and the formation of small solute-defect complexes have been observed in several studies [4–12] and leads to hardening and embrittlement [9, 13], even when the thermodynamic driving forces for solute precipitation are feeble.

Efforts have been recently devoted to investigating the conditions under which solute-defect flux coupling arises. It was discovered that solute drag by vacancies is a widespread phenomenon that arises both in body-centered (bcc) and face-centered (fcc) cubic metals, whenever the vacancy-solute interaction is sufficiently strong [14, 15]. Moreover, in ferritic dilute alloys there exists for all transition-metal impurities a threshold temperature, under which solute diffusion occurs via vacancy drag, whereas at high-temperature diffusion occurs via

the traditional inverse-Kirkendall mechanism [16, 17]. This threshold can be quantitatively estimated by computing the Onsager coefficients of the matrix, which depend on the extent of the vacancy-solute interaction, as well as on the combination of vacancy jump frequencies in the local chemical environment around the solute atom. Thanks to this analysis, it is possible to provide a kinetic-induced (rather than thermodynamic-induced) explanation to solute precipitation in RPV steels, as well as to the observed RIS solute enrichment tendencies at defect sinks [16]. Flux coupling is therefore very important for the description of defect-driven microstructure phenomena.

Kinetic studies on ferritic alloys have been so far focused exclusively on vacancy-assisted diffusion. However, in irradiated materials an equal amount of vacancies and self interstitial atoms (SIA) is created. Single SIA's and small SIA loops are more mobile than vacancies because of their lower migration barrier, and might hence strongly affect solute diffusion to a similar extent. Among the solutes analyzed in [16], it is known from previous *ab initio* calculations that the mixed Fe-P, Fe-Mn, and Fe-Cr dumbbells are thermodynamically stable [18–20]. It is thus possible to suppose that for such solutes dumbbell-assisted transport might be relevant. On the other hand, solute-SIA correlations might also strongly affect the mobility of SIA's, which in turn can have significant effects on the microstructure evolution. It was shown for instance that small concentrations of Cr can slow down interstitial loops and reduce the alloy swelling tendency [21]. In the same fashion, it is suspected that the presence of Mn could have the same effect on interstitial loops

[6, 8, 22], in this case forming an unwanted nucleation site for the precipitation of Mn-Ni-Si-rich clusters. Moreover, Cr transport by interstitials was suggested [23] to be necessary to explain the experimental RIS tendencies, namely the presence of a threshold temperature from enrichment to depletion [24]. Since according to [16, 23] vacancy-mediated diffusion leads to depletion only, interstitial transport might counterbalance this effect.

A quantitative extensive investigation of solute transport by SIA's is therefore necessary and is still missing. Interstitial-solute flux coupling can be analyzed by computing the Onsager coefficients. Experiments in this sense are extremely difficult to perform because of the impossibility of observing low-temperature diffusion and because of the very low interstitial equilibrium concentration in non-irradiated materials. To the authors' knowledge, the only attempt of computing full transport-coefficient matrices was done by Choudhury *et al.* [23] for FeCr and FeNi dilute alloys, by applying the self-consistent mean field (SCMF) method [25, 26]. The RIS discussion therein provided, however, neglected the effect of flux coupling, which led to the conclusion that Ni should deplete at grain boundaries, in disagreement with the experimental observations [24].

The aim of this work is therefore to study interstitial-assisted solute transport and correlations in ferritic dilute Fe- X alloys ($X = \text{Cr, Cu, Mn, Ni, P, Si}$), by using a combined ab initio-mean field approach, similar to that used for vacancy-solute diffusion [16], to determine the transport coefficients of each binary alloy. Density functional theory (DFT) is applied in order to obtain sets of defect jump frequencies, which are then used as input for the SCMF method. The available most complete kinetic model for dilute alloys [26] is here extended to improve the description of thermodynamic and kinetic correlations. In addition to the calculation of diffusion coefficients and solute-SIA correlations, the SIA transport coefficients are combined with the vacancy-related transport coefficients in order to provide prediction of steady-state RIS tendencies, taking fully into account the effects of flux coupling.

METHOD

In the framework of linear thermodynamics of irreversible processes, transport coefficients relate the atomic flux to the thermodynamic force causing it [27]. The full knowledge of the transport coefficient matrix allows for the analysis of flux coupling between different species, for instance solute transport induced by defect fluxes. They are defined as:

$$J_i = - \sum_j \frac{L_{ij}}{k_B T} \nabla \mu_j, \quad (1)$$

where J_i is the flux of species i and $\nabla \mu_j$ the chemical potential gradient (CPG) of species j . For interstitial-mediated transport, the most complete expressions for the calculations of the L_{ij} 's in dilute bcc alloys were provided by Barbe *et al.* [26] in the framework of SCMF theory [25, 28]. In this theory, the transport coefficients are obtained by introducing a non-equilibrium distribution function in a system characterized by a small homogeneous CPG. One key-concept is the distinction between thermodynamic and kinetic interactions among atoms and with the defect. Thermodynamic interactions determine the equilibrium Hamiltonian and are related to all equilibrium properties, such as binding energies and migration barriers. Hence, they define the configurations that need to be accounted for when computing the equilibrium properties. On the contrary, kinetic interactions are fictitiously introduced to define the perturbed Hamiltonian, and are null in thermodynamic equilibrium conditions [25, 28]. The degree of symmetry is in this case lowered by the presence of a CPG, and determines the number of independent kinetic equations to be solved in order to obtain the transport coefficients.

For a dilute bcc alloy, the SCMF equations were presented and solved in three different models (zero-, first-, and second-shell approximation), depending on the considered extent of kinetic interactions in [26]. In the most advanced case (second shell), the model includes kinetic interactions inside the dumbbell and with a solute atom in first nearest-neighbor (nn) position. This model was tested on fictitious alloys and benchmarked with Monte Carlo simulations. Since then, it has been applied to the analysis of FeCr and FeNi dilute alloys [23]. Since the solute-dumbbell thermodynamic interactions can reach beyond the 1nn distance, as is the case for the alloys object of this study, this work extends the second-shell kinetic model to 2nn sites.

Relevant configurations for thermodynamic interactions

The dilute-alloy limit entails that only one solute atom and no other defects can be present in the interaction shell of the SIA. The thermodynamic interaction shell is defined as the group of atomic sites around the SIA in which the solute has a non-negligible thermodynamic interaction with the defect, in analogy with the vacancy case [14, 16]. In this work 1nn and 2nn models are used, which entails that all sites reachable within one jump from 1nn or 2nn sites need to be included. In this respect, this thermodynamic model represents an extension of the traditional 9-frequency model for vacancy diffusion [29].

In bcc iron, the most stable interstitial configuration is the $\langle 110 \rangle$ dumbbell [18, 30]. The analysis of symmetries for dumbbells are more involved than for vacancies because of the presence of two atoms in the defect. Differ-

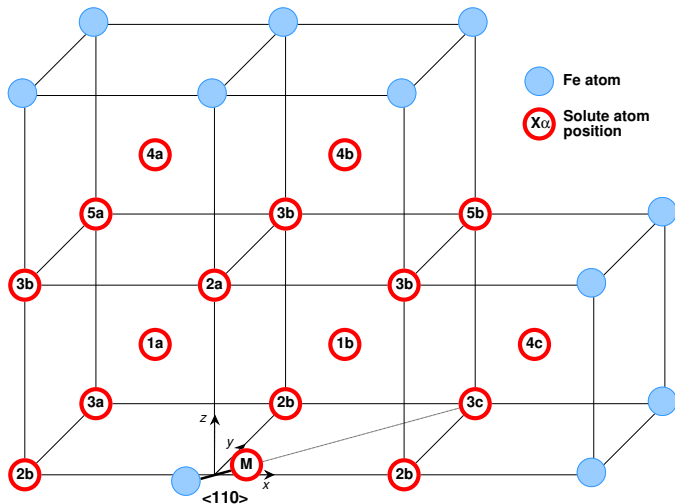


FIG. 1: Nomenclature of different dumbbell-solute configurations. In the label $x\alpha$, x is the solute nearest-neighbor position with respect to the dumbbell, whereas α stands for different combinations with respect to the dumbbell orientation (see Table IV). The colored atoms are located outside the interaction shell and the first shell reachable within one jump. The mixed dumbbell configuration is marked with 'M'.

ent thermodynamic interactions are distinguished based not only on the nearest-neighbor distance with the defect, but also on the distance of the solute to each atom in the dumbbell. This entails, for instance, the common distinction between compressed and tensile 1nn sites [20].

This is generalized to sites beyond the 1nn and up to the 5nn in Fig. 1, where the possible positions of the solute in the interaction zone or in the adjacent area are marked with the nomenclature $x\alpha$. x stands for the nearest-neighbor distance (1, 2, etc.), whereas α marks mutual distance between the solute and each of the atoms forming the dumbbells. For instance, in configurations of type a the solute is equidistant from the two dumbbell atoms A and B, and as the letter index is changed to b , c , etc. the solute is closer to either A or B. A more detailed description of this nomenclature is available in Table IV in the appendix. Note that this type of nomenclature is valid as long as a dilute alloy is concerned: for instance, in a concentrated alloy a target site (1b) next to atom A must be distinguished from the symmetric site next to atom B.

Transitions between equilibrium configurations

In bcc crystals three possible types of transitions involving $\langle 110 \rangle$ dumbbells are usually considered [28, 31]: four onsite rotations by 60° towards another $\langle 110 \rangle$ orientation (R), one translation to a 1nn site (τ) and two

TABLE I: Possible transitions in a bcc dilute alloy, for an interaction shell including 1nn and 2nn. τ stands for pure translation, ω for rotation-translation and R for onsite rotation. Mixed-dumbbell transitions involving solute migration are marked with '1'. 2nn jumps are not considered in this work.

	M	1a	1b	2a	2b	3b	3c	4b	4c	5b
M	ω_1, τ_1 R ₁		ω, τ							
1a		R	R	ω	ω, τ	ω, τ	ω			
1b		R	R	τ	ω	ω, τ	τ			ω, τ
2a		ω	τ		R			τ	ω	
2b		ω, τ	ω	R	R			ω	ω, τ	
3b		ω, τ	ω							
3c		ω	τ							
4b				τ	ω					
4c				ω	ω, τ					
5b			ω, τ							

rotation-translations by 60° to a 1nn site forming a dumbbell in another $\langle 110 \rangle$ direction (ω). There is also the possibility of a 2nn jump with rotation by 90° , however the latter is normally less likely and is therefore not treated in the current SCMF model. As opposed to the vacancy case, an SIA jump (of type τ or ω) can occur only towards four target sites among the eight nearest neighbors (those marked in the 1b configuration).

The jump-frequency nomenclature defined in [26] is here generalized beyond 1nn sites. The labels '0' and '1' are still used to mark the jumps occurring in a pure-iron environment and for mixed-dumbbell transitions, respectively. For the other pure-dumbbell transitions in the vicinity of a solute atom, the label $\omega_{x\alpha y\beta}$ is defined, where $x\alpha$ marks the starting configuration and $y\beta$ the final one. The allowed jumps between configurations are listed in Table I, and depicted in Fig. 2.

In the 1nn-interaction model of [26], the transitions of type $\omega_{1b \rightarrow \infty}$ (where ∞ marks any site beyond the 1nn distance) are assimilated to the same frequency ω_4 , as well as the transitions of type $\omega_{1a \rightarrow \infty}$ which are all included in ω_6 . As a matter of fact, Fig. 2 shows that such transitions must be distinguished depending on the final configuration, as they are characterized by different migration barriers (as is shown as well in Table II). For instance, the frequency ω_4 is actually given by the following average:

$$6\omega_4 = 2\omega_{1b2b} + 2\omega_{1b3b} + 2\omega_{1b5b}. \quad (2)$$

Analogous expressions can be written for ω_6 and the reverse jumps ω_5 and ω_7 .

Ab initio methodology

The solute-dumbbell interaction energies and the dumbbell jump frequencies are calculated in the framework of Density Functional Theory (DFT) with the Vi-

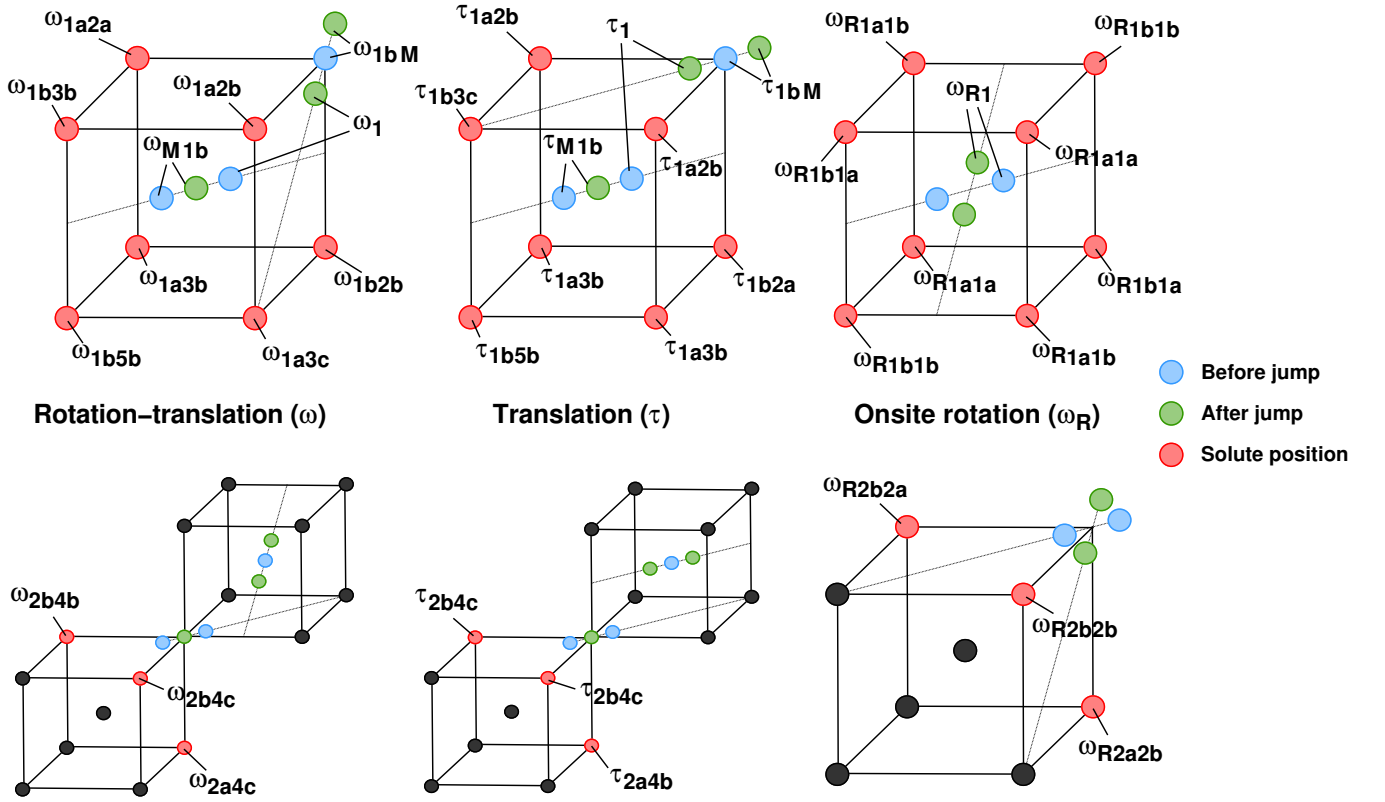


FIG. 2: Allowed transitions $\omega_{x\alpha y\beta}$ for an interstitial next to a solute atom, with a thermodynamic range extending to the $2nn$.

enna *ab initio* Simulation Package (VASP) [32–34]. The standard VASP pseudopotentials developed within the projector augmented wave (PAW) method [35, 36] are employed for all elements included in this study (Fe, Cr, Cu, Mn, Ni, P, Si). The Perdew-Burke-Ernzerhof (PBE) parameterization [37] of the generalized gradient approximation (GGA) is used to describe the exchange-correlation function. The calculations are spin-polarized, and make use of the Vosko-Wilk-Nusair (VWN) interpolation scheme of the correlation potential. As pointed out in previous studies [16, 20], the energy landscape related to the magnetic moment of Mn in an iron alloy is rather shallow. An antiferromagnetic state for the Mn solute atom is reached in most cases by applying linear mixing in the starting guess of the charge dielectric function, in place of the default Kerker model [38, 39]. However, in a few cases a positive magnetic moment is obtained regardless of the calculation settings.

Ionic relaxations are performed in a 251-atom supercell, whose volume and shape are maintained to that of a bcc iron cell. Following previous convergence studies [19], the lattice parameter is set to $a_0 = 2.831$ Å. The Brillouin zone is sampled with a Monkhorst-Pack $3 \times 3 \times 3$ k-point grid, and a plane-wave cutoff energy of 350 eV is used. For the Fe(Cr) alloy, the simulations are performed with increased accuracy ($4 \times 4 \times 4$ k-point grid and 400

eV cutoff), since for this alloy the transport coefficients and the properties derived from them are more sensitive to the *ab initio* input data.

The dumbbell formation energy is obtained as $E^f = E(N+1) - (N+1)/N \cdot E(N)$, where $E(N+1)$ and $E(N)$ are the energies of the supercell with and without dumbbell, respectively. The formation of a $\langle 110 \rangle$ -dumbbell ($E_{\langle 110 \rangle}^f = 4.08$ eV) is energetically more favorable than that of a $\langle 111 \rangle$ -dumbbell ($E_{\langle 111 \rangle}^f = 4.86$ eV), in agreement with previous studies [18, 30]. Furthermore, the binding energies of the mixed dumbbell and of the solute-dumbbell configurations $x\alpha$ shown in Fig. 1 are evaluated as:

$$E_{x\alpha}^b = E(\text{SIA} + \text{sol}) - E(\text{SIA}) - E(\text{sol}) + E_{\text{ref}}, \quad (3)$$

where the terms on the right-hand side are the energy of the supercell containing one dumbbell and one solute, one dumbbell, one solute, and no defect, respectively. In this convention, a negative sign stands for an attractive interaction.

The transitions shown in Fig. 2 are modeled according to transition-state theory as thermally-activated processes with frequency [27]:

$$\omega_{x\alpha y\beta} = \nu \exp\left(-\frac{E_{x\alpha y\beta}^{\text{mig}}}{k_B T}\right), \quad (4)$$

where the attempt frequency ν and the migration energy $E_{x\alpha y\beta}^{\text{mig}}$ are functions of the jumping atom type and the local chemical environment (LAE). The migration barriers are obtained in this work by means of nudged-elastic band (NEB) calculations [40, 41], implemented with the climbing-image algorithm [42] and three intermediate images. In each case, the migration barrier for each forward and backward transition is obtained as energy difference between the NEB saddle-point and the end-states. In order to reduce the computational load, the computation is limited to the rotation-translation mechanism only, with the exception of the pure and mixed dumbbell transitions. The accuracy on each migration barrier is estimated in less than 5 meV. For some cases where the end-point energy difference is large (> 0.5 eV), the NEB algorithm yields a spontaneous transition with no energy barrier. The absence of barriers in such cases is confirmed by additional NEB tests performed with nine intermediate images.

The attempt frequency ν can be in principle computed by means of DFT frozen-phonon calculations [17, 43, 44]. However, such calculations are very computationally demanding, especially in the case of SIA-type defects. No studies of this kind are to be found in the literature for SIA migration in iron. The combination of some molecular dynamics simulations [45] with the DFT calculation of the SIA formation entropy ($0.24 k_B$) [44], yields $\nu = 56$ THz. However, the heterogeneity of such data suggests that a more in-depth DFT study is required, which is outside the scope of this work. Therefore, it is here chosen to assign the Debye frequency value (6 THz), for the sake of consistency with the vacancy study [16].

Migration barrier manipulation

The input parameters of the SCMF method are the transition rates in thermodynamic equilibrium conditions [28]. In such conditions, they must fulfill the detailed balance principle (DBP). This means that a given pair of forward-backward jumps between states i and j must occur at the same rate:

$$\omega_{ij}^{(0)} p_i^{(0)} = \omega_{ji}^{(0)} p_j^{(0)}, \quad (5)$$

where p_i and p_j are the Boltzmann probabilities of the two states. It was explained in [16] that the application of this principle leads necessarily to a manipulation of the DFT-computed migration barriers, which depends on the choice of the thermodynamic interaction range cutoff R . Analogously to the vacancy case, the interaction energies outside the interaction area, which are not null in the *ab initio* calculations, must be set to zero. The same practical approach is here applied: the migration barriers of backward jumps of type $\omega_{y\beta x\alpha}$ (with $y > R$ and $x \leq R$) are modified by adding the DFT value of $E_{y\beta}^b$ (maintaining the negative sign in case of a binding interaction). In

this way, the energy of configuration $y\beta$ is modified so that the solute-dumbbell binding energy is null, whereas the NEB saddle-point energy is kept constant.

Steady-state RIS tendencies

RIS occurs in the presence of flux coupling between solute atoms and point defects (and mobile defect clusters) diffusing to sinks (grain boundaries, dislocations or other interfaces). Following a previous work [46], it is possible to express the steady-state solute concentration profiles as functions of the transport coefficients calculated in this work for interstitials and in [16] for vacancies.

The flux of each species and point-defect type can be written using Eq. 1 to include the chemical potential gradients due to vacancies and interstitials. These gradients are then expressed in terms of the thermodynamic interactions $E_{x\alpha}^b$, applying the low-temperature expansion method. A system of flux equations is obtained and can be solved in steady-state conditions by setting $J_V = J_I$ and $J_B = 0$. The steady-state solution reads [16, 46]:

$$\frac{\nabla c_B}{\nabla c_V} = \frac{c_A c_B d_{AV} d_{AI}}{c_A d_{AI} D_B + c_B d_{BI} D_A} \left(\frac{d_{BV}}{d_{AV}} - \frac{d_{BI}}{d_{AI}} \right), \quad (6)$$

where the terms in parenthesis are the ratios of partial diffusion coefficients (PDC) for vacancies (V) and interstitials (I):

$$d_{\alpha\delta} = \frac{L_{A\alpha}^\delta + L_{B\alpha}^\delta}{c_\alpha c_\delta} \quad ; \quad \alpha = A, B \quad , \quad \delta = I, V \quad . \quad (7)$$

c_i and c_δ represent the equilibrium concentrations of species i and defect type δ , respectively, whereas D_i is the intrinsic diffusion coefficient of species i defined in [46].

The Lij coefficients depend in first order on the solute concentration c_B , with the exception of L_{AA} which contains also a zero-order term:

$$L_{BB}^\delta = l_{BB}^\delta c_B c_\delta \quad (8)$$

$$L_{AB}^\delta = l_{AB}^\delta c_B c_\delta \quad (9)$$

$$L_{AA}^\delta = l_{AA}^{\delta,0} - l_{AA}^\delta c_B c_\delta \quad . \quad (10)$$

In the dilute limit, all terms of second order or higher in c_B must be neglected in the final RIS expression. Hence, the dilute-limit form of Eq. 6 reads:

$$\frac{\nabla c_B}{c_B} = \gamma_{\text{RIS}} \frac{\nabla c_V}{c_V}, \quad (11)$$

where the factor γ_{RIS} is given by:

$$\gamma_{\text{RIS}} = \frac{l_{AA}^{V,0}}{l_{BB}^V + \frac{c_I}{c_V} l_{BB}^I} \left(\frac{l_{AB}^V + l_{BB}^V}{l_{AA}^{V,0}} - \frac{l_{AB}^I + l_{BB}^I}{l_{AA}^{I,0}} \right) \quad . \quad (12)$$

The equivalent expression as a function of the interstitial concentration gradient can be obtained by replacing $\nabla c_V/c_V$ with $\nabla c_I/c_I$.

This model allows for a description of the solute concentration gradients near defect sinks, which are computed as the *average* of the vacancy-induced and the interstitial-induced tendencies. The enrichment/depletion tendency is determined by the terms in parenthesis. Since the point-defect gradient towards sinks is negative, solute enrichment occurs if the ratio of Eq. 11 is negative, and depletion otherwise. The transport coefficients are more suitable to describe RIS with respect to tracer diffusion coefficient ratios (such as in [23]) because they carry as well the effect of A - B correlations. For instance, in the dumbbell case a solute B can migrate either as a mixed dumbbell AB , or by kinetic coupling with a self interstitial AA . The tracer diffusion coefficient D_B^* derived from L_{BB} as:

$$D_B^* = \frac{L_{BB}}{nc_B} \quad (13)$$

(where n is the atomic density) contains the mixed-dumbbell contribution, but not the contribution from the AA - B coupling.

The defect concentration ratio c_I/c_V depends on the system and the irradiation conditions. The steady-state defect concentrations depend on temperature and sink density, and are most often of comparable orders of magnitude [47]. Hence, the ratio c_I/c_V should be calculated with proper rate-theory models. In most cases, the solution of rate-theory equations in [47] leads to the relationship $c_I/c_V = D_V/D_I$, or in terms of transport coefficients:

$$\frac{c_I}{c_V} = \frac{l_{VV}}{l_{II}} \approx \frac{l_{VV}^{A,0}}{l_{II}^{A,0}}, \quad (14)$$

where the final approximation applies for the dilute limit.

When the defect concentration ratio is given by Eq. 14, it is convenient to reformulate the factor γ_{RIS} in the following way:

$$\gamma_{\text{RIS}}^V = -\frac{\chi^V G^V}{1 + \frac{G^V}{G^I} (\chi^V - 1)} \quad (15)$$

$$\gamma_{\text{RIS}}^I = -\frac{\chi^I G^I}{1 + \frac{G^I}{G^V} (\chi^I - 1)}, \quad (16)$$

respectively from a vacancy perspective (γ_{RIS}^V) or a dumbbell perspective (γ_{RIS}^I). The two factors are indeed the same quantity as in Eq. 12. The RIS tendency is hence expressed as a function of the flux-coupling factors (G^δ) and the relative strength of interstitial transport over vacancy transport or vice versa (χ^δ). The flux-coupling factors are given by:

$$G^V = -\left(1 + \frac{l_{AB}^V}{l_{BB}^V}\right) \quad \text{and} \quad G^I = 1 + \frac{l_{AB}^I}{l_{BB}^I}, \quad (17)$$

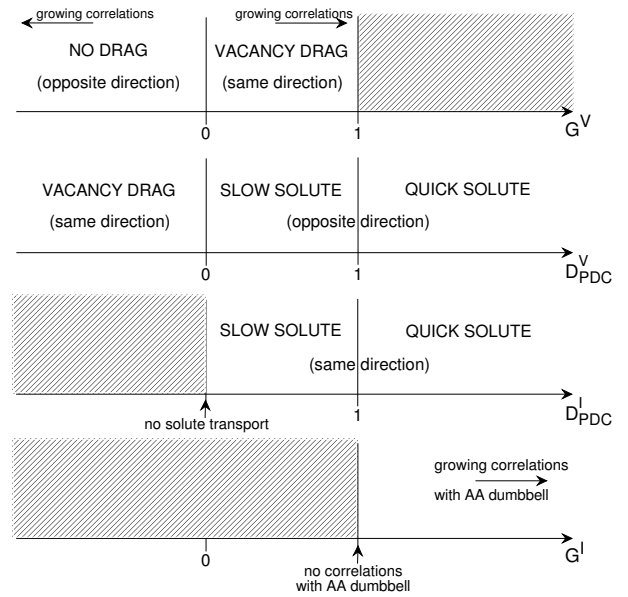


FIG. 3: Different defect-solute flux-coupling regimes, as functions of the partial diffusion coefficient ratios D_{PDC}^x and the wind factors G^x ($x=V, I$). Solute diffusion is "slow" or "quick" with respect to self diffusion. The flux direction is indicated with respect to the direction of the defect flux.

where the vacancy-wind factor G^V [14, 16, 48] can be recognized. Furthermore, the χ^δ factors are defined as:

$$\chi^V = 1 - \frac{D_{\text{PDC}}^I}{D_{\text{PDC}}^V} \quad \text{and} \quad \chi^I = 1 - \frac{D_{\text{PDC}}^V}{D_{\text{PDC}}^I}, \quad (18)$$

where $D_{\text{PDC}}^V = -G^V l_{BB}^V / l_{AA}^{V,0}$ and $D_{\text{PDC}}^I = G^I l_{BB}^I / l_{AA}^{I,0}$ are the PDC ratios appearing in parenthesis in Eq. 11. For instance, $\chi^I = 1$ when the vacancy contribution to solute transport is negligible ($D_{\text{PDC}}^V \approx 0$).

The link between the factors G^δ , D_{PDC}^δ and the solute-transport mechanisms is summarized in Fig. 3. The main difference between vacancy and interstitial quantities is represented by the sign of D_{PDC}^δ . The PDC ratio for interstitial is always positive because, according to the SCMF model, the L_{AB}^I cannot change sign. This entails that a flux of dumbbells cannot induce a flux of solute atoms in the opposite direction. Conversely, the PDC ratio for vacancies can change sign, namely it is negative under vacancy-drag conditions, and positive otherwise [16]. The relative contributions of each term to the RIS tendencies are analyzed in the next section.

RESULTS AND DISCUSSION

Ab initio interactions and migration barriers

The calculated solute-dumbbell interactions are shown in Fig. 4, according to the nomenclature defined in Fig.

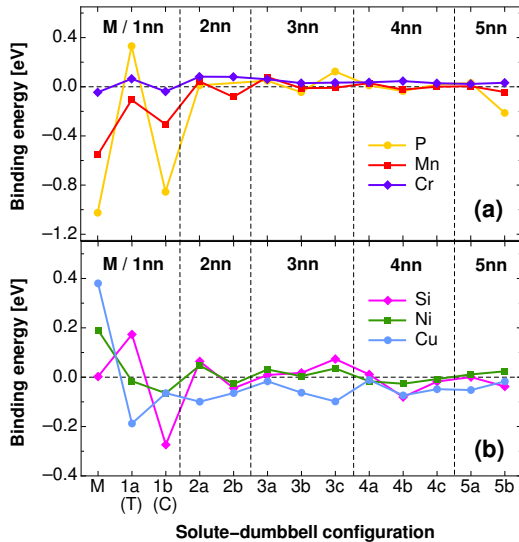


FIG. 4: *Ab initio* solute-dumbbell interaction energies computed in this study, in the α configurations of Fig. 1 from 1nn to 5nn. The labels 'M', 'T', and 'C' refer to the mixed dumbbell, the compressed 1nn configuration (1b) and the tensile 1nn configuration (1a), respectively.

Negative signs stand for attractive interactions. The SIA-P interaction in the 2b configuration is not shown, as the latter is unstable and collapses to the mixed Fe-P dumbbell.

1. Configurations 1a and 1b are marked with the labels 'T' and 'C' respectively, in reference to the more traditional definitions of *tensile* (non-target) and *compressive* (target) sites. In Table II, the migration barriers obtained with the NEB method are presented. The nomenclature therein employed refers to Fig. 2, as well as to the former nomenclature for the former 1nn kinetic model [26]. In some cases, the NEB algorithm yields a barrierless transition from initial to final state, and these cases are marked in the table with a zero barrier. The analysis is limited mainly to the rotation-translation mechanism, because it is in most cases characterized by lower migration barriers with respect to the translation and the onsite rotation mechanisms. The latter mechanisms are anyway considered for the pure and mixed dumbbell transitions. In addition, results from previous studies [20, 49, 50] are taken for 2nn jumps leading to a mixed dumbbell transition ($\omega_{1,2nn}$) or association/dissociation (ω_{M2b}).

The obtained solute-dumbbell interactions are in good agreement with the latest DFT calculations on the same alloys [18, 20, 49–51], although the investigations were never extended to further-than-1nn sites. According to classic misfit-strain arguments, the dumbbell interaction with oversized impurities is expected to be repulsive in 'M' and 'C', and attractive in 'T', whereas undersized im-

purities should be characterized by the opposite behavior. The trends in Fig. 4 are in agreement with such argument, concerning some oversized impurities (Cu, Ni) and the undersized ones (P, Si). On the contrary, Cr and Mn (oversized) show a binding character in 'M' and 'C', in disagreement with the misfit-strain argument. This was already pinpointed in a previous study [20], and is probably to ascribe to chemical and magnetic reasons (both species are antiferromagnetic). Some studies on solute-vacancy binding energies have shown that electronic interactions represent the major contributions to the total interaction energy, whereas the size factor contribution is usually small [17, 52, 53].

The 2nn interactions are weaker than the 1nn ones, although they are not negligible (e.g. 0.10 eV for Cu). As it is difficult to assess *a priori* the effect on kinetics, the shell of thermodynamic interactions is extended to 2nn sites. The interaction fades at longer distances, with the exception of Cu because of the pronounced size factor. Moreover, the SIA-P interaction in the 5b configuration is relatively strong, most likely because of the relaxation of the atom between the dumbbell and the solute atom (along the cubic cell diagonal) towards the solute, "resembling" the considerably stable mixed dumbbell. It is also worth mentioning some convergence issues in the FeMn alloy: the expected Mn negative magnetic moment is not obtained in configurations 2a and 3a. The latter cases are likely to represent some local minima of a shallow energy landscape, and the interaction energy might therefore be overestimated.

In Fig. 4, the solutes are grouped according to the stability of the mixed dumbbell: above are the solutes forming a stable mixed dumbbell (P, Mn, and Cr at a lesser extent), and below the ones for which the mixed dumbbell is not thermodynamically favorable (Si, Ni, Cu). Si represents a border-line case, as the interaction energy is null. The stability of the Fe-P, Fe-Mn, and Fe-Cr dumbbells in bcc iron emerged already from resistivity recovery experiments [56–58] and from previous studies [18–20], and indicates that such solutes are likely to diffuse via a dumbbell mechanism. However, solute transport depends as well on the mobility of the mixed dumbbell and on the correlations with the self dumbbell. For this reason, the calculation of the full transport matrix is necessary.

In FeP, the 'M' and 'C' configurations are remarkably stable, whereas the 'T' configuration is characterized by a strong repulsion. Moreover, configuration 2b is found to be unstable, as during ionic relaxation it collapses to the 'M' configuration. For this reason, the migration barriers for the transitions involving this unstable configuration are not calculated. Such large energy differences and stability issues make the analysis of this system rather involved: for instance, all transitions leading to the 1b configuration occur with no energy barrier. Therefore, the dumbbell is unable to leave the P solute behind and

TABLE II: DFT migration barriers for rotation-translation dumbbell transitions (ω), as a function of the local chemical environment, according to the nomenclature of Fig. 2, compared with previous calculations: [49] (V), [50] (M), [54] (O), [23] (C) or experiments [55] (T). The energy barriers for the pure translation (τ) and onsite rotation (ω_R) mechanisms of the pure (0) and mixed (1) dumbbells are also reported. The second column shows the jump types in Barbe's nomenclature [26].

Jump type	Barbe type	P	Mn	Cr	Si	Ni	Cu						
Pure iron													
ω_0	ω_0	0.34	[0.32] ^T , [0.37] ^V , [0.34] ^M , [0.34] ^O , [0.35] ^C										
τ_0	$\tau_0\omega_0$	0.78	[0.78] ^O , [0.84] ^C , [0.80] ^V , [0.78] ^M										
ω_{R0}	ω_{R0}	0.61	[0.63] ^V										
Mixed dumbbell transitions													
ω_1	ω_1	0.22	0.32	0.24	0.57	0.46	0.36						
		[0.18] ^M	[0.34] ^V	[0.23] ^O , [0.25] ^C	[0.52] ^V	[0.41] ^C , [0.45] ^V	[0.32] ^V						
τ_1	$\tau_1\omega_1$	0.49	0.65	0.41	0.57	0.63	0.37						
		[0.24] ^M	[0.66] ^V	[0.42] ^O , [0.48] ^C	[0.37] ^V	[0.69] ^C , [0.46] ^V	[0.26] ^V						
ω_{R1}	ω_{R1}	0.33	0.31	0.40	– ^b	– ^b	– ^b						
		[0.24] ^M	[0.45] ^V	[0.36] ^O	[0.48] ^V	[0.36] ^V	[0.32] ^V						
$\omega_{1, 2nn}$	–	–	–	–	–	–	–						
		[0.18] ^M	[0.53] ^V	[0.43] ^O	[0.67] ^V	[0.84] ^V	[0.59] ^V						
Mixed dumbbell dissociation/association													
$\omega_{M1b}, \omega_{1bM}$	ω_2, ω_3	0.23	0.06	0.45	0.20	0.36	0.36	0.07	0.35	0.08	0.34	0.00 ^a	0.45
		[1.26] ^M	[0.34] ^M	[0.49] ^V	[0.22] ^V	[0.33] ^O	[0.30] ^O	[0.06] ^V	[0.35] ^V	[0.09] ^C	[0.33] ^V	[0.00] ^V	[0.50] ^V
$\omega_{M2b}, \omega_{2bM}$	–	–	–	–	–	–	–	–	–	–	–	–	–
				[0.80] ^V	[0.04] ^V	[0.52] ^O	[0.36] ^O	[0.26] ^V	[0.14] ^V	[0.23] ^V	[0.45] ^V	[0.05] ^V	[0.33] ^V
Transitions from 1nn													
$\omega_{1b2b}, \omega_{2b1b}$	ω_4, ω_5	–	– ^c	0.38	0.16	0.37	0.25	0.44	0.21	0.31	0.27	0.31	0.31
						[0.35] ^O	[0.22] ^O			[0.31] ^C	[0.27] ^C		
$\omega_{1b3b}, \omega_{3b1b}$	ω_4, ω_5	0.81	0.00 ^a	0.52	0.23	0.39	0.32	0.48	0.18	0.40	0.33	0.30	0.30
$\omega_{1b5b}, \omega_{5b1b}$	ω_4, ω_5	0.64	0.00 ^a	0.51	0.29	0.40	0.33	0.48	0.24	0.41	0.32	0.36	0.31
$\omega_{1a2a}, \omega_{2a1a}$	ω_6, ω_7	0.19	0.50	0.35	0.20	0.33	0.31	0.29	0.40	0.35	0.29	0.36	0.27
$\omega_{1a2b}, \omega_{2b1a}$	ω_6, ω_7	–	– ^c	0.37	0.35	0.41	0.39	0.23	0.45	0.31	0.32	0.32	0.20
						[0.36] ^C	[0.37] ^C			[0.36] ^C	[0.34] ^C		
$\omega_{1a3b}, \omega_{3b1a}$	ω_6, ω_7	0.13	0.50	0.37	0.27	0.32	0.36	0.28	0.43	0.36	0.34	0.39	0.26
$\omega_{1a3c}, \omega_{3c1a}$	ω_6, ω_7	0.28	0.49	0.37	0.27	0.35	0.38	0.31	0.41	0.37	0.31	0.36	0.27
Transitions from 2nn													
$\omega_{2a4c}, \omega_{4c2a}$	–	0.44	0.43	0.34	0.38	0.31	0.36	0.39	0.47	0.30	0.36	0.35	0.30
$\omega_{2b4b}, \omega_{4b2b}$	–	–	– ^c	0.33	0.27	0.31	0.35	0.29	0.32	0.29	0.27	0.26	0.27
$\omega_{2b4c}, \omega_{4c2b}$	–	–	– ^c	0.38	0.29	0.32	0.38	0.36	0.33	0.34	0.32	0.30	0.29

^a The transition occurs spontaneously with no energy barrier.

^b No energy barrier is calculated because of the intricated transition energy path.

^c The transition is not simulated because the SIA-P 2b configuration is unstable.

can migrate as a mixed dumbbell only, in a continuous oscillation between 'M' and 'C'. The probability of escaping the 1b configuration, as well as that of forming the 1a configuration, is very small. However, the high mobility of the mixed dumbbell (0.22 eV) compared to the pure dumbbell excludes in the dilute limit the presence of trapping configurations, as was instead pointed out in the presence of more than one P atom [18, 50]. Finally, it is necessary to remark that P can also reside as a foreign interstitial in an octahedral position with an equal stability, and can also migrate from mixed dumbbell to octahedral position with a relatively low barrier (0.17 eV) [50]. The

barrier for a 2nn mixed dumbbell jump is also low (0.18 eV). Several migration paths are therefore available for P solute atoms, and are likely to induce an even stronger transport tendency than what is calculated in this work, where the only rotation-translation mechanism is taken into account.

In the FeMn system, the mixed dumbbell is considerably stable, and its mobility is close to that of the pure dumbbell, as suggested by resistivity recovery experiments [57]. The low dissociation probability and the low probability to escape from a 1nn configuration indicate that correlations in this system might be strong. In

[49] a very low mixed-dumbbell association barrier via a 2nn jump was found (0.04 eV). If confirmed, this would entail a practical impossibility for the solute-dumbbell pair to dissociate, and a consequent further enhancement of solute-dumbbell correlations.

The SIA-Cr interaction is binding but weak, analogously to the vacancy-Cr interaction in iron [16]. Moreover, the binding energies of the 'M' and 'C' configurations are very close. According to earlier DFT calculations based on the PW91 potential [20], the mixed dumbbell is more stable. The PBE method applied in this work is in agreement with PW91 only when the accuracy is increased to $4 \times 4 \times 4$ k-points and 400 eV. The mixed dumbbell is found to be extremely mobile, in accordance with resistivity recovery experiments [56], and all migration barriers are close to the background values because of the weak interactions. The comparison with the barriers calculated in [23] yields a mismatch in the mixed dumbbell association/dissociation rate. The predictions therein might hence be slightly underestimated with respect to the results of this work. Moreover, Olsson [54] highlighted the possibility of a 2nn association jump (0.36 eV), which would enhance the solute-dumbbell correlations.

The instability and large migration barriers of the Fe-Cu and Fe-Ni dumbbells do not prevent such impurities from affecting interstitial diffusion, as the dumbbell can be trapped in certain SIA-solute binding configurations. For instance, the trapping due to the strong binding between SIA and a Cu atom in tensile position (1a) was shown [59] to be the cause for the observed disappearance of the single-SIA migration peak in resistivity recovery experiments [57]. This is clearly visible in Table II, as the transition rates from 2nn and 5nn to this configuration are higher than ω_0 . The absence of an energy barrier for the mixed-dumbbell dissociation shows that in FeCu dilute alloys the mixed dumbbell does not exist and Cu cannot therefore migrate through a dumbbell mechanism.

An analogous trapping mechanism was observed in the FeSi alloy, and was explained either by a trapping effect [60] or by the formation of the FeSi mixed dumbbell [58]. The substantial neutrality of the Fe-Si dumbbell found in this work is likely to exclude the latter hypothesis, whereas the former one is supported by the strong binding interaction in the compressive position. The possibility of Si transport via dumbbell cannot be assessed based on thermodynamic arguments only, but is seemingly unlikely due to the high mixed-dumbbell migration barrier and dissociation probability. Since the dissociation from the 1b configuration is quite unlikely, the latter might be a good candidate for the experimentally observed trapping effect. The same configuration might be also the cause for dumbbell trapping in the FeNi alloy, which is observed in resistivity recovery experiments on this alloy [57]. The mixed dumbbell is slow and also very likely to

dissociate, to a larger extent with respect to what suggested by previous calculations [49]. A dissociation path is also open through a 2nn jump. For this reason, Ni transport by dumbbell migration is very unlikely to occur.

In this work two thermodynamic models are tested, with cutoff ranges set to 1nn and 2nn respectively ($R=1$ and $R=2$). The FeP requires a special treatment because of the instability of configuration 2b. In principle, a barrier-less 2nn transition from 2b to the mixed dumbbell should be introduced in the SCMF kinetic model. However, such type of transition is currently not implemented. In order to overcome this issue, it is chosen for the 2nn model to artificially set a very highly repulsive interaction energy in configuration 2b, so to inhibit all transitions to and from this unstable position. Conversely, in the 1nn model the DBP requires the interaction energy E_{2b}^b to be null. In this way, the jump from 1a to 2b is assumed to have no barrier, and since $E_{1a}^b > E_{2b}^b$, the transition 1a \rightarrow 2b occurs smoothly towards 2b instead of the opposite way. Such adjustments are anyway likely to have a negligible impact on the results, given the dominance of the configurations M and 1b.

Table III shows the resulting modified migration barriers, which are then used as input for the mean-field calculation of the Onsager matrix. The modified values are reported in bold fonts. The modifications required in the 1nn model are significant because of the non-negligible magnitude of many solute-dumbbell interactions beyond the 1nn. The need to limit the extent of such manipulation justifies the necessity to extend the interaction range to (at least) 2nn sites. A further extension would complicate the already lengthy set of barriers to compute. The convergence with respect to the interaction range is tested in the last section.

Transport coefficients

The transport coefficients obtained with the 2nn thermodynamic and kinetic SCMF models are shown in Fig. 5, where they are normalized with respect to the solute and defect concentration. The $L_{AA}^{1,0}$ coefficient is the same for all solutes and is characterized by an Arrhenius shape with slope equal to the dumbbell migration barrier in pure iron (0.34 eV).

The L_{BB}^I coefficient describes the diffusivity of the mixed dumbbell, and its slope is given in first approximation by $-(E_{\omega_1}^{\text{mig}} + E_M^b)$. Analogously to the vacancy coefficient L_{BB}^V [17], it is also affected by the correlation factor f_B discussed in the following section. It is shown in Fig. 9a that this factor is anyway close to unity for Cu, Ni, and Si. On the other hand, the L_{AB}^I coefficient describes the flux of solute atoms due to exchanges with the self dumbbell AA. Even when the mixed dumbbell is not thermodynamically stable, the combination of AA

TABLE III: List of modified migration barriers, according to the detailed balance principle, used as input for the SCMF method. The modified values with respect to the DFT calculations are reported in bold.

Jump type	P		Mn		Cr		Si		Ni		Cu	
1nn thermodynamic model												
$\omega_{1b2b}, \omega_{2b1b}$	0.85	0.00	0.38	0.07	0.37	0.33	0.44	0.16	0.31	0.25	0.31	0.24
$\omega_{1b3b}, \omega_{3b1b}$	0.85	0.00	0.52	0.22	0.39	0.35	0.48	0.20	0.40	0.33	0.30	0.24
$\omega_{1b5b}, \omega_{5b1b}$	0.85	0.00	0.51	0.25	0.40	0.36	0.48	0.20	0.41	0.34	0.36	0.29
$\omega_{1a2a}, \omega_{2a1a}$	0.19	0.52	0.35	0.24	0.33	0.39	0.29	0.47	0.35	0.34	0.36	0.17
$\omega_{1a2b}, \omega_{2b1a}$	0.00	0.33	0.37	0.27	0.41	0.48	0.23	0.40	0.31	0.29	0.32	0.13
$\omega_{1a3b}, \omega_{3b1a}$	0.13	0.46	0.37	0.26	0.32	0.39	0.28	0.45	0.36	0.34	0.39	0.20
$\omega_{1a3c}, \omega_{3c1a}$	0.28	0.61	0.37	0.26	0.35	0.42	0.31	0.48	0.37	0.35	0.36	0.17
2nn thermodynamic model												
$\omega_{1b2b}, \omega_{2b1b}$	∞	0.00	0.38	0.16	0.37	0.25	0.44	0.21	0.31	0.27	0.31	0.31
$\omega_{1b3b}, \omega_{3b1b}$	0.85	0.00	0.52	0.22	0.39	0.35	0.48	0.20	0.40	0.33	0.30	0.24
$\omega_{1b5b}, \omega_{5b1b}$	0.85	0.00	0.51	0.25	0.40	0.36	0.48	0.20	0.41	0.34	0.36	0.29
$\omega_{1a2a}, \omega_{2a1a}$	0.19	0.50	0.35	0.20	0.33	0.31	0.29	0.40	0.35	0.29	0.36	0.27
$\omega_{1a2b}, \omega_{2b1a}$	∞	0.00	0.37	0.35	0.41	0.39	0.23	0.45	0.31	0.32	0.32	0.20
$\omega_{1a3b}, \omega_{3b1a}$	0.13	0.46	0.37	0.26	0.32	0.39	0.28	0.45	0.36	0.34	0.39	0.20
$\omega_{1a3c}, \omega_{3c1a}$	0.28	0.61	0.37	0.26	0.35	0.42	0.31	0.48	0.37	0.35	0.36	0.17
$\omega_{2a4c}, \omega_{4c2a}$	0.44	0.45	0.34	0.38	0.31	0.39	0.39	0.45	0.30	0.35	0.35	0.25
$\omega_{2b4b}, \omega_{4b2b}$	0.00	∞	0.33	0.25	0.31	0.39	0.29	0.24	0.29	0.24	0.26	0.19
$\omega_{2b4c}, \omega_{4c2b}$	0.00	∞	0.38	0.29	0.32	0.40	0.36	0.32	0.34	0.31	0.30	0.24

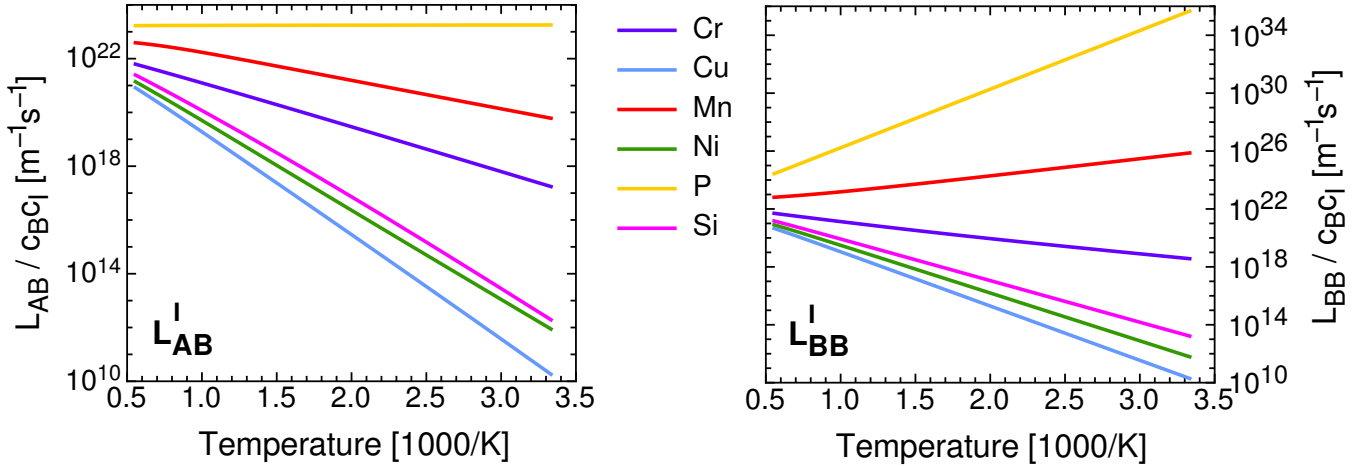


FIG. 5: Transport coefficients for the Fe(X) dilute alloys, normalized with respect to the solute and defect concentrations, as obtained with a 2nn thermodynamic model.

migration frequencies around B can induce a kinetic coupling and cause the solute to "follow" the dumbbell. The PDC ratio $D_{\text{PDC}}^{\text{I}}$ includes both contributions.

The combined high stability and mobility of the Fe-P and Fe-Mn mixed dumbbells yields very large values of L_{BB}^{I} . Because of the very large binding energy, the coefficient decreases with increasing temperature, and since it is proportional to the solute diffusion coefficient, it is possible to draw the counterintuitive conclusion that the diffusivity of P and Mn solute atoms due to dumbbell migration is larger at low temperatures. This applies in particular in irradiated materials, where the interstitial concentration is usually fixed by the source term and is independent of temperature. In thermal-equilibrium

conditions, this effect would be "masked" by the high dumbbell formation energy (4.08 eV). The solute diffusion coefficient can be obtained by means of Eq. 13, if the total interstitial concentration is known. For the other solutes, the mixed dumbbell mobility is considerably lower and follows the usual Arrhenius behavior. In spite of the small difference in thermodynamic stability between the Fe-Cr and the Fe-Si mixed dumbbell, the former one is considerably more mobile because of the lower migration barrier.

The L_{AB}^{I} coefficient follows roughly the same trend. Fe(P) represents a limit case, where the coefficient is independent of temperature. In this system, the frequency ω_1 is dominant over any other frequency, and it can be

seen in Eq. 38 of [26] that in such a case L_{AB}^I is constant. At any rate, it is more interesting to analyze the ratio between L_{AB}^I and L_{BB}^I , which is expressed by the factor G^I shown in Fig.6a. G^I describes the fraction of solute transport that is due to kinetic coupling with a pure Fe-Fe dumbbell. For P and Mn, this factor is equal to one, or in other words $L_{AB}^I \ll L_{BB}^I$. This entails that solute transport occurs only via an efficient mixed-dumbbell diffusion, which does not produce any net displacement of solvent atoms. As a matter of fact, the rotation-translation mechanism in bcc crystals allows for a long-ranged diffusion of the mixed dumbbell without dissociation, if the dissociation probability is very low and the mixed-dumbbell stability is very high, as is the case for Fe-P and Fe-Mn. For the other solutes, correlations with the pure dumbbells are certainly not negligible, but the low magnitude of both coefficients for Si, Ni, and Cu suggests the absence of solute transport.

This is better explained by Fig. 7, which depicts the ratios of partial diffusion coefficients D_{PDC}^I . This ratio shows if solute transport, due to both the mixed dumbbell and the coupling with the pure dumbbell, is faster than solvent transport ($D_{\text{PDC}}^I > 1$) or slower ($D_{\text{PDC}}^I < 1$). Here emerges that the dumbbell mechanism leads to transport of P, Mn and Cr, while transport of Si, Ni, and Cu is not favorable. Therefore, this mechanism is expected to cause enrichment at sinks for the former three solutes, and depletion for the latter ones. In comparison with the vacancy prediction [16], the interstitial contribution enhances the enrichment tendency due to vacancy for P and Mn, counteracts it for Ni, Si, and Cu, whereas it counteracts the depletion tendency due to vacancy-Cr diffusion. The quantitative balance depends anyway on the χ^I and χ^V parameters, which determine the relative strength of the two mechanisms.

At this point, it is worth underlining that the mixed dumbbell stability is by no means the only factor determining the possibility of solute transport, although this is seemingly the accidental outcome of this study for the considered impurities. It is indeed possible to have $D_{\text{PDC}}^I > 1$ even when the mixed dumbbell is unstable, if the ω_1 migration barrier is sufficiently low. Fig. 8 shows for instance a parametric study on the PDC ratio, where the migration barrier $E_{\omega_1}^{\text{mig}}$ of the Fe-Ni and Fe-Si dumbbells are artificially varied. It emerges that D_{PDC}^I increases with decreasing barrier. Neglecting correlations, it is possible to state that solute transport occurs when $E_{\omega_0}^{\text{mig}} - E_{\omega_1}^{\text{mig}} > E_M^b$. For instance, the PDC ratio for Ni becomes larger than one when the difference with the pure-dumbbell barrier exceeds roughly 0.20 eV, which corresponds to the repulsive energy of the mixed dumbbell. Correlations introduce a secondary effect, producing a slight shift of the curves to the right (enhancing in this case solute transport). It is therefore possible to conclude that the possibility of solute transport can be analyzed based at least on the mixed-dumbbell stabil-

ity and migration barrier, and that an unstable mixed dumbbell does not rule out *a priori* this possibility.

This insight allows for a brief prediction of dumbbell transport for the other transition-metal impurities, for which the mixed-dumbbell stability was analyzed in [20]. In almost all cases the mixed dumbbells are considerably unstable ($E_M^b > 0.8$ eV), to an extent that cannot be counterbalanced by a quick mobility, since the maximum ΔE^{mig} is 0.34 eV. Cobalt is the only exception, as the repulsion energy in the mixed-dumbbell configuration is only 0.25 eV. Therefore, cobalt transport by dumbbells might occur if the migration barrier of the mixed dumbbell is particularly low. Otherwise, all transition-metal impurities are expected to deplete for what concerns dumbbell migration, counteracting the predominant enrichment tendency due to vacancies [17]. The balance can be quantitatively completed only by extending this kinetic study to the missing impurities, and calculating the G^I and χ^I parameters.

Correlation factors

The solute correlation factor f_B can be obtained as

$$f_B = \frac{L_{BB}^I}{L_{BB}^{I,0}}, \quad (19)$$

and accounts for the solute slowdown due to repeated forward-backward jumps that do not effectively contribute to diffusion. The results are shown in Fig. 9a. The dashed line represents the geometric correlation factor $f_0 = 0.42$ in a pure bcc metal, which is consistent with the theoretical predictions [27]. This value is much lower than that of vacancies (0.73 [27]) because of the lower coordination number for interstitial jumps (four target sites in place of eight).

The solutes can be split into two groups: correlations are strong for P, Mn, and Cr, and negligible for the other solutes. This accidentally corresponds to the division between "transported" solutes and "non-transported" ones, although it can be seen in Fig. 8b that the PDC ratio can be larger than one even when $f_B \approx 1$, if the mixed-dumbbell migration barrier is sufficiently low. For the latter group, $f_B \approx 1$ entails that the dumbbell can easily leave the solute behind, and when sporadically a mixed dumbbell is formed, its migration is 100% effective because the probability for a backward jump is negligible. For the former group, the slowdown effect is important, and can be observed for instance in the uncorrelated PDC ratios in Fig. 7 (dashed lines). This effect is surprisingly more pronounced for Cr with respect to P at low temperature, in spite of the much weaker mixed-dumbbell binding energy. This depends on an intricate combination between thermodynamic stability and the migration barriers in the local atomic environment. The energy

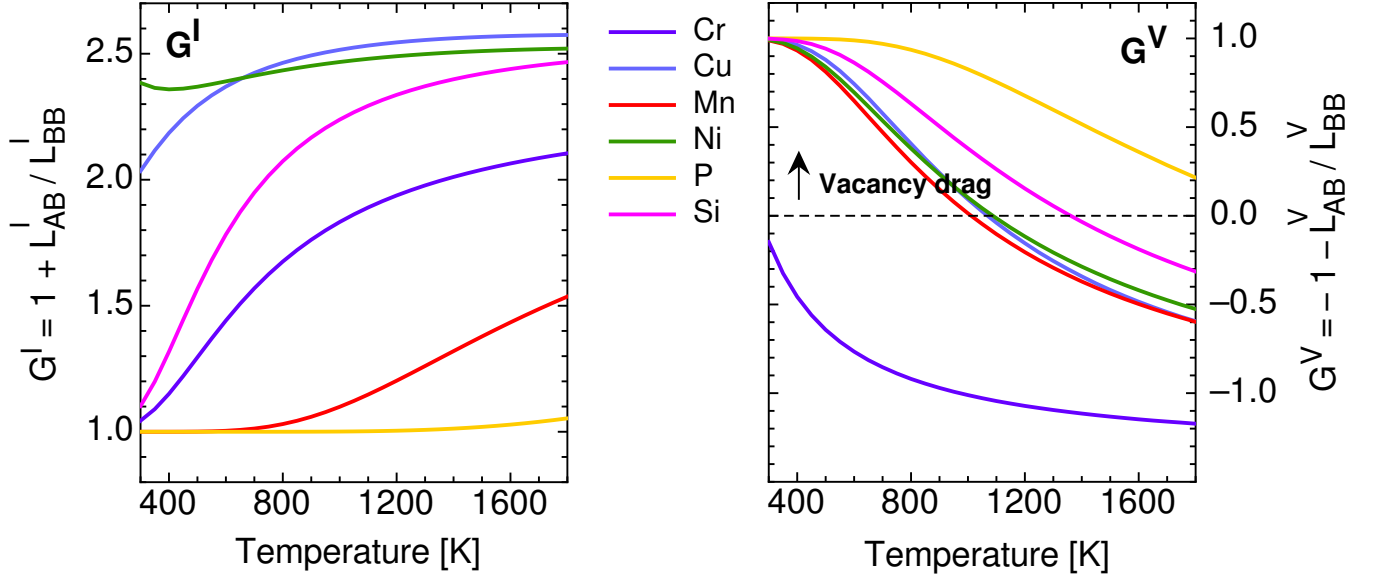


FIG. 6: Wind factors G^x ($x=V, I$) obtained by means of Eq. 17. The vacancy wind factors were computed in a previous work [16].

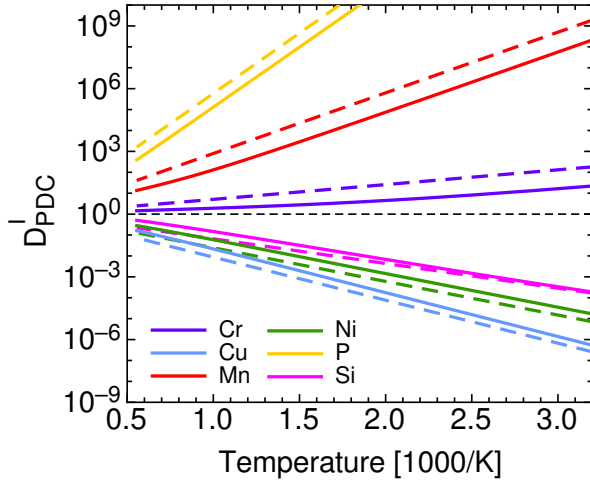


FIG. 7: Ratio of partial diffusion coefficients for dumbbell-assisted diffusion. Solute transport occurs when the ratio is larger than 1. The dashed lines refer to the same quantity, when correlations are neglected ($D_{\text{PDC}}^I = l_{BB}^{I,0} / l_{AA}^{I,0}$).

landscape of a few mixed dumbbells AB is represented schematically in Fig. 9b with respect to the configuration 1b (AA/B) and any configuration further than 2nn (AA), where the interaction is null. In the case of Mn and Cr, the energy barriers to escape the mixed-dumbbell configurations are high compared to the rather shallow landscape of P. For this reason, in spite of the very large barriers beyond the 1nn, in the Fe-P system the mixed dumbbell can sometimes dissociate to a 1b configuration.

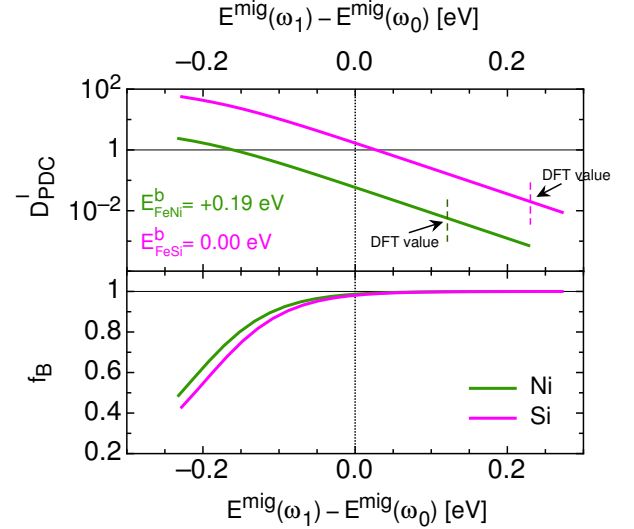


FIG. 8: Variation of the partial diffusion coefficient ratio (above) and the correlation factor (below), when the Fe-Si and Fe-Ni mixed-dumbbell migration barriers $E^{\text{mig}}(\omega_1)$ are artificially modified. All other properties (binding energies and migration barriers) are left unchanged. $E^{\text{mig}}(\omega_0)$ refers to the migration barrier of the pure dumbbell.

Conversely, for the Fe-Mn and Fe-Cr mixed dumbbells the dissociation is rare at low temperatures, and their low migration barrier (compared to the pure dumbbell) leads to stronger correlations. This difference progressively disappears with increasing temperature, because as the thermal oscillations grow larger, the escapes paths

for FeMn and FeCr are activated, whereas the dumbbell-P pair is confined within very high walls. Finally, the energy landscape of the Fe-Cu system depicted also in Fig. 9b shows that the Fe-Cu mixed-dumbbell is not only characterized by a repulsive interaction, but decays spontaneously into a more stable 1b configuration. This entails that an Fe-Cu mixed dumbbell does not exist under whichever condition.

Radiation induced segregation

The dumbbell transport coefficients obtained here, combined with the vacancy coefficients of a previous work [16] yield the RIS tendencies, which are shown in Fig. 10. The factor γ_{RIS} is defined according to Eq. 12. Solute enrichment occurs for $\gamma_{\text{RIS}} < 0$, and depletion in the opposite case. According to this dilute model, solute enrichment is expected for all solutes in the low-temperature end, below approximately 460 K for Cr, 1000 K for Ni and Cu, 1400 K for Si, and at all temperatures for P and Mn. This is in qualitative agreement with previous RIS measurements in ferritic steels [24]. The actual magnitude of the experimental enrichment tendency cannot be compared with this theoretical model, as it is affected by many factors, such as solute concentration, equilibrium segregation, and strain fields near the grain boundary. The Cr switchover at 460 K is also in qualitative agreement with the experimental evidence [24], where for a concentrated Fe-Cr alloy (8.37% Cr) the enrichment tendency disappeared above ≈ 900 K. This shows that, as was suggested in [24], the conflicting results of several RIS experiments in ferritic FeCr alloys are due to a fine balance between opposite transport mechanisms. The mismatch between switchover temperatures is most likely due to the effect of Cr concentration.

This RIS tendencies can be analyzed more in details by comparing the contributions given by vacancy and interstitial diffusion by means of the factor χ^{I} defined in Eq. 18. This factor, shown as a function of temperature in Fig. 11, compares the magnitude of the PDC ratios between vacancies and interstitials. It is 1 when interstitial diffusion is dominant, and takes large positive values when vacancy drag is dominant, or large negative values when vacancy diffusion via a traditional vacancy-solute exchange (inverse-Kirkendall mechanism) dominates. When the two contributions are evenly balanced, both χ^{I} and the RIS tendency γ_{RIS} are null.

As can be inferred from Fig. 11, P and Mn atoms diffuse predominantly via the dumbbell mechanism, as the factor χ^{I} is 1 or close to 1 at all temperatures. The additional contribution to RIS given by the low-temperature vacancy drag is negligible. For this reason, the RIS tendency is $\gamma_{\text{RIS}} = -1$ because only the mixed dumbbell (carrying one solute atom) contributes to solute enrichment. As temperature increases, the effect is partially at-

tenuated because of the decreasing dumbbell-solute correlations. However, the enrichment tendency is slightly enhanced for P ($\gamma_{\text{RIS}} < -1$), because vacancy drag occurs also at high temperature, whereas it is reduced for Mn, which is not characterized by vacancy drag above 1100 K [16].

For Ni, Si, and Cu, vacancy drag is dominant at low temperatures, since solute transport by dumbbells is not efficient. This leads, at 300 K, to $\gamma_{\text{RIS}} = -1$ because each vacancy going to a sink carries one solute atom. For Cu, the RIS tendency is entirely determined by vacancy diffusion at all temperatures, because of the impossibility for a mixed dumbbell to form. For Ni and Si, above the transition temperature the two contributions (vacancies and interstitials) become comparable. Finally, the FeCr alloy is characterized by two opposite tendencies, namely the enrichment tendency due to interstitials and the depletion one due to vacancies, that are close to each other in magnitude at all temperatures. At low temperature the Cr-dumbbell correlations are enhanced, which leads to a slight predominance of the interstitial contribution; with increasing temperature, the vacancy effect grows stronger, until the two contributions are more or less even. For this reason, the RIS behavior of the FeCr system is expected to be very sensitive to the accuracy of the migration-barrier calculations, as well as to any external variable during experiments.

Convergence check

The results obtained in this work can be compared with the previous SCMF models [26] in order to verify if the extension of the SCMF framework of kinetic and thermodynamic interactions leads to large changes in the transport coefficients. In [26], three different kinetic models were defined: zero, first, and second shell. The zero-shell approximation was the solution of the SCMF system in the absence of correlations; the first-shell model referred only to the kinetic interactions in the dumbbell ("0nn"), whereas the second-shell one was featuring kinetic interactions up to the 1nn. Here, the kinetic interaction shell is extended to the 2nn. The variation in terms of diagonal coefficients (L_{AA}^{I} and L_{BB}^{I}) are minimal, if not null. Some appreciable variations are observed for the alloys here investigated for the off-diagonal coefficient L_{AB}^{I} , and consequently on the wind factor G^{I} .

The convergence of G^{I} with respect to the several interaction models is shown in Fig. 12 for Cr, Cu, Ni, and Si. In the crude zero-shell approximation, the absence of correlations leads to $L_{AB}^{\text{I}} = 0$ and hence $G^{\text{I}} = 1$. The extension of the model to the 2nn modifies the correlations only slightly, with the exception of Cu where the variation is more important. This is due to the larger dumbbell-copper thermodynamic (repulsive) interactions observed at 2nn (Fig. 4). For the other elements (Mn,

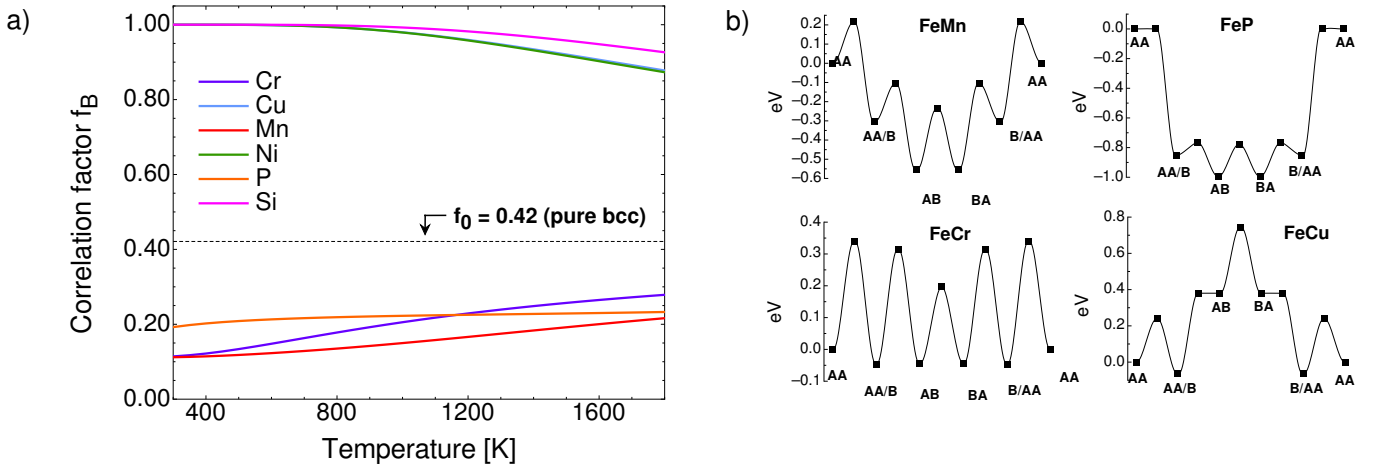


FIG. 9: a) Correlation factor for solute migration via dumbbell mechanism $f_B = L_{BB}^I/L_{BB}^{I,0}$. b) Qualitative representation of the energy landscape of the mixed dumbbell AB and the 1nn (target) configuration AA/B , for selected impurities. The AA label marks any dumbbell-solute configuration outside the interaction range.

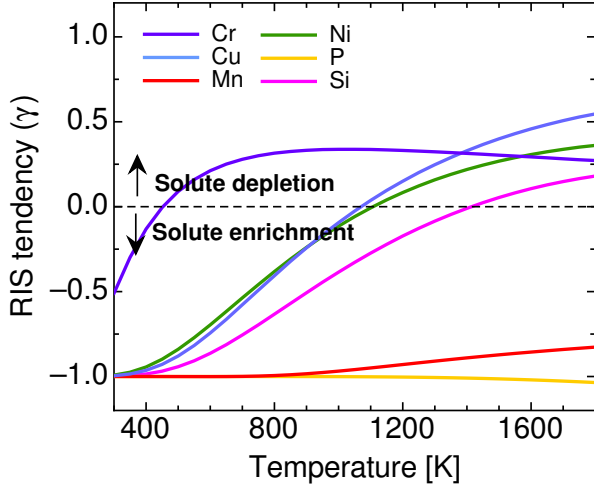


FIG. 10: Radiation induced segregation tendency γ_{RIS} (defined according to Eq. 12) as a function of temperature. Solute enrichment occurs for negative values of γ_{RIS} .

P) the variation of G^I is negligible. This shows that the extension of the SCMF model is needed when the solute-dumbbell interactions reach longer than the 1nn distance. In certain conditions, a variation of G^I can have a considerable impact on the RIS tendencies. However, for the impurities treated in this work, this has little (if no) effect on the solute-transport and RIS tendencies, because solute transport for Cu is dominated by vacancy drag, and because for the solutes diffusing via a vacancy mechanism (P, Mn, Cr) the off-diagonal coefficient is either negligible or unvaried.

CONCLUSIONS

Here has been presented an investigation of solute transport via a dumbbell mechanism in dilute iron alloys, with the aim of completing the diffusion mechanisms for selected impurities (Cr, Cu, Mn, Ni, P, Si) treated in a previous work [16], and of determining global radiation-induced segregations tendencies that take into account both vacancies and interstitial contributions. This has been achieved by combining *ab initio* calculations of dumbbell migration barriers in a multifrequency network with a self-consistent mean field model [28] that allows for the determination of transport coefficients and flux-coupling tendencies. The mean-field model has been extended in order to include solute-dumbbell thermodynamic interactions up to the second nearest-neighbor position. Moreover, a new mathematical framework has been developed in order to express the steady-state radiation-induced segregation profiles in dilute alloys as functions of the solute-defect flux coupling and the relative efficiency of vacancy versus interstitial transport. This framework allows for the identification of the dominant diffusion mechanisms and for the prediction of RIS profiles without computing the full set of transport coefficients.

The results show that the mixed dumbbell is stable and mobile for Cr, Mn, and P impurities, whereas it is unstable and immobile for Cu, Ni, and Si. The combination of stability and mobility of the mixed dumbbell leads to solute transport only for the first group of impurities. Correlations in this case play only a secondary role. In particular, Mn and P transport is dominated by the mixed dumbbell, whose migration occurs independently of Fe atoms and is dominant over the vacancy mechanism. This leads for P and Mn atoms to an almost

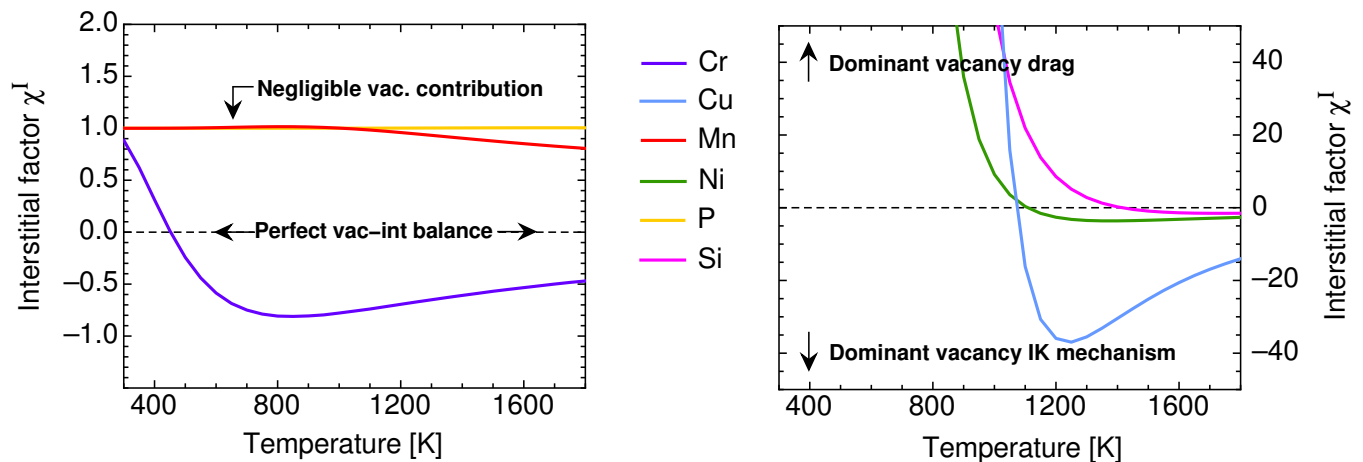


FIG. 11: Variation with temperature of the interstitial factor χ^I defined according to Eq. 18. This factor is equal to 1 when interstitial-assisted diffusion dominates over vacancy-assisted diffusion, whereas it takes very large positive values when vacancy drag is dominant, or very large negative values when inverse-Kirkendall (IK) diffusion dominates. $\chi^I = 0$ when the two diffusion mechanisms are in perfect equilibrium (and the total RIS tendency is hence null).

temperature-independent enrichment tendency, which is confirmed by the experimental evidence of heavy P and Mn segregation on grain boundaries and dislocations. The peculiarity of these two systems is confirmed also by an anomaly in the solute diffusion coefficient, which is predicted to decrease with increasing temperature, if the interstitial concentration is fixed. On the other hand, dumbbell transport does not occur for Ni, Si, and especially Cu impurities, for which the vacancy diffusion dominates. In this case, enrichment at defect sinks is predicted on the low-temperature end because of the vacancy-drag mechanism, in agreement with experimental observations. These solute can anyway affect interstitial migration because they can bind in first nearest-neighbor positions with the dumbbell, in agreement with resistivity-recovery experiments. Finally, Cr transport by dumbbells is in opposition with the vacancy-diffusion mechanism, which leads to a fine balance between enrichment and depletion tendency and to a switchover at 460 K. This can explain the variety of RIS tendencies arisen from several experiments and is in qualitative agreement with the switchover observed in concentrated alloys [24]. The extension of this model to concentrated FeCr alloys is therefore of great interest and will be pursued in future works..

ACKNOWLEDGMENTS

This work was financially supported by Vattenfall AB, Göran Gustafsson Stiftelse, and the Euratom research and training programme 2014-2018 under the grant agreement No 661913 (SOTERIA). The paper reflects only the authors' view and the European Commis-

sion is not responsible for any use that may be made of the information it contains. It contributes to the Joint Program on Nuclear Materials (JPNM) of the European Energy Research Alliance (EERA). The high-performance computing resources were provided by the Swedish National Infrastructure for Computing (SNIC). Moreover, the authors acknowledge T. Garnier for the help in the extension of the SCMF model.

* messina@kth.se

- [1] F. Danoix, E. Bémont, P. Maugis, and D. Blavette, *Adv. Eng. Mater.* **8**, 1202 (2006).
- [2] Z. Mao, C. K. Sudbrack, K. E. Yoon, G. Martin, and D. N. Seidman, *Nat. Mater.* **6**, 210 (2007).
- [3] C. A. English, S. M. Murphy, and J. M. Perks, *Faraday Trans.* **86**, 1263 (1990).
- [4] M. K. Miller, *J. Mater. Sci.* **41**, 7808 (2006).
- [5] Y. Nishiyama, K. Onizawa, M. Suzuki, J. W. Andereg, Y. Nagai, T. Toyama, M. Hasegawa, and J. Kameda, *Acta Mater.* **56**, 4510 (2008).
- [6] M. Lambrecht and A. Almazouzi, *J. Nucl. Mater.* **385**, 334 (2009).
- [7] E. Meslin, B. Radiguet, P. Pareige, C. Toffolon, and A. Barbu, *Exp. mech.* **51**, 1453 (2011).
- [8] E. Meslin, B. Radiguet, and M. Loyer-Prost, *Acta Mater.* **61**, 6246 (2013).
- [9] M. K. Miller, K. A. Powers, R. K. Nanstad, and P. Efsing, *J. Nucl. Mater.* **437**, 107 (2013).
- [10] P. B. Wells, T. Yamamoto, B. Miller, T. Milot, J. Cole, Y. Wu, and G. R. Odette, *Acta Mater.* **80**, 205 (2014).
- [11] C. Pareige, V. Kuksenko, and P. Pareige, *J. Nucl. Mater.* **456**, 471 (2015).
- [12] P. D. Styman, J. M. Hyde, D. Parfitt, K. Wilford, M. G. Burke, C. A. English, and P. Efsing, *J. Nucl. Mater.*

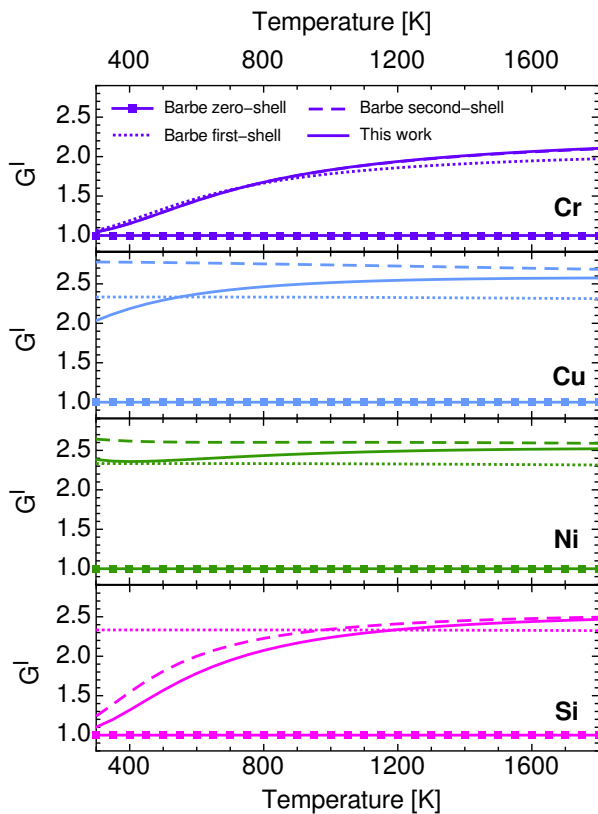


FIG. 12: Comparison of the wind factor G^I with respect to the thermodynamic models used in the previous work by Barbe *et al.* [26].

- 459, 127 (2015).
- [13] G. R. Odette and R. K. Nanstad, *JOM* **61**, 17 (2009).
- [14] T. Garnier, M. Nastar, P. Bellon, and D. R. Trinkle, *Phys. Rev. B* **88**, 134201 (2013).
- [15] T. Garnier, D. R. Trinkle, M. Nastar, and P. Bellon, *Phys. Rev. B* **89**, 144202 (2014).
- [16] L. Messina, M. Nastar, T. Garnier, C. Domain, and P. Olsson, *Phys. Rev. B* **90**, 104203 (2014).
- [17] L. Messina, M. Nastar, N. Sandberg, and P. Olsson, submitted to *Physical Review B*.
- [18] C. Domain and C. S. Becquart, *Phys. Rev. B* **71**, 214109 (2005).
- [19] P. Olsson, C. Domain, and J. Wallenius, *Phys. Rev. B* **75**, 014110 (2007).
- [20] P. Olsson, T. P. C. Klaver, and C. Domain, *Phys. Rev. B* **81**, 054102 (2010).
- [21] D. Terentyev, L. Malerba, and A. V. Barashev, *Philos. Mag. Lett.* **85**, 587 (2005).
- [22] G. Bonny, D. Terentyev, E. E. Zhurkin, and L. Malerba, *J. Nucl. Mater.* **452**, 486 (2014).
- [23] S. Choudhury, L. Barnard, J. D. Tucker, T. R. Allen, B. D. Wirth, M. Asta, and D. Morgan, *J. Nucl. Mater.* **411**, 1 (2011).
- [24] J. P. Wharry and G. S. Was, *J. Nucl. Mater.* **442**, 7 (2013).
- [25] M. Nastar, *Philos. Mag.* **85**, 3767 (2005).
- [26] V. Barbe and M. Nastar, *Philos. Mag.* **87**, 1649 (2007).
- [27] A. R. Allnatt and A. B. Lidiard, *Atomic Transport in Solids* (Cambridge University Press, 2003).
- [28] V. Barbe and M. Nastar, *Philos. Mag.* **86**, 3503 (2006).
- [29] A. D. Le Claire, *J. Nucl. Mater.* **69-70**, 70 (1978).
- [30] C.-C. Fu, F. Willaime, and P. Ordejón, *Phys. Rev. Lett.* **92**, 175503 (2004).
- [31] J.-L. Bocquet, *Res. Mech.* **22**, 1 (1987).
- [32] G. Kresse and J. Hafner, *Phys. Rev. B* **47**, 558 (1993).
- [33] G. Kresse and J. Hafner, *Phys. Rev. B* **49**, 14251 (1994).
- [34] G. Kresse and J. Hafner, *J. Phys. Condens. Matter* **6**, 8245 (1994).
- [35] P. E. Blöchl, *Phys. Rev. B* **50**, 17953 (1994).
- [36] G. Kresse and D. Joubert, *Phys. Rev. B* **59**, 1758 (1999).
- [37] J. P. Perdew, K. Burke, and Y. Wang, *Phys. Rev. B* **54**, 16533 (1996).
- [38] P. Pulay, *Chem. Phys. Lett.* **73**, 393 (1980).
- [39] G. P. Kerker, *Phys. Rev. B* **23**, 3082 (1981).
- [40] G. Mills, H. Jonsson, and G. K. Schenter, *Surf. Sci.* **324**, 305 (1995).
- [41] H. Jonsson, G. Mills, and K. W. Jacobsen, in *Classical and quantum dynamics in condensed phase simulations*, edited by B. J. Berne, G. Ciccotti, and D. F. Coker (World Scientific, 1998).
- [42] G. Henkelman, B. P. Uberuaga, and H. Jonsson, *J. Chem. Phys.* **113**, 9901 (2000).
- [43] G. H. Vineyard, *J. Phys. Chem. Solids* **3**, 121 (1957).
- [44] G. E. Lucas and R. Schäublin, *Nucl. Instrum. Methods Phys. Res. B* **267**, 3009 (2009).
- [45] N. Anento, A. Serra, and Y. N. Osetsky, *Modell. Simul. Mater. Sci. Eng.* **18**, 025008 (2010).
- [46] M. Nastar and F. Soisson, in *Comprehensive Nuclear Materials*, edited by R. J. M. Konings, T. R. Allen, R. E. Stoller, and S. Yamanaka (Elsevier Inc., Amsterdam, 2012) pp. 471–496.
- [47] R. Sizmann, *J. Nucl. Mater.* **69**, 386 (1978).
- [48] T. R. Anthony, in *Diffusion in Solids: Recent Developments*, edited by A. S. Nowick and J. J. Burton (Academic Press, New York, 1975) pp. 353–378.
- [49] E. Vincent, C. S. Becquart, and C. Domain, *J. Nucl. Mater.* **359**, 227 (2006).
- [50] E. Meslin, C.-C. Fu, A. Barbu, F. Gao, and F. Willaime, *Phys. Rev. B* **75**, 094303 (2007).
- [51] A. Bakaev, D. Terentyev, G. Bonny, T. P. C. Klaver, P. Olsson, and D. Van Neck, *J. Nucl. Mater.* **444**, 237 (2014).
- [52] A. Janotti, M. Krčmar, C. L. Fu, and R. C. Reed, *Phys. Rev. Lett.* **92**, 085901 (2004).
- [53] T. Ohnuma, N. Soneda, and M. Iwasawa, *Acta Mater.* **57**, 5947 (2009).
- [54] P. Olsson, *J. Nucl. Mater.* **386-388**, 86 (2009).
- [55] S. Takaki, J. Fuss, H. Kuglers, U. Dedek, and H. Schultz, *Rad. Eff.* **79**, 87 (1983).
- [56] F. Maury, P. Lucasson, A. Lucasson, F. Faudot, and J. Bigot, *J. Phys. F* **17**, 1143 (1987).
- [57] F. Maury, A. Lucasson, P. Lucasson, P. Moser, and F. Faudot, *J. Phys. Condens. Matter* **2**, 9291 (1990).
- [58] H. Abe and E. Kuramoto, *J. Nucl. Mater.* **271**, 209 (1999).
- [59] R. Ngayam-Happy, P. Olsson, C. S. Becquart, and C. Domain, *J. Nucl. Mater.* **407**, 16 (2010).
- [60] F. Maury, A. Lucasson, P. Lucasson, P. Moser, and Y. Loreaux, *J. Phys. F* **15**, 1465 (1985).

APPENDIX A: Equilibrium configuration nomenclature

The procedure for the categorization of the atomic sites in the LAE of the dumbbell is shown in Table IV. Each site C is assigned a label $x\alpha$ according to Fig. 1. x marks the nearest-neighbor distance to the dumbbell and α depends on the symmetry with respect to the dumbbell atoms A and B: a is assigned if $AC = BC$, whereas b and c are assigned for sites with decreasing distance to either A or B. In this specific example, the dumbbell is placed in the centre of the reference system (as shown in Fig. 1) and is oriented towards the $\langle 110 \rangle$ direction. The

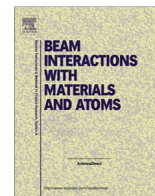
dumbbell atoms are assumed to be placed symmetrically and spaced by 2δ , with δ much smaller than a_0 . The coordinates of A and B are then $[-\delta, -\delta, 0]$ and $[\delta, \delta, 0]$, respectively. All site coordinates and distances are expressed in units of $a_0/2$.

As can be seen from Table IV, in the shell including up to the 5nn there are 12 non-equivalent equilibrium configurations that need to be distinguished when computing the solute-dumbbell interaction. In the 1nn, '1a' and '1b' correspond to the traditional definition of 'tensile' and 'compressive' site. Two configurations are distinguished also for 2nn and 5nn sites, whereas three different configurations a , b , and c are needed for 3nn and 4nn sites.

TABLE IV: Procedure for the atomic-site labelling of Fig. 1. The coordinates of the dumbbell atoms A and B are respectively $[-\delta, -\delta, 0]$ and $[\delta, \delta, 0]$, where 2δ is the distance between the dumbbell atoms. The dumbbell is placed in the centre of the reference system and oriented along the $\langle 110 \rangle$ direction. Lengths are given in units of $a_0/2$.

Site coordinates	Label	Distance to A	Distance to B
$[-1, 1, 1]$	1a	$\sqrt{2\delta^2 + 3}$	$\sqrt{2\delta^2 + 3}$
$[1, 1, 1]$	1b	$\sqrt{2\delta^2 + 4\delta + 3}$	$\sqrt{2\delta^2 - 4\delta + 3}$
$[0, 0, 2]$	2a	$\sqrt{2\delta^2 + 4}$	$\sqrt{2\delta^2 + 4}$
$[2, 0, 0]$	2b	$\sqrt{2\delta^2 + 4\delta + 4}$	$\sqrt{2\delta^2 - 4\delta + 4}$
$[0, 2, 0]$	2b	$\sqrt{2\delta^2 + 4\delta + 4}$	$\sqrt{2\delta^2 - 4\delta + 4}$
$[-2, 0, 0]$	2b	$\sqrt{2\delta^2 - 4\delta + 4}$	$\sqrt{2\delta^2 + 4\delta + 4}$
$[-2, 2, 0]$	3a	$\sqrt{2\delta^2 + 8}$	$\sqrt{2\delta^2 + 8}$
$[2, 0, 2]$	3b	$\sqrt{2\delta^2 + 4\delta + 8}$	$\sqrt{2\delta^2 - 4\delta + 8}$
$[0, 2, 2]$	3b	$\sqrt{2\delta^2 + 4\delta + 8}$	$\sqrt{2\delta^2 - 4\delta + 8}$
$[-2, 0, 2]$	3b	$\sqrt{2\delta^2 - 4\delta + 8}$	$\sqrt{2\delta^2 + 4\delta + 8}$
$[2, 2, 0]$	3c	$\sqrt{2\delta^2 + 8\delta + 8}$	$\sqrt{2\delta^2 - 8\delta + 8}$
$[-1, 1, 3]$	4a	$\sqrt{2\delta^2 + 11}$	$\sqrt{2\delta^2 + 11}$
$[1, 1, 3]$	4b	$\sqrt{2\delta^2 + 4\delta + 11}$	$\sqrt{2\delta^2 - 4\delta + 11}$
$[3, 1, 1]$	4c	$\sqrt{2\delta^2 + 8\delta + 11}$	$\sqrt{2\delta^2 - 8\delta + 11}$
$[-2, 2, 2]$	5a	$\sqrt{2\delta^2 + 12}$	$\sqrt{2\delta^2 + 12}$
$[2, 2, 2]$	5b	$\sqrt{2\delta^2 + 8\delta + 12}$	$\sqrt{2\delta^2 - 8\delta + 12}$

Paper IV



Stability and mobility of small vacancy–solute complexes in Fe–MnNi and dilute Fe–X alloys: A kinetic Monte Carlo study



Luca Messina^{a,*}, Lorenzo Malerba^b, Pär Olsson^a

^a KTH Royal Institute of Technology, Reactor Physics, 106 91 Stockholm, Sweden

^b Structural Materials Group, Institute of Nuclear Materials Science, SCK-CEN, Boeretang 200, B-2400 Mol, Belgium

ARTICLE INFO

Article history:

Received 11 July 2014

Received in revised form 30 November 2014

Accepted 15 December 2014

Available online 13 January 2015

Keywords:

Ferritic alloys

AKMC

Vacancy diffusion

Solute clusters

ABSTRACT

Manganese and nickel solute atoms in irradiated ferritic steels play a major role in the nanostructural evolution of reactor pressure vessels (RPV), as they are responsible for the formation of embrittling nanofeatures even in the absence of copper. The stability and mobility of small vacancy–solute clusters is here studied with an atomistic kinetic Monte Carlo approach based on *ab initio* calculations, in order to investigate the influence of Mn and Ni on the early life of small radiation-induced vacancy clusters, and to provide the necessary parameters for advanced object kinetic Monte Carlo simulations of the RPV long-term nanostructural evolution. Migration barriers are obtained by direct *ab initio* calculations or through a binding energy model based on *ab initio* data. Our results show a clear immobilizing and stabilizing effect on vacancy clusters as the solute content is increased, whereas the only evident difference between the two solute species is a somewhat longer elongation of the cluster mean free path in the presence of a few Mn atoms.

© 2014 Elsevier B.V. All rights reserved.

1. Introduction

The influence of manganese and nickel on the microstructural evolution of reactor pressure vessel (RPV) steels under irradiation has recently become of great interest. The observed formation of Mn–Ni–Si-rich nanoclusters is responsible for a possible unexpected acceleration of the RPV embrittlement process and might jeopardize the RPV structural integrity in the long term [1]. The analysis of neutron-irradiated model materials [2–4] combined with atomistic simulations [5] suggests that such clusters form from the very beginning of irradiation, despite the apparently missing thermodynamic driving force, even in case of low- or no-copper alloys.

The emerging mechanism for the nanocluster formation is segregation of solute atoms (Mn, Ni, Si) on small point-defect (PD) clusters, the mobility of which is progressively reduced by the presence of the solutes themselves. Such complexes act then as sinks for other mobile defects and small defect–solute complexes. As a matter of fact, solute atoms can be transported by defects towards these nucleation sites, causing the clusters to grow in size. The effective “pinning effect” of solute atoms on SIA loops emerges from several studies [6–8], whereas the systematic arising

of a vacancy drag effect in iron dilute alloys has been recently shown [9] to be a very effective means of solute transport towards defect sinks in RPV steels, and could hence confirm this mechanism. In particular, Mn is expected to have a specifically strong effect on SIA-loop mobility because of the strong interaction between Mn and crowdion, in analogy with the effect of Cr [7] and because it is known to efficiently diffuse via a dumbbell mechanism. However, no full nanostructural evolution model has been yet developed to prove that this mechanism actually occurs.

Object kinetic Monte Carlo (OKMC) simulations are a powerful tool to describe the evolution of materials under irradiation up to approximately 1 dpa. In these simulations, the evolution of objects such as single PD, PD clusters and mixed clusters is followed without any atomic-level description of their structure, allowing for better computational efficiency than atomistic kinetic Monte Carlo (AKMC) simulations. The first steps towards the development of an OKMC model for the Fe–MnNi system are described in [10]. The necessary information about the stability and mobility of each object is usually not available experimentally; however, such quantities can be computed via AKMC simulations, as was recently done for Fe–Cu alloys [11–13].

The objective of this work is therefore to obtain the stability and mobility of small vacancy–solute complexes with AKMC simulations, exclusively based on *ab initio*-computed binding energies and migration barriers. This study provides a preliminary insight

* Corresponding author.

E-mail address: messina@kth.se (L. Messina).

on the effect of Mn and Ni on the small vacancy cluster behavior, as well as the necessary parameters for the development of an OKMC model for dilute Fe–MnNi alloys. In addition, it completes the diffusion study in [9] by providing some kinetic properties of solute–vacancy pairs in iron dilute alloys that could not be obtained with the mean field approach therein applied.

2. Calculation method

2.1. AKMC algorithm

The LAKIMOCA code [14] is employed to perform the AKMC simulations. In the AKMC approach, the evolution of the system is modeled as a sequence of vacancy jumps occurring at a rate $\Gamma = \nu \exp(-E_a/k_B T)$, where ν is the attempt frequency and E_a is the vacancy migration energy. At each jump, the time step is estimated through the residence time algorithm [15].

Clusters containing up to two atoms of each kind and up to four vacancies are here considered. The algorithm used in this work is the same as in [12,13], where analogous calculations were performed for vacancy–copper clusters. A given cluster is introduced in the center of a 16,000-atom simulation box in its assumed most stable configuration (a core of vacancies surrounded by solute atoms progressively filling the nearest neighbor (nn) shells). The position of the cluster center of mass (COM) is tracked until the cluster dissociation. In this work, a cluster is defined by any constituent (other than Fe) being within 5nn distance of each other. In order to gather sufficient statistical data, each simulation (same cluster and temperature) is repeated with 10^2 to 10^3 different seeds.

At the end of each stack of calculations, the lifetime is given by the average of the simulation times τ_{life}^i at cluster dissociation. The dissociation energy E_{diss} and the lifetime prefactor τ_0 can be then calculated by linear regression in the Arrhenius domain: $\tau(T) = \tau_0 \exp(E_{\text{diss}}/k_B T)$.

For the diffusion coefficient calculation, the trajectories obtained with different seeds are chained together to form a unique long trajectory. Subsequently, this trajectory is divided in small segments corresponding to a given Δt . The diffusion coefficient is then computed as:

$$D(T) = \frac{1}{N^{\text{II}}} \sum_{j=1}^{N^{\text{II}}} \frac{R_j^2}{6\Delta t_j}, \quad (1)$$

where R_j^2 is the COM square displacement in segment j and N^{II} is the number of segments. Note that the Δt of each segment might differ slightly due to the stochastic advancement of the AKMC time. The procedure is repeated for several values of Δt . The diffusion coefficient $D(T)$ is taken as the average diffusion coefficient in the convergence zone [12]. The migration barrier E_{mig} and diffusion prefactor D_0 are again obtained by linear regression: $D(T) = D_0 \exp(-E_{\text{mig}}/k_B T)$.

Lastly, the mean free path (MFP) of the cluster is obtained from Eq. (1):

$$\delta(T) = \sqrt{6D\tau}. \quad (2)$$

2.2. AKMC parametrization

The activation energies defining the event probability in the AKMC simulations depend on the local atomic environment (LAE) around the exchanging vacancy–atom pair. In this respect, two distinct approaches are here applied for two different sets of simulations.

In the binary dilute limit (only one vacancy and one solute atom in the LAE), a limited amount of jump frequencies is needed; hence the corresponding activation energies can be computed by means of *ab initio* methods. In [9], a full set of activation energies was obtained for dilute Fe–X alloys with density functional theory (DFT), and the self-consistent mean field method [16] was applied to analyze the drag tendency of a solute atom by a vacancy. However, no information about the migration and the lifetime of the vacancy–solute pair was calculated. Therefore, in the first set of simulations of this work, the Fe–X alloys are simulated in LAKIMOCA by providing the complete table of DFT migration barriers, limited to a 2nn-shell approximation (which entails 10 jump frequencies totally). The mobility and stability of the vacancy–solute pairs are computed, and the results are shown in the following section.

In the general case of a non-dilute alloy, the number of possible LAE configurations is extremely large. In [12,13], the activation energies were obtained by interpolation with an artificial neural network algorithm on a (large) amount of barriers calculated by means of an interatomic potential. This method is not viable at the moment for the Fe–MnNi system, given the lack of fully reliable interatomic potentials. Therefore, the common final-to-initial-state-energy (FISE) approach is applied:

$$E_{\text{mig}} = E_{\text{mig}}^0 + \frac{E_f - E_i}{2}. \quad (3)$$

E_{mig}^0 is the reference migration barrier of the jumping species and E_i , E_f are the energy of the initial and final configurations. For the latter parameters, pair-interaction cohesive models are usually employed, as done in [17] with DFT-computed properties and fitting on experimental data. Despite the good results obtained in terms of resistivity recovery experiments [18] and cluster precipitation [5], such a model fails in reproducing the drag effect that is dominant at low temperatures [9].

Here the emphasis is on the vacancy–solute interaction, in order to reproduce the drag effect as closely as possible. For this reason, the energy of a given configuration is calculated as the total binding energy between vacancies, Mn and Ni pairs in 1nn and 2nn. The energy difference appearing in Eq. (3) is therefore expressed as

$$\Delta E = \sum_{j=1}^{N^{\text{obj}}} \left[\left(E_{V-X_j}^{\text{b,i}} - E_{V-X_j}^{\text{b,f}} \right) + \left(E_{\text{AT}-X_j}^{\text{b,i}} - E_{\text{AT}-X_j}^{\text{b,f}} \right) \right], \quad (4)$$

where X_j are all the non-iron objects interacting with the jumping atom (AT) and with the vacancy (V) and N^{obj} is the amount of such objects.

Jump frequencies also depend on the attempt frequency ν , which is in principle a function of the LAE. Although the migration barrier term is dominant, the attempt frequency might affect solute–vacancy correlations when the differences between migration barriers in the LAE are small, as discussed in [9,19]. However, the qualitative effect on the cluster stability and mobility tendencies would be negligible. In consideration of the large amount of computational time required for DFT attempt frequency calculations, the Debye frequency ($\nu = 6$ THz) is assumed throughout this work.

Table 1 provides a complete overview on the DFT data employed in the AKMC parametrization. The binding energies were taken from previous DFT calculations [20–22], with the exception of the Mn–Ni interaction, which was computed in this work with the Vienna *ab initio* simulation package vasp [23–25] and the same parameters as in [20] for the sake of consistency. The reference migration barriers were computed in [9]. The much lower migration barrier for Mn with respect to the previous AKMC parametrization [17] results in time-consuming trapping effects at low temperatures. For this reason, many of the cluster simulations were not performed below 450 K.

Table 1

Ab-initio interaction energies between vacancies, Mn and Ni atoms and reference migration energies E_{mig}^0 , as calculated in this work or in previous studies [9,20–22]. Positive signs stand for attractive (binding) interactions.

	V–V [21]	V–Mn [22]	V–Ni [20]	Mn–Mn [22]	Mn–Ni	Ni–Ni [20]
<i>Interaction energies (eV)</i>						
1nn	0.16	0.17	0.12	0.26	0.04	0.02
2nn	0.23	0.11	0.20	–0.02	–0.01	0.01
	Fe	Mn	Ni			
<i>Migration energies (eV) [9]</i>						
E_{mig}^0	0.70	0.42	0.63			

3. Results and discussion

3.1. Vacancy–solute pairs in dilute alloys

In dilute alloys, vacancy drag affects all solutes observed in radiation-induced nanoclusters (Cu, Mn, Ni, Si, P) at RPV temperatures [9]. This analysis is now extended by calculating the diffusion coefficient, mean lifetime and MFP of the vacancy–solute pairs. The results are shown in Fig. 1, while the output of the Arrhenius fitting is reported in Table 2(a).

The behavior of Cr is remarkably different due to the lack of interaction with vacancies. Therefore, in dilute Fe(Cr) alloys the vacancy–solute complex is very unstable and does not lead to

diffusion of Cr via vacancy drag. In the other cases, the mobility of solute–vacancy pairs is influenced by the combined effect of vacancy–solute exchange rates and kinetic correlations. Specifically, the latter ones reduce the diffusion coefficient of the pair, since the vacancy performs many ineffective jumps (from a diffusion standpoint) as it turns around the solute. For instance, the mobility of the V–Mn complex is larger than that of V–P because of the stronger V–P kinetic correlations, although the solute migration barriers would suggest the opposite trend. In the same way, the V–Cr diffusion coefficient is higher than that of V–Cu and V–Si. Therefore, vacancy drag has the counterintuitive effect of reducing the solute mobility that would be expected in the absence of drag, whereas it has the opposite effect on the solute diffusion coefficient, as was shown in [9].

On the other hand, because of the strong binding tendency, the V–Mn and V–P pairs are remarkably stable. The combination of high stability and fast diffusion leads to very long MFP's, which in the case of P is consistent with the observed heavy segregation at grain boundaries or dislocations [26]. Concerning the other species, the V–Cu and V–Si complexes are more stable than V–Mn and V–Ni because of the larger binding energy (in first approximation E_{diss} can be estimated as the sum of binding and migration energy [14]).

Finally, the computed MFP of the V–Ni pair is shorter than the other solutes with similar drag tendencies (Mn, Cu). This is a direct consequence of the reduced mobility of the V–Ni pair given by the considerably higher migration barrier of Ni with respect to the other solutes. The combination of high stability and short MFP is likely to make Ni especially efficient in reducing the effective diffusion coefficient of the single vacancy, comparable with the more strongly bound Si and Cu.

3.2. Vacancy–solute clusters in Fe–MnNi

The lifetimes, diffusion coefficients and mean free paths as functions of temperature for all analyzed clusters are shown in Fig. 2(a), while the results of the linear regression in the Arrhenius domain are listed in Table 2(b). The clusters are grouped according to the number of vacancies, to understand how the evolution of a given vacancy cluster is affected by the presence of solutes.

A comparison between the vacancy–solute pairs (V–Mn and V–Ni) of this section and the previous one shows that the binding tendency is well reproduced, as the obtained lifetimes and dissociation energies are comparable. On the other hand, this binding energy model systematically yields smaller diffusion coefficients and MFP's. The reason lies on the sets of Fe–V migration barriers around the solute, which are all larger than the corresponding DFT values. The mobility of such pairs is therefore underestimated.

As far as the $V_xMn_yNi_z$ clusters are concerned, the cluster stability (lifetime and dissociation energy) is enhanced by the addition of solutes in all cases, sometimes significantly. By definition, this model cannot reproduce as much as the previous one the difference in vacancy migration barriers around Ni and Mn solute atoms. For this reason, at this preliminary stage no difference is observed between these two solutes, aside from the isolated case of the V_2 clusters, where a single Ni does not seem to affect much the life of the di-vacancy. The addition of undistinguished solute atoms has a strong effect, but no Mn–Ni synergy is found, as the lifetime increment is always given by the superposition of the effect of each species alone.

The expected decrease of diffusion coefficient with increasing cluster size is quite significant (three orders of magnitude when adding four solute atoms). This clearly suggests that small vacancy clusters are severely hindered in their motion when encountering solute atoms. Once more, no visible difference in the behavior of Mn and Ni is observable. The sharp increase of migration energy

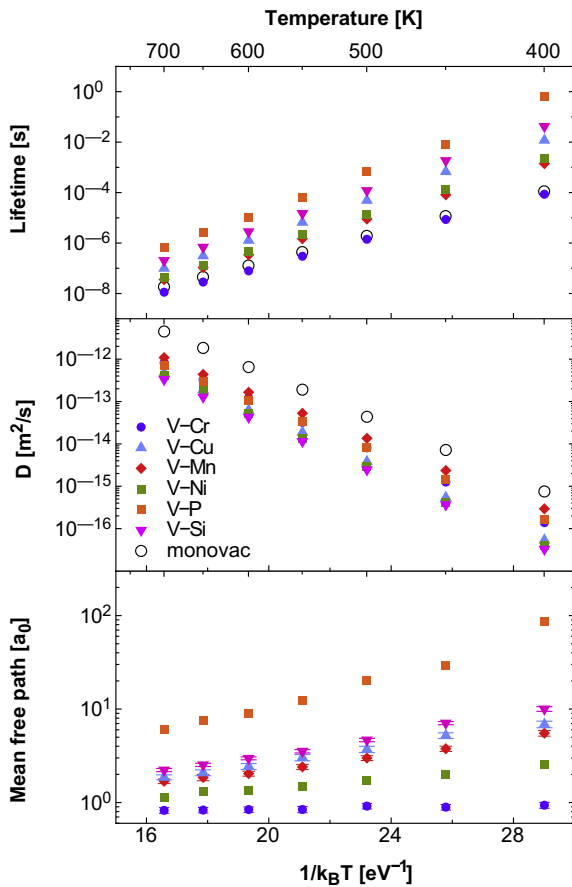


Fig. 1. Mean lifetimes, diffusion coefficients and mean free paths of vacancy–solute pairs in dilute binary alloys, as obtained by using the DFT-computed migration barriers in [9] for the AKMC parametrization. The monovacancy lifetime is defined as the average time intercurring between two consecutive vacancy jumps in a pure Fe matrix.

Table 2
Migration energies, dissociation energies, corresponding prefactors and mean free paths at 550 K (in atomic lattice units, $a_0 = 2.855 \text{ \AA}$) for: (a) vacancy–solute pairs in different Fe–X dilute binary alloys, as obtained by using the DFT-computed migration barriers in [9]; (b) vacancy–solute complexes, as obtained by means of the DFT binding-energy model.

Cluster	D_0 ($10^{-8} \text{ m}^2/\text{s}$)	E_{mig} (eV)	τ_0 (10^{-15} s)	E_{diss} (eV)	MFP (550 K) (a_0)
<i>Vacancy–solute pairs in dilute alloys (a)</i>					
V–Cr	8.85 ± 0.68	0.70 ± 0.003	73.2 ± 5.3	0.72 ± 0.003	0.84 ± 0.06
V–Cu	9.11 ± 0.69	0.73 ± 0.003	14.7 ± 2.1	0.95 ± 0.007	3.03 ± 0.24
V–Mn	5.89 ± 0.39	0.66 ± 0.003	29.6 ± 4.4	0.84 ± 0.007	2.41 ± 0.15
V–Ni	10.2 ± 1.43	0.75 ± 0.006	24.4 ± 1.5	0.87 ± 0.003	1.49 ± 0.10
V–P	4.95 ± 0.10	0.67 ± 0.001	7.34 ± 4.86	1.10 ± 0.023	12.4 ± 0.8
V–Si	7.03 ± 0.21	0.74 ± 0.001	17.2 ± 3.5	0.98 ± 0.009	3.54 ± 0.14
<i>One-vacancy clusters (b)</i>					
V_1	47.3	0.70			
$V_1\text{Mn}_1$	7.58 ± 0.32	0.74 ± 0.002	30.3 ± 6.3	0.85 ± 0.008	1.37 ± 0.07
$V_1\text{Mn}_2$	2.34 ± 0.12	0.71 ± 0.002	27.5 ± 3.2	0.93 ± 0.006	2.18 ± 0.09
$V_1\text{Ni}_1$	9.84 ± 0.55	0.75 ± 0.002	36.2 ± 2.0	0.85 ± 0.003	1.37 ± 0.05
$V_1\text{Ni}_2$	3.68 ± 0.23	0.79 ± 0.003	31.4 ± 1.8	0.93 ± 0.003	1.28 ± 0.08
$V_1\text{Mn}_1\text{Ni}_1$	5.10 ± 0.43	0.80 ± 0.004	29.8 ± 3.1	0.94 ± 0.005	1.39 ± 0.06
$V_1\text{Mn}_2\text{Ni}_2$	5.14 ± 0.68	0.93 ± 0.006	28.5 ± 4.9	1.07 ± 0.008	1.46 ± 0.12
<i>Two-vacancy clusters (b)</i>					
V_2	24.8 ± 0.6	0.74 ± 0.001	16.0 ± 1.1	0.88 ± 0.003	2.53 ± 0.10
$V_2\text{Mn}_1$	11.0 ± 0.2	0.79 ± 0.001	4.13 ± 0.41	1.05 ± 0.005	2.76 ± 0.11
$V_2\text{Mn}_2$	2.95 ± 0.45	0.76 ± 0.007	6.99 ± 2.12	1.08 ± 0.014	3.76 ± 0.18
$V_2\text{Ni}_1$	4.46 ± 0.60	0.73 ± 0.006	16.5 ± 3.2	0.93 ± 0.009	1.96 ± 0.15
$V_2\text{Ni}_2$	3.68 ± 0.09	0.79 ± 0.001	9.50 ± 1.32	1.03 ± 0.007	2.18 ± 0.10
$V_2\text{Mn}_1\text{Ni}_1$	3.32 ± 0.23	0.78 ± 0.003	11.2 ± 2.4	1.04 ± 0.010	2.53 ± 0.12
$V_2\text{Mn}_2\text{Ni}_2$	10.1 ± 1.0	0.98 ± 0.005	4.59 ± 2.05	1.22 ± 0.019	2.61 ± 0.20
<i>Three-vacancy clusters (b)</i>					
V_3	11.2 ± 0.4	0.73 ± 0.002	7.51 ± 1.22	0.98 ± 0.008	3.24 ± 0.14
$V_3\text{Mn}_1$	5.38 ± 0.46	0.77 ± 0.004	3.44 ± 0.72	1.12 ± 0.010	4.35 ± 0.26
$V_3\text{Mn}_2$	10.2 ± 1.0	0.87 ± 0.004	1.41 ± 0.32	1.25 ± 0.010	5.05 ± 0.32
$V_3\text{Ni}_1$	8.89 ± 0.60	0.80 ± 0.003	1.69 ± 0.27	1.15 ± 0.008	2.95 ± 0.19
$V_3\text{Ni}_2$	8.83 ± 0.71	0.87 ± 0.004	1.58 ± 0.52	1.22 ± 0.014	3.44 ± 0.20
$V_3\text{Mn}_1\text{Ni}_1$	8.68 ± 0.56	0.87 ± 0.003	2.19 ± 0.45	1.21 ± 0.009	4.20 ± 0.22
$V_3\text{Mn}_2\text{Ni}_2$	6.91 ± 1.92	0.98 ± 0.012	1.46 ± 0.54	1.34 ± 0.016	3.83 ± 0.29
<i>Four-vacancy clusters (b)</i>					
V_4	17.1 ± 1.2	0.82 ± 0.003	1.37 ± 0.21	1.19 ± 0.007	6.58 ± 0.36
$V_4\text{Mn}_1$	15.1 ± 1.3	0.88 ± 0.004	0.94 ± 0.42	1.28 ± 0.018	6.83 ± 0.44
$V_4\text{Ni}_1$	7.03 ± 0.35	0.84 ± 0.002	1.77 ± 0.50	1.23 ± 0.012	5.89 ± 0.39
$V_4\text{Ni}_2$	20.0 ± 1.0	0.98 ± 0.002	0.54 ± 0.15	1.37 ± 0.012	5.76 ± 0.33
$V_4\text{Mn}_1\text{Ni}_1$	18.4 ± 1.5	0.97 ± 0.004	1.18 ± 0.47	1.33 ± 0.017	5.94 ± 0.37
$V_4\text{Mn}_2\text{Ni}_2$	5.72 ± 0.43	0.99 ± 0.003	1.28 ± 0.30	1.39 ± 0.011	4.87 ± 0.31
<i>Larger pure vacancy clusters (b)</i>					
V_5	12.1 ± 1.7	0.85 ± 0.006	1.63 ± 0.33	1.23 ± 0.008	6.47 ± 0.42
V_6	64.4 ± 9.6	1.05 ± 0.006	0.28 ± 0.07	1.44 ± 0.010	6.97 ± 0.39

ensures that the vacancy clusters are slowed down, though not completely immobilized.

The only visible difference between Mn- and Ni-containing clusters is in the MFP: while it is clearly prolonged by Mn, it is not affected (or is even decreased) by Ni atoms. In other words, vacancy clusters show a capability of dragging Mn atoms, which does not apply for Ni. This occurs because the addition of a second Ni solute to the cluster always increases the pair effective migration barrier, while the latter is often lowered by the addition of a second Mn atom. As a consequence, the diffusion coefficient of Ni-containing clusters is smaller and the MFP shorter.

In summary, even at this early stage of the analysis it is possible to establish that the addition of solute atoms systematically increases the stability of the vacancy clusters and decreases their mobility, in some cases at a large extent. On the other hand, it is not possible to observe any significant difference between the influence of Mn and Ni, at such small sizes, in terms of cluster stability and mobility, apart from a clearly longer MFP in presence of Mn. A more systematic approach embracing larger clusters with a smart sampling of the cluster composition (as in [13]), and with a more reliable energy model for the migration barrier calculation, is required in order to analyze more in depth possible disparities between the two solute species. This preliminary study based on

few DFT data allows therefore to conclude that Mn and Ni are likely to have a non negligible hampering effect on small vacancy clusters, although the extent of such effect – and the possible total cluster immobilization – cannot be assessed with certainty at this point.

3.3. Comparison with previous work

The results of our calculations are compared to [13] in Fig. 2(b), limited to the pure vacancy clusters from two to six elements. The calculations of this study replicate the same trends, which ensures the reliability of the results from a qualitative standpoint. The difference in lifetime (and lifetime prefactor) is due to the more restrictive cut-off condition for cluster dissociation applied in [13] with respect to this work (2nn vs 5nn). On the other hand, the mobility and MFP are here considerably underestimated. It is well known that the di-vacancy and the tri-vacancy are characterized by a lower migration barrier than the monovacancy [13,21,27]. In the case of di-vacancies, the dominant migration mechanism was identified in [21]: given the higher stability of the 2nn configuration and a particular combination of jump frequencies, the di-vacancy can easily switch from 2nn to 4nn and diffuse through the lattice. Evidently, this mechanism is not

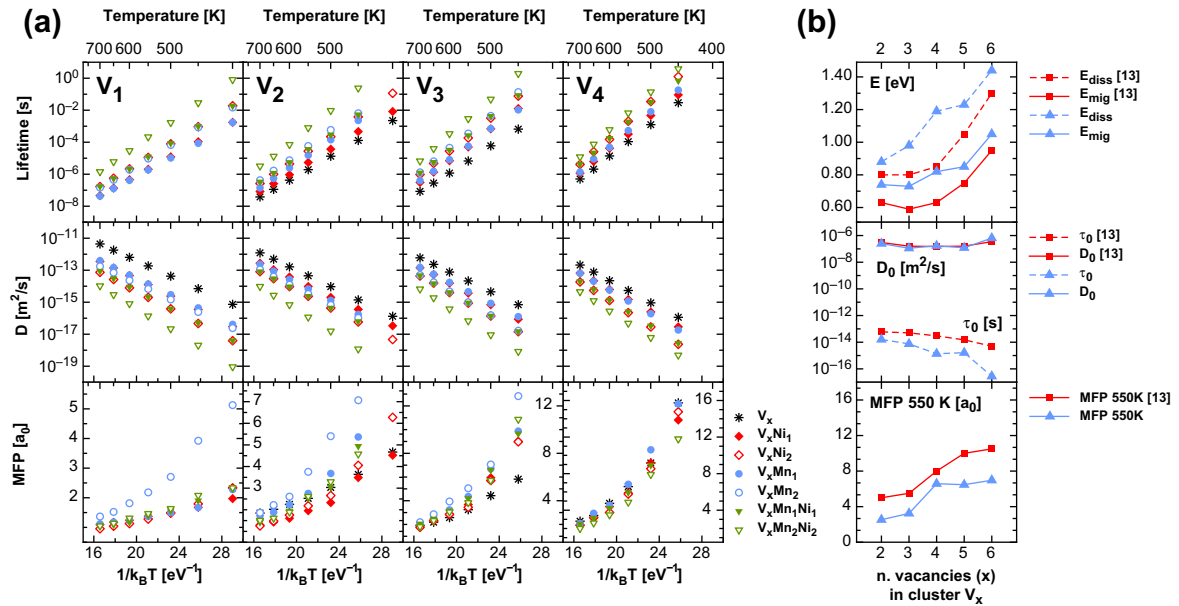


Fig. 2. (a) Mean lifetimes, diffusion coefficients and mean free paths of vacancy–solute complexes $V_xMn_yNi_2$ in Fe–MnNi, obtained with AKMC simulations based on the binding energy model for the calculation of migration barriers. (b) Migration and dissociation energies, corresponding prefactors and mean free paths of pure vacancy clusters, obtained in this work (blue lines) and compared to previous calculations (red lines) [13]. (For interpretation of the references to color in this figure legend, the reader is referred to the web version of this article.)

well reproduced by our binding energy model. A close look to the migration barriers for a di-vacancy complex reveals that the $\omega_{2nn-4nn}$ frequency is excessively large compared to the DFT value [21] and this atypical diffusion mechanism is therefore impeded. Moreover, the more common 1nn–2nn mechanism described in [27] is also underestimated, as the migration barriers predicted by our model are not significantly lower than the background barrier, as is the case for the DFT values [21]. A more accurate energy model is therefore needed in order to reproduce the correct behavior of vacancy clusters in bcc Fe and confirm the extent of the vacancy cluster immobilization and stabilization. At any rate, this does not affect the conclusions about the effect of solutes on vacancy cluster mobility, as the effect is relative to the case of pure vacancy clusters with no solutes.

4. Conclusions

The stability and mobility of vacancy–solute pairs in dilute alloys and of small vacancy–solute complexes was quantitatively analyzed with AKMC simulations. For the dilute alloys, DFT-calculated migration barriers were directly introduced in the AKMC code, whereas for the Fe–MnNi alloy the migration barriers were obtained with a DFT binding energy model including interactions between vacancies, Mn and Ni.

In the dilute case, the results complete the vacancy–solute interaction analysis performed in [9] and show that, even if the drag tendency is equally strong, the dissociation energy and mean free path of the various solute–vacancy pairs are considerably different. As for the Fe–Mn–Ni alloy, the trends in terms of mobility and stability of vacancy clusters of increasing size are in good agreement with previous calculations. This work shows that even the presence of few solute atoms in the vacancy clusters reduces their mobility and increases their stability significantly. Such considerable effect raises the interest for the development of a more accurate AKMC model, which will be the object of future work, in order to estimate the change of vacancy cluster mobility and stability as function of Mn and Ni concentration. The final output will provide the necessary parameters for the development of OKMC models, which in turn will give valuable insights on the formation,

growth and long-term evolution of the embrittling nanostructures in RPV steels.

Acknowledgments

This work was accomplished thanks to the financial support from Vattenfall, the Göran Gustafsson Foundation and the European Commission, in the framework of the MatISSE project under Grant No. 604862. It contributes to the Joint Programme on Nuclear Materials (JPNM) of the European Energy Research Alliance (EERA). The authors acknowledge N. Castin, M.I. Pascuet, C. Domain and M. Nastar for their valuable contributions.

References

- [1] G.R. Odette, R.K. Nanstad, Predictive reactor pressure vessel steel irradiation embrittlement models: issues and opportunities, *JOM* 61 (7) (2009) 17–23.
- [2] E. Meslin, M. Lambrecht, M. Hernández-Mayoral, F. Bergner, L. Malerba, P. Pareige, B. Radiguet, A. Barbu, D. Gómez-Briceño, A. Ulbricht, A. Almazouzi, Characterization of neutron-irradiated ferritic model alloys and a RPV steel from combined APT, SANS, TEM and PAS analyses, *J. Nucl. Mater.* 406 (1) (2010) 73–83.
- [3] E. Meslin, B. Radiguet, P. Pareige, C. Toffolon, A. Barbu, Irradiation-induced solute clustering in a low nickel FeMnNi ferritic alloy, *Exp. Mech.* 51 (9) (2011) 1453–1458.
- [4] E. Meslin, B. Radiguet, M. Loyer-Prost, Radiation-induced precipitation in a ferritic model alloy: an experimental and theoretical study, *Acta Mater.* 61 (16) (2013) 6246–6254.
- [5] R. Ngayam-Happy, C.S. Becquart, C. Domain, L. Malerba, Formation and evolution of MnNi clusters in neutron irradiated dilute Fe alloys modelled by a first principle-based AKMC method, *J. Nucl. Mater.* 426 (1–3) (2012) 198–207.
- [6] J. Marian, B. Wirth, J. Perlado, Mechanism of formation and growth of 100 interstitial loops in ferritic materials, *Phys. Rev. Lett.* 88 (25) (2002) 255507.
- [7] D. Terentyev, L. Malerba, A.V. Barashev, On the correlation between self-interstitial cluster diffusivity and irradiation-induced swelling in Fe–Cr alloys, *Philos. Mag. Lett.* 85 (11) (2005) 587–594.
- [8] Y. Osetsky, N. Anento, A. Serra, D. Terentyev, The role of nickel in radiation damage of ferritic alloys, *Acta Mater.* 84 (2015) 368–374.
- [9] L. Messina, P. Olsson, M. Nastar, T. Garnier, C. Domain, Exact *ab initio* transport coefficients in bcc Fe–X (X = Cr, Cu, Mn, Ni, P, Si) dilute alloys, *Phys. Rev. B* 90 (2014) 104203.
- [10] M. Chiappetto, C.S. Becquart, C. Domain, L. Malerba, Nanostructure evolution under irradiation of Fe(C)MnNi model alloys for reactor pressure vessel steels, *Nucl. Instr. Meth. Phys. Res. B* 352 (2015) 56–60.

- [11] F.G. Djurabekova, L. Malerba, C. Domain, C.S. Becquart, Stability and mobility of small vacancy and copper-vacancy clusters in bcc-Fe: an atomistic kinetic Monte Carlo study, *Nucl. Instr. Meth. Phys. Res. B* 255 (1) (2007) 47–51.
- [12] M.I. Pascuet, N. Castin, C.S. Becquart, L. Malerba, Stability and mobility of Cu-vacancy clusters in Fe–Cu alloys: a computational study based on the use of artificial neural networks for energy barrier calculations, *J. Nucl. Mater.* 412 (1) (2011) 106–115.
- [13] N. Castin, M.I. Pascuet, L. Malerba, Mobility and stability of large vacancy and vacancy-copper clusters in iron – an atomistic kinetic Monte Carlo study, *J. Nucl. Mater.* 429 (1–3) (2012) 315–324.
- [14] C. Domain, C.S. Becquart, L. Malerba, Simulation of radiation damage in Fe alloys: an object kinetic Monte Carlo approach, *J. Nucl. Mater.* 335 (1) (2004) 121–145.
- [15] A.B. Bortz, M.H. Kalos, J.L. Lebowitz, A new algorithm for Monte Carlo simulation of Ising spin systems, *J. Comput. Phys.* 17 (1) (1975) 10–18.
- [16] M. Nastar, A mean field theory for diffusion in a dilute multi-component alloy: a new model for the effect of solutes on self-diffusion, *Philos. Mag.* 85 (32) (2005) 3767–3794.
- [17] E. Vincent, C.S. Becquart, C. Domain, Microstructural evolution under high flux irradiation of dilute Fe–CuNiMnSi alloys studied by an atomic kinetic Monte Carlo model accounting for both vacancies and self interstitials, *J. Nucl. Mater.* 382 (2–3) (2008) 154–159.
- [18] R. Ngayam-Happy, P. Olsson, C.S. Becquart, C. Domain, Isochronal annealing of electron-irradiated dilute Fe alloys modelled by an *ab initio* based AKMC method: influence of solute-interstitial cluster properties, *J. Nucl. Mater.* 407 (1) (2010) 16–28.
- [19] T. Garnier, M. Nastar, P. Bellon, D.R. Trinkle, Solute drag by vacancies in body-centered cubic alloys, *Phys. Rev. B* 88 (2013) 134201.
- [20] P. Olsson, T.P.C. Klaver, C. Domain, *Ab initio* study of solute transition-metal interactions with point defects in bcc Fe, *Phys. Rev. B* 81 (5) (2010) 054102.
- [21] F. Djurabekova, L. Malerba, R.C. Pasianot, P. Olsson, K. Nordlund, Kinetics versus thermodynamics in materials modeling: the case of the di-vacancy in iron, *Philos. Mag.* 90 (19) (2010) 2585–2595.
- [22] A. Bakaev, D. Terentyev, G. Bonny, T.P.C. Klaver, P. Olsson, D. Van Neck, Interaction of minor alloying elements of high-Cr ferritic steels with lattice defects: an *ab initio* study, *J. Nucl. Mater.* 444 (1–3) (2014) 237–246.
- [23] G. Kresse, J. Hafner, *Ab initio* molecular-dynamics for liquid-metals, *Phys. Rev. B* 47 (1) (1993) 558–561.
- [24] G. Kresse, J. Hafner, Norm-conserving and ultrasoft pseudopotentials for first-row and transition-elements, *J. Phys.: Condens. Matter* 6 (40) (1994) 8245–8257.
- [25] G. Kresse, J. Hafner, *Ab-initio* molecular-dynamics simulation of the liquid-metal amorphous-semiconductor transition in germanium, *Phys. Rev. B* 49 (20) (1994) 14251–14269.
- [26] M.K. Miller, K.A. Powers, R.K. Nanstad, P. Efsing, Atom probe tomography characterizations of high nickel, low copper surveillance RPV welds irradiated to high fluences, *J. Nucl. Mat.* 437 (1–3) (2013) 107–115.
- [27] C.C. Fu, J. Dalla Torre, F. Willaime, J.L. Bocquet, A. Barbu, Multiscale modelling of defect kinetics in irradiated iron, *Nat. Mater.* 4 (1) (2005) 68–74.

Paper V

Introducing ab initio-based neural networks for transition-rate prediction in kinetic Monte Carlo simulations

L. Messina,^{1, a)} N. Castin,² C. Domain,³ and P. Olsson¹

¹⁾*KTH Royal Institute of Technology, Reactor Physics, SE-106 91 Stockholm, Sweden*

²⁾*Structural Materials Group, Institute of Nuclear Materials Science, SCK-CEN, Boeretang 200, B-2400 Mol, Belgium*

³⁾*Département Matériaux et Mécanique des Composants, EDF-R&D, Les Renardières, F-77250 Moret sur Loing, France*

(Dated: 13 November 2015)

This work presents an innovative approach to kinetic Monte Carlo (KMC) simulations, in which atomic transition rates are predicted by an artificial neural network trained on *ab initio* migration barriers. The method is applied to the parameterization of a hybrid atomistic-object KMC model to simulate copper precipitation during thermal aging in iron. The stability and mobility of copper clusters containing one vacancy is analyzed by means of independent atomistic KMC simulations driven by the same neural network, with the aim of parameterizing the object KMC part of the model. Copper clusters are found to be more stable and mobile with respect to previous studies, and can cover longer diffusion paths, reaching up to a few lattice units. The mean free path increases with cluster size up to around 100 copper atoms. In addition, the emission of the vacancy often occurs concurrently with the emission of one or more copper atoms, because of strong vacancy-copper correlations and kinetic coupling. In the hybrid KMC simulations, the density of copper clusters is overestimated because of the excessively high solution energy predicted by the *ab initio* method. Nevertheless, this work proves the capability of neural networks to transfer detailed *ab initio* thermodynamic and kinetic properties to the KMC model, and sets the ground for reliable microstructure evolution simulations in a wide range of alloys.

I. INTRODUCTION

Ferritic and ferritic-martensitic alloys are used in a wide range of industrial applications. Different types of impurities are purposely included to improve the mechanical properties, or inadvertently added as a result of the manufacturing processes. Defect-driven diffusion of such impurities plays a key role in driving the microstructure evolution of the alloy and in determining consequently its mechanical properties. The knowledge of the detailed atomic-transport processes and their accurate reproduction in microstructure-evolution simulation models is essential for the prediction of the mechanical-property evolution due to chemical redistribution, as well as to model the alloy radiation response. A typical example are irradiated reactor-pressure vessel (RPV) steels in nuclear power plants, where the formation of solute-defect precipitates¹⁻³, as well as solute segregation on grain boundaries and dislocations^{2,4,5} lead to hardening and embrittlement^{6,7}.

Modeling the long-term microstructure evolution is a common practice to understand the diffusion phenomena at the atomic scale, to predict the evolution of existing components, as well as to provide guidelines for more endurable alloys. Kinetic Monte Carlo (KMC) methods⁸ are a common choice, as they allow for the simulation of microstructure evolution up to the real time scales

and beyond, and for a complete spatial description of this evolution, as opposed for instance to rate theory models⁹. In particular, in atomistic KMC (AKMC) the alloy evolution is modeled as a sequence of atomic jumps, whose transition rates Γ need to be known as accurately as possible. In transition-state theory they are usually expressed as¹⁰:

$$\Gamma = \Gamma_0 \exp\left(\frac{E^{\text{mig}}}{k_B T}\right), \quad (1)$$

where Γ_0 is the attempt frequency and E^{mig} the migration energy. These transition rates must be determined with great accuracy, since they incorporate most of the physical properties of the alloy. Both quantities depend on the migrating chemical species and the local atomic environment (LAE). Although accurate methods are available to determine both Γ_0 and E^{mig} , such as for instance *ab initio* calculations, it is problematic to determine all needed transition rates because of the large amount of possible LAE configurations. Several methods are employed in order to work around this limitation. The most common choice is to infer the barriers from the end-state energies calculated by means of a cohesive model. The latter can be based on pair-interaction models, cluster expansion methods, or interatomic potentials⁸. Alternatively, the saddle-point energies can be obtained with a broken-bond approach^{8,11}. In any case, the reliability of the KMC simulation strictly depends on the quality of the cohesive model, which is for this reason fitted on *ab initio*-calculated properties, or experimental data. A complete review of the modeling

^{a)}Electronic mail: messina@kth.se

strategies is provided by Becquart and Domain⁹.

A different approach to the migration-barrier prediction consists in using regression scheme based on artificial neural networks (ANN)¹². This method allows for the prediction of migration barriers in unknown LAE's, after training of the ANN on a set of known barriers. It was applied to copper precipitation in iron^{13,14}, where the migration-barrier training set was obtained by means of an embedded-atom method (EAM)-based interatomic potential. It allows for an efficient "on-the-fly" calculation of migration barriers, provided that the employed energy model (e.g. the interatomic potential) correctly describes the physics of the alloy. It requires however the existence or development of a reliable alloy-specific potential. From this perspective, replacing the interatomic potential with density functional theory (DFT) can potentially improve the physical description. Moreover, it can allow for the application of ANN schemes to a wide variety of alloys, since DFT calculations can be performed on alloys of any chemical composition and complexity without loss of accuracy. However, it has been so far limited by computational-power issues. In the previous work¹³ the training set consisted of 10^4 NEB calculations, which was by then out of reach for *ab initio* methods. Nowadays, this is achievable thanks to the increased computational capabilities, and is performed for the first time in this work.

As a first test case, this novel approach is applied to the simulation of the relatively simple and well-studied case of copper precipitation under thermal aging in Fe(Cu) dilute alloys. This system is well-suited because the microstructure evolution is driven by the mobility of copper atoms and clusters in the presence of a single vacancy, and in the absence of strong magnetic interactions¹⁵. It also allows for a direct comparison with the EAM-based ANN¹³, as well as with previous KMC simulations¹¹. Thermal aging is simulated here by means of a hybrid atomistic-object KMC approach (AKMC-OKMC), where the transition rates are determined by the DFT-ANN interpolation scheme. In addition, the behavior of copper clusters is analyzed in comparison with previous studies^{11,13}. One caveat of the application of DFT on this specific alloy is represented by the copper solubility limit in iron. The solution energies obtained by various DFT methods are in fact in mutual disagreement^{15,16}, and this can strongly affect the copper precipitation kinetics.

At any rate, the combination of accurate *ab initio* computations with the regression capabilities of the ANN algorithm can potentially provide an efficient and reliable tool to predict migration barriers for KMC simulations as well as for other modeling tools, while ensuring an accurate description of the thermodynamic and kinetic properties of the investigated alloy. This study demonstrates the feasibility of the DFT-ANN approach, and prepares the ground for its application to more complex systems, such as for instance the evolution of RPV multicomponent alloys under irradiation.

II. METHODOLOGY

A. DFT-ANN training

Neural networks refer in general to a broad range of methods aimed at analyzing large databases and extract hidden useful information¹⁷. In this application, an ANN provides a non-linear regression scheme that allows for the prediction of unknown migration barriers as functions of the LAE that can be encountered by the vacancy during the KMC simulation. The ANN consists of a group of interconnected nodes, each of them transforming an input variable into an output variable through certain parameter-dependent mathematical functions. The training consists in determining the best-fitting node parameters based on a set of known migration barriers. Another set of barriers is calculated in order to validate the performance of the trained ANN. A thorough description of different ANN architectures, features, and training strategies can be found in previous publications^{12,13,18}.

Nowadays, DFT allows for the calculation of migration barriers in diverse atomic configurations to a high degree of accuracy, ensuring a reliable physical description of the alloy. However, the main limitation is represented by the computational time. The best compromise in terms of supercell size and minimum amount of training configurations must be achieved. For single vacancy-jump barrier calculations in iron, 250-atom supercells allow for a sufficient precision, but they are not suited for large solute clusters. Furthermore, the set of training configurations must be carefully selected, as it must be the most representative of the several LAE's encountered during the simulation.

Here, three LAE types are distinguished (Fig. 1): I) a random FeCu alloy, with a Cu concentration between 0.5% and 5%, II) a vacancy jumping in the vicinity or inside small Cu clusters (up to 80 atoms), and III) a vacancy jumping inside or across the surface of large spherical Cu clusters (up to 1000 atoms). Given the novelty of this approach, a scrupulous two-step procedure is followed in order to find the best minimum set of training configurations that allow for a satisfactorily small prediction error. In the first step, a large amount of LAE's is randomly created for each of the three LAE types. The corresponding migration barriers are calculated with an FeCu EAM potential¹³ in 250-atom supercells, with the exception of type-III configurations where the cell size is extended to 8192 atoms. From this large initial database, a subset of relevant atomic configurations is selected, with the aim of maximizing the LAE variety in each type, as well as obtaining an evenly-spread distribution of migration barriers. In the second step, a number x of configurations is randomly selected from the previous subset and used for ANN training and validation with the EAM values. The amount x is progressively increased until the ANN yields a satisfactory prediction of the validation data. In this phase, 75% of the x barriers are used for training, and the remaining ones for

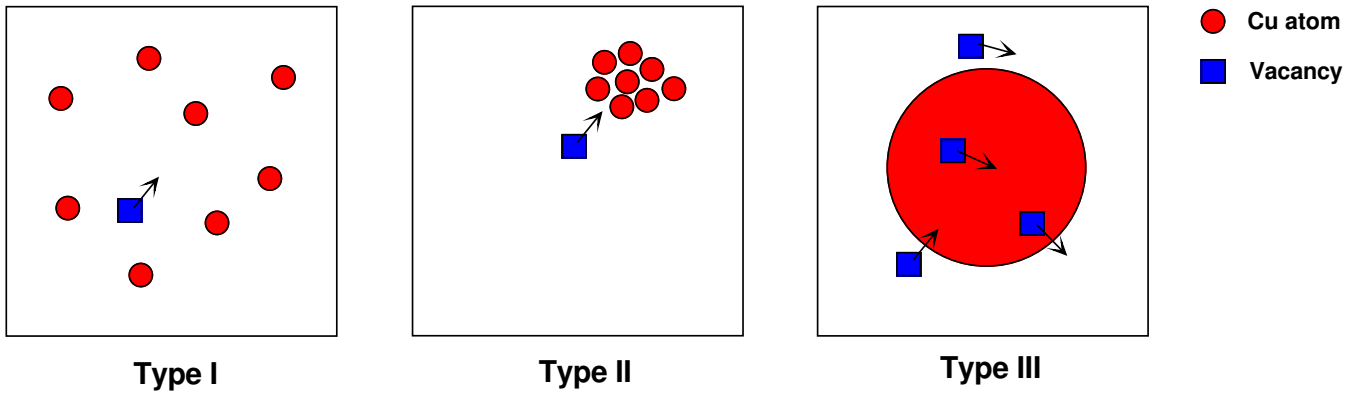


FIG. 1. Types of local atomic environment for the selection of sample configurations to be used for training and validation of the neural network.

validation. Configurations of type I and II are used for both sets, whereas type-III configurations are employed for validation only, as their DFT treatment is prevented by cell-size limitations.

In conclusion, a satisfactory ANN performance is reached with $x = 2000$. A majority of type-II barriers is needed to minimize the prediction error. The prediction error of type-III barriers does not exceed 15%, which allows for the assumption that type-III jumps will be well reproduced during the KMC simulations, even though none of them is included in the training procedure. It is worth mentioning that the use of the EAM potential is here aimed at providing a guideline for the selection of the training set, but is by no means necessary.

The migration barriers for the selected 2000 configurations are then recomputed by DFT. The calculations are performed using the Vienna *ab initio* simulation package (VASP)^{19–21} on a plane-wave basis, using the standard projector-augmented wave (PAW) pseudopotentials^{22,23} available in the VASP library. The Perdew-Burke-Erzerhof (PBE) parameterization²⁴ of the generalized-gradient approximation is employed to sample the exchange-correlation function. All calculations are spin polarized, and the spin interpolation of the correlation potential is achieved by means of the Vosko-Wilk-Nusair algorithm²⁵. The Brillouin zone is sampled with the Monkhorst-Pack scheme. The simulations are performed in 250-atom supercells containing a vacancy and a varying number of Cu atoms, in fully periodic boundary conditions. The plane-wave cutoff is set to 300 eV, and a k-point mesh of $3 \times 3 \times 3$ is chosen in accordance with the convergence tests of a previous work²⁶. The resulting equilibrium lattice parameter is $a_0 = 2.831 \text{ \AA}$. For each of the 2000 transitions, the end-state energies are calculated allowing for ionic relaxations but restraining the cell volume. The migration barriers are calculated with the nudged-elastic band (NEB) method^{27,28}, using three intermediate images and the climbing-image algorithm²⁹. Some tests performed on a few problematic cases with complex EAM energy paths confirm the

suitability of this choice. In order to limit the computational time required, each NEB calculation is performed first with a reduced amount of k-points ($2 \times 2 \times 2$), and the energy of the found saddle-point is then recalculated with the full k-point mesh without allowing for ionic relaxation. This accelerated procedure was tested on a few cases and proved not to be detrimental for the calculation accuracy. It is worth mentioning that in some cases the convergence of the end-state relaxation is greatly improved by providing an initial magnetic moment that is only slightly enhanced (2.3 Bohr magnetons). The total computational power required to complete the 2000 barriers is about 3 Mcore-hours.

After training, the ANN performance on the DFT validation set is shown in Fig. 2. The low prediction error confirms the quality of this approach for predicting unknown migration barriers. The few outliers correspond to configurations where the DFT energy difference between the end states is very large (up to 1.8 eV), and the migration barrier coincides with the large end-state energy difference. Such extreme cases are not well described by the ANN algorithm, but since they lead to very unstable high-energy configurations they are unlikely to affect the KMC simulations.

B. Hybrid AKMC-OKMC method

The thermal aging of a few FeCu alloys is simulated by means of a combined AKMC-OKMC model, which is fully described in a previous work¹³. The system is represented by a periodic bcc crystal containing an initially random mix of iron and copper atoms on a rigid lattice in a $128 \times 128 \times 128$ supercell, with a vacant site. The evolution of the system proceeds through a series of vacancy jumps, which are randomly selected based on the LAE-dependent transition rates as in Eq.1. The migration barriers of such rates are predicted "on the fly" by the ANN described in the previous section. The attempt frequencies Γ_0 are also in principle LAE dependent: for instance,

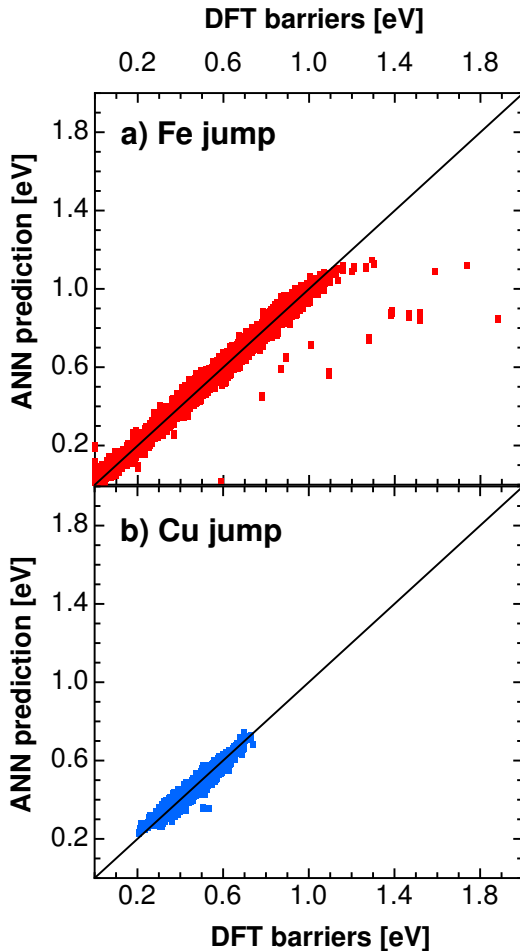


FIG. 2. Neural-network prediction of DFT migration barriers from the validation set for a) Fe-atom and b) Cu-atom jumps.

the attempt frequency for an iron jump is about 2.5 times larger than that of a copper jump³⁰. However, since DFT calculations of attempt frequencies are computationally demanding, it is here assumed $\Gamma_0 = 6$ THz for any transition, in analogy to previous studies^{13,31}. The simulation time is advanced with the traditional residence-time algorithm³².

Given the strong vacancy trapping of copper clusters due to the low vacancy formation energy in bcc copper, the simulation is accelerated by introducing a coarse-grain approximation and treating clusters above a certain size as objects. The cluster stability and mobility parameters (i.e. dissociation and migration frequencies) are obtained with independent AKMC simulations based on the same DFT-ANN model, using a common procedure that has been employed by several previous works^{14,33,34}.

Hence, in this hybrid approach the AKMC algorithm is applied when the vacancy is located outside any Cu cluster, which allows for the detailed reproduction of the drag mechanism of single Cu atoms³⁵. When the vacancy reaches a Cu cluster above the assigned size threshold, the evolution of that cluster is simulated with an

OKMC algorithm until the vacancy is re-emitted. The size threshold is set to 15 atoms, corresponding to the very stable configuration of one central atom surrounded by a fully-occupied first and second nearest-neighbor (nn) shell. Once activated, the cluster immediately absorbs all Cu atoms located within the 2nn distance from its surface. Three events are then allowed.

1. Vacancy emission, combined with the separate emission of n single Cu atoms.
2. Migration of the cluster by a 1nn distance $\Delta = \sqrt{3}a_0/2$, where a_0 is the lattice parameter, and subsequent absorption of all Cu atoms within the interaction range in the new position.
3. Coalescence of clusters with overlapping interaction ranges.

The maximum Cu-cluster size is set to 6000 atoms in order to remain within the coherent-precipitation stage¹³.

The simulation time t_{MC} needs to be rescaled in order to match the real thermal-equilibrium vacancy concentration:

$$t_{\text{real}} = t_{MC} \frac{c_v^{MC}}{c_v^{\text{real}}} . \quad (2)$$

As highlighted by previous works^{11,13}, the vacancy concentration of the simulation (c_v^{MC}) must be corrected with the fraction of time f_v spent by the vacancy far from Cu atoms:

$$c_v^{MC} = \frac{f_v}{N_{\text{at}} c_{Fe}} , \quad (3)$$

where N_{at} is the number of atoms in the simulation cell, and c_{Fe} is the concentration of Fe atoms. This correction is necessary because the vacancy-copper binding energy modifies the local vacancy formation energy. On the other hand, the real vacancy concentration in thermal equilibrium can be expressed as:

$$c_v^{\text{real}} = A \exp\left(-\frac{H_v^f}{k_B T}\right) \exp\left(\frac{S_v^f}{k_B}\right) . \quad (4)$$

The DFT vacancy formation enthalpy $H_v^f = 2.18$ eV and entropy $S_v^f = 4.1 k_B$ in pure iron were calculated in previous studies^{35,36}. Following the previous EAM-ANN work¹³, an additional factor A is introduced in order to account for various uncertainties, such as the presence of other impurities and the simplifications regarding the attempt frequencies. This factor was therein treated as a fitting parameter to the experimental results, but ideally it should be close to 1 independently of temperature and composition. This issue is discussed in Section IV.

C. OKMC parameterization

The OKMC part of the algorithm is parameterized by means of independent AKMC simulations aimed at obtaining the cluster migration and dissociation frequencies

as functions of size and temperature, as well as to determine the possible dissociation patterns. This is achieved by applying the procedure fully explained in previous works^{13,33,34}. A given cluster $v\text{Cu}_n$ is introduced in an otherwise pure-Fe simulation cell ($50 \times 50 \times 50$), and its evolution is simulated with the traditional AKMC algorithm until the vacancy is emitted. The transition rates are given by the trained DFT-ANN network. The "experiment" is repeated several times to gather sufficient statistics about the cluster lifetime τ_N and diffusion coefficient D_N . The latter is obtained from the cluster free path \bar{R}_N as:

$$D_N = \frac{(\bar{R}_N)^2}{6\tau_N}. \quad (5)$$

The average lifetime and diffusion coefficients are calculated in the high-temperature range and extrapolated down to the experimental temperatures with a linear fitting in the Arrhenius domain, as shown in Fig. 3. The dissociation frequency is given by the inverse of the lifetime:

$$\Gamma_N^{\text{diss}} = \frac{1}{\tau_N}. \quad (6)$$

Upon dissociation, the cluster can also emit single Cu atoms, as is discussed in the next section. The average number of emitted Cu atoms $\bar{n}_{\text{Cu}}^{\text{diss}} = 1.25$ is independent of temperature and cluster size.

The migration frequency is obtained as:

$$\Gamma_N^{\text{mig}} = \frac{6D_N}{\Delta^2}, \quad (7)$$

where the jump distance is $\Delta = \sqrt{3}a_0/2$. In Eq. 7 correlations are neglected, which is acceptable as long as a large number of trajectories is simulated and averaged. A continuous variation of D_N and τ_N is obtained by fitting with the following smooth functions:

$$\Gamma_N^{\text{mig}} = \begin{cases} A (\ln N)^B & \text{for } N \leq 450 \\ C \exp(D \ln N) & \text{for } N > 450 \end{cases} \quad (8)$$

$$\Gamma_N^{\text{diss}} = \begin{cases} \exp[E (\ln N)^F] & \text{for } N \leq 450 \\ \exp[G \ln(\ln N) + H] & \text{for } N > 450 \end{cases} \quad (9)$$

The values of the numerical parameters (A through H) are summarized in Table I.

III. CU CLUSTER BEHAVIOR

The DFT-ANN model is used firstly to determine the stability and mobility of Cu clusters of various sizes. The diffusion coefficients and lifetime of a few selected cluster

TABLE I. Parameters used to fit the cluster properties in the hybrid KMC model.

Γ_N^{diss}	773 K	823 K	873 K	973 K
A	$6.89 \cdot 10^8$	$1.74 \cdot 10^9$	$3.95 \cdot 10^9$	$1.58 \cdot 10^{10}$
B	-6.980	-7.130	-7.262	-7.487
C	$2.57 \cdot 10^{10}$	$3.44 \cdot 10^{10}$	$4.45 \cdot 10^{10}$	$6.88 \cdot 10^{10}$
D	-2.683	-2.628	-2.579	2.496
Γ_N^{mig}	773 K	823 K	873 K	973 K
E	32.935	27.879	25.946	24.808
F	-1.174	-0.905	-0.744	-0.560
G	-7.200	-6.929	-6.689	-6.283
H	16.862	17.899	18.820	20.372

sizes are shown in Fig. 3, where they are compared to the calculations of the EAM-ANN method¹³. The continuous lines show the results of the linear fitting in the Arrhenius domain, which yields activation energies and prefactors for migration and dissociation (the slopes in Fig. 3a and 3b, respectively). The latter parameters are presented in Fig. 6.

Copper clusters are here found to be considerably more stable and slightly more mobile with respect to the EAM-ANN prediction, as they are characterized by larger dissociation and lower migration energies. Most importantly, the mean free paths (MFP) are significantly longer, reaching up to several lattice units, as is shown in Fig. 4, mainly because of the increased stability. This entails that according to this method copper-cluster migration is notably longer-ranged. In addition, the MFP increases with cluster size up to approximately 100 atoms, and this effect disappears above 1125 K. This suggests that larger clusters can actually cover longer distances, although in a longer time because of the lower diffusion coefficients. In general, the coalescence of medium-sized clusters, which was already previously¹³ found to be one of the main features driving Cu precipitation, is expected to play an even more important role.

The AKMC simulations have also shown a different dissociation behavior with respect to the EAM-ANN work¹³. Here, in several occasions the cluster dissociates after emission of several copper atoms, as opposed to the EAM-ANN case where the sporadic emission of a vacancy-Cu pair was recorded. The average number of emitted atoms is independent of cluster size and temperature up to 1125 K. For this reason, in the hybrid KMC simulations the vacancy emission by a Cu cluster is accompanied by the emission of n Cu atoms, according to a probability distribution with average $\bar{n}_{\text{Cu}}^{\text{diss}} = 1.25$.

In summary, the DFT-ANN approach leads to copper clusters that are more stable, more mobile, and that can cover considerable distances in the lattice. The stability is strongly enhanced by the low vacancy formation energy in bcc copper (0.85 eV), compared to that in bcc iron (2.18 eV³⁵). Furthermore, the peculiar loss of single Cu atoms might be related to the strong kinetic coupling with single vacancies that was highlighted in an-

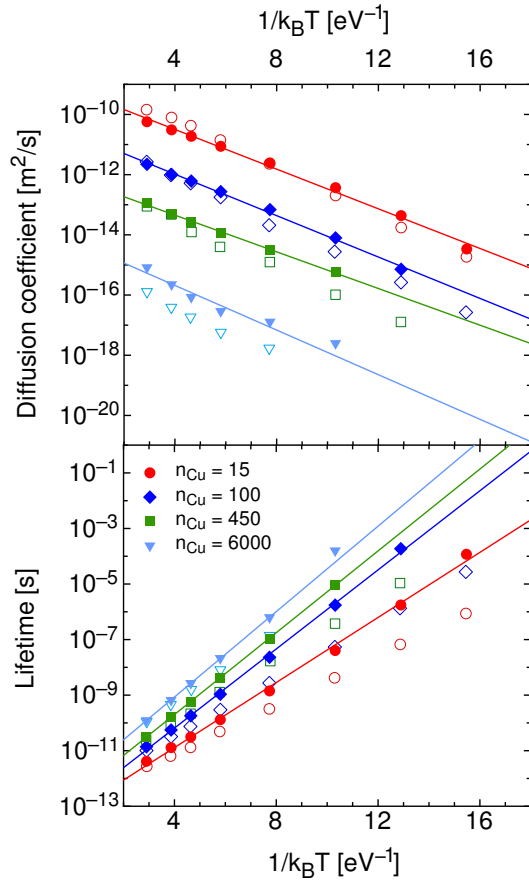


FIG. 3. a) Average diffusion coefficients and b) average lifetime of copper clusters containing a vacancy, as obtained by means of AKMC simulations based on the *ab initio*-trained neural network. The open symbols represent the results obtained with the previous EAM-ANN approach¹³.

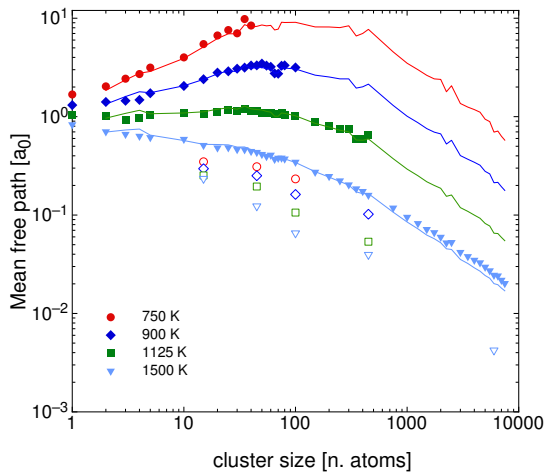


FIG. 4. Average mean free path of copper clusters of increasing size, as obtained with the DFT-ANN approach and compared to the EAM-ANN work¹³ (open symbols).

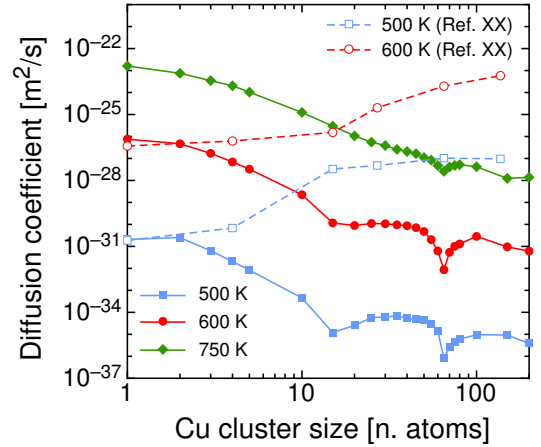


FIG. 5. Diffusion coefficient of copper clusters as a function of size, compared to KMC simulations based on a broken-bond model¹¹. The coefficients are scaled based on the tracer Cu diffusion coefficient calculated by a mean-field method³⁵.

other work³⁵. In dilute iron alloys, Cu atoms are strongly coupled to vacancies (i.e. they are dragged by vacancies) up to approximately 1100 K. This threshold coincides with the threshold temperature above which the Cu clusters cease to emit Cu atoms. In addition, it corresponds as well to the temperature where the long-ranged cluster diffusion is damped. This suggests that the drag mechanism might be in competition with the strong Cu cluster stability, although the actual flux-coupling tendency in a Cu-rich environment is yet unknown.

The cluster behavior can be compared to the work of Soisson and Fu¹¹, where it was investigated with AKMC simulations based on a pair-interaction broken-bond model. That model was fitted on a set of *ab initio* data, including a few jump frequencies. The authors found an increasing diffusion coefficient with cluster size up to approximately 150 atoms. This was explained by an increased vacancy concentration near the surface with respect to the bulk, under the assumption that cluster migration is driven only by vacancy jumps occurring next to the surface.

The aforementioned study¹¹ is compared with the cluster properties predicted by the DFT-ANN method in Fig. 5. With the approach pursued in this work, the cluster diffusion coefficient is overestimated because the vacancy reside always inside the cluster, whereas the simulation time should be rescaled according to the amount of time the vacancy spends in a pure-iron environment^{11,13}. In Fig. 5, the simulation time has been rescaled based on the diffusion coefficient of the Cu monomer in pure iron³⁵, and the curves for increasing cluster sizes have been shifted accordingly. The single copper and the duple are in substantial agreement with the previous KMC work¹¹, but the diffusion coefficient does not increase with size in the investigated temperature range. Interestingly, the diffusion enhancement evidenced by Sois-

son and Fu matches the MFP increase shown in Fig. 4, which is at any rate due to the enhanced stability rather than to an improved mobility. The DFT-ANN model therefore predicts that medium-sized clusters are slower, but considerably more stable than the smaller ones, and are therefore "more mobile" in the sense that longer distances can be covered. Moreover, Fig. 6 shows a decrease of migration energy from approximately 50 to 400 atoms, which is "masked" by the decreasing prefactor D_0 . It should be mentioned, however, that the time-rescaling approach here applied neglects the effect of the increasing cluster-vacancy binding energy with cluster size. This term entails an increase of the equilibrium vacancy concentration, with a consequent diffusivity increase. The mismatch between this and the previous work¹¹ might therefore be smaller than shown in Fig. 5. Finally, it is worth highlighting the appearance of "magic" cluster sizes, corresponding to particularly stable configurations, in analogy with what was found for pure vacancy clusters¹⁴. Such configurations correspond to complete filling of atomic shells: for instance, at $n = 15$ the 1nn and 2nn shells are completely full, and the same applies at $n = 65$ for all shells from the 1nn to the 6nn. This effect disappears with increasing temperature because of the overall decrease of stability.

In Fig. 6, the binding energy of the $v\text{Cu}_n$ clusters is obtained as $E^b = E^{\text{diss}} - E^{\text{mig}}$. It increases steadily with cluster size up to about 300 atoms, before reaching a plateau. The latter corresponds for very large clusters to the segregation energy of a vacancy on an Fe/Cu interface. Moreover, Fig. 6 (dashed line) shows as well the cluster binding energies computed directly with DFT, using the same settings as for the migration-barrier calculations. The same trend is found, with a shift due to the vacancy-copper binding energy. The agreement between the direct DFT measurement and the indirect AKMC calculation proves the capability of the ANN to transfer the properties of the cohesive model into the KMC simulations.

As a further benchmark, the stability and mobility properties of vacancy-Cu pairs are compared to those obtained in a previous study³⁴ based on the same AKMC algorithm. In that case, the *ab initio* jump frequencies of the dilute alloy were directly implemented. Table II shows the comparison in terms of dissociation and activation energies and prefactors, obtained by fitting in the temperature range 400-750 K. The results are in good agreement, with the exception of the dissociation energy which is here slightly lower because of a stricter cluster definition (3nn here with respect to the previous 5nn condition³⁴), which leads to faster dissociation. This shows once again that the DFT thermodynamic and kinetic properties are correctly transferred by the ANN. In particular, copper-vacancy flux-coupling tendencies are known to be very sensitive to the migration barriers in the vacancy LAE³⁵, but are nevertheless well reproduced. The migration barrier of the two-copper cluster is considerably lower than that of the vacancy-copper pair, in

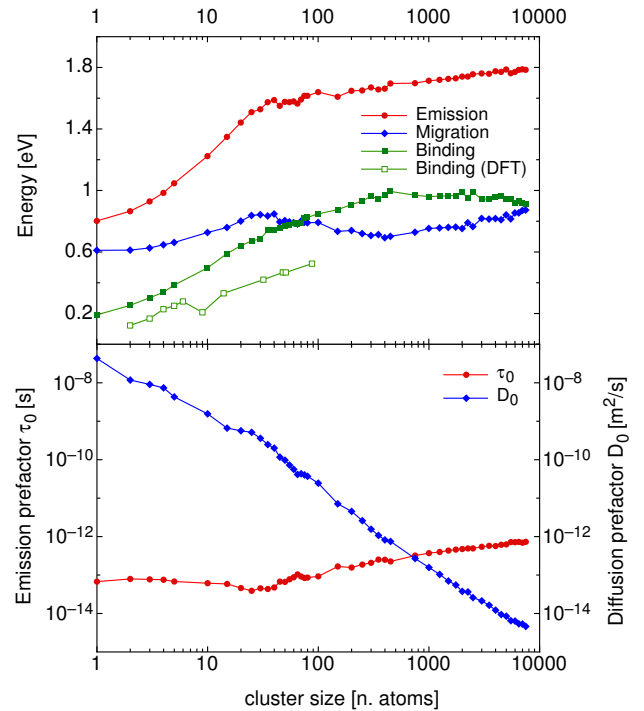


FIG. 6. Migration, dissociation, and binding energy (above), and emission and diffusion prefactors (below) for copper clusters of increasing size, obtained by Arrhenius fitting in the temperature range 750-4000 K. The AKMC binding energy (full symbols) is compared to direct DFT calculations of the binding energy of pure Cu clusters (open symbols).

analogy with the case of two- and three-vacancy clusters with respect to the monovacancy^{14,37}. Finally, it is worth evidencing the large difference between the fitted activation energies in Table II below 750 K, and those above 750 K in Fig. 6. This observation, combined with the other aforementioned property changes across 1100 K, suggests a strong difference in the physical behavior of copper clusters between the low and the high temperature range, which is due to the strong vacancy-copper correlations arising at low temperature. The use of DFT for the ANN training ensures that the low-temperature behavior of the system is correctly described.

IV. SIMULATION OF THERMAL AGEING

The thermal-aging evolution of three different FeCu alloys containing respectively 1.34%, 1.1%, and 0.6% Cu is simulated here with the hybrid KMC approach described in the methodology section. The average cluster size and number density are compared with neutron-scattering and atom-probe measurements³⁸⁻⁴³. For the cluster-population analysis, only clusters larger than 25 atoms are considered, accordingly with the minimum cluster size detectable with the aforementioned experimental techniques (≈ 0.5 nm). The choice of the size

TABLE II. Diffusion and dissociation parameters of vacancy-copper pairs and clusters obtained by Arrhenius fitting in the temperature range 400-750 K, compared with the results of analogous AKMC simulations with a direct implementation of an *ab initio* multifrequency model³⁴.

	E^{diss} (eV)	τ_0 (10^{-14} s)	E^{mig} (eV)	D_0 (10^{-8} m ² /s)
Dilute alloy³⁴				
v-Cu ₁	0.95	1.47	0.73	9.11
This work				
v-Cu ₁	0.87	2.54	0.72	14.6
v-Cu ₂	0.93	2.87	0.58	0.83
v-Cu ₃	1.01	2.48	0.67	1.52
v-Cu ₄	1.12	1.18	0.72	1.68

cutoff has anyway little effect on the results, which are reported in Fig. 7.

In all cases, the simulation time has been rescaled according to the procedure described above, and setting $A = 1$. The OKMC evolution in the Fe-1.34%Cu alloy at 773 K is seemingly in good agreement with experiments. At higher temperatures, the simulation has not reached the experimental time but the size evolution seems to be compatible with the experimental one. The precipitation seems however slightly anticipated, which suggests the arising of some entropic effects ($A \neq 1$). The cluster-size evolution in the Fe-1.1%Cu alloy is seemingly well reproduced, but the prediction of the number density is in disagreement, analogously to the simulations with the EAM-ANN method¹³. This suggests that the analysis of the experiments for this alloy⁴⁰ may be incorrect, considering the incompatibility of the number-density evolution with respect to the other alloys (1.34% and 0.6%Cu).

Finally, the evolution of the Fe-0.6%Cu alloy matches the experimental cluster size, but not in terms of number density: namely, the OKMC simulations here overestimate the amount of Cu precipitates. This is likely driven by the solution energy of Cu in bcc Fe, which is known to be predicted by DFT as significantly higher (PAW-PBE gives 0.76 eV¹⁵) than the value that can be deduced from the measured solubility limit (0.5 eV¹¹). Less exact DFT implementations, such as the ultrasoft pseudopotential (USPP) method, do predict values in close agreement with experiments^{15,16}, but most likely due to fortuitous cancellation of errors. The USPP method is known to provide inaccurate predictions of several other properties, such as solute-defect interactions, magnetic moments and solubility of other transition-metal solutes (e.g. Cr)¹⁵.

The copper solubility is therefore underestimated here. The stronger driving force to precipitation leads to an excessively high density of Cu clusters, especially noticeable for the alloy with the lowest Cu concentration. This issue might be solved by employing the USPP method to calculate the migration barriers for the ANN training, although the USPP reliability for saddle-point calculations

has to be carefully verified. Alternatively, two neural networks can be implemented in parallel: one aimed at interpolating the energy of the equilibrium configurations, and the other focused on the saddle-point energies. This different approach would allow for the use of two different DFT methods for thermodynamic and kinetic properties. This issue will be addressed in future works.

At any rate, such simulations show that the ANN application to DFT migration barriers is able to transfer the properties described by the chosen DFT method to the KMC model. This approach can therefore allow for the direct introduction in KMC simulations of DFT calculations. Moreover, it can also be applied to more complex alloys, without the necessity of developing purposed interatomic potentials. A great advantage of this approach is in fact the simple transferrability that DFT allows automatically for complex chemistry. Making truly reliable multicomponent interatomic alloy potentials is extremely difficult, while in DFT it represents no particular obstacle.

V. CONCLUSIONS

The main objective of this work is to present a novel approach for the prediction of unknown transition rates in kinetic Monte Carlo simulations. This approach takes advantage of an artificial neural network to perform non-linear regression in a dataset of accurate *ab initio* migration barriers, replacing the use of interatomic potentials¹³. The main advantage is the possibility of directly implementing the DFT thermodynamic and kinetic information into the KMC simulation, which would be difficult to achieve with the traditional methods. For instance, solute-defect flux-coupling tendencies³⁵ are very sensitive to the variation of transition rates in the local atomic environment, and require therefore an accurate prediction of the migration barriers. A careful selection of the sample transitions for the neural network training is necessary, as it must ensure that all possible local atomic environments are sufficiently sampled, while limiting the amount of DFT calculations required.

The application to thermal aging in dilute Fe(Cu) alloys shows that the DFT properties are correctly transferred to the hybrid KMC model. The low vacancy formation energy in copper and the strong vacancy-copper correlations make the copper cluster particularly stable. Thanks to the enhanced stability, the clusters are able to cover long distances in the lattice, which confirms the role of large-cluster coagulation in the copper precipitation process. Kinetic coupling between the vacancy and single copper atoms is also observed to cause loss of copper atoms during the cluster motion, and marks the temperature range in which the clusters are mobile. As opposed to previous calculations¹¹, clusters of increasing size are not faster, but are more mobile in terms of longer distances covered. Finally, the evolution of Cu precipitation is well simulated in all cases except a very dilute

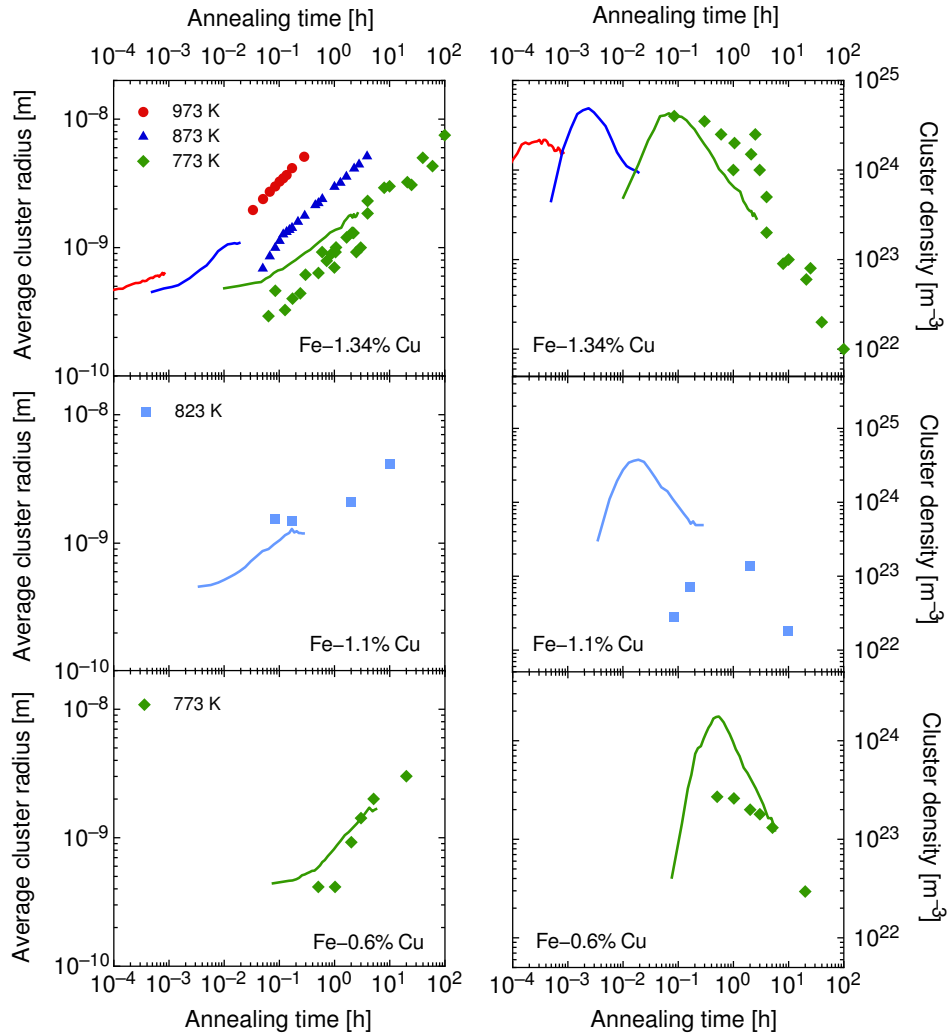


FIG. 7. Comparison with experimental data^{38–43} of the microstructure evolution of thermally aged FeCu alloys, obtained by means of the hybrid KMC model based on the DFT-ANN prediction of transition rates and copper-cluster properties.

FeCu alloy, where an excessively high cluster density is recorded. This is due to the incorrect prediction of the Cu solution energy in Fe by DFT. At any rate, this test shows that the ANN has been successful in carrying the information contained in the DFT dataset. Splitting the thermodynamic and kinetic parameterization in two separate parallel neural networks would allow for the use of two different cohesive models. In this way, the most suitable ones could be chosen to improve the description of both the equilibrium and the saddle-point energies.

In conclusion, the method has been shown to be feasible with a significant but affordable computational effort, and can potentially allow for a more direct application of massive amounts of *ab initio* calculations to KMC simulations, as opposed to the usual approaches (e.g. pair-interaction or broken-bond models) where only few *ab initio* data can be fitted. With a modest increase of computational effort, the method can be easily extended to more complex systems, without requiring the

cumbersome purposed development of multicomponent interatomic potentials. For this reason, it surely represents a promising tool for simulating the microstructure evolution of alloys in a wide range of applications and conditions.

ACKNOWLEDGMENTS

The authors acknowledge the financial support from Vattenfall AB, Göran Gustafsson Stiftelse, and the Euratom research and training programme 2014-2018 under the grant agreement No 661913 (SOTERIA). This work contributes to the Joint Programs of Nuclear Materials (JPNM) of the European Energy Research Alliance (EERA). The high-performance computing resources were provided by EDF-R&D and by the Swedish National Infrastructure for Computing (SNIC). In addition, the authors acknowledge L. Malerba and F. Soisson for the valu-

able discussions.

- ¹E. Meslin, B. Radiguet, P. Pareige, and A. Barbu, *J. Nucl. Mater.* **399**, 137 (2010).
- ²M. K. Miller, K. A. Powers, R. K. Nanstad, and P. Efsing, *J. Nucl. Mater.* **437**, 107 (2013).
- ³P. B. Wells, T. Yamamoto, B. Miller, T. Milot, J. Cole, Y. Wu, and G. R. Odette, *Acta Mater.* **80**, 205 (2014).
- ⁴J. P. Wharry and G. S. Was, *J. Nucl. Mater.* **442**, 7 (2013).
- ⁵C. Pareige, V. Kuksenko, and P. Pareige, *J. Nucl. Mater.* **456**, 471 (2015).
- ⁶G. R. Odette and R. K. Nanstad, *JOM* **61**, 17 (2009).
- ⁷P. Efsing, J. Roud en, and M. Lundgren, in *Effects of Radiation on Nuclear Materials: 25th Volume*, edited by T. Yamamoto (ASTM International, West Conshohocken, 2012) pp. 52–68.
- ⁸C. S. Becquart and C. Domain, *Phys. Status Solidi B* **247**, 9 (2010).
- ⁹C. S. Becquart and C. Domain, *Metall. Mat. Trans. A* **42**, 852 (2010).
- ¹⁰A. R. Allnatt and A. B. Lidiard, *Atomic Transport in Solids* (Cambridge University Press, 2003).
- ¹¹F. Soisson and C.-C. Fu, *Phys. Rev. B* **76**, 214102 (2007).
- ¹²N. Castin, R. Pinheiro Domingos, and L. Malerba, *Int. J. Comput. Int. Sys.* **1**, 340 (2008).
- ¹³N. Castin, M. I. Pascuet, and L. Malerba, *J. Chem. Phys.* **135**, 064502 (2011).
- ¹⁴N. Castin, M. I. Pascuet, and L. Malerba, *J. Nucl. Mater.* **429**, 315 (2012).
- ¹⁵P. Olsson, T. P. C. Klaver, and C. Domain, *Phys. Rev. B* **81**, 054102 (2010).
- ¹⁶C. Domain and C. S. Becquart, *Phys. Rev. B* **65**, 024103 (2001).
- ¹⁷C. M. Bishop, *Rev. Sci. Instrum.* **65**, 1803 (1994).
- ¹⁸N. Castin and L. Malerba, *J. Chem. Phys.* **132**, 074507 (2010).
- ¹⁹G. Kresse and J. Hafner, *Phys. Rev. B* **47**, 558 (1993).
- ²⁰G. Kresse and J. Hafner, *Phys. Rev. B* **49**, 14251 (1994).
- ²¹G. Kresse and J. Hafner, *J. Phys. Condens. Matter* **6**, 8245 (1994).
- ²²P. E. Bl ochl, *Phys. Rev. B* **50**, 17953 (1994).
- ²³G. Kresse and D. Joubert, *Phys. Rev. B* **59**, 1758 (1999).
- ²⁴J. P. Perdew, K. Burke, and Y. Wang, *Phys. Rev. B* **54**, 16533 (1996).
- ²⁵S. H. Vosko, L. Wilk, and M. Nusair, *Can. J. Phys.* **58**, 1200 (1980).
- ²⁶P. Olsson, C. Domain, and J. Wallenius, *Phys. Rev. B* **75**, 014110 (2007).
- ²⁷G. Mills, H. Jonsson, and G. K. Schenter, *Surf. Sci.* **324**, 305 (1995).
- ²⁸H. Jonsson, G. Mills, and K. W. Jacobsen, in *Classical and quantum dynamics in condensed phase simulations*, edited by B. J. Berne, G. Ciccotti, and D. F. Coker (World Scientific, 1998).
- ²⁹G. Henkelman, B. P. Uberuaga, and H. Jonsson, *J. Chem. Phys.* **113**, 9901 (2000).
- ³⁰L. Messina, M. Nastar, N. Sandberg, and P. Olsson, submitted to *Phys. Rev. B*.
- ³¹E. Vincent, C. S. Becquart, and C. Domain, *J. Nucl. Mater.* **382**, 154 (2008).
- ³²A. B. Bortz, M. H. Kalos, and J. L. Lebowitz, *J. Comput. Phys.* **17**, 10 (1975).
- ³³M. I. Pascuet, N. Castin, C. S. Becquart, and L. Malerba, *J. Nucl. Mater.* **412**, 106 (2011).
- ³⁴L. Messina, L. Malerba, and P. Olsson, *Nucl. Instrum. Methods Phys. Res. B* (2015).
- ³⁵L. Messina, M. Nastar, T. Garnier, C. Domain, and P. Olsson, *Phys. Rev. B* **90**, 104203 (2014).
- ³⁶G. E. Lucas and R. Sch aublin, *Nucl. Instrum. Methods Phys. Res. B* **267**, 3009 (2009).
- ³⁷F. Djurabekova, L. Malerba, R. C. Pasianot, P. Olsson, and K. Nordlund, *Philos. Mag.* **90**, 2585 (2010).
- ³⁸S. R. Goodman, S. S. Brenner, and J. R. Low, *Metall. Trans.* **4**, 2371 (1973).
- ³⁹R. Kampmann and R. Wagner (Springer, New York, 1986) p. 76.
- ⁴⁰J. T. Buswell, C. A. English, M. G. Hetherington, W. J. Pythian, G. D. W. Smith, and G. M. Worrall, *Effects of radiation on materials: 14th International Symposium (Volume II), ASTM STP 1046*, edited by N. H. Packan, R. E. Stoller, and A. S. Kumar (American Society for Testing and Materials, Philadelphia, 1990).
- ⁴¹M. H. Mathon, A. Barbu, F. Dunstetter, F. Maury, N. Lorenzelli, and C. H. De Novion, *J. Nucl. Mater.* **245**, 224 (1997).
- ⁴²M. Perez, F. Perrard, V. Massardier, X. Kleber, A. Deschamps, H. de Monestrol, P. Pareige, and G. Covarel, *Philos. Mag.* **85**, 2197 (2007).
- ⁴³E. Vincent, C. S. Becquart, C. Pareige, P. Pareige, and C. Domain, *J. Nucl. Mater.* **373**, 387 (2008).